MODELING MULTISYSTEM BIOLOGICAL EFFECTS OF MULTIROUTE EXPOSURES TO AIR POLLUTANTS

By

LONGFEI CHAO

A dissertation submitted to the

Graduate School—New Brunswick

Rutgers, The State University of New Jersey

In partial fulfillment of the requirements

For the degree of

Doctor of Philosophy

Graduate Program in Chemical and Biochemical Engineering

Written under the direction of

Panos G. Georgopoulos

And approved by

_____

_____

_____

_____

New Brunswick, New Jersey

October, 2020

ABSTRACT OF THE DISSERTATION

MODELING MULTISYSTEM BIOLOGICAL EFFECTS OF MULTIROUTE EXPOSURES TO AIR POLLUTANTS

By LONGFEI CHAO

Dissertation Director:

Panos G. Georgopoulos

Nine out of ten people are breathing polluted air worldwide. Health concerns associated with human exposures to air pollutants, such as ozone and particulate matter (PM), have become a persisting and widespread problem around the globe. Interconnected, multiscale, mechanistic models were developed to study the exposure biology of air pollution in the respiratory, cardiovascular and integumentary systems, resulting from inhalation and dermal contact exposure routes. Lung function alterations were linked with ozone inhalation using a multiscale model that considers pulmonary surfactant depletion by ozone reactions, pulmonary inflammation after ozone exposure and the expansion / contraction of the alveolar units. A computational model for cardiovascular effects of air pollution was developed and implemented for human PM exposure using heart rate variability (HRV) as the health endpoint. Specific considerations were given to PM-initiated excessive oxidative stress and pro-

/ anti-inflammatory signaling at cellular level, neuroendocrine-immune system interactions and systemic inflammation propagation. The skin biology after air pollutant exposure was studied by mechanistic models that respectively addressed skin surface reactions, AhR activation and cell cycle regulation in keratinocytes. Inflammatory responses are often evoked when air pollutants exert their detrimental effects in any physiological system mentioned above. Macrophage is an essential type of immune cell that plays critical roles in the regulation of inflammation. An agent-based model that spans molecular, cellular and tissue levels was developed aiming at reproducing and elucidating the dynamics of macrophage polarization under various complex activation signals, while considering system stochasticity and heterogeneity. Key factors in signaling cascades were included in this model, and critical underlying regulatory controls influencing the polarization process were explored and quantified. All models were evaluated with data of *in vitro* and *in vivo* measurements from different sources. These models formed a platform that integrates physiological, biochemical and experimental information for various organ systems to mechanistically investigate biological effects initiated by air pollutants.

Acknowledgment

I would like to express my sincerest thanks to my advisor Dr. Panos G. Georgopoulos for his guidance and endless support over my years in the Computational Chemodynamics Laboratory (CCL) at Rutgers University. He accepted me as his PhD student at the toughest moment of my graduate study and really changed my life trajectory. The advice he provides during tough times and his great work ethic have been and will be always inspiring me.

I am also grateful to my committee members Dr. Andrew Gow, Dr. Henrik Pedersen and Dr. Marianthi Ierapetritou for their insightful comments and for taking time to guide me through my dissertation. I really appreciate Dr. Gow's help for providing experimental data and supports which tremendously help the completion of this dissertation.

I would like to thank Dr. Dwaipayan Mukherjee who introduced me to computational modeling and shared a lot of his knowledge and experiences with me. I appreciate Dr. Tung Nguyen's help for teaching me agent-based modeling techniques. I would like to thank Dr. Marianthi Ierapetritou, who as the department chair, encouraged me to overcome setbacks and helped me start my research in CCL. I am grateful to Dr. Charles Roth, who as the graduate director, has always been patient and supportive.

I would like to extend my gratitude to my CCL colleagues Ms. Helene Derisi, Ting Cai, Zhongyuan Mi, Xiang Ren and Tasha Turner. They have created such an

encouraging and friendly atmosphere in the lab and made my experiences in CCL wonderful and memorable. I wish to thank all other friends who I met at Rutgers for their help and companionship.

I cannot emphasize enough the thankfulness I have for my wife, Wenjun Zheng. She has always been by my side, giving me encouragement and support in every possible way. My deepest gratitude goes to my beloved mother Yufang Zhang. Without her unconditional love, this dissertation would not have been possible.

Dedication

To my mother Yufang Zhang

And to my wife Wenjun Zheng

Table of Contents

List of Tables

List of Figures

Chapter 1

Introduction

1.1 Background

Concerns about air pollution have a long and complex history. Problems caused by air pollution can be traced back to the days of ancient Rome. After the Industrial Revolution, air quality worsened considerably due to the wide use of fossil fuels, especially in the urban areas of some European countries and the United States. In December 1952, the 5-day London Smog Episode led to the deaths of 12,000 people caused by heavy exposures to airborne mixtures of soot, sulfur dioxide and calcium sulfate particles. From the 1940s to the 1960s, photochemical smog characterized by high concentrations of ground-level ozone hovered over Los Angeles, CA in the United States causing detrimental health effects to millions of people. Since then, modern air pollution legislation and abatement measures for air quality control have been implemented and air quality in industrialized countries (e.g. the US and European countries) has been greatly improved over the past six decades. In developing countries (e.g. China and India), however, air pollution problems have become much more severe in recent years due to large-scale industrialization and urbanization coupled with rapid transportation development. Nowadays, air pollution has become a universal issue around the globe. According to data from the World Health Organization

(WHO), more than 92% of the world population live in places where the WHO air quality guidelines levels are not met [1]. Even in the United States, more than 40% of the population are living in areas with unhealthy air pollution levels [2].

It is well established that air pollution is associated with various health effects. For sensitive and susceptible people, even low air pollution levels can exert significant detrimental effects on their health. Short-term exposure to air pollution can cause cough, asthma, COPD (chronic obstructive pulmonary disease) and other respiratory disease. Long-term effects of air pollution are associated with chronic asthma, pulmonary insufficiency, diabetes, cardiovascular diseases, etc [3]. Collectively, air pollution has become a major risk factor for increased human morbidity and mortality. Figure 1.1 shows the number of deaths attributable to ambient air pollution in

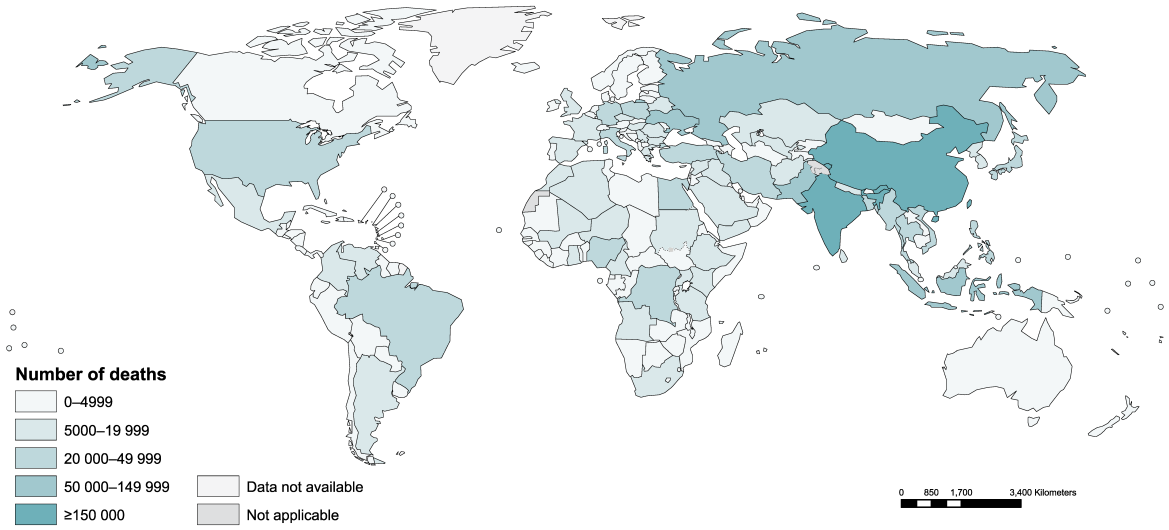

Figure 1.1: Death attributable to ambient air pollution in 2012 [1]

2012 [1]. Ambient air pollution alone kills about 3 million people each year globally. If we count in household indoor air pollution, nearly 7 million premature deaths per year - one in eight of total global deaths - are associated with air pollution exposures. Therefore, studying the biological effects of air pollution is of great importance. Air pollution is a mixture of thousands of components. Among them, ground level ozone

and airborne particulate matter (PM) are considered as probably the most significant causes of premature deaths related to poor ambient air quality [4]. This thesis aims to develop and apply computational models that span multiple biological scales to study the biological effects of air pollutants, especially ozone and PM, in multiple physiological systems.

1.2 Multi-routes exposure and multi-system effects of air pollution

The health impacts of an air pollutant depend on the route through which it enters the human body and the subsequent interactions it undergoes once inside the body. There are three major exposure routes through which humans get in contact with pollutions: inhalation, ingestion and dermal adsorption. Inhalation exposure results from breathing air that is contaminated with airborne pollutants and it is the primary route of exposure to air pollution. Pollutants can deposit in water and soil to contaminate potential sources of food and drinking water which will be consumed by people and cause ingestion exposures to contaminants. Dermal contact is another important route. Although skin provides a good protection against many pollutants, it is highly possible that airborne contaminates can enter the body when skin cracks and aberrations are present. Highly oxidative pollutants like ozone can also react with skin surface components forming secondary products that penetrate the skin. The different exposure routes do not function independently. For example, during inhalation the mucociliary clearance process filters the air we breathe and forms pollutants-containing phlegm which can be swallowed to enter the digestive tract. During dermal contact with ozone, skin surface lipids can react with ozone to form secondary organic aerosol that enhances the pollutant exposure via inhalation. In this thesis, primary focus is given to modeling the biological events initiated by ozone and

PM due to inhalation exposures with a secondary focus on dermal exposures. Figure

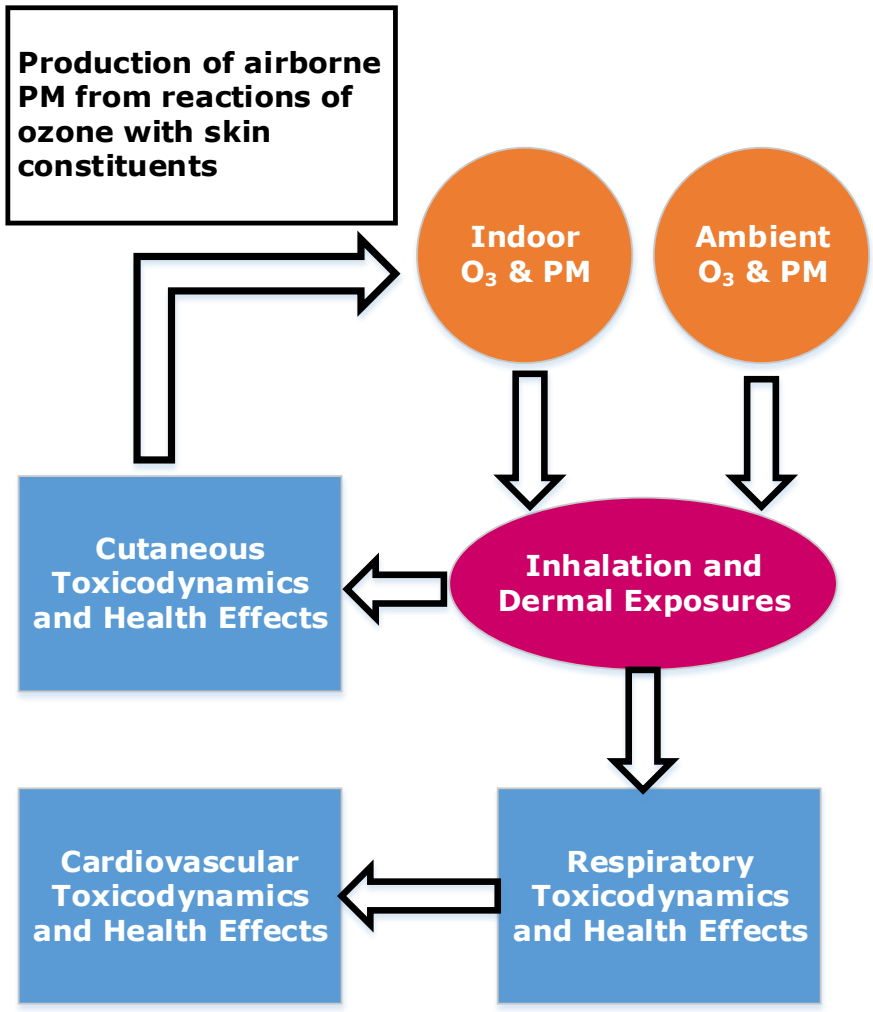

Figure 1.2: Multiple exposure routes and physiological systems considered in this thesis

1.2 shows the two exposure routes and multiple physiological systems considered in this thesis. Exposures to ozone and/or PM via inhalation and dermal contact cause primary health effects in the respiratory and integumentary system, respectively. In addition to local biological events, health effects of ozone and PM extend beyond the lung and skin to other physiological systems, especially the cardiovascular system which is well-known for being affected by ozone and PM exposure. The mechanisms

underlying the multi-system effects of ozone and PM often involve the generation of reactive oxygen species (ROS). For example, ROS result from reactions of ozone with skin lipids during dermal contact and from reactions with lung lining fluid components following inhalation. These secondary ROS initiate series of cascading events, such as release of pro-inflammatory mediators, infiltration of immune cells, activation of aryl hydrocarbon receptor (AhR) pathways, etc. Other physiological systems are subsequently affected: for example, the respiratory-originated pro-inflammation mediators can enter the circulatory system to cause systemic inflammation and subsequent adverse effects in the cardiovascular system.

1.2.1 Respiratory effects associated with air pollutants

First target of inhaled air pollutants is the respiratory tract. The structure of the human respiratory tract is shown in the Appendix. It is well established that air pollutants are strongly associated with adverse respiratory outcomes. According to the Integrated Science Assessment of Ozone and Related Photochemical Oxidants by the U.S. EPA [5], the most salient observations from controlled human ozone-exposure studies include the following: (1) young healthy adults exposed to ozone concentrations $\geq$ 80 ppb develop significant reversible, transient decrements in pulmonary function and symptoms of breathing discomfort if minute ventilation or duration of exposure is increased sufficiently; (2) relative to young adults, children experience similar spirometric responses but lower incidence of symptoms from ozone exposure; (3) relative to young adults, ozone-induced spirometric responses are decreased in older individuals; (4) there is a large degree of intersubject variability in physiologic and symptomatic responses to ozone, but responses tend to be reproducible within a given individual over a period of several months; (5) subjects exposed repeatedly to ozone for several days experience an attenuation of spirometric and symptomatic responses on successive exposures, which is lost after about a week without exposure;

and (6) acute ozone exposure initiates an inflammatory response that may persist for at least 18 to 24 hours postexposure. Epidemiological studies also provide clear evidence for the associations between increases in ambient ozone concentration and increases in respiratory hospital admissions and ER visits [6].

According to the Integrated Science Assessment for Particulate Matter by the U.S. EPA [7], the association between PM and respiratory effects is weaker than that of ozone, but epidemiological studies still demonstrate positive correlations between increases in ambient PM concentrations and increases in respiratory hospitalizations and ER visits. Altered pulmonary function, mild pulmonary inflammation and injury, oxidative responses, airway hyperresponsiveness and exacerbations of allergic responses were observed in a large number of controlled human studies and toxicological studies involving exposure to different types of PM, providing biological plausibility for associations between PM and respiratory morbidity observed in epidemiological studies.

1.2.2 Cardiovascular effects associated with air pollutants

The cardiovascular system and the respiratory system are both hemodynamically and neuronally connected. Detrimental effects initiated in the respiratory system can be propagated to the cardiovascular system. In fact, evidence from epidemiologic studies has consistently supported the link between exposure to air pollution and cardiovascular morbidity and mortality [8–10].

Among all the pollutants associated with cardiovascular impacts, the evidence for PM is the strongest [11]. According to the Integrated Scientific Assessment for PM [7], the preponderance of evidence suggests a causal relationship between PM exposure and increased risk of cardiovascular health outcomes. It is debatable whether there is a certain causal relationship between ozone exposures and cardiovascular impacts. The Integrated Scientific Assessment for Ozone [5] suggests a likely causal

relationship, while others claim that current evidence is not sufficient to support a scientific judgment about this issue [12].

However, in reality people always get exposed to mixtures of co-occurring air pollutants (including both PM and ozone). So we should never rule out the potential effects of ozone when studying cardiovascular effects. Toxicological studies and controlled human studies have been conducted to investigate the cardiovascular effects of PM/ozone. In toxicological studies, *in vivo* assessments demonstrated that PM, including concentrated ambient particles (CAP), diesel exhaust, urban dust and engineered nanoparticles, can enhance vasoconstriction and decrease vasodilatory responses in different species [11]. Although fewer data are available for ozone, Chuang *et al.* observed vascular dysfunction and atherogenesis in mice after a single exposure to ozone [13]. Two other studies using *ex vivo* methods showed that vasorelaxation responses in aortas of mice and coronary arteries of rats were impaired following ozone exposure. Kumarathasan *et al.* demonstrated that plasma endothelin (a vasoconstrictor) levels increased after inhalation of ozone or PM, but co-exposure to ozone and PM seemed to attenuate these effects [14]. Furthermore, other pollutants can sensitize the cardiovascular system to the effects of exposure to ozone. For example, Farraj *et al.* conducted a study where hypertensive rats were exposed to NO_2 in the morning followed by same day ozone exposure in the afternoon [15]. Compared to the control group, rats treated with NO_2 and ozone showed decreased heart rate, increased heart rate variability, decreased blood pressure and increased pulse pressure, suggesting that the cardiovascular system became more sensitive to ozone after pre-exposure to NO_2. In controlled human studies, diesel exhaust, ultrafine carbon particles and CAP were all associated with alteration of vascular function. Brook *et al.* observed that exposure to a mixture of ozone and CAP caused vasoconstriction, but the effect of ozone alone was not tested [16]. Fakhri *et al.* demonstrated that exposure to mixture of ozone and CAPs increased diastolic bold pressure, while

single exposure to ozone did not cause significant changes [17]. Some other studies demonstrated similar effects of co-exposure to PM and ozone, whereas single exposure to ozone decreased blood pressure [18, 19]. Collectively, the association between cardiovascular effects and exposures to PM or mixtures of PM and ozone is strongly supported by toxicological and controlled human studies.

1.2.3 Skin effects associated with air pollutants

Skin (integumentary system) is the largest organ of the human body. Human skin is regularly exposed to many pollutants in gas, liquid and solid forms [20]. In particular, both ozone and PM are associated with multiple skin disorders. Previous studies have shown that PM can affect the progression of inflammatory skin diseases, enhance skin aging and promote skin cancer. Song *et al.* recruited 44 elementary school students with atopic dermatitis, a chronic and recurrent inflammatory skin disease, and significant associations were discovered between ultrafine particle concentrations and the itchiness symptom in the study participants [21]. In a cohort study, Vierkotter *et al.* found that people living in urban areas with higher ambient PM concentrations demonstrated 20% more facial pigment spots formation than those living in rural areas, suggesting that traffic-related PM exacerbates skin aging [22]. A survey conducted by Puntoni *et al.* shows that occupational exposure to black carbon is positively associated with the incidence of melanoma, the most serious type of skin cancer [23].

Although ozone has a history of being used as a therapeutic treatment for skin diseases [24], exposures to air pollutant ozone are associated with skin disorders. A time-series analysis by Xu *et al.* investigated ozone exposure and emergency-room visits for skin diseases [25]. An increase of 10 $\mu g/m^3$ ozone resulted in 0.78% increase in urticarial, 3.84% increase in eczema, 2.86% increase in contact dermatitis, 3.22% increase in rash/other nonspecific eruption and 2.72% increase in infected skin

disease. In addition, ozone may also contribute to premature skin aging. In a cohort study, ozone exposure was found significantly associated with the formation of deeper wrinkles in a group of elderly people, suggesting the potential role of ozone in the extrinsic aging of human skin [26].

1.3 Multiscale modeling with MENTOR

Living organisms are inherently complex biological systems consisting of functional networks operating at various scales. From the human health perspective, any detrimental effects induced by air pollutants are the results of a series of biological events across multiple scales, extending from gene transcription inside the cell nucleus to clinical symptoms at the physiome level. This multiscale nature of air pollution exposure biology requires knowledge and experimental information for each biological level in order to fully understand the health effects of the pollutants. The adverse outcome pathways (AOP) framework is employed here to illustrate current understandings of the mechanisms underlying health effects of air pollution. AOP is a conceptual construct that portrays existing knowledge regarding the linkages between direct molecular initiating events and adverse health outcomes at a biological level of organization relevant to risk assessment [27]. In general, an AOP consist of a series of causally connected events that span multiple levels of biological organization, including molecular initiating events, cellular/extracellular responses, tissue/organ responses and individual responses. Two case examples, shown in Figure 1.3 and Figure 1.4 respectively, demonstrate AOPs of ozone in respiratory, dermal and cardiovascular systems, and AOPs of PM in respiratory and cardiovascular systems (details of these AOP can be found in the Appendix).

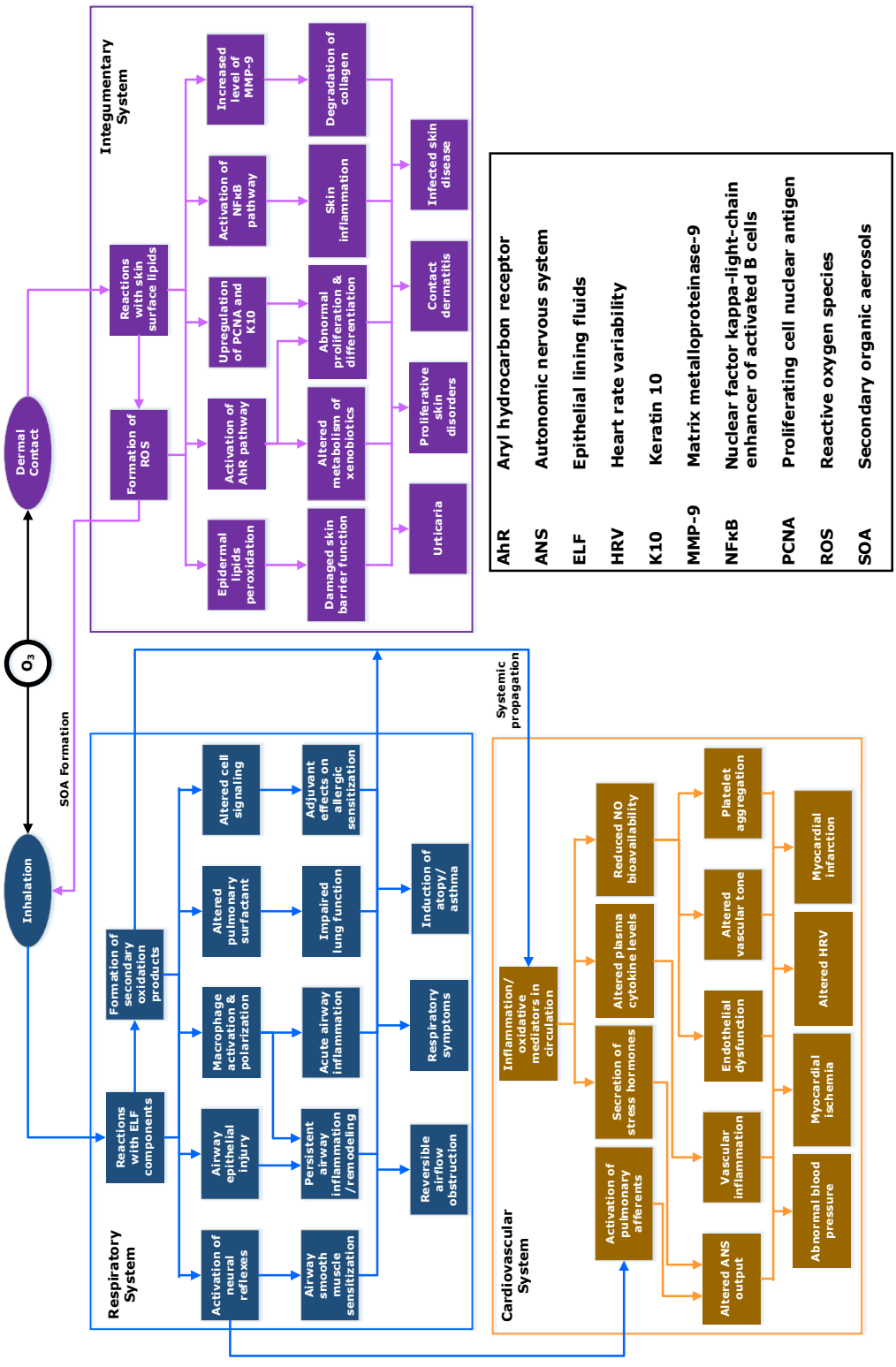

Figure 1.3: Adverse outcome pathways for ozone in the respiratory, dermal and cardiovascular systems

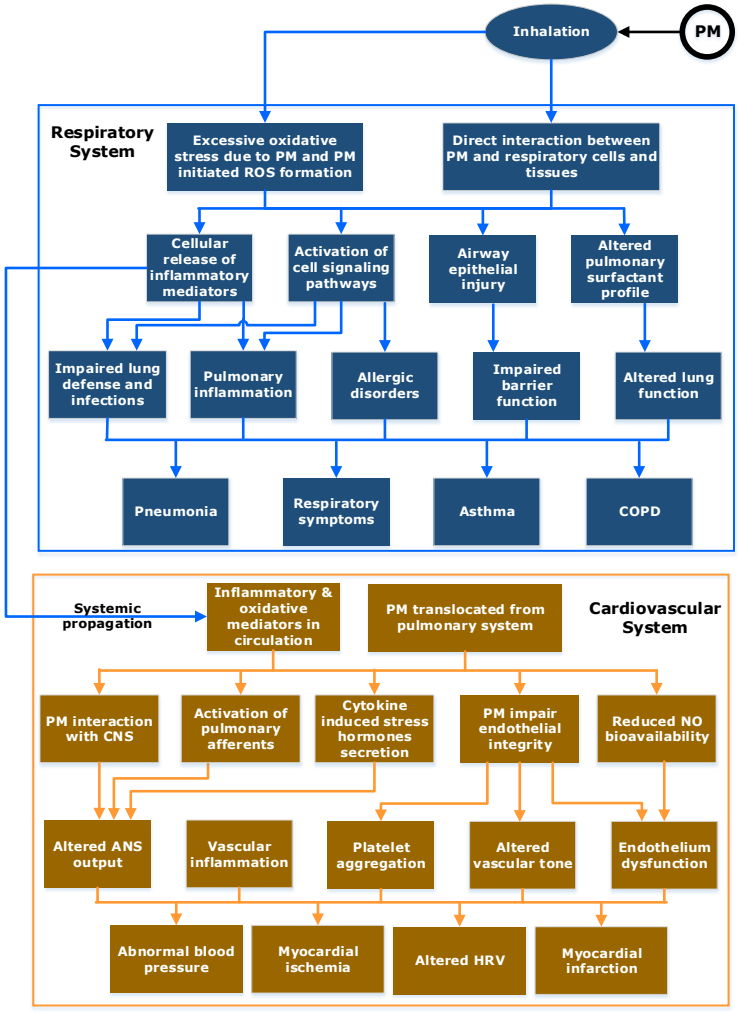

Figure 1.4: Adverse outcome pathways for particulate matter in the respiratory and cardiovascular systems. (CNS: central nervous system; ANS: autonomic nervous system)

Behind each health endpoint induced by ozone and PM are biological events that form interrelated networks across molecular, cellular, tissue and organ scales. This complexity makes it hard to thoroughly investigate the health effects of air pollution using only experimental approaches and brings the need for multiscale modeling. Multiscale computational models are uniquely positioned to study such complex biological systems because they can:

- Bridge the gap in understanding between isolated *in vitro* and *in vivo* experi-

mental studies to capture the connectivity between various scales of biological functions

- Evaluate variables that are not measurable by experimental techniques
- Offer unique advantages to explore complex mechanisms by allowing precise perturbation of any variable/parameter of interest in any biological level involved in the system

The primary focus of this thesis is on developing multiscale computational models which integrate existing mechanisms and experimental information for multiple biological scales to support comprehensive understanding of health effects induced by air pollutants, in particular ozone and PM. This approach originates from the MENTOR (Modeling ENvironment for TOtal Risk) computational platform for human toxicokinetics and toxicodynamics developed by Georgopoulos *et al.* (Figure 1.5) [28], which serves as a foundation for modeling adverse health effects due to hazardous exposures.

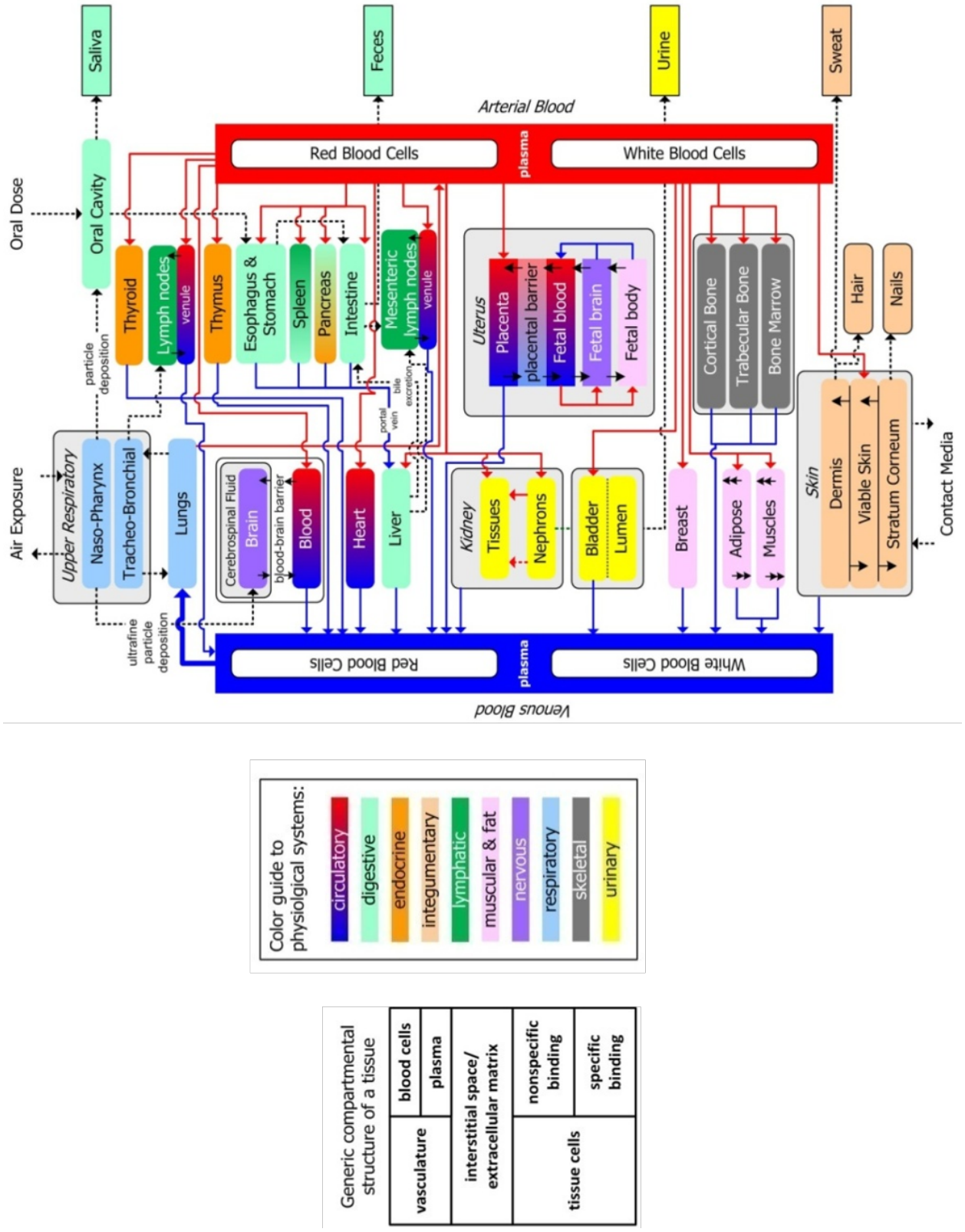

Figure 1.5: The MENTOR integrative multiscale whole body platform for human toxicokinetics and toxicodynamics [28]

The integrative multiscale whole body platform of MENTOR incorporates sufficient physiological and biochemical information for the various organ systems to address the exposure biology modeling needs for a wide range of xenobiotics, including air pollutants such as ozone and PM. The structure of individual tissues and organs is described by multicompartmental formulations that reflect the specific attributes of intracellular and extracellular media, complemented by more detailed models that span multiple scales of biological organization [28]. The multiscale computational models developed in this thesis follow the concepts and structure of MENTOR to specifically address the toxicokinetics and toxicodynamics of air pollutants in respiratory, cardiovascular and integumentary systems by integrating detailed modules for biological processes at various scales, such as gene transcription, intracellular signaling pathway activation, cell-cell interactions, macrophage polarization, biochemical reactions of ozone, inflammation regulation across physiological systems, etc. The mechanistic and multiscale design of the models developed in this thesis is consistent with a computational platform that incorporates different mechanisms across multiple biological levels, thus providing a promising *in silico* tool to study a wide range of other air pollutants in addition to ozone and PM. The models demonstrated here can also be envisioned as "hypothesis generators" that will allow formulation and testing of various hypotheses regarding the mechanisms underlying the health effects of air pollution, and therefore, will support the development of potential therapeutic interventions to attenuate the adverse health outcomes of air pollution.

1.4 Main objectives of the thesis

- Modeling ozone induced lung function changes
  - Modeling interfacial ozone reactions with pulmonary surfactant in the alveolar region of mammalian lungs and the changes of pulmonary surfactant

dynamics at the tissue level

  - Modeling immune responses initiated by ozone-macrophage interactions
  - Integrating information on pulmonary surfactant dynamics and immune responses with the alveolar recruitment/derecruitment model to link ozone inhalation with lung function alterations in mice

- Modeling reduced heart rate variability (HRV) due to exposure to particulate matter (PM)
  - Developing models for cellular inflammatory signaling pathways and cross-systems regulation of inflammatory responses initiated by PM exposures
  - Linking systemic pro-inflammatory signals to HRV changes

- Development of models for skin biology initiated by exposures to air pollutants
  - Modeling the formation of secondary organic aerosol via ozone skin surface reactions
  - Modeling AhR activation and subsequent gene transcription in response to air pollution related environmental agents
  - Developing a model to study the regulatory roles of AhR on cell cycle progression in keratinocytes

- Agent-based modeling of macrophage polarization, to assess the dynamic of macrophage activation
  - Building a model for macrophage polarization by incorporating relevant transcription factors in macrophages for different external stimuli
  - To capture the dynamic of macrophages polarization by implementing the model using an agent-based modeling approach

Chapter 2

A Multiscale Computational Model for Ozone Induced Lung Function Changes in Mice

2.1 Introduction

Ground-level ozone is a major air pollutant with adverse health effects associated with respiratory morbidity and mortality [29]. Emerging evidence has shown that exposure to ozone concentrations at or below the current regulatory standards are associated with increased mortality due to respiratory diseases [30]. Currently more than 40% of the people in the United States are still living in areas with unhealthy levels of ozone pollution [2], requiring focus on pulmonary mechanisms of ozone toxicity. Since it is a potent oxidative gas, ozone exposures through inhalation cause oxidative damages to pulmonary cells and lining fluids, and subsequent immune-inflammatory responses within the respiratory system, leading to breathing difficulty, reduced lung function and exacerbation of various lung diseases.

The multiscale model developed in this study is an attempt to link cellular and tissue level toxicodynamics changes induced by ozone inhalation to measurable changes in lung function from a mechanistic point of view. The mathematical model described

here simulates the mechanical operation of the mouse lung, involving the expansion and compression of alveoli, and links pulmonary tissue resistance with surfactant dynamics in the alveolar hypophase, pulmonary inflammatory responses and the dynamic surface tension of the alveolar air-liquid interface. The effect of progressive chronic inflammation is also explored by implementing the model for mice deficient in surfactant protein D, a pulmonary collectin that functions as an anti-inflammatory protein [31]. The multiscale model can be decomposed into three functional modules: Surfactant Dynamics Module, Immune Responses Module and Lung Mechanics Module (Figure 2.1). It serves as a tool which can be further expanded and extended to other species, to provide system level predictions and develop key insights to systemic behavior due to inhalation of ozone and related air pollutants.

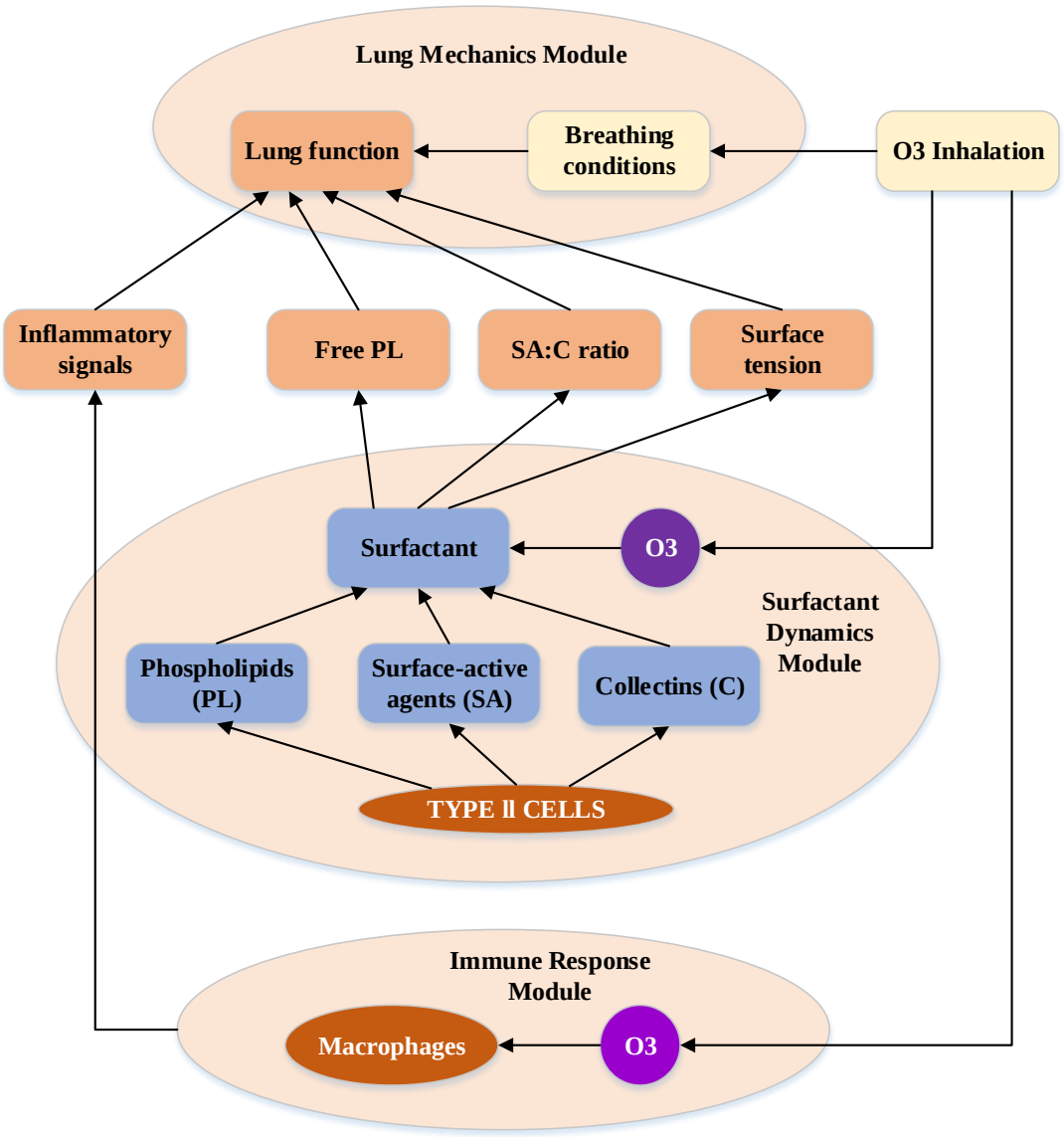

Figure 2.1: Schematic describing the modularization of the multiscale lung model into mechanistic modules capturing various structural and functional properties of the mammalian respiratory system.

2.2 Methods

2.2.1 Modeling surfactant dynamics with ozone exposure

The pulmonary surfactant consists of 90% phospholipids and about 10% of lipoproteins [32]. There are generally 4 types of lipoproteins in the pulmonary surfactant: Surfactant protein (SP) A, B, C and D. SP-B and SP-C make up the surface-active agents which are involved in the regulation of surface properties of the air-liquid interface in the alveolar region. SP-A and SP-D are pulmonary collectins that participate in the immune responses to xenobiotic. The mathematical model of Mukherjee *et al.* [33] is adapted here to simulate the pulmonary surfactant dynamics, including surfactant secretion, surfactant adsorption to the air-liquid interface, surfactant recycling and the regulation of surfactant dynamics. Briefly, all surfactant components are secreted into lamellar bodies in alveolar type II cells. These lamellar bodies are exocytosed from alveolar type II cells to the alveolar fluids and the secreted surfactant components are released [34]. In addition, pulmonary collectins (SP-A & SP-D) can be secreted directly into the alveolar fluids from alveolar type II cells in a lamellar bodies-independent manner [35]. Once in the alveolar fluids, surfactant components are adsorbed onto the alveolar air-liquid interface where they maintain a normal surface tension for the lung [36]. In the meantime, surfactant components can also recycle back into alveolar type II cells [37]. Some of the surfactant is also lost to the airway [38]. Furthermore, the various pulmonary surfactant components do not function independently. The surfactant proteins participate in the regulation of secretion, adsorption and recycling of phospholipids in the alveolar fluids [39]. SP-A binds strongly to phospholipids and promotes the formation of the interfacial surfactant films [40, 41]. SP-B and SP-C enhance the adsorption of phospholipids to the alveolar surface [42, 43]. SP-A also inhibits the secretion of phospholipids by alveolar type II cells and promotes the recycling of phospholipids back to alveolar type

II cells [37]. The mathematical model for the surfactant dynamics module involves five compartments: alveolar type II cells (AT2), lamellar bodies (LB), alveolar fluids (AF), alveolar air-liquid interface (Int) and a purely mathematical compartment called "Loss", which represents the net loss of surfactant from the system. The mass balance equations for the five compartments are as follows:

$$\frac{dM_{AT2,i}}{dt} = R_{Gen,i} - (K_{Sec,i} + K_{DSec,i})M_{AT2,i} + K_{Re}M_{AF,i} \tag{2.1}$$

$$\frac{dM_{LB,i}}{dt} = K_{Sec,i}M_{AT2,i} - K_{LB}M_{LB,i} \tag{2.2}$$

$$\begin{aligned}\frac{dM_{AF,i}}{dt} &= K_{LB}M_{LB,i} + K_{DSec,i}M_{AT2,i} + K_{Des}M_{Int,i} - (K_{Re} + K_{Deg})M_{AF,i} \\ &\quad - K_{Ad,i}M_{AF,i}(M^{eq}_{Int,i} - M_{Int,i})\end{aligned} \tag{2.3}$$

$$\frac{dM_{Int,i}}{dt} = K_{Ad,i}M_{AF,i}(M^{eq}_{Int,i} - M_{Int,i}) - K_{Des}M_{Int,i} - K_{AW,i}M_{Int,i} \tag{2.4}$$

$$\frac{dM_{Loss,i}}{dt} = K_{AW,i}M_{Int,i} + K_{Deg}M_{AF,i} \ - R_{Gen,i} \tag{2.5}$$

Here, M stands for the amount of a particular compound in mol and K represents the rate constant for a particulate process with a unit of min^{-1}. The subscript "i" represents the three surfactant components: PL, SA and C. Gen stands for generation, Sec for secretion, $DSec$ for direct secretion, LB for exocytosis of lamellar bodies, Des for desorption, Re for recycle, Ad for adsorption, Deg for degradation and AW for airway loss. K_{DSec} represents the rate constant for direct secretion into the alveolar fluid, which only happens for collectins. So K_{DSec} for PL and SA is zero. The regulatory effects of surfactant proteins on phospholipid dynamics are included with the following equations:

$$K_{Ad,PL} = K^0_{Ad,PL}(1 + k^{SA}_{Ad}C_{SA} + k^{C}_{LB}C_C) \tag{2.6}$$

$$K_{LB} = K^0_{LB}(1 - k^{C}_{LB}C_C) \tag{2.7}$$

$$K_{Re,PL} = K^0_{Re,PL}(1 + k^{C}_{Re}C_C) \tag{2.8}$$

Here, K^0 represents the rate constant without the regulation effect, K stands for the rate constant with regulation and k_i^j represents the regulatory constant of species j on process i. C stands for the concentration of the particular components in the alveolar fluids with a unit of mol/ml.

Under ozone exposure conditions, surfactant dynamics are also affected by the presence of ozone due to its high oxidative potential. Ozone reactions with the unsaturated phospholipids in the alveolar surfactant result in degradation and rearrangement of lung surfactant lipids and subsequently impair the physical properties of the surfactant films at the alveolar air-liquid interface [44]. Ozone exposure can damage SP-B by changing its structure, thus impairing the ability of SP-B to interact with phospholipids [45]. SP-A has also been found to be damaged structurally by ozone exposure [46]. Therefore, it is important to include the effect of ozone in the surfactant dynamics module. Kim *et al.* found that the kinetics of ozone reactions with phospholipids and surfactant protein-B at the air-liquid interface can be described as pseudofirst order reactions [47, 48]. Thus equation 2.3 and 2.4 are modified as follows:

$$\begin{aligned}\frac{dM_{AF,i}}{dt} &= K_{LB}M_{LB,i} + K_{DSec,i}M_{AT2,i} + K_{Des}M_{Int,i} - (K_{Re} + K_{Deg})M_{AF,i} \\ &\quad - K_{Ad,i}M_{AF,i}(M_{Int,i}^{eq} - M_{Int,i}) - K_{O3,i}M_{AF,i} \qquad (2.9)\\ \frac{dM_{Int,i}}{dt} &= K_{Ad,i}M_{AF,i}(M_{Int,i}^{eq} - M_{Int,i}) - K_{Des}M_{Int,i} \\ &\quad - K_{AW,i}M_{Int,i} - K_{O3,i}M_{AF,i} \qquad (2.10)\end{aligned}$$

where $K_{O3,i}$ represents the reaction rate constant of ozone and surfactant component i. The values of $K_{O3,i}$ are estimated based on the study from Kim *et al.* [47] and the study from Uppu *et al.* [49] where they compared the relative reactivities of ozone with phospholipids and surfactant proteins.

The outcomes of the surfactant dynamics module are time profiles of surfactant components which will be used to link surfactant profiles with the surface tension at

the alveolar air-liquid interface.

2.2.2 Modeling immune responses after ozone exposure

In addition to direct reactions with alveolar surfactant components, ozone may also affect lung functions by initiating pulmonary inflammation [50–52]. In the alveolar region, secondary ozone reaction products can stimulate on site macrophages in the lining fluid to produce various pro-inflammatory cytokines, including TNF-α, IL-1, IL-6, etc. These pro-inflammatory mediators will further signal the influx of more macrophages into the lung from the blood circulation, leading to a cascade of inflammatory events. To address the inflammation-related lung function alteration induced by ozone, a cellular level immune response module is included in the current model (Figure 2.2).

Although ozone itself does not enter cells due to its reactions with alveolar lining fluid components before reaching the cells, ozonation products can lead to the intracellular production of reactive oxygen species (ROS) and cause excessive oxidative stress [53]. These ROS will activate transcriptional signaling pathways that regulate pro- and anti-inflammatory events that comprise immune responses. Among many transcription factors involved in inflammation, NFκB is of critical importance because of its ability to regulate the expressions of a wide variety of pro-inflammatory cytokines [54]. Therefore, NFκB pathway is chosen as the representative pro-inflammatory signaling pathway activated by ROS in the current model. An average delegator P is used to represent the various pro-inflammatory cytokines induced by NFκB activation. These pro-inflammatory cytokines can induce the generation of intracellular ROS, which further activate NFκB forming a positive feedback loop [55]. The anti-inflammatory response (A) is the essential immunoregulatory signal that can dampen pro-inflammatory responses and maintain homeostasis in the host defense system. In the current model, the anti-inflammatory response stimulated by the activation

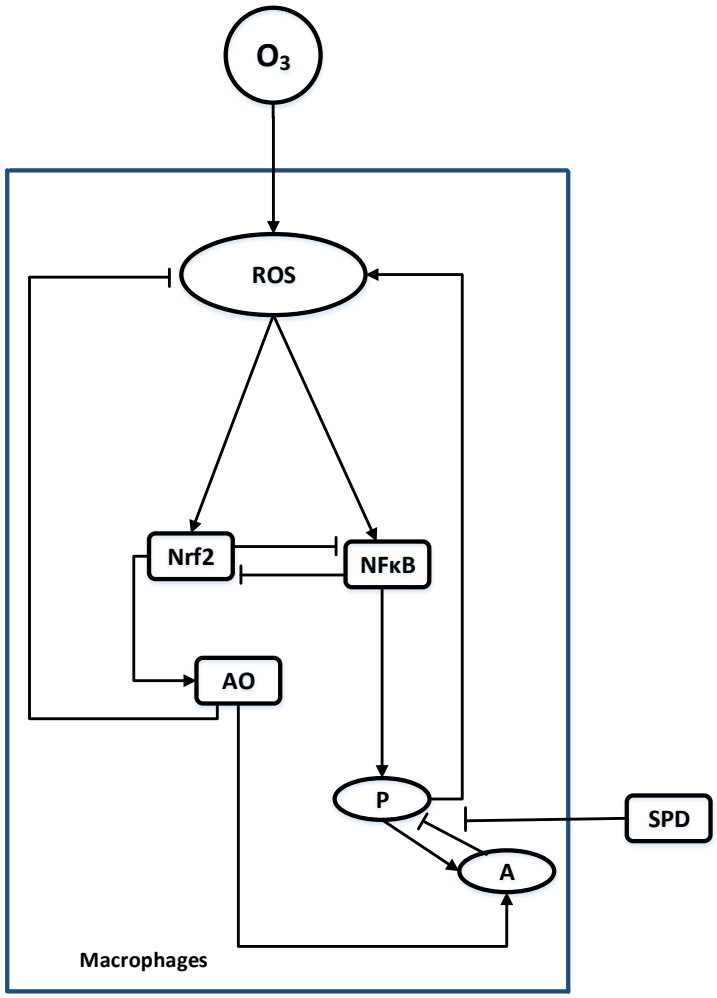

Figure 2.2: Immune response module that captures the inflammation induced by ozone exposure.(ROS: reactive oxygen species; AO: anti-oxidants; P: inflammatory signals; A: anti-inflammatory signals; SPD: surfactant protein-D)

of pro-inflammation negatively affects the production of pro-inflammatory cytokines. Surfactant protein D (SP-D) is a pulmonary collectin that plays an important role in regulating innate immunity of the respiratory system. Various studies have demonstrated that SP-D can suppress inflammatory responses induced by xenobiotics including ozone [31, 56–58]. The anti-inflammatory function of SP-D is incorporated in the current model by reducing the production of pro-inflammatory cytokines. Nrf2 is a key transcription factor for controlling cell homeostasis in response to oxidative stress [59]. It mediates basal and induced transcription of an array of antioxidant

proteins (AO) to promote oxidant resistance [60]. Nrf2 signaling cascades also inhibit the activity of the NFκB pathway leading to reduced production of pro-inflammatory cytokines [61], and vice versa, the NFκB pathway negatively affects Nrf2 mediated gene expressions [62]. The mathematical equations for the immune responses module are presented below:

$$\frac{dC_{NF\kappa B}}{dt} = K_{G,NF\kappa B}C_{ROS}(1 + \frac{x_{NF\kappa B,Nrf2}}{x_{NF\kappa B,Nrf2} + C_{Nrf2}}) - K_{deg,NF\kappa B}C_{NF\kappa B} \tag{2.11}$$

$$\frac{dC_{Nrf2}}{dt} = K_{G,Nrf2}C_{ROS}(1 + \frac{x_{Nrf2,NF\kappa B}}{x_{Nrf2,NF\kappa B} + C_{NF\kappa B}}) - K_{deg,Nrf2}C_{Nrf2} \tag{2.12}$$

$$\frac{dC_{AO}}{dt} = K_{G,AO}C_{Nrf2} - K_{deg,AO}C_{AO} \tag{2.13}$$

$$\begin{aligned}\frac{dC_P}{dt} &= K_{G,P}(1 + \frac{C_{NF\kappa B}^{n_{P,NF\kappa B}}}{x_{P,NF\kappa B} + C_{NF\kappa B}^{n_{P,NF\kappa B}}} \times \frac{x_{P,A}}{x_{P,A} + C_A} \\ &\quad \times \frac{x_{P,SP-D}}{x_{P,SP-D} + C_{SP-D}}) - K_{deg,P}C_P\end{aligned} \tag{2.14}$$

$$\frac{dC_A}{dt} = K_{G,A}(1 + \frac{C_{AO}^{n_{A,AO}}}{x_{A,AO} + C_{AO}^{n_{A,AO}}} \times \frac{C_P^{n_{A,P}}}{x_{A,P} + C_P^{n_{A,P}}}) - K_{deg,A}C_A \tag{2.15}$$

$$\begin{aligned}\frac{dC_{ROS}}{dt} &= K_{G,ROS}C_{O3}(1 + \frac{x_{ROS,AO}}{x_{ROS,AO} + C_{AO}}) - K_{deg,ROS}C_{ROS} \\ &\quad + C_P\frac{C_{ROS}^2}{1 + C_{ROS}^2}\end{aligned} \tag{2.16}$$

Here, C stands for the concentration of the particular compound, K_G represents the generation rate constant, and K_{deg} stands for the degradation rate constant. x_{ij} is the regulatory constant of compound j on compound i. The power n_{ij} controls the strength of the regulation effect of compound j on compound i.

2.2.3 Modeling lung mechanics

Modeling lung impedance

Pulmonary impedance can be described as the opposition to the flow of air into the lungs, and, like electrical impedance, is defined as the ratio of the driving force causing the flow (in this case, pressure) and the rate of flow (in this case, air flow rate). The relation between pressure and volume of air in the lung has been modeled since Otis *et al.* (1956) [63] using the analogy of an electric R-C circuit, with pressure and flow rate analogous to voltage and electric current respectively. Therefore, P and V are related as $P = \dot{V}Z$, where Z is the pulmonary impedance and $\dot{V}$ is the air flow rate. Taking the Fourier transform of both sides of $Z(t) = P(t)/\dot{V}(t)$, we obtain

$$Z(\omega) = \frac{P(\omega)}{i\omega\dot{V}(\omega)} \tag{2.17}$$

where ω is the angular frequency that is related to time-based frequency f ($\omega = 2\pi f$). Pulmonary impedance is intrinsically dependent on lung viscoelasticity. Many formulations have been developed over the years to relate various frequency dependent and independent lung parameters with impedance. In Hildebrandt's experiments with cat lungs [64], the author first demonstrated that the viscoelastic modulus of the system varies linearly with the logarithm of time. Hantos and co-workers [65, 66] then made modifications to Hildebrandt's original theory with their Constant-Phase Model (CPM), where they decomposed the complex pulmonary impedance into components due to airway resistance (R_{aw}), inertance (I), tissue damping (G) and tissue elastance (H). The CPM can be expressed as:

$$Z(\omega) = \left(R + \frac{G}{\omega^{\alpha}}\right) + i\left(I\omega - \frac{H}{\omega^{\alpha}}\right) = Z_{re} + iZ_{im} \tag{2.18}$$

The CPM has been widely used to characterize pulmonary mechanics in mammals because of its apparent simplicity, elegance and the fact that it can be readily separated into dissipative and capacitive effects of the lung [67–69]. Physically, the real part of the pulmonary impedance Z_{re} captures the dissipative effects of pulmonary mechanics and represents the physical impedance to airflow and energy loss due to impedance. The imaginary part of impedance Z_{im} captures the capacitive effects and represents energy storage due to the recoil forces in the lung. They can be written as:

$$Z_{re} = R + \frac{G}{\omega^{\alpha}} \tag{2.19}$$

$$Z_{im} = I\omega - \frac{H}{\omega^{\alpha}} \tag{2.20}$$

Relating impedance to alveolar properties

In the CPM equations, R represents airway resistance [68, 70]. Inertance I is also a parameter of the airways and is expected to vary between animals but is not expected to change due to tissue-level changes in surfactant dynamics. The real part of the pulmonary impedance is generally considered to be composed of two resistances: airway resistance (R_{AW}) and pulmonary tissue resistance (R_T) [68, 69].The real part of impedance Z_{re} then can be written as composed of different resistive components as $Z_{re} = R_{AW} + R_T$. So, if we ignore the airway contributions, we have the pulmonary tissue resistance as:

$$R_T = \frac{G}{\omega^{\alpha}} \tag{2.21}$$

Similarly, the pulmonary tissue elastance E_T can be expressed as:

$$E_T = \frac{H}{\omega^{\alpha}} \tag{2.22}$$

The variables R_T and E_T are expected to depend on pulmonary tissue properties including surfactant profiles. It should be pointed out that the CPM parameters G and

H, which represent pulmonary tissue resistance and elastance, do not change independent of each other, and are in fact related. The ratio $\eta = H/G$ is known as tissue hysteresivity and remains fairly unchanged in a particular subject, unless there is a very high extent of lung injury [71]. η has been measured in a number of mammalian species and was found to be in the range of 0.1-0.2 [68]. Therefore a model that is able to predict pulmonary tissue elastance (H) under various conditions, is considered sufficiently equipped to predict overall pulmonary function under conditions of limited lung injury. The following sections describe an alveolar recruitment model that has been developed to link pulmonary tissue properties to pulmonary tissue elastance, H.

Alveolar recruitment model

Alveolar recruitment is a key mechanism in the process of breathing by mammals. Recruitment refers to the opening of alveolar air spaces so that air can flow into these spaces. During the normal breathing process, most of the alveoli remain open and they only expand and contract during inspiration and expiration. Recruitment and decruitment (R/D) changes substantially during lung injury [72] and is also a significant factor during normal tidal breathing [73]. Small airway and alveolar closure is known to occur at low lung volumes in normal lungs and may exist even at larger lung volumes in subjects with lung obstruction [74]. Alveolar R/D has been shown to modulate pulmonary tissue resistance and elastance [75] in mice with acute lung injury. Increase in alveolar surface tension has been known to cause derecruitment of alveolar units leading to an increase in both G and H [68], which represent pulmonary tissue resistance and elastance respectively. More severe pulmonary injury, which leads to remodeling of the lung tissue, can independently increase G, without an associated increase in H. The alveolar recruitment model described here predicts the fractional alveolar recruitment and its effect on tissue elastance, H. The alveolar R/D model follows the models developed by Bates *et al.* [76] and Massa *et al.* [75].

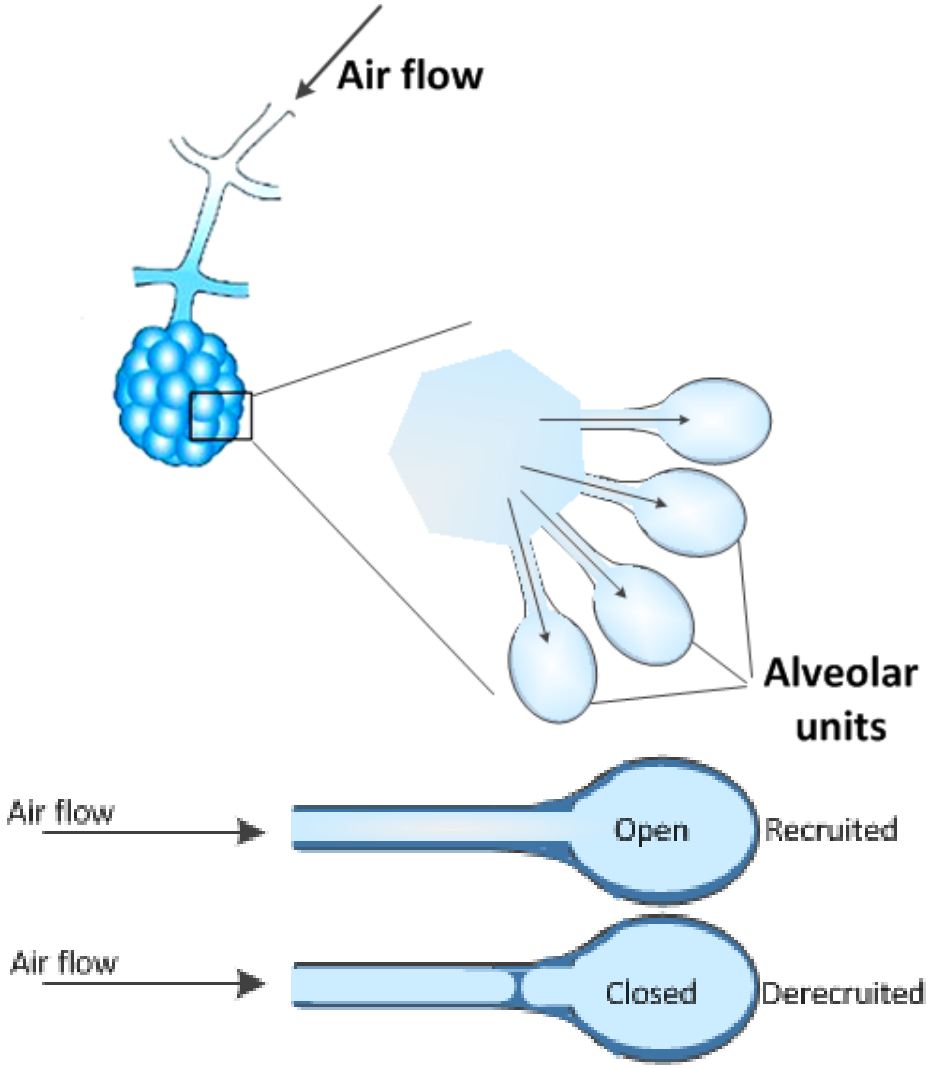

Figure 2.3: Schematic representation of the alveolar recruitment model: (top) integration of alveolar units at the terminus of an airway; (bottom) opening and closing of individual airways due to surfactant dynamics

Figure 2.3 shows a graphical representation of the model. The model simulates alveolar R/D based on a pressure signal using the following key alveolar parameters: critical opening pressure (P_O), critical closing pressure (P_C), rate of opening (S_O) and rate of closing (S_C). Opening and closing of alveolar units and the smallest airways are dependent on a number of surfactant and airway properties. Gaver *et al.* [74] and Halpern *et al.* [77] studied surfactant effects in liquid-lined flexible tubes which were used as physical models of the small airways in the lung. The effects of surfactant

properties on the four alveolar properties are discussed in detail later. The model considers a set of N individual alveolar units and simulates their opening and closing as well as expansion/contraction due to a selected air flow. A variable x is defined such that $0 < x < 1$ which determines if an alveolar unit is open or closed with $x = 0$ representing the closed state and $x = 1$ representing the open state. The dynamics of variable x_i for the ith airway are described as follows:

$$\frac{dx_i}{dt} = \begin{cases} S_{Oi}(P - P_{Oi}) & \text{if } P > P_{Oi} \\ S_{Ci}(P - P_{Ci}) & \text{if } P < P_{Ci} \\ 0 & \text{otherwise} \end{cases} \tag{2.23}$$

Here, P represents the external applied pressure which is provided as a sinusoidal function as $P = P_m \sin(\omega t)$, where P_m is the pressure amplitude determined by the actual tidal volume of the species and ω is the frequency of breathing.

A binary variable y is also defined, taking values of 0 or 1, to signify closed or open status of a particular airway unit. At a particular time t, y_t takes on values according to the following rule:

$$y_t = \begin{cases} 0 & \text{if } x_t = 0 \mid 0 < x_t < 1 \text{ and } x_{t-1} < x_t \\ 1 & \text{if } x_t = 1 \mid 0 < x_t < 1 \text{ and } x_{t-1} > x_t \end{cases} \tag{2.24}$$

Lung tissue heterogeneity is taken into account by considering the values of the four parameters as distributions rather than as single values. The opening and closing pressures, P_{Oi} and P_{Ci} for the ith alveolar unit are randomly selected from normal distributions as:

$$P_O \in N(\mu_{P_O}, \sigma^2_{P_O}) \tag{2.25}$$

$$P_C \in N(\mu_{P_C}, \sigma^2_{P_C}) \tag{2.26}$$

Here, $N(\mu, \sigma^2)$ is a normal distribution with mean μ and standard deviation σ. The rate of opening (S_O) and the rate of closing (S_C) are selected from hyperbolic distributions as described below:

$$S_O \in \frac{\beta_O}{unif[0,1]} \tag{2.27}$$

$$S_C \in \frac{\beta_C}{unif[0,1]} \tag{2.28}$$

Here, $unif[0,1]$ is a uniform distribution between 0 and 1, and β_O and β_C are scaling parameters for the rate of opening and closing respectively. In the subsequent sections, the effect of O_3 on these key parameters (μ and β) has been investigated; σ essentially reflects the extent of heterogeneity in the alveoli and is assumed to be unchanged due to O_3 exposure.

The air flow rate, Q_i into an individual unit is defined by

$$Q_i = \frac{y_i}{R_i}(P_i - V_{i0}E_i) \tag{2.29}$$

Here, y_i represents the open/close status of the ith unit, P_i is the air pressure at the airway inlet which is assumed equal to the input dynamic pressure signal to the model, V_{i0} is the residual volume in the ith unit at the end of expiration. R_i and E_i are the individual unit resistance and elastance for the ith alveolar unit. They are assumed to be identical for all units and their values were optimized by Massa *et al.*[75] using *in vivo* data from mice. The residual volume V_{i0} is estimated based on the value of Positive End Expiratory Pressure (PEEP) in each experimental scenario. And the relationship between V_{i0} and PEEP is described using the Salazar-Knowles equation [78]:

$$V = A - Be^{-kP} \tag{2.30}$$

Where A, B and k are intrinsic parameters of the lung. The parameter A can be considered equal to the total lung capacity (TLC) and parameter B is equal to functional

residual capacity (FRC) [79]. However, for individual airway unit in this model, the values of TLC or FRC were divided by n, the number of airway units in the model. The individual airway volumes at any time t ($V_{i,t}$) is estimated as:

$$V_{i,t} = V_{i,0} + \Delta t \cdot Q_i \tag{2.31}$$

The total dynamic volume of the lung is calculated by summing up all the individual airway volumes as: $V_t = \Sigma_{i=1}^{n} V_{i,t}$

Alveolar surface tension

The primary function of pulmonary surfactant is to reduce the surface tension at the air-liquid interface in the alveolar region to make the work of breathing easier. Since 90% of pulmonary surfactant, surface tension is largely controlled by the phospholipid concentration at the alveolar surface. The functional form was derived using data from Walter *et al.* [36]. The surface tension γ_{PL} is dependent on the concentration of PL in the alveolar lining and can be expressed using the following equation:

$$\gamma_{PL} = \gamma_{max} \left(1 - \frac{C_S^n}{K + C_S^n} \right) \tag{2.32}$$

where C_S is the surface concentration of free PL at the alveolar air-liquid interface; K and n are Hill-type coefficients.

Surface tension γ is also known to depend on the presence of SA (SP-B and SP-C) in the alveolar lining. During the process of breathing, PL bilayers are repeatedly squeezed out from dynamically compressed surface films and suffer respreading during expansion [80]. The ability of PL bilayers to function repeatedly in this fashion is significantly dependent on the presence of SA in close association to the PL bilayers [81]. Wang *et al.* [82] measured the surface tension produced by various surfactant formulations and showed that the minimum surface tension produced by natural

calf lung surfactant extracts was about 50% lower than PL by itself. The actual surface tension γ of the alveolar interface is a result of PL adsorption to the interface, composition of bilayers, and spreading of the PL bilayers which requires the presence of SA. To take this into consideration, the effective surface tension γ is modified by a surface-active factor f_{SA} as:

$$\gamma = \gamma_{PL} \cdot f_{SA} \tag{2.33}$$

where f_{SA} is estimated by $f_{SA} = k_{surf,SA}(1 - C_{SA})$. Here C_{SA} is the fractional concentration (by weight) of SA in surfactant and $k_{surf,SA}$ is a constant quantifying the effect of SA on γ. The value of $k_{surf,SA}$ is estimated using measurements from Wang *et al.* [82].

Effects of ozone on alveoli recruitment

Alveolar surface tension is regulated by the concentrations of lung surfactant components. Being a highly oxidative compound, ozone can react with phospholipids and proteins in the lung surfactant [45, 46, 50, 83] and therefore affect the alveolar surface tension. The alveolar recruitment model described earlier contains four key alveolar parameters: mean critical opening pressure (μ_{PO}), mean critical closing pressure (μ_{PC}), scaling parameter for rate of opening (β_O) and scaling parameter for rate of closing (β_C). All of these parameters are expected to be affected by changes in the surfactant profile caused by ozone-induced surface tension changes. Gaver *et al.* [74] found both airway opening pressure and opening rate to be affected by the surface tension (γ) at the air-liquid interface in the alveolar region. Based on Gaver study, Mukherjee [84] linked μ_{PO} and β_O to the surface tension using the following mathematical equations:

$$\mu_{PO} = \mu^*_{PO} \left(\frac{\gamma}{\gamma^*} \right) \tag{2.34}$$

$$\beta_O = \beta^*_O \left(\frac{\gamma}{\gamma^*} \right) \tag{2.35}$$

where γ^* is the control value of surface tension in the alveolar fluid, and μ^*_{PO} and β^*_O are the control values obtained for normal mice [75].

Effects of inflammation on pulmonary tissue elastance

Pulmonary inflammation is known to cause alterations of pulmonary tissue elastance. Starling *et al.* found that chronic pulmonary inflammation contributed to increased tissue elastance in guinea pigs [85]. Xisto and co-workers demonstrated that pulmonary tissue elastance was significantly increased due to allergic inflammation in a murine model [86]. Dixon *et al.* found that tissue elastance increased in a dose-dependent manner for LPS-induced inflammation in rats [87]. As mentioned before, inhaled ozone can interact with the immune system to initiate pulmonary inflammation. In order to incorporate the effect of ozone-induced inflammation on tissue elastance, a *Damage* variable is defined to quantify the adverse effect of inflammation [88]:

$$\frac{dD}{dt} = \frac{C_P^{h_1}}{C_P^{h_1} + x_{D,P}^{h1}} \tag{2.36}$$

where D stands for *Damage* caused by inflammation, C_P is the concentration of pro-inflammatory cytokines obtained from the immune response module, $x_{D,P}$ stands for the regulatory constant of pro-inflammatory cytokines on *Damage*, h_1 controls the strength of the regulation effect. The final tissue elastance is then described as:

$$H = H^*(1 + D) \tag{2.37}$$

Here, H is the tissue elastance considering the effect of inflammation, H^* stands for the tissue elastance without the effect of inflammation.

2.2.4 *In vivo* measurements of lung functions

In vivo measurements of ozone effects on lung functions were done in experiments involving male C57BL/6J wild type mice and SP-D knockout ($Sftpd^{-/-}$) mice bred at Rutgers University [89]. All procedures were reviewed and approved by the Rutgers University Institutional Animal Care and Use Committee. Mice were euthanized 72h following exposure (3h) to ozone (0.8ppm) or air in whole body Pleiglas chambers. Pulmonary mechanics was measured using a flexiVent (SCIREQ, Montreal, PQ, Canada). Mice were ventilated at a frequency of 150 breaths/min and a tidal volume of 10 ml/kg. The *in vivo* measurements consisted of overall pulmonary resistance and elastance that are related to the real and imaginary parts of lung impedance as $R_L = Z_{Re}$ and $E_L = \omega|Z_{Im}|$. Further details of the measurement protocols are presented in Grove *et al.* (2013) [89].

2.3 Results

The model described above simulated the conditions of mice exposed to ozone through inhalation. The model was run for 10 additional days prior to dosing of ozone to allow the levels of surfactant components to reach steady state that reflects the normal physiological conditions of mice. In order to capture the alterations in lung function, the first issue that needed to be addressed is how lung surfactant components are responding to ozone inhalation. Figure 2.4 demonstrates the relative fold change of concentration for surfactant components at different time points after ozone exposure. The fold changes are calculated using the concentrations at selected time points divided by the corresponding steady state values before applying ozone exposure to mice. All surfactant components including PL, SA and C experienced a continuous decrease in the first 12 hours after ozone exposure. Then the levels of surfactant components started to recover gradually and were restored back to normal level at

around 72 hours after exposure.

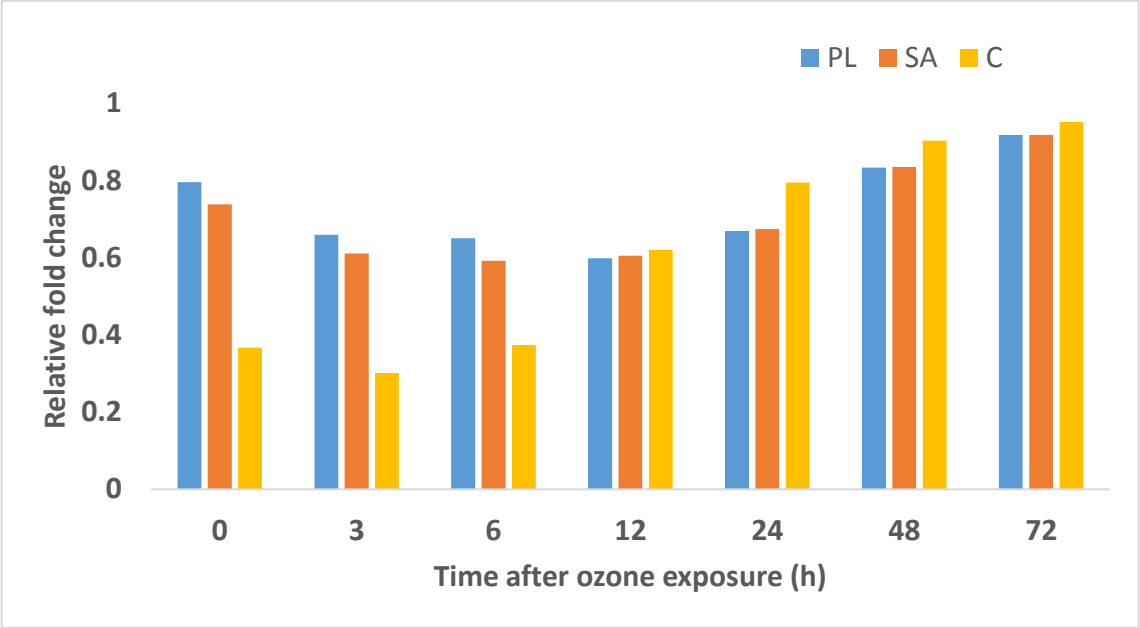

Figure 2.4: Relative fold change of surfactant component levels after 3 hours of ozone exposure (0.8 ppm) in mice. (PL: Phospholipids in the alveolar fluid; SA: surface-active agents in the alveolar fluid; C: collectins in the alveolar fluids). Values are normalized using the corresponding values at the control condition (before ozone exposure)

The immune response module was run for wild type and $Sftpd^{-/-}$ mice to simulate the inflammatory responses initiated by ozone with and without surfactant protein D. Figure 2.5 shows the time course of pro-inflammatory signals induced by ozone. The intensity of the pro-inflammatory signal was calculated through normalizing the level of pro-inflammatory cytokines by the basal level before applying ozone dosage. Simulation results demonstrate that ozone exposure induced acute pulmonary inflammation in both wild type and $Sftpd^{-/-}$ mice, indicated by the rapid increase of pro-inflammatory signals within the first 10 hours after ozone exposure. After 10 hours, inflammation in wild type mice started to be attenuated by the anti-inflammatory mechanisms of the host defense system while in $Sftpd^{-/-}$ mice, the attenuation process is much slower. The pro-inflammatory signal level in $Sftpd^{-/-}$ mice is higher than the level in wild type mice for the entire simulation time. At the

end of simulation when lung function indexes were experimentally measured (72 h after ozone exposure), $Sftpd^{-/-}$ mice still have a significantly higher level of inflammation than wild type mice.

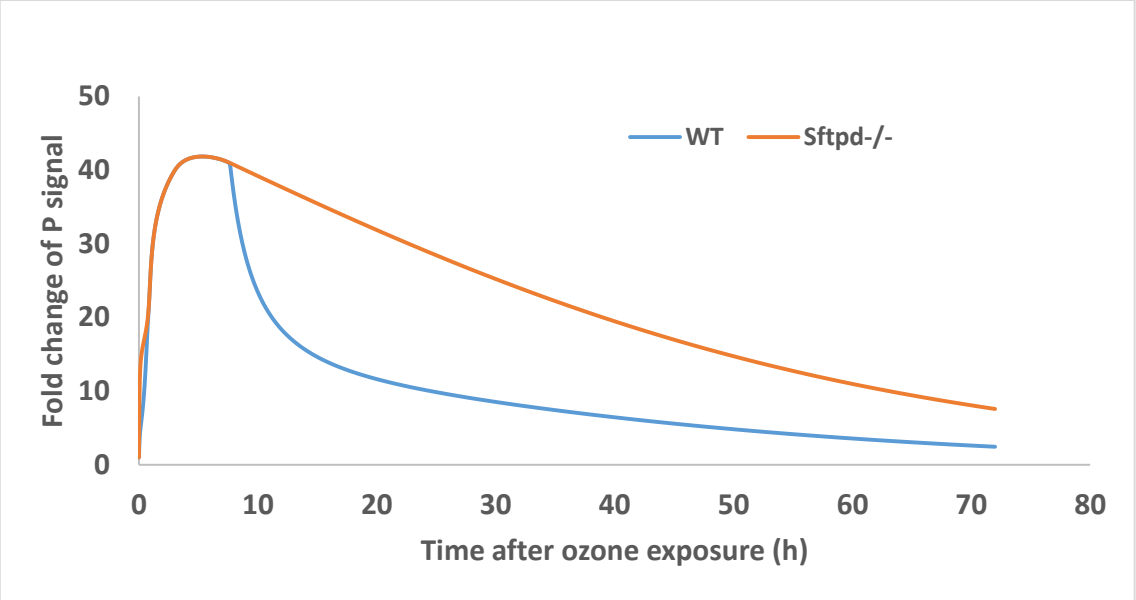

Figure 2.5: Simulated time course of the pro-inflammatory signal (P) in wild type (WT) and SP-D knockout ($Sftpd^{-/-}$) mice after 3 hours of ozone exposure (0.8 ppm). Values are normalized using corresponding values at control condition (before ozone exposure)

The surfactant component profiles estimated by the Surfactant Dynamics Module and the inflammatory responses from the Immune Responses Module were used in the Lung Mechanics Module to estimate changes in alveolar surface tension and overall lung function. Model predictions of tissue elastance H were compared with values of H from *in vivo* lung function measurements in mice at PEEP ranging from 0 to 6 cmH_2O by use of a flexiVent. Figure 2.6a shows the comparison between model predicted and experimentally measured H for wild (WT) type mice, and Figure 2.6b shows the comparison for SP-D knockout ($Sftpd^{-/-}$) mice. In all scenarios, model predictions successfully capture the changes in H. To have a better comparison between wild type and $Sftpd^{-/-}$ mice in terms of their lung function alteration upon ozone exposure, tissue elastance H changes over time were simulated at different

PEEPs and are shown in Figure 2.7. Model simulation results were normalized by corresponding control values (tissue elastance level before ozone exposure). In both wild type and $Sftpd^{-/-}$ mice, tissue elastance increased immediately after 3 hours of ozone exposure and this increase continued up to 12 hours. Then tissue elastance started to decrease but still persisted at a level higher than control values until 72 hours after ozone exposure. $Sftpd^{-/-}$ mice demonstrated significantly higher levels of tissue elastance over the entire time of the simulation, suggesting the protective role of surfactant protein D in response to ozone-initiated lung function changes.

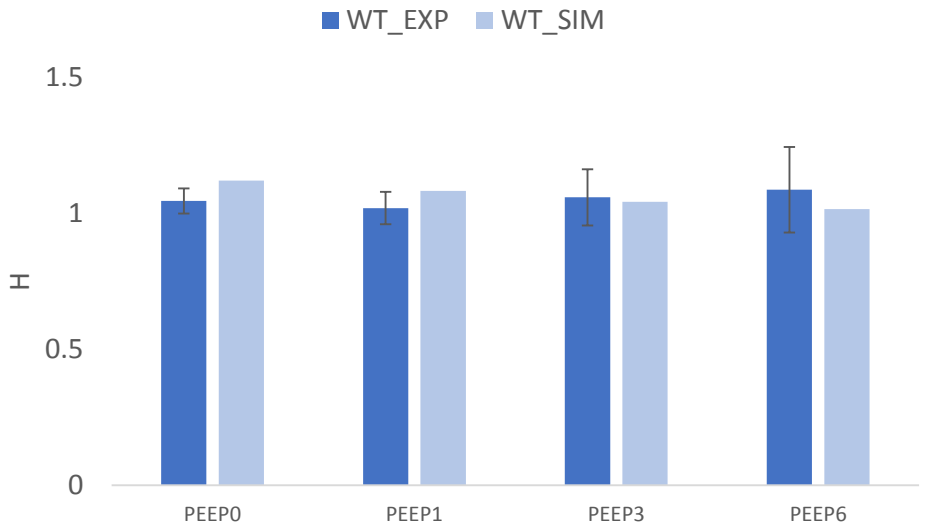

(a) wild type mice

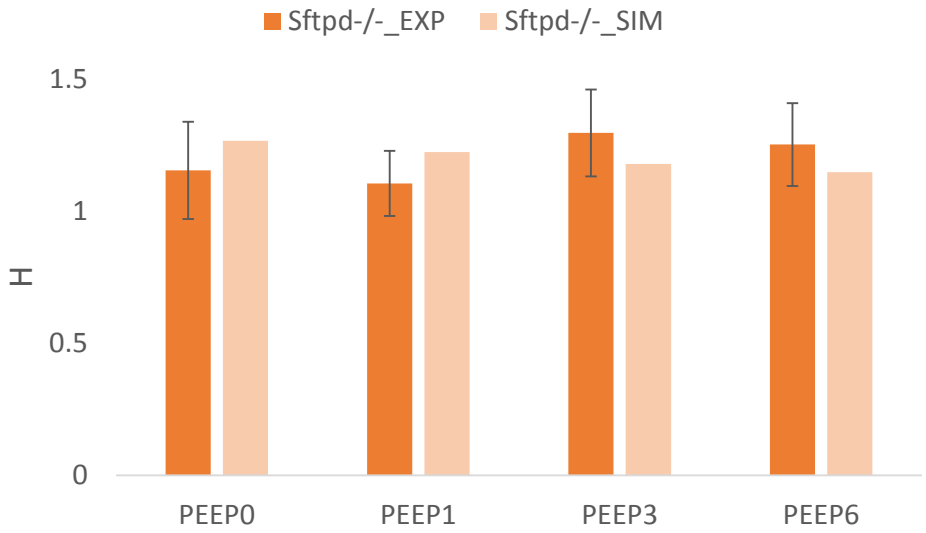

(b) SP-D knockout mice

Figure 2.6: Comparison of measured (EXP) and model simulated (SIM) lung tissue elastance (H) with different PEEPs at 72 hours after 3 hours of ozone exposure: (a) wild type mice; (b) SP-D knockout mice. Experimental measurements are obtained from Grove *et al.* [89]. H values are normalized using corresponding values at the control condition (before ozone exposure)

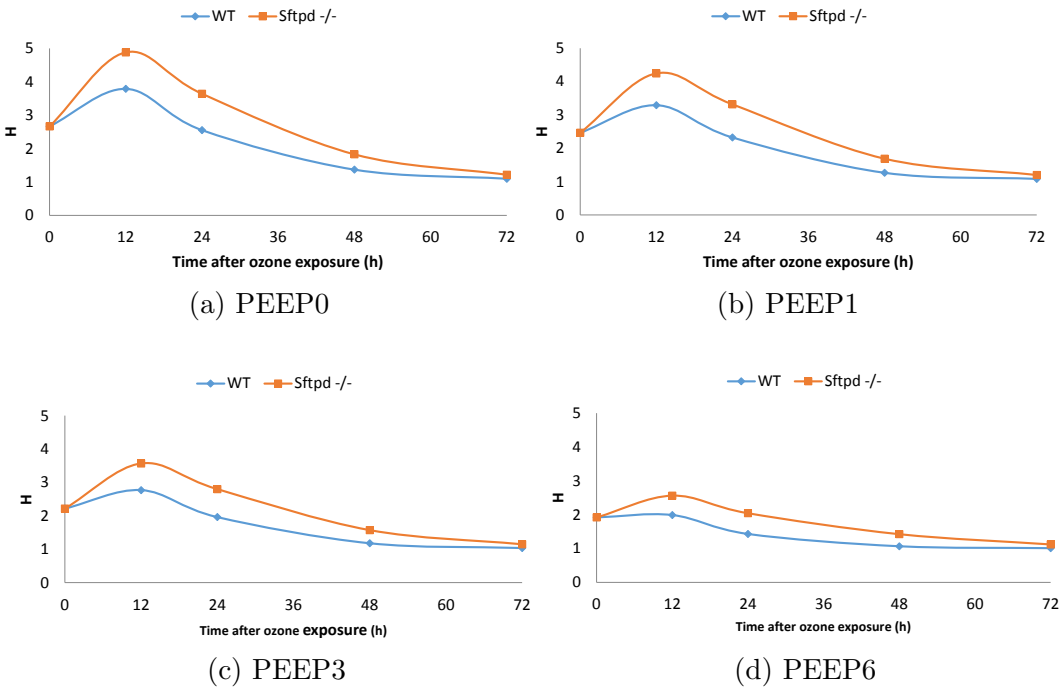

(a) PEEP0 (b) PEEP1

(c) PEEP3 (d) PEEP6

Figure 2.7: Simulated temporal effect of ozone exposure on lung tissue elastance after 3 hours of ozone exposure (0.8 ppm) in wild type and SP-D knockout mice. Values are normalized using corresponding values at control condition (before ozone exposure).

2.4 Discussion

Ozone is a ubiquitous air pollution known to cause lung function alterations. In this model, two main biological mechanisms are included to simulate lung function changes in response to ozone: ozone-induced pulmonary surfactant perturbation and ozone-initiated pulmonary inflammation. These two mechanisms are then coupled with a lung mechanics module capturing the expansion and contraction of the alveoli and its mechanistic representation of pulmonary impedance. The fact that this model successfully predicted the changes of tissue elastance H (Figure 2.6) strongly supports the selection of biological mechanisms involved in the model construction. After short-term ozone exposure, simulation results demonstrate that the levels of pulmonary surfactant components are immediately lowered, which has also been observed in previous studies [90, 91]. Although ozone itself does not stay for a long

time due to its high reactivity, the protracted effect of ozone on lung function (Figure 2.7) can be partially explained by the persistent surfactant depletion after ozone exposure (Figure 2.4). The model also simulates the initiation and resolution of pulmonary inflammation. The trend for inflammation signals (Figure 2.5) is consistent with the changes of tissue elastance H over time shown in Figure 2.7, confirming that pulmonary inflammation is another mechanism through which ozone negatively affect lung functions. Surfactant protein D is an important surfactant component associated with immune responses. The model explores the differences between wild type and $Sftpd^{-/-}$ mice regarding inflammation and lung function alteration upon ozone exposure. Compared with wild type mice, pulmonary inflammation is significantly prolonged in $Sftpd^{-/-}$ mice (Figure 2.5), which is correlated with the more significantly altered lung functions (Figure 2.7). Considering the fact that surfactant components levels are almost restored back to normal physiological levels at 72 hours after exposure (Figure 2.4), pulmonary inflammation is the dominant mechanism affecting lung functions at later times after ozone exposure. Also, the higher sensitivity to ozone in $Sftpd^{-/-}$ mice is mainly attributed to the development of progressive chronic inflammation.

This model is the first attempt, to the authors' knowledge, to illustrate the connection between ozone exposure and lung function changes from a mechanistic point of view, considering pulmonary surfactant dynamics, cellular inflammation responses and alveoli expansion/contraction simultaneously. The modular nature of the model allows flexible modifications to incorporate newer findings and additional experimental data regarding surfactant dynamics and pulmonary immune responses. Although the current model is run for mice, this model can be extended to other mammalian species, including human, to access pulmonary effects due to ozone inhalation. The model successfully quantifies cellular level immune responses and tissue level surfactant perturbations, and links them to organism level changes. This multiscale

modular approach would be valuable in understanding cell and tissue scale mechanisms associated with various pulmonary diseases such as asthma, COPD, etc. which can all be exacerbated due to ozone inhalation.

Chapter 3

Modeling Reduced Heart Rate Variability due to Exposures to Particulate Matter

3.1 Introduction

The adverse health effects of air pollution have long been recognized and exposures to air pollution have become a major problem leading to deaths and diseases worldwide [1, 92]. Among different air pollutants, particulate matter (PM) is a mixture of solid particles and/or liquid droplets suspended in the air with significant impacts on human health. Epidemiological studies have shown strong associations between exposures to PM and human morbidity and mortality [93–95]. The respiratory effects of PM include increased respiratory symptoms, altered lung function, pulmonary inflammation and increased incidence of chronic obstructive pulmonary disease and asthma. In addition, PM is associated not only with pulmonary effects but also with cardiovascular diseases. Acute exposure to PM has been linked to various adverse cardiovascular events including emergency department visits and hospital admissions for ischemic heart disease and congestive heart failure [96].

Heart rate variability (HRV) is the variation in the time interval between one heartbeat and the next and is usually characterized by time domain and frequency

domain indices. HRV is controlled by the autonomic nervous system (ANS) and clinical measurement of HRV is a noninvasive way to identify cardiac autonomic dysfunction. It has been suggested that a reduction in HRV represents increased isolation of the heart from other organs [97] and decreased HRV has been demonstrated as a predictive factor for cardiovascular mortality, such as myocardial infarction, arrhythmias and heart failure [98, 99]. Previous studies have demonstrated the association between decreased HRV and exposures to PM [100–102]. Although the evidence is strong, the exact mechanisms underlying PM induced HRV reduction are not fully understood yet. One hypothesized and well-studied mechanism suggests that diminished HRV is induced by systemic inflammations due to the release of inflammatory cytokines initiated by PM inhalation in the pulmonary region [103]. A recent study conducted a meta-analysis of human studies to estimate the relationship between HRV and inflammatory markers [104]. The study results showed a negative association between HRV and inflammation markers; in particular, the time domain HRV index SDNN (the standard deviation of the interbeat interval of normal sinus beats) showed the most robust associations with markers of inflammation, indicating the importance of inflammation in mediating HRV in humans. In the context of PM exposures, intracellular pathways are activated upon recognition of PM by cells in the pulmonary region leading to the excretion of pro- and anti-inflammatory cytokines. These cytokines can enter the circulation to further propagate systemic inflammatory cascades. The physiological mechanisms regulating inflammation include not only the local release of pro- and anti-inflammatory cytokines but also influences from the neuroendocrine system. It has been shown that the central nervous system (CNS) plays a critical role in regulating anti-inflammatory responses. [105] The primary pathway by which the CNS regulates the immune system is the hypothalamic-pituitary-adrenal (HPA) axis who can produce glucocorticoid to enhance anti-inflammatory responses [105]. Furthermore, the sympathetic nervous system (SNS), a main division of the

ANS that controls HRV, can release neurotransmitters to inhibit the production of pro-inflammatory cytokines [106]. These functions form a complex network of interactions among the immune, neuroendocrine and autonomic systems for regulating HRV upon exposures to PM.

Although extensive efforts have been made to understand how PM can induce HRV reduction, we still lack of a systems-level understanding due to the complex interacting pathway networks involved in the process, thus rising the need for a systems biology approach. In the present study, a multiscale mechanism-based model is developed to simulate HRV changes resulting from exposures to PM. The model contains a cellular level immune response module that connects PM exposure to intracellular signaling cascades leading to the transcriptions of pro- and anti-inflammatory cytokines. Considering the importance of the neuroendocrine system in regulating inflammatory responses and HRV, a module describing the bidirectional communication between the immune system and the neuroendocrine axis is also included. Furthermore, the dynamic signals evoked via immune-neuroendocrine interactions are propagated to the heart to assess how HRV is altered on a systemic level following exposures to PM. The proposed multiscale model consists of 27 coupled ordinary differential equations, and it is parameterized by fitting to experimental measurements from the literature. The output of the model is shown to capture experimentally observed HRV changes in different human PM exposure studies. Furthermore, the relative importance of biological processes involved in the complex interacting pathway networks is evaluated by performing sensitivity analysis.

This work is an attempt to explore the feasibility of using a systems biology approach to integrate the complex biological events involved in the HRV alteration induced by PM exposures, including transcriptional dynamics, signaling cascades, immune-neuroendocrine interactions and signal propagation into the heart. Such a modeling approach can serve as a step towards gaining insight into how air pollu-

tants containing particulate matter exert detrimental effects in multiple organs and contribute to cardiovascular mortality.

3.2 Model and Methods

3.2.1 Modeling cellular level responses to oxidative stress agents

One of the critical mechanisms through which PM exert its toxic effects is via generating excessive oxidative stress and triggering inflammatory responses. At the cellular level, we established a semi-mechanistic model to characterize the increase of intracellular oxidative stress as well as the activation of pro- and anti-inflammatory signaling pathways. Among the many transcription factors involved in inflammation, NFκB is known for its prominent role in the development and function of the immune system [107]. It has been widely studied as a major mediator of cellular inflammatory responses and mathematical modeling approaches have been developed to quantify the dynamics of NFκB signaling cascades [108, 109]. Therefore, the NFκB signal transduction cascade is chosen as the representative signaling pathway that initiates and regulates the transcription of pro-inflammatory genes in our model. Nrf2 is a key transcription factor for controlling cell homeostasis in response to oxidative stress [59]: it mediates basal and induced transcription of an array of antioxidant proteins to promote oxidant resistance [60]. The Nrf2 signaling cascade also inhibits the activity of the NFκB pathway leading to reduced production of pro-inflammatory cytokines [61], and vice versa, the NFκB pathway negatively affects Nrf2 mediated gene expressions [62]. Because of the anti-oxidative/ anti-inflammatory role of Nrf2 and the cross-talk between Nrf2 and NFκB, we selected the Nrf2 signaling cascade as the representative pathway that mediates cellular defense responses against PM in our model. The level of oxidative stress in the cell is characterized by the intracellular concentration of

reactive oxygen species (ROS) whose intracellular production is associated with the secretion of pro-inflammatory cytokines [110, 111].

Upon contact with cells, PM is recognized via a receptor mediated mechanism. Depending on the size and composition of the PM, different pattern recognition receptors (e.g. TLR 2, TLR 4, RAGE) could be activated to initiate subsequent signaling cascades [112–114]. For modeling simplicity, an average delegator R is used to represent the various pattern recognition receptors activated during the PM recognition process. Once PM binds to its receptor, the PM-receptor complex (PM-R) induces the activation of IκB kinase (IKK) which phosphorylates the inhibitor protein IκB to activate NFκB resulting in the production of many pro-inflammatory cytokines, including TNF-α, IL-1, IL-6, etc. [115–117]. An average delegator P is used to represent the pro-inflammatory cytokines induced by NFκB activation. These pro-inflammatory cytokines induce alterations of the cellular energetic responses (E) whilst a dysregulation in the cellular bioenergetics serves a positive feedback danger signal to the pro-inflammatory response [118, 119]. The anti-inflammatory response (A) is the essential immunoregulatory signal that can dampen pro-inflammatory responses and maintain homeostasis in the host defense system. We hypothesize that the anti-inflammatory response is stimulated by the activation of pro-inflammation and the energetic response, and it negatively affects the production rate of the pro-inflammation and energetic response. These pro-inflammatory cytokines produced via the NFκB pathway also induce the generation of intracellular ROS which further activate NFκB, forming a positive feedback loop [55]. In the meanwhile, intracellular ROS activate Nrf2 resulting in its translocation to the nucleus and subsequent activation of antioxidant response element (ARE)-mediated gene transcriptions. A variety of endogenous anti-oxidant proteins (represented by the delegator AO) are produced via the Nrf2-ARE pathway to reduce the level of intracellular ROS in the cell [120, 121]. Furthermore, mutually inhibiting effects between NF$\varkappa$B and Nrf2

signaling pathways are modeled using an indirect response approach [122].

3.2.2 Modeling neuroendocrine immune system interactions

Pro-inflammatory response originating from exposures to air pollutants in the pulmonary region can induce neuroendocrine responses, which then mediate the pulmonary inflammation and a wide range of systemic effects in distant organs [123, 124]. A neuroendocrine-immune system model developed for human endotoxemia [125] is adapted here to simulate the interaction effects between inflammation and neuroendocrine responses. Briefly, the hypothalamic-pituitary adrenal axis (HPA) serves as the primary stress response pathway through which the central nervous system (CNS) regulates the immune system. In response to the pro-inflammatory cytokines entering the circulation from pulmonary inflammation, HPA releases cortisol (F) to inhibit the expression of pro-inflammatory cytokines via a receptor/gene-mediated mechanism [126]. Along the same line, the hormone epinephrine (EPI) also regulates a series of immune functions [127]. The sympathetic nervous system (SNS) secretes epinephrine upon stimulation by the pro-inflammatory cytokines [128]. The secreted epinephrine then binds to adrenergic receptors to form the epinephrine-receptor complex which activates the cAMP pathway, resulting in the upregulation of anti-inflammatory cytokines expression [129].

3.2.3 Modeling HRV changes associated with exposures to air pollutants

HRV is the variation in the time interval between one heartbeat and the next. It is commonly used to index autonomic nervous system activity. Decreased HRV is an important marker for autonomic dysfunction and it has been shown to correlate well with increased risk of cardiovascular events [130, 131]. Exposures to ambient air pollu-

tants, especially particulate matter, have been associated with reduced HRV involving pulmonary and systemic inflammations [132–134]. A nonlinear model [135] is adapted to quantify the relationship between pro-inflammatory mediators and autonomic dysfunction. The effect of pro-inflammation on HRV is mathematically approximated by using a sigmoid activation function which involves signal transduction mechanisms in the sinus node of the heart [136] and the activation of efferent nerve activity on the heart [125]. A schematic illustration of the multilevel model connecting cellular response, neuroendocrine immune system interactions and HRV is shown in Figure 3.1.

3.2.4 Model Equations

The principles of indirect response model theory [122] are applied in developing the mathematical equations for our model. Indirect response models are commonly used to describe the dynamics of physiological responses of a system induced by external stimuli [137]. The mathematical equations for this model are presented at the end of this section.

Equation 3.1 describes the recognition process of PM via a receptor mediated pathway. The dynamics of PM (Eq.3.1a) depend on the PM concentration in the air (C_{pm}), tidal volume (TV), breathing frequency (BF) and a first order elimination rate constant k_{pm}. Also, we assume that approximately 10 percent of the inhaled PM eventually deposit in the alveolar region [138] and get in contact with cells. The dynamics of the PM receptor R (Eq.3.1b) depend on the association/dissociation of PM-receptor interaction with corresponding rate constants k_1 and k_2 as well as the translation rate of its mRNA to surface protein (k_{syn}). The dynamics of the PM-receptor complex (Eq. 3.1c) are characterized by the binding parameters k_1, k_2 and the parameter k_3 that describes the rate of formation of IKK. The dynamics of the receptor mRNA (Eq.3.1d) are described by a production rate ($K_{in,mR}$) and a degra-

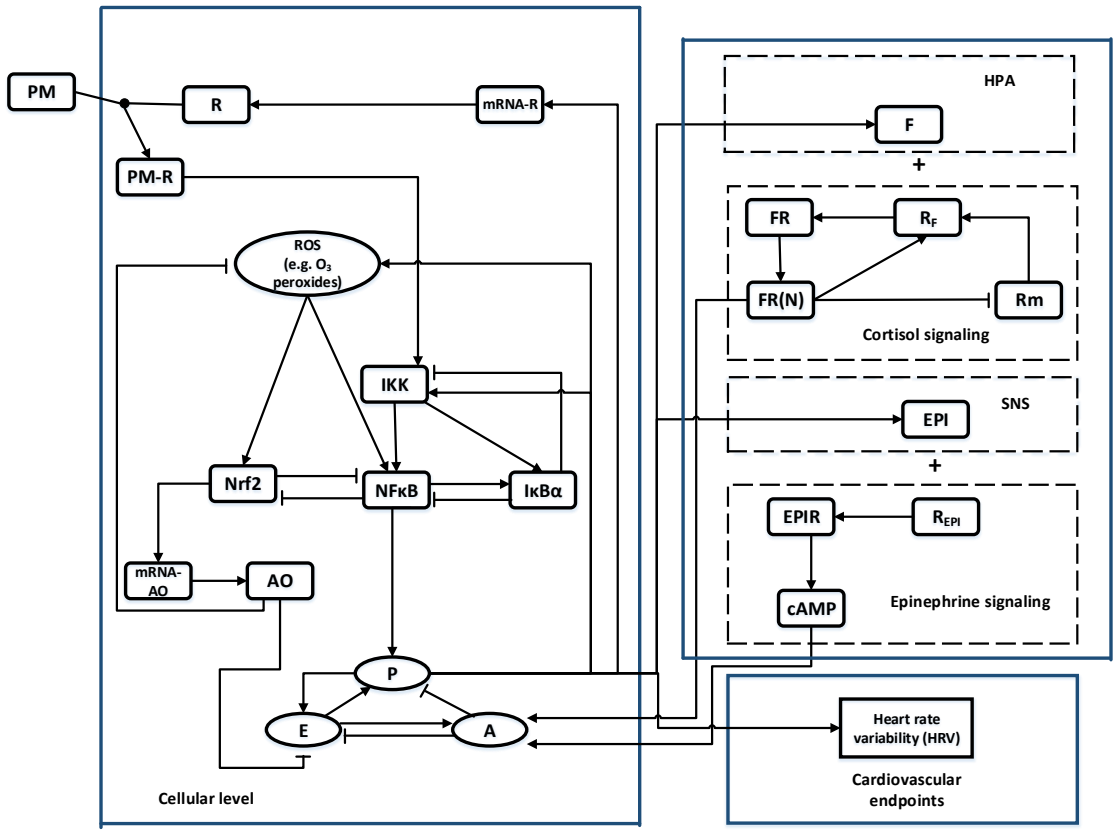

Figure 3.1: A schematic illustration of the multilevel model of air pollutant induced inflammation and cardiovascular effects. At the cellular level, PM induced transcriptional responses (P, A, E) are regulated through NFκB and Nrf2 pathways involving excessive oxidative stress. Neuroendocrine immune interactions mainly involve the release of stress hormones cortisol (F) and epinephrine (EPI) and their anti-inflammatory effects. Finally, adverse health effects on the cardiovascular system are quantified by heart rate variability.

dation rate ($K_{out,mR}$), and is indirectly affected by the pro-inflammatory cytokines ($k_{mR,P}$).

The activation of NFκB pathways is described in Equation 3.2. The dynamics of IKK (Eq.3.2a) depend on the formation rate (k_3) induced by the PM-receptor complex and an elimination rate k_4, and is indirectly affected by the pro-inflammatory cytokines [139]. The nonlinear function of Hill-type is an essential functional form in order to achieve a bistability response [119]. The dynamics of NFκB activity (Eq.3.2b) depend on the import rate ($k_{NF\kappa B1}$) of cytoplasmic NFκB into the nucleus induced by

IKK and the deactivation rate ($k_{NF\kappa B2}$) associated with its primary inhibitor IkBa and the presence of Nrf2. The dynamics of the mRNA for IkBa (Eq. 3.2d) are described by a production rate ($K_{in,mIkBa}$) and a degradation rate ($K_{out,mIkBa}$), and are indirectly affected by NFκB (k_{IkBa1}). The dynamics of inhibitor IkBa (Eq. 3.2d) involve the translation of its mRNA and the degradation associated with IKK and NFκB.

Equation 3.3 describes the activation of Nrf2 pathway. As seen in Eq. 3.3a, Nrf2 is generated with a production rate ($k_{syn,Nrf2}$) which is induced by ROS and negatively affected by NFκB, and it degrades with a first order elimination rate $k_{deg,Nrf2}$. The dynamics of anti-oxidant proteins AO (Eq. 3.3b) are described by a first order production rate ($k_{syn,AO}$) and a first order degradation rate ($k_{deg,AO}$). As shown in Eq. 3.3c, the production of mRNA for anti-oxidant proteins (mAO) is governed by a production rate (k_{mAO}) and the presence of Nrf2 ($k_{syn,mAO}$); mAO degrades with a first order rate $k_{deg,mAO}$.

Equation 3.4 describes the dynamics of the pro-inflammatory cytokines (P), the anti-inflammatory cytokines (A), the cellular energetic response (E) and the intracellular ROS. As seen in Eq. 3.4a, the generation of the pro-inflammatory cytokines is associated with a production rate ($K_{in,P}$) and is assumed to be indirectly stimulated by NFκB ($k_{P,NF\kappa B}$) and the cellular energetic response ($k_{P,E}$). The anti-inflammatory cytokine is assumed to inhibit the production rate of the pro-inflammatory cytokines. The inflammatory cytokines degrade with a rate of $K_{out,P}$. The dynamics of the anti-inflammatory cytokines (Eq. 3.4b) involve a production rate ($K_{in,A}$) and are indirectly affected by the cellular energetic response ($k_{A,E}$). They are also assumed to be stimulated by cAMP ($k_{A,cAMP}$) and cortisol ($k_{A,FRN}$) resulting from the neuroendocrine immune system interactions. The anti-inflammatory cytokines decay with a rate of $K_{out,A}$. As shown in Eq. 3.4c, the production of energetic responses ($K_{in,E}$) is indirectly stimulated by the pro-inflammatory cytokines ($k_{E,P}$) and is inhibited

by the presence of anti-inflammatory cytokines and anti-oxidant proteins. The energetic responses decay with a rate of $K_{out,E}$. The dynamics of ROS (Eq. 3.4d) are characterized by a production rate ($k_{in,ROS}$) indirectly affected by anti-oxidant proteins, a degradation rate ($k_{deg,ROS}$) and a positive feedback loop representing the ROS generation induced by pro-inflammatory cytokines.

The production of cortisol (F) via HPA due to the stimulation of pro-inflammatory cytokines and the subsequent cellular signaling pathway are mathematically expressed by Equation 3.5. The dynamics of cortisol (Eq. 3.5a) are governed by a production rate ($K_{in,F}$) stimulated by the pro-inflammatory cytokines ($k_{F,P}$) and have a first order elimination rate of $K_{out,F}$. Cortisol binds to its cytosolic receptor to form the cortisol-receptor complex (FR). The dynamics of the cortisol-receptor complex in the cytosol (Eq. 3.5b) depend on the cortisol binding rate (k_{on}) and its translocation rate (k_T) to the nucleus. In the nucleus, the active nuclear receptor complex (FRN) mediates the transcriptional induction of various genes. The dynamics of the nuclear cortisol receptor complex (Eq. 3.5c) are characterized by the nucleus translocation rate and the recycling rate (k_{re}) of cortisol from nucleus to the cytosol. The dynamics of the mRNA of cortisol receptor (Eq. 3.5d) involve a zero order production rate (k_{syn,mR_F}) inhibited by the nuclear cortisol-receptor complex and a first order degradation rate (k_{deg,mR_F}). The parameter IC_{50,mR_F} represents the concentration of the nuclear cortisol-receptor complex FRN at which the synthesis rate of the receptor drops at 50% of its baseline value. The dynamics of the cytosolic cortisol receptor are expressed in Eq. 3.5e where k_{syn,R_F} is the synthesis rate due to transcription and k_{deg,R_F} is the degradation rate. In addition, the dynamics of the receptor are also affected by the cortisol binding process and the cortisol recycling from nucleus to the cytosol. The parameter r_f denotes the fraction of the cortisol that is recycled.

The secretion of epinephrine (EPI) by the sympathetic nervous system in response to the stimulation of pro-inflammatory cytokines and the subsequent cellular signaling

pathway are mathematically expressed by Equation 3.6. The dynamics of EPI (Eq. 3.6a) are governed by a production rate ($K_{in,EPI}$) stimulated by the pro-inflammatory cytokines ($k_{EPI,P}$) and have a first order elimination rate ($K_{out,EPI}$). Epinephrine binds to its receptor to form the epinephrine-receptor complex which induces the increase of the cAMP intracellular levels [140]. The dynamics of the epinephrine receptor are characterized by Eq. 3.6b where $K_{R_{EPI}}$ is the zero order production rate, $k_{1,R_{EPI}}$ and $k_{2,R_{EPI}}$ are first order rate constants for the loss of the receptor, $k_{R_{EPI},EPI}$ represents the epinephrine binding to its receptor. The formation of the epinephrine-receptor complex is shown in Eq. 3.6c with a first order decay rate ($k_{3,EPIR}$). The dynamics of cAMP are simulated using the principles of a transit compartment model [137]. As seen in Eq. 3.6d, the production and loss of the cAMP signaling depend on a first order rate constant which is equal to the reciprocal of the transit times (τ). The parameter n is a scaling factor that is used to amplify the signal transduction cascade associated with the effect of EPI [125].

Changes of HRV in response to pro-inflammation induced by exposure to air pollutants are simulated using nonlinear sigmoid functions [125] and are mathematically expressed by Equation 3.7. The nonlinear effect of pro-inflammatory responses (P) on HRV is described by the dynamics of f_P (Eq. 3.7a), which reflects the activation of efferent nerve activity on the heart. A sigmoid function $\tanh(P-\omega)$ is used to determine the switch-like behavior, where ω is a parameter greater than the pro-inflammatory responses induced by exposure to air pollutants. This nonlinear modulatory function should be active under conditions of pro-inflammation and inactive when the system is in its homeostasis. A function $\tanh(P^{\phi}-1)^{\phi}$ is employed to model such events, where φ is an artificial big number which ensures that $\tanh(P^{\phi}-1)^{\phi}$ takes values 1 when pro-inflammatory responses occur, and 0 when the system is in homeostasis. The activation of efferent nerve activity leads to the upregulation of the signal transductions in the sinus node of the heart [136], which is characterized by the dynamics

of S_f (Eq. 3.7b). The production and loss of S_f depend on a first order rate constant equal to the reciprocal of the transit times (τ_s) and the scaling factor ns. The dynamics of the HRV (Eq. 3.7c) are governed by a production rate ($K_{in,HRV}$) and a degradation rate ($K_{out,HRV}$) stimulated by S_f

$$\begin{cases} \dfrac{d[PM]}{dt} = C_{pm} \times TV \times BF - k_{pm}[PM] & \text{(3.1a)} \\ \dfrac{d[R]}{dt} = k_{syn}[mR] + k_2[PMR] - k_1[PM][R] - k_{syn}[R] & \text{(3.1b)} \\ \dfrac{d[PMR]}{dt} = k_1[PM][R] - k_3[PMR] - k_2[PMR] & \text{(3.1c)} \\ \dfrac{d[mR]}{dt} = K_{in,mR}(1 + k_{mR,P}[P]) - K_{out,mR}[mR] & \text{(3.1d)} \end{cases}$$

$$\begin{cases} \dfrac{d[IKK]}{dt} = \dfrac{k_3[PMR]}{1 + [IkBa]} - k_4[IKK] + [P]\dfrac{[IKK]^2}{1 + [IKK]^2} & \text{(3.2a)} \\ \dfrac{d[NF\kappa B]}{dt} = \dfrac{k_{NF\kappa B1}([IKK] + [ROS])(1 - [NF\kappa B])}{1 + [IkBa] + [Nrf2]} \\ \qquad\qquad - k_{NF\kappa B2}[NF\kappa B]([IkBa] + [Nrf2]) & \text{(3.2b)} \\ \dfrac{d[mIkBa]}{dt} = K_{in,mIkBa}(1 + k_{IkBa1}[NF\kappa B]) - K_{out,mIkBa}[mIkBa] & \text{(3.2c)} \\ \dfrac{d[IkBa]}{dt} = k_{I,1}[mIkBa] - k_{I,2}(1 + [IKK])[IkBa](1 - [NF\kappa B]) - k_{I,1} & \text{(3.2d)} \end{cases}$$

$$\begin{cases} \dfrac{d[Nrf2]}{dt} = \dfrac{k_{syn,Nrf2}[ROS]}{1 + [NF\kappa B]} - k_{deg,Nrf2}[Nrf2] & \text{(3.3a)} \\ \dfrac{d[AO]}{dt} = k_{syn,AO}[mAO] - k_{deg,AO}[AO] & \text{(3.3b)} \\ \dfrac{d[mAO]}{dt} = k_{mAO}(1 + k_{syn,mAO}[Nrf2]) - k_{deg,mAO}[mAO] & \text{(3.3c)} \end{cases}$$

$$
\begin{cases}
\dfrac{d[P]}{dt} = K_{in,P}(1 + k_{P,NF\kappa B}[NF\kappa B])\dfrac{1 + k_{P,E}[E]}{[A]} - K_{out,P}[P] & \text{(3.4a)} \\
\dfrac{d[A]}{dt} = K_{in,A}(1 + k_{A,cAMP}[cAMP])(1 + k_{A,E}[E])(1 + k_{A,FRN}[FRN]) & \\
\qquad - K_{out,A}[A] & \text{(3.4b)} \\
\dfrac{d[E]}{dt} = K_{in,E}\dfrac{1 + k_{E,P}[P]}{[A] + [AO]} - K_{out,E}[E] & \text{(3.4c)} \\
\dfrac{d[ROS]}{dt} = \dfrac{k_{in,ROS}}{1 + [AO]} - k_{deg,ROS}[ROS] + [P]\dfrac{[ROS]^2}{1 + [ROS]^2} & \text{(3.4d)}
\end{cases}
$$

$$
\begin{cases}
\dfrac{d[F]}{dt} = K_{in,F}(1 + k_{F,P}[P]) - K_{out,F}[F] & \text{(3.5a)} \\
\dfrac{d[FR]}{dt} = k_{on}([F] - 1)[R_F] - k_T[FR] & \text{(3.5b)} \\
\dfrac{d[FRN]}{dt} = k_T[FR] - k_{re}[FRN] & \text{(3.5c)} \\
\dfrac{d[mR_F]}{dt} = k_{syn,mR_F}(1 - \dfrac{[FRN]}{IC_{50,mR_F} + [FRN]}) - k_{deg,mR_F}[mR_F] & \text{(3.5d)} \\
\dfrac{R_F}{dt} = k_{syn,R_F}[mR_F] + r_f k_{re}[FRN] - k_{on}([F] - 1)[R_F] - k_{deg,R_F}[R_F] & \text{(3.5e)}
\end{cases}
$$

$$
\begin{cases}
\dfrac{d[EPI]}{dt} = K_{in,EPI}(1 + k_{EPI,P}[P]) - K_{out,EPI}[EPI] & \text{(3.6a)} \\
\dfrac{d[R_{EPI}]}{dt} = K_{R_{EPI}} - k_{1,R_{EPI}}[R_{EPI}](1 + k_{R_{EPI},EPI}[EPI]) - k_{2,R_{EPI}}[R_{EPI}] & \text{(3.6b)} \\
\dfrac{d[EPIR]}{dt} = k_{1,R_{EPI}}[R_{EPI}](1 + k_{R_{EPI},EPI}[EPI]) - k_{3,EPIR}([EPIR] + 1) & \text{(3.6c)} \\
\dfrac{d[cAMP]}{dt} = \dfrac{1}{\tau}((1 + [EPIR])^n - [cAMP]) & \text{(3.6d)}
\end{cases}
$$

$$\begin{cases} \dfrac{d[f_P]}{dt} = (1 + tanh([P] - \omega) - [f_P])tanh([P]^{\phi} - 1)^{\phi} & \text{(3.7a)} \\ \dfrac{d[S_f]}{dt} = \dfrac{1}{\tau_S}(tanh([P]^{\phi} - 1)^{\phi}[f_P]^{\text{ns}} - [S_f]) & \text{(3.7b)} \\ \dfrac{d[HRV]}{dt} = K_{in,HRV} - K_{out,HRV}(1 + k_{HRV,S}[S_f])[HRV] & \text{(3.7c)} \end{cases}$$

3.3 Results and Discussion

3.3.1 Model parameterization

The estimation of appropriate model parameters is conducted using results and data from literature. For those that are not directly available in literature, parameterization data were estimated by fitting the simulated HRV changes with experimental measurements extracted from a cohort study conducted by Magari, *et al.* (2001)[141]. In this longitudinal study, an occupational cohort consisting of 40 men were continuously monitored during and away from work. Their work environment was under continuous PM2.5 exposure with an average concentration of 167 µg/m^3 [141]. The data of 5-minute SDNN during the 6 hours work period is used in our model for parameterization purpose. Measurements of 5-minute SDNN are normalized by taking the ratio of the measured SDNN at each time point with respect to the control time point (work start time, t = 0). All model parameters are shown in Table 3.1. The performance of our model is shown in Figure 3.2. Experiment measurements demonstrate a visible depression of HRV throughout the 6 hours of working period under continuous PM2.5 exposure. The relative fluctuations in HRV can be attributed to the fact that HRV is affected by many factors, including environmental hazards, age, gender, circadian rhythm, physical health conditions, psychological factors, lifestyle habits, etc. [142]. Our model not only generates simulation results that are quan-

titatively close to the experimental measurements, but also qualitatively captures the decreasing trend of HRV dynamics proofing the applicability of our model for simulating air pollutants exposure induced HRV reduction.

Table 3.1: Parameter values used to model HRV alteration due to PM exposure

Parameters	Values	Parameters	Values	Parameters	Values
k^c_{pm}	1.8788	$k^c_{deg,mAO}$	7.7562	k^b_{deg,mR_F}	0.1124
k^c_{syn}	3.3241	$K^a_{in,P}$	0.0331	k^b_{syn,R_F}	1.1990
k^c_1	3.0990	$k^a_{out,P}$	0.3328	k^b_{deg,R_F}	0.0572
k^c_2	2.8971	$k^a_{P,NF\kappa B}$	29.7410	r^b_f	0.4900
k^c_3	5.1998	$k^a_{P,E}$	9.0505	$K^b_{in,EPI}$	5.9209
k^a_4	2.2400	$K^b_{in,A}$	0.4609	$k^b_{out,EPI}$	7.2857
$K^a_{in,mR}$	0.0914	$K^b_{out,A}$	0.8095	$k^b_{EPI,P}$	0.2305
$K^a_{out,mR}$	0.2505	$k^b_{A,cAMP}$	0.1450	$K^b_{R_{\mathrm{EPI}}}$	11.0100
$k^a_{mR,P}$	1.7402	$k^b_{A,E}$	0.5340	$k^b_{1,R_{\mathrm{EPI}}}$	3.0055
$k^a_{NF\kappa B1}$	16.2940	$K^a_{in,E}$	0.0800	$k^b_{R_{\mathrm{EPI}},EPI}$	0.8453
$k^a_{NF\kappa B2}$	1.1861	$k^a_{out,E}$	0.2573	$k^b_{2,R_{\mathrm{EPI}}}$	5.4651
$K^a_{in,mIkBa}$	0.4634	$k^a_{E,P}$	2.2160	$k^b_{3,EPIR}$	5.5460
$k^a_{out,mIkBa}$	0.4634	$k^c_{in,ROS}$	9.3119	τ^b	0.0525
k^a_{IkBa1}	13.2730	$k^c_{deg,ROS}$	17.8088	n^b	5.5088
$k^a_{I,1}$	1.4000	$K^b_{in,F}$	0.8425	ω^c	13.2134
$k^a_{I,2}$	0.8700	$k^b_{out,F}$	1.0583	τ^c_S	3.4166
$k^c_{syn,Nrf2}$	9.2733	$k^b_{F,P}$	0.2562	ns^c	0.4707
$k^c_{deg,Nrf2}$	27.7926	k^b_{on}	0.0033	$K^c_{in,HRV}$	12.5175
$k^c_{syn,AO}$	6.2552	k^b_T	0.6300	k^c_{HRV,S_f}	0.8044
$k^c_{deg,AO}$	14.3091	$k^b_{A,FRN}$	0.4010	$K^c_{out,HRV}$	15.1522
k^c_{mAO}	7.7562	k^b_{re}	0.5700		
$k^c_{syn,mAO}$	14.4721	k^b_{syn,mR_F}	2.9000		

[a]:Parameters are taken from Foteinou *et al.*(2009) [119]; [b]:Parameters are taken from Foteinou *et al.*(2010) [125]; [c]:Parameters with optimized value

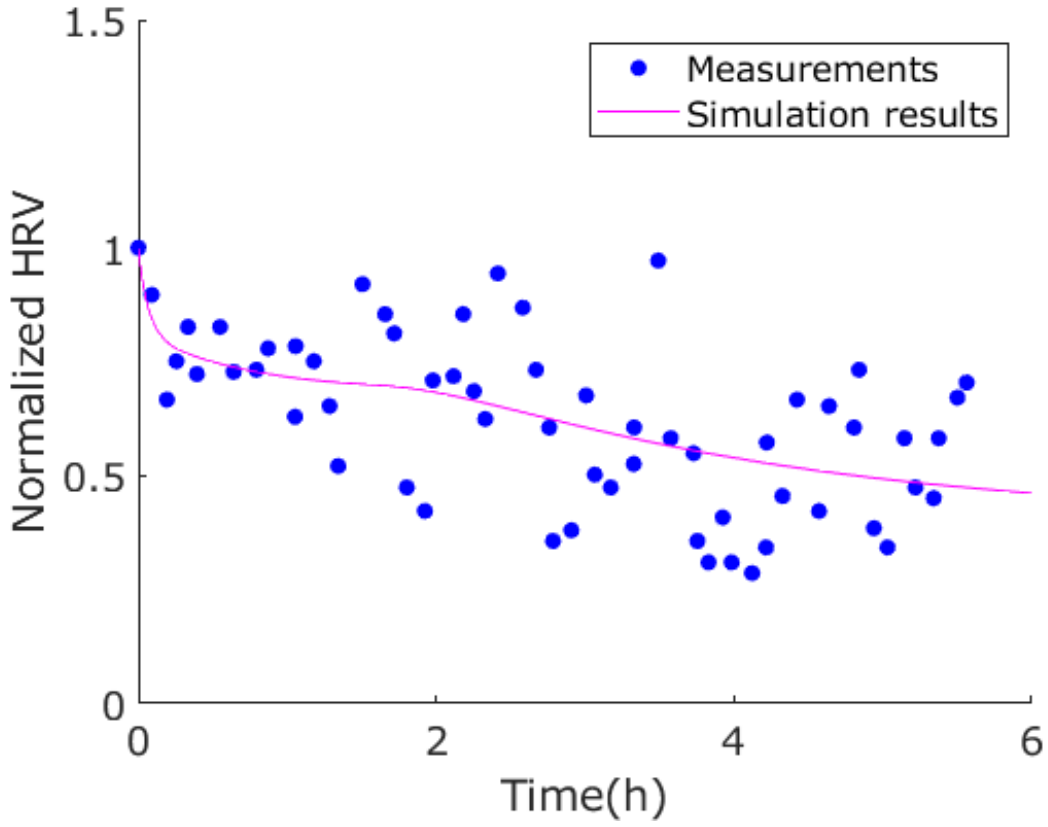

Figure 3.2: Estimation of relevant model parameters intending to capture the trend of HRV changes during 6 hours of continuous exposure to PM2.5 at an average concentration of 167 µm/m3. The time domain measure SDNN is used to assess overall HRV. Data are normalized by taking the ratio of the measured SDNN at each time point with respect to the control time point (work start time, t = 0).

3.3.2 Model evaluation

In order to evaluate our model and test its predictive capability, it was applied to two case-studies where information about PM exposure conditions and SDNN changes overtime were available. In case 1, a group of healthy elderly adults between 60 and 80 years old were continuously exposed to concentrated ambient air pollution particles (CAPs) for 2 hours with an average PM2.5 concentration of 40.5 µg/m^3 [143]. Changes in SDNN were measured immediately before, immediately following, and 24 hour after exposure. In case 2, a group of healthy young adults were exposed to di-

lute wood smoke (PM1) for 3 hours continuously with an average concentration of 314 µg/m^3 [144]. Changes in SDNN were measured before and immediately after exposure. Comparisons between model simulation results and experimental measurements for both cases are shown in Figure 3.3. Simulation results agree well with experimental measurements in both cases. However, our model tends to slightly overestimate the reduction of HRV in both scenarios. Possible explanations are that our model only simulates the effects on HRV exerted by PM via an inflammation mediated mechanism. Other factors that can alter HRV, including physical and psychological conditions during the data collection process, are not included in the current model. Nevertheless, these two case studies provide a preliminary evaluation of the applicability of our model in different exposure scenarios and build confidence to the predictive ability of the current model.

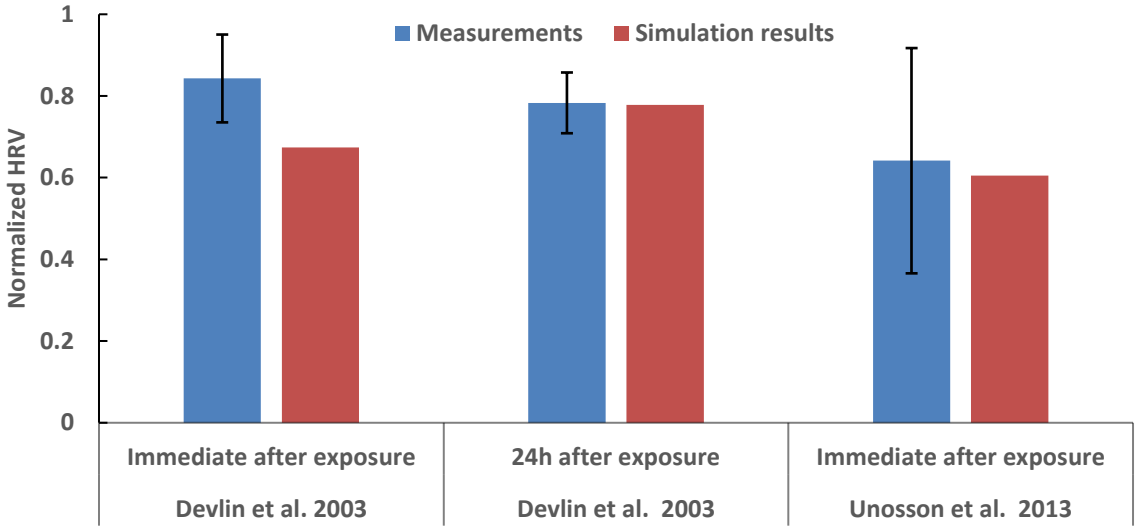

Figure 3.3: Comparison between model predictions and measurements in two case-studies: Devlin *et al.* (2003)[143] measured HRV changes immediately after and 24 hours after exposure to PM2.5 at an average concentration of 40.5 µg/m^3 for 2 hours; Unosson *et al.* (2013) [144] measured HRV changes immediately after exposure to PM2.5 at an average concentration of 314 µg/m^3 for 3 hours. HRV assessed by evaluating SDNN. Data are normalized by taking the ratio of the measured SDNN at each time point to SDNN measured before exposure; measurements expressed as mean ± standard deviation.

3.3.3 Sensitivity analysis

Sensitivity analysis was performed for all the kinetic parameters in the model to explore and identify biological pathways that have significant influences on heart rate variability upon exposure to particulate matter. Each kinetic parameter was sequentially perturbed under the exposure scenario used for the model parameterization, which is a 6 hour continuous exposure to PM2.5 with an average concentration of 167 $\mu g/m^3$. Area under the SDNN time profile curve (AUC) is calculated to characterize the model performance on overall HRV changes during the 6 hour exposure period. In this case, 75% is selected as the cutoff to have a clear impact of parameter perturbations on percentage change of AUC. Out of all 64 kinetic parameters evaluated in the sensitivity analysis, 14 of them are identified as significant as they introduce at least 10% change in AUC of the SDNN time profile curve upon 75% perturbation of the parameter. Results are shown in Figure 3.4. Three parameters that have significant effects are $K_{in,HRV}$, $K_{out,HRV}$ and k_{HRV,S_f}. As shown in Equation 3.7c, they directly control the dynamics of HRV signal and the effects of signal transduction in the sinus node, therefore they should have large impacts on HRV. Previous studies have documented that heart rate variability is inversely associated with inflammation markers in both healthy subjects and patients with pre-existing health conditions across different gender and age groups, indicating the critical role of inflammation in HRV regulation [145, 146]. In our model, kinetic parameters involved in the dynamics of pro-inflammatory cytokines also exert large impacts on HRV. Consistent with literature findings, parameters that govern the production of pro-inflammatory cytokines ($K_{in,P}$, $k_{P,E}$ and $k_{P,NF\kappa B}$) are negatively correlated with HRV; $K_{out,P}$, which controls the degradation of pro-inflammatory cytokines, is positively correlated with HRV. The anti-inflammatory cytokines are the essential immunoregulatory response that can dampen pro-inflammation to restore homeostasis in the host defense system. In our model, the presence of anti-inflammatory cytokines reduces the production

of pro-inflammatory cytokines (Eq. 3.4a), therefore, the anti-inflammatory cytokine related kinetic parameters ($K_{in,A}$ and $K_{out,A}$) have significant impacts on HRV, suggesting the importance of anti-inflammatory pathways in HRV regulation. Previous studies have documented the anti-inflammatory role of the sympathetic nervous system [129, 147]. Animal studies also demonstrated the association between increased time-domain HRV indices and the epinephrine infusion [148, 149]. Our sensitivity analysis has revealed that the interactions between epinephrine and its adrenergic receptors are critical for SNS mediated HRV changes. Two parameters ($k_{1,R_{\mathrm{EPI}}}$ and $k_{3,EPIR}$) control the formation and decay of the epinephrine-receptor complex which induces subsequent upregulation of anti-inflammatory responses; therefore they have large impacts on HRV changes. $K_{R_{\mathrm{EPI}}}$ and $k_{2,R_{\mathrm{EPI}}}$ are relevant to the production and elimination of the adrenergic receptors. Their significant effects indicate that the availability of cellular adrenergic receptors is important for SNS to regulate HRV. Finally, $K_{out,EPI}$, which directly controls the level of circulation epinephrine also has a large impact on HRV.

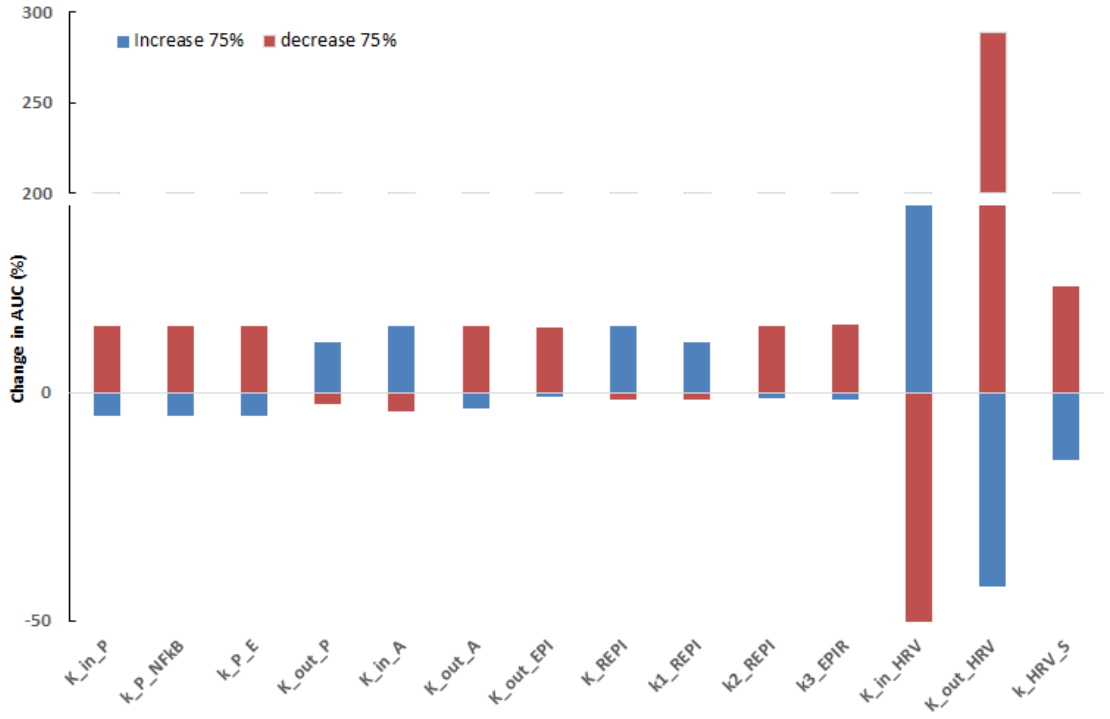

Figure 3.4: Sensitivity analysis for kinetic parameters in the HRV model. Sensitivity analysis is performed under the scenario of 6 hour continuous exposure to PM2.5 with an average concentration of 167 µg/m3. 75% is selected as the cutoff to perturb the kinetic parameters. Only parameters that cause at least 10% change in AUC of the SDNN time profile curve are shown.

3.4 Summary

In summary, a multiscale model has been developed to bridge the complex biological processes involved in the alteration of HRV following exposure to particulate matter. At the cellular level, an inflammation module addresses the recognition of PM by cells, the activation of intracellular signaling pathways (NFκB and Nrf2) as well as the transcription of pro- and anti-inflammatory cytokines. The secretion of endocrine stress hormones and their anti-inflammatory role are taken into consideration in a module built for the bidirectional communication between the immune

response and the neuroendocrine system. The systemic alteration (changes of HRV) is further incorporated in the model by propagating the dynamic signal evoked via immune-neuroendocrine interactions into the heart. This work connects PM exposure and HRV changes via a semi-mechanistic model that includes biological events from the cellular to the systemic level. Model parameters were evaluated to generate simulation results that are quantitatively consisted with measurements in a human PM exposure study. Model performance and its predictive capability were further evaluated by applying the model to two different PM exposure scenarios. Sensitivity analysis for all kinetic parameters was also performed to identify biological pathways with significant impact on HRV. This modeling approach provides insight into the mechanisms underlying the cardiovascular mortality induced by air pollutants and can support the future exploration of potential clinical measures to attenuate the adverse health effects of air pollution.

Chapter 4

Modeling Skin Biology Initiated by Air Pollutants Exposures

4.1 Background

Skin is both a complex biological interface between the human organism and the environment, and a toxicological target for a wide range of hazardous agents, including UV radiation, photochemical oxidants, polycyclic aromatic hydrocarbons, halogenated hydrocarbons, fine particles, etc. Existence of associations between air pollution and adverse skin effects has been supported by many recent studies. Lefebvre *et al.* [150] compared biochemical and clinical skin parameters of two populations living in areas with different levels of air pollution in Mexico. 93 volunteers living in Cuernavaca (the less polluted area) participated in the study from September 7, 1999 to January 5, 2000; 96 volunteers living in Mexico City (the most polluted area) participated in the study from February 3 to March 23, 2000. The population from Mexico City showed a lower level of antioxidants and squalene in sebum, an increased level of sebum excretion rate and a higher erythematous index on the face of the participants. From a clinical point of view, a higher frequency of red dermographism and a higher frequency of atopic and urticarial skins were observed in the Mexico

City population. In 2008/2009, Vierkotter *et al.* assessed the influence of PM on skin aging in 400 Caucasian women aged 70-80 years living in urban and rural areas in Germany [22]: they demonstrated, for the first time that chronic traffic-related PM exposure was significantly correlated to extrinsic skin aging signs, especially pigment spots formation. In Shanghai, China, Xu *et al.* evaluated the association between emergency-room visits for skin conditions and ozone exposure [25]. An increase of 10 $\mu g/m^3$ ozone resulted in 0.78% increase in urticarial, 3.84% increase in eczema, 2.86% increase in contact dermatitis, 3.22% increase in rash/other nonspecific eruption and 2.72% increase in infected skin disease. Figure 4.1 shows the correlation between ozone exposure and the relative risk of Emergency Room (ER) visits for total skin conditions. The relative risk of ER visits for total skin conditions increases monotonically as ozone concentrations increase up to a level of approximately 100 $\mu g/m^3$, while data for higher concentrations are too variable to allow derivation of a definite trend.

The mechanisms behind air pollutants induced adverse health effects in the cutaneous system involve skin surface reactions, subsequent activations of cell signaling pathways, as well as potential alterations in skin cell cycle regulation. In the following sections, different computational models are developed to simulate air pollution-initiated skin effects, mediated by the biological events mentioned above.

4.2 Modeling ozone reactions with skin surface lipids

Human skin consists of two major layers: epidermis and dermis. The epidermis is predominately made up of keratinocytes which account for 95% of the cells; however, the epidermis also houses melanocytes as well as immune cells such as Langerhans cells. In the epidermis, keratinocytes proliferate and divide in the epidermal basal layer and move upward as they differentiate to form cornified cells at the outermost

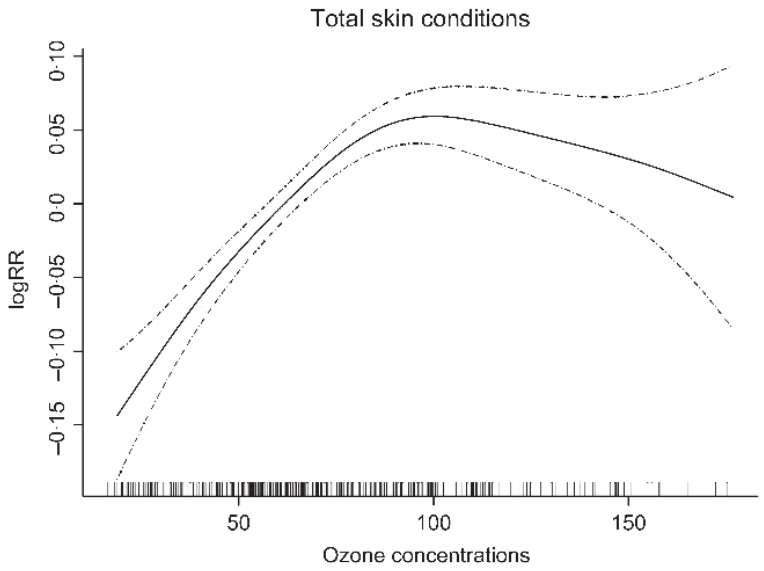

Figure 4.1: Ambient ozone concentration vs. relative risk of increase in emergency room visits for skin conditions in Shanghai, China [25].
(Data were collected from February 10, 2007 to December 31, 2008; ozone concentration is in the unit of $\mu g/m^3$; minimal, mean and maximal daily 8-h average ozone concentrations were 5.0, 71.6 and 225 $\mu g/m^3$; increase of ER visits was analyzed against 10 $\mu g/m^3$ increase of 7-day average ozone concentration; RR: relative risk)

surface of skin. Depending on their differentiation stages, keratinocytes are arranged into four layers as shown in Figure 4.2 [151]: the stratum corneum and lucidum (cornified cell layer and clear cell layer), the stratum granulosum (granular cell layer), the stratum spinosum (spinous cell layer) and the stratum basale (basal cell layer). The primary cell types in the dermis are fibroblasts which produce components of the extracellular matrix (ECM) such as collagen, elastin and extracellular structural proteins. In addition, many different types of immune cells also populate the dermis. These cells undergo dynamic changes during immune responses.

Human skin surface is covered with a layer of lipids which can be divided into two groups [152]: the majority of the surface lipids are sebaceous lipids; the rest of the surface lipids are produced by the epidermis (Figure 4.3). Ozone, being a highly oxidative molecule, reacts rapidly with components of skin surface lipids by attacking C=C bonds [153–155].

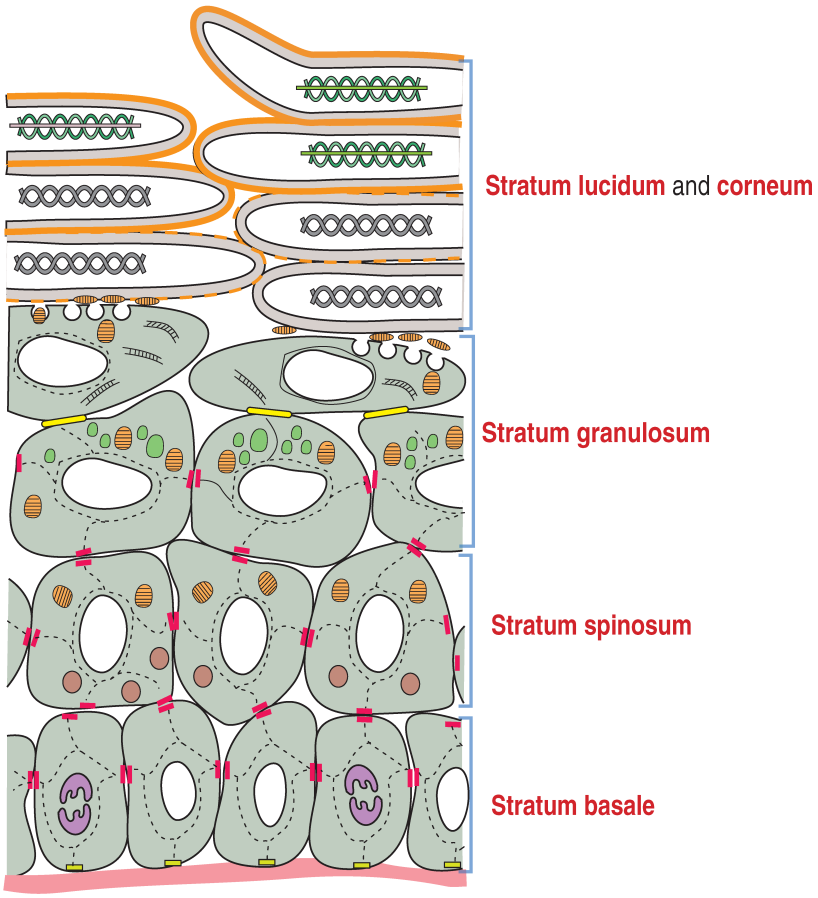

Figure 4.2: Keratinocyte layers in the human epidermis [151]

Among all the skin lipids, squalene (Figure 4.3) is a specific marker of human sebum since it is absent in the sebum of almost all other mammalian species. The six C=C bonds in squalene make it a major target for ozone. Reactions between ozone and squalene can generate secondary organic aerosol (SOA), a source of fine particle exposure that is associated with an increase in both morbidity and mortality. Especially in the indoor environment, where people spend most of their time, inhalation exposure to ozone-induced SOA may become significant in terms of causing respiratory and cardiovascular health outcomes. This phenomenon also links the two exposure routes, single dermal exposure may enhance inhalation exposures to air pollutants.

Here, we developed a semi-empirical model to simulate the indoor formation of fine

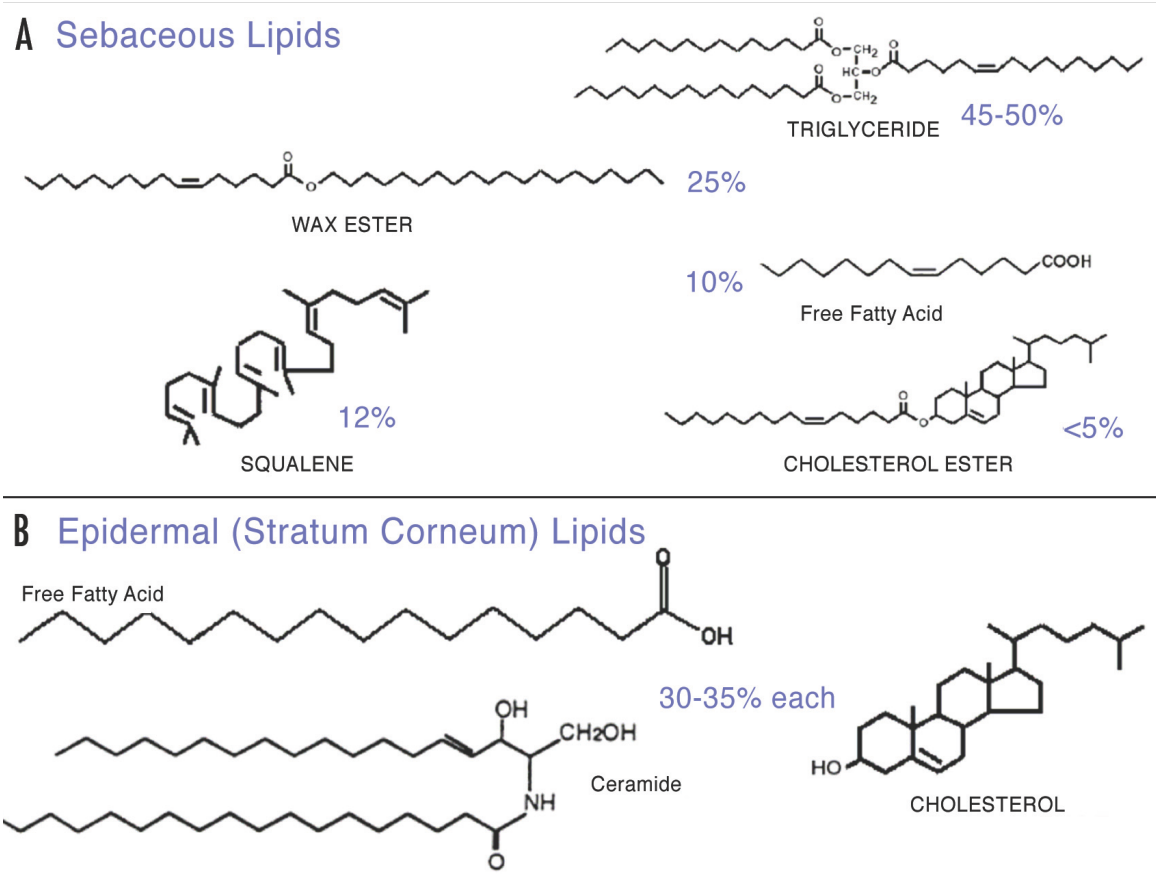

Figure 4.3: Representative structure of skin surface lipids with relative percentage by weight [152]

particles due to the reaction between ozone and squalene. The model is parameterized based on the chamber experiments conducted by Wang *et al.* [156]. Briefly, four petri dish bottoms with surfaces covered with squalene were placed in a reaction chamber. Ozone and air mixture flows into the reaction chamber which is operated at constant relative humidity, temperature and air exchange rate for each experiment. Concentration of ozone and SOA formation in the chamber were measured by an ozone monitor (2B Technologies model 205, 10 s intervals) and Scanning Electrical Mobility Sizer, respectively.

The model considers the reaction between ozone and squalene, deposition of ozone to chamber walls, SOA deposition to chamber walls and mass transfer due to air

exchange. Mass balance equations for ozone and SOA are presented below:

$$\frac{dC_{O_3}}{dt} = \lambda C_{O_3,inlet} - \left(\lambda + \frac{v_{d,w}(A_w - A_{sq})}{V} + \frac{v_{d,sq} - A_{sq}}{V}\right) C_{O_3} \tag{4.1}$$

Here C_{O_3} and $C_{O_3,inlet}$ are the ozone mole fractions in the chamber and the inlet flow, respectively; λ is the air exchange rate ($\lambda = 5.42$/h); $v_{d,w}$ and $v_{d,sq}$ are the deposition velocities to the chamber walls and the squalene surface, respectively; A_w and A_{sq} are the surface areas of the chamber walls and the squalene-sorbed zones, respectively; V (V=37.1L) is the volume of the reaction chamber.

$$\frac{dC_{SOA,M}}{dt} = \xi_{O_3/SQ,M} C_{O_3,M} \frac{v_{d,sq} A_{sq}}{V} - (\lambda + \beta_{SOA,M}) C_{SOA,M} \tag{4.2}$$

$C_{O_3,M}$ and $C_{SOA,M}$ are the chamber ozone and SOA mass concentration, respectively; $\beta_{SOA,M}$ is the loss rate of SOA mass to the chamber surfaces; $\xi_{O_3/SQ,M}$ is the ratio of SOA produced to the amount of ozone reacted with surface squalene. $v_{d,w}$ is a function of the chamber ozone mole fraction, in the form of:

$$v_{d,w} = a \times C_{O_3}^b \tag{4.3}$$

Values of a and b depend on the relative humidity and will be estimated from experimental measurements. $v_{d,sq}$ and $\xi_{O_3/SQ,M}$ are assumed to be constant and equal to their steady state values. At steady state, $\frac{dC_{O_3}}{dt}$ and $\frac{dC_{SOA,M}}{dt}$ equal to zero. From equation 4.1 and 4.2,

$$v_{d,sq} = \frac{\lambda V}{A_{sq}}\left(\frac{C_{O_3,inlet}}{C_{O_3}} - 1\right) - \frac{v_{d,w}(A_w - A_{sq})}{A_{sq}} \tag{4.4}$$

$$\xi_{O_3/SQ,M} = \frac{V}{A_{sq} v_{d,sq}} \times \frac{(\lambda + \beta_{SOA,M}) C_{SOA,M}}{C_{O_3,M}} \tag{4.5}$$

In equations 4.1 to 4.5, the only unknown or unmeasured parameter is $\beta_{SOA,M}$.

$\beta_{SOA,M}$ represents the particle deposition rate onto chamber walls and depends on the particle size distribution, therefore, $\beta_{SOA,M}$ has different values for different experiments. Combining the theory of Lai *et al.* [157] and laboratory measurements, values of $\beta_{SOA,M}$ are estimated for each steady state SOA mass distribution.

Time profiles of model predicted SOA and ozone concentrations are compared with laboratory measurements in low and high ozone experiments at 21% and 51% humidity levels (Figure 4.4). The model is able to predict the steady state level of SOA and ozone under all circumstances. Under the same humidity level, higher ozone concentrations lead to higher steady state SOA concentrations; at high ozone levels, a more humid environment tends to generate higher levels of SOA. Both simulation results and laboratory measurements show that the low ozone experiments require more time for SOA to approach steady state than the high ozone experiments. However, model simulated SOA formation reaches a steady state faster than experimental measurements in all four conditions. This may be caused by overly simplified assumptions in our model that use constant values for several parameters (i.e. $\xi_{O_3/SQ,M}$, $v_{d,sq}$) throughout the process. A mechanistic model that considers the real time kinetics of ozone-squalene reaction would be needed to better characterize ozone induced SOA formation in indoor environment.

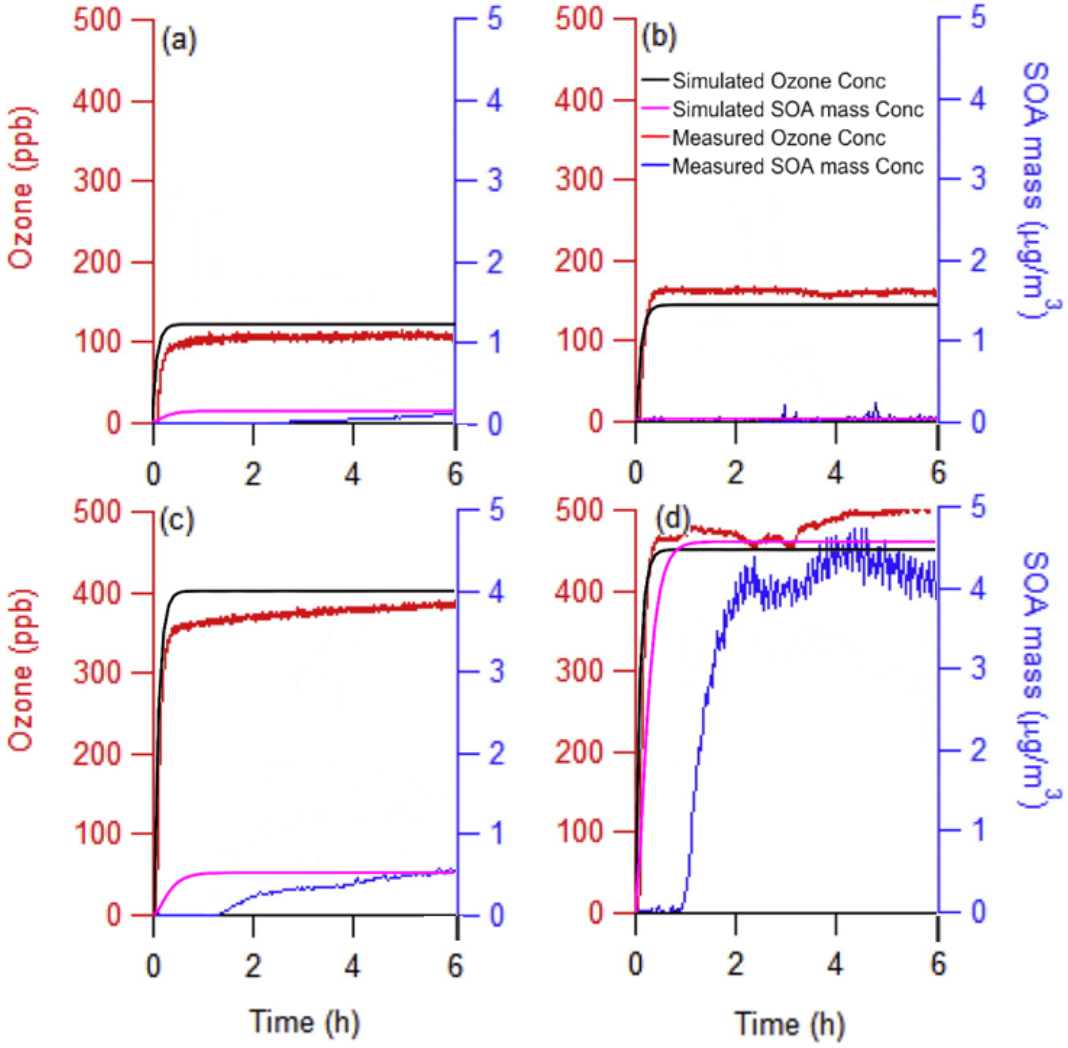

Figure 4.4: Comparisons of model simulation and measurements for chamber experiments exploring SOA formation initiated by surface reactions between ozone and sorbed squalene: (a)inlet ozone 241 ppb, relative humidity (RH) 21%; (c) inlet ozone 771 ppb, RH 21%; (b) inlet ozone 275 ppb, RH 51%; (d) inlet ozone 877 ppb, RH 51%.

4.3 Modeling AhR activation in keratinocyte upon exposure to air pollutants

The aryl hydrocarbon receptor (AhR) is a member of the basic helix-loop-helix Per-ARNT-Sim family. It is a transcription factor that mediates toxic and carcinogenic effects of a very wide range of environmental agents. Many air pollutants can either act as ligands or induce ligands that activate the AhR. A "generic" mechanism in skin exposure biology involves AhR-mediated inflammatory responses: upon binding with ligands, cytoplasmic AhR translocates to the nucleus and heterodimerizes with ARNT; this heterodimer binds to DNA response elements and initiates the transcription of target genes encoding CYP1 proteins and subsequent production of ROS, leading to activation of pro-inflammatory NFκB signaling pathways. In addition, the AhR-ARNT complex induces translocation of Nrf2 from cytosol to the nucleus, resulting in anti-inflammatory effects. Figure 4.5 presents a diagram summarizing the key signaling and regulatory processes occurring in keratinocytes upon exposure to air pollutants and other AhR ligands.

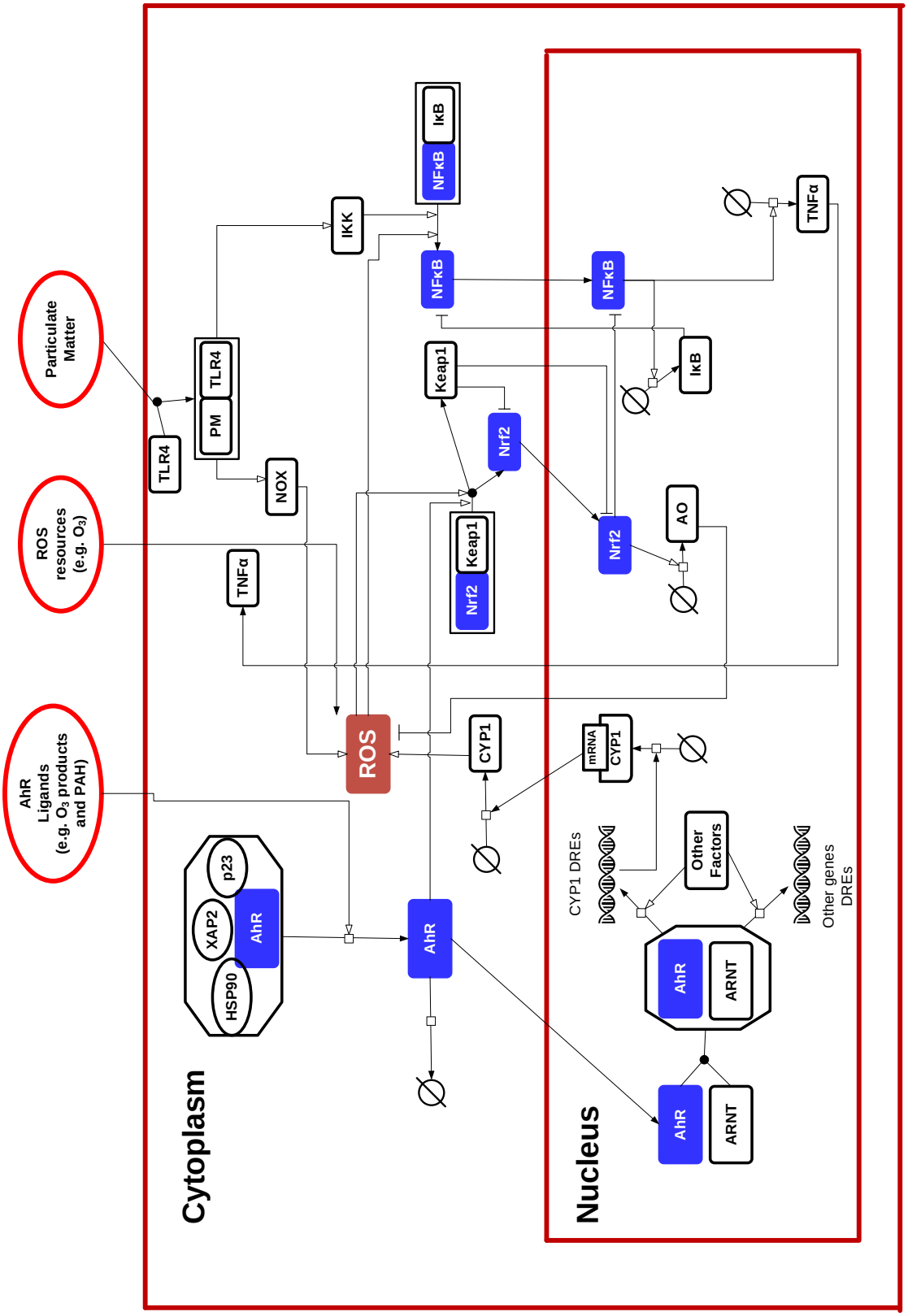

Figure 4.5: AhR-mediated signaling pathways upon exposure to air pollutants (the diagram follows SBGN standards; SBGN:Systems Biology Graphical Notation)

As an initial step towards building a comprehensive model for the complex signaling network in keratinocytes, a specific model for AhR activation and subsequent gene transcriptions is first developed independently, i.e. without considering interactions with NFκB and Nrf2 pathways. A model designed for 2,3,7,8-tetrachlorodibenzodioxin (TCDD) initiated transcription in T47D cells [158] was adapted and modified to simulate AhR activation in human keratinocytes upon exposure to air pollutants. AhR is an ozone sensor in human skin and ozone exposure has been shown to activate AhR in cultured normal human epidermal keratinocytes [159]. However, ozone is highly reactive and itself does not directly bind to AhR because of its rapid depletion via reactions with skin lipids (*in vivo*), cell culture media (*in vitro*) and components of the cell membrane. The exact ozone reaction products that work as the directly binding ligands to AhR have not been clearly identified. It is well known that FICZ (6-formyl-indolo[3,2-b]carbazole, $C_9H_{12}N_2O$), a tryptophan photo-oxidation product, mediates the activation of AhR upon UV radiation [160]. Sindhu *et al.* conducted *in vitro* experiments in Hepa lclc7 cells and demonstrated that both ozone-oxidized tryptophan and photo-oxidized tryptophan induced the transcription of CYP1 mRNA, a commonly used marker for the activation of AhR [161, 162]. Therefore, it is postulated that AhR activation in keratinocytes after ozone treatment is mediated by ozone/tryptophan products following a mechanism similar to FICZ. The model is implemented for AhR activation in human keratinocytes assuming FICZ as the activating agent.

The biological events included in the model are briefly described as follows:

- FICZ diffuses into keratinocyte cells and binds to cytoplastic AhR that is synthesized at a constant rate. The AhR-FICZ complex can degrade in the cytoplasm or move to the nucleus.

- Once inside the nucleus, FICZ-AhR can bind to the aryl hydrocarbon nuclear translocator (ARNT) to form a heterodimer or undergo degradation. The het-

erodimer binds cofactors [163] to form a transcription complex. The complex then binds to xenobiotic response elements on DNA (XREs) that regulate the expression of CYP1 proteins. The transcription complex, consisting of AhR, ARNT and the cofactor, can also bind to other DNA sites associated with the transcription of other genes.

- Once the transcription complex binds to an XRE, RNA polymerase also binds, and the XRE-bound transcription complex can undergo transcription initiation. Once initiated, the complex starts transcription.

- ARNT may dissociate from the transcription complex without interrupting the transcription. The transcription complex could reversibly bind to another co-regulator protein and increase the rate of transcription [158].

- Transcription is modeled with irreversible mass action kinetics. Any transcribed mRNA can degrade or exit the transcription complex. In an attempt to handle the complexity of the transcription process, the model includes four states of the transcription complex and each state has a slightly different rate of transcription.

Gene expression is a fundamentally stochastic process involving discrete and inherently biochemical reactions for the production of mRNA and proteins [164]. Ordinary differential equations (ODEs) based models do not capture the stochastic nature of AhR mediated gene expression. Therefore, the direct method of Gillespie's stochastic simulation algorithm (SSA) was selected for model implementation and simulation. The reaction network in the model consists of 32 reactions of either one of the following types:

- $A + B \rightarrow C$

- $A \rightarrow B + C$

- $A \rightarrow B$

All the reactions follow the law of mass action in the form of propensity $a = k[A][B]$ or propensity $a = k[A]$. During a stochastic simulation, k is the molecular rate constant in units of 1/(molecules × s) or 1/s. [A] or [B] is the number of molecules for each reactant. Propensity is the probability of the reaction occurring in the next time interval. The steps for running the model with Gillespie's stochastic simulation algorithm can be summarized as follows:

1. Pass initial amount of each species to the model (time is $t_0 = 0$)
2. Calculate propensity a_i for each reaction R_i ($i = 1$ —32)
3. Calculate total propensity $a_{total} = a_1 + a_2 + a_3 + ...a_{32}$
4. Generate a random number $rand_1$ between 0 and 1 from a uniform distribution
5. $\Delta t = \frac{1}{a_{total}} \times \ln(\frac{1}{rand_1})$
6. Generate another random number $rand_2$ between 0 and 1 from a uniform distribution
7. Find the smallest q such that $a_1 + a_2 + ... + a_q > a_{total} \times rand_2$
8. At time $(t_0 + \Delta t)$, only the q_{th} reaction happens
9. Update the amount of each species accordingly
10. Repeat steps 2 —9 until time reaches the pre-decided simulation time

The model considers 29 compounds, 32 reactions and 4 compartments. Full details of the model parameters and variables are presented in Table 4.1. The model is implemented using Simbiology toolbox of Matlab. For model simulations, 100 runs were conducted for every experimental scenario and the average values are used as results.

Simulation results are compared with laboratory measurements from a study conducted by Nair *et al* [165] in which CYP1B1 mRNA levels were measured in HaCaT cells after 6 hours of treatment with FICZ at different concentrations. The model faithfully reproduces the increase of CYP1B1 mRNA expressions (Figure 4.6), indicating the applicability of the model in FICZ initiated AhR activation and subsequent gene transcription. To further evaluate the model and test its extensibility to other AhR ligands, the model was implemented for benzo(a)pyrene (BaP) exposure. BaP is a carcinogenic polycyclic aromatic hydrocarbon formed through incomplete combustion of organic matter. It can be found in emissions from burning plants, wood, coal and from internal combustion engine operating in cars and trucks. The major sources of population exposures to atmospheric BaP are residential wood-burning fireplaces and cooking stoves, as well as tobacco smoking. Tsuji *et al* [166] measured the expression of CYP1A1 mRNA in normal human epidermal keratinocytes (NHEKs) after treatment with BaP for 3 hours at concentrations of 20 nM, 40 nM, 100 nM and 1000 nM. Figure 4.7 shows an overall agreement between model simulation results and laboratory measurements at all concentrations, suggesting the potential to apply adaptations of the current model to various AhR ligands originating from air pollution.

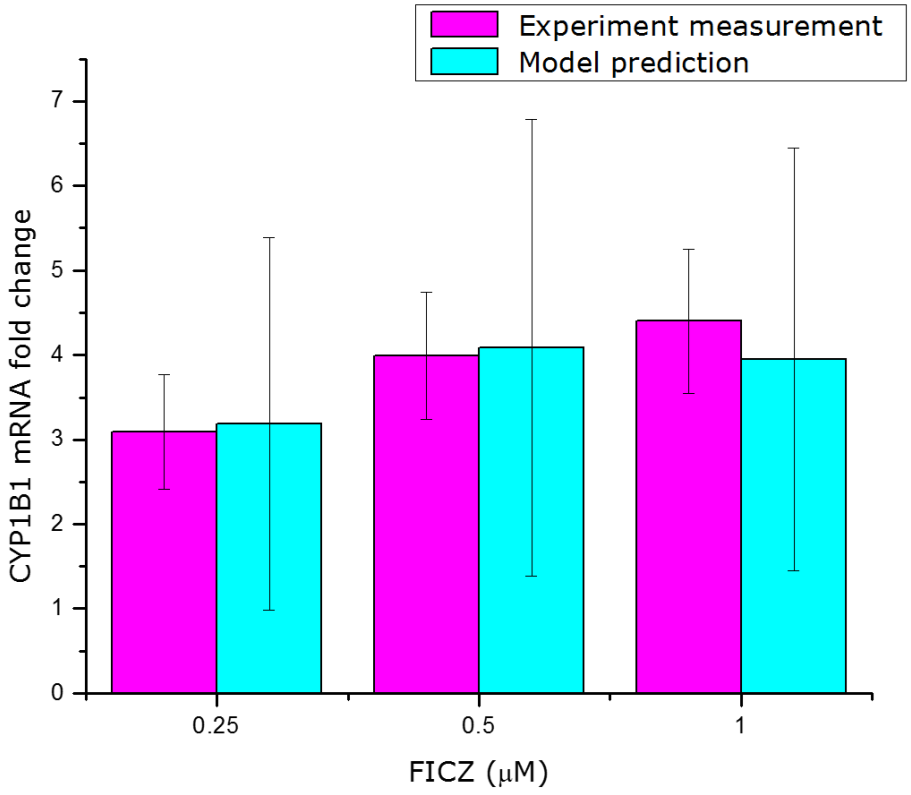

Figure 4.6: Comparison between model predictions and laboratory measurements for CYP1B1 mRNA expression in keratinocytes in an *in vitro* system for different concentrations of FICZ.
(*Experimental data were extracted from the study conducted by Nair et al. [165]; column, means: for experimental measurement n =3 and for model prediction, n=100; bars: standard deviation*)

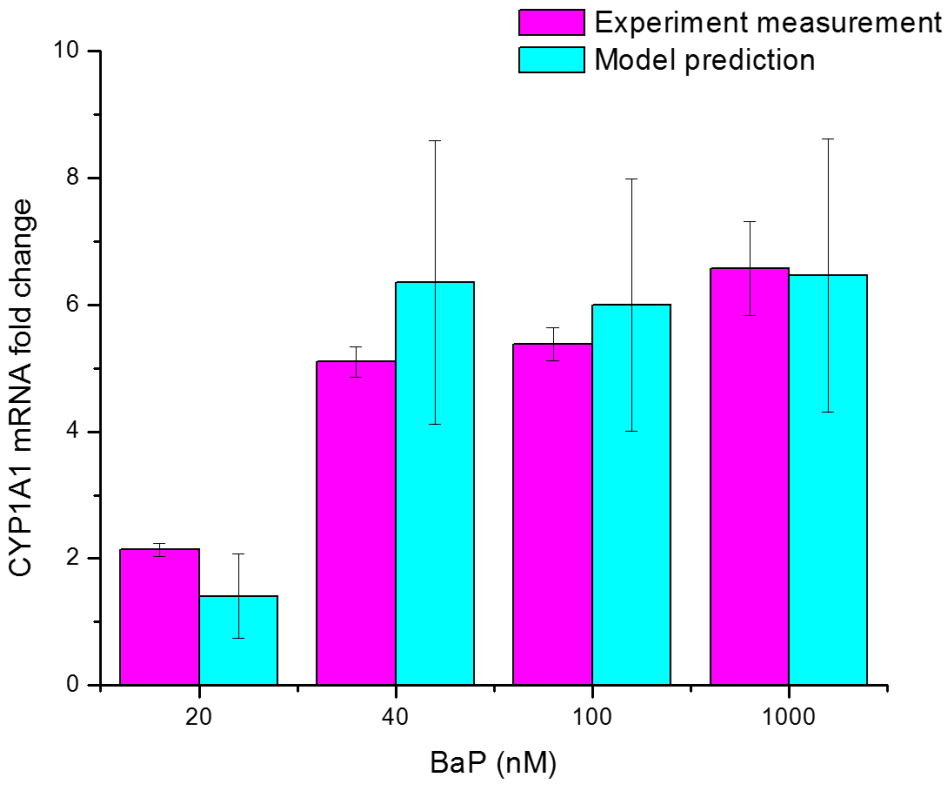

Figure 4.7: Comparison between model predictions and laboratory measurements for CYP1A1 mRNA expression in keratinocytes in an *in vitro* system for different concentrations of Benzo(a)pyrene.
(*Experimental data were extracted from the study conducted by Tsuji et al. [166]; column, means: for experimental measurement n =3 and for model prediction, n=100; bars: standard deviation*)

Table 4.1: Reactions and rate constants in the model for AhR activation and subsequent gene transcriptions

Reaction #	Description	Reversibility	Forward rate	Backward rate	Forward equation	Backward equation
1	Diffusion of FICZ into cell	Reversible	8E-07/s	8E-07/s	kf_1[FICZ]	kb_1[FICZ]
2	FICZ binding to AhR	Reversible	10.02E-07/(molecule×s)	0.002/s	kf_2[FICZ][AhR]	kb_2[AhR-FICZ]
3	Nuclear translocation	Reversible	1.51E-03/s	8.33E-05/s	kf_3[AhR-FICZ]$_{cyto}$	kb_3[AhR-FICZ]$_{nuc}$
4	Cytoplasmic AhR degradation	Irreversible	4.167E-04/s	NA	kd_4[AhR-FICZ]$_{cyto}$	NA
5	ARNT binding	Reversible	1.357E-07/(molecule×s)	8.33E-06/s	kf_5[AhR-FICZ][ARNT]	kb_5[AhR-ARNT]
6	ARNT-AhR complex degradation	Irreversible	1.25E-03/s	NA	kd_6[AhR-ARNT]	NA
7	Nuclear AhR degradation	Irreversible	4.167E-04/s	NA	kd_7[AhR-FICZ]$_{nuc}$	NA
8	Cofactor binding	Reversible	1.628E-06/(molecule×s)	2.5E-04/s	kf_8[AA][CoF]	kb_8[AA-CoF]
9	Cofactor binding to other sites	Reversible	1.628E-06/(molecule×s)	2.5E-04/s	kf_9[Other][CoF]	kb_9[Other-CoF]
10	AA-CoF binding to CYP1 XREs	Reversible	4.33E-07/(molecule×s)	1.67E-03/s	kf_{10}[AA-CoF][CYPXRE]	kb_{10}[bound CYPXRE]
11	AA-CoF binding to other XREs	Reversible	1.628E-06/(molecule×s)	1.67E-03/s	kf_{11}[AA-CoF][XRE]	kb_{11}[bound XRE]
12	RNA polymerase binding to CYP1-XRE complex	Reversible	0.4/(molecule×s)	0.145/s	kf_{12}[CYP-AA-CoF][RNAPol]	kb_{12}[CYP-AA-CoF-RNAPol]
13	RNA polymerase binding to non CYP1-XRE complex	Reversible	0.4/(molecule×s)	0.145/s	kf_{13}[XRE-AA-CoF][RNAPol]	kb_{13}[XRE-AA-CoF-RNAPol]
14	CYP initialization	Irreversible	0.03/s	NA	kf_{14}[CYP-AA-CoF-RNAPol]	NA
15	ARNT escape	Reversible	0.05/s	5.5E-03/(molecule×s)	kf_{15}[CYP_init]	kb_{15}[CYP_init_Am][ARNT]
16	Termination	Irreversible	0.019/s	NA	$k_{term,16}$[CYP_init]	NA

Table 4.1 Reactions and rate constants in the model for AhR activation and subsequent gene transcriptions —Continued

Reaction #	Description	Reversibility	Forward rate	Backward rate	Forward equation	Backward equation
17	Termination	Irreversible	0.01/s	NA	$k_{term,17}$[CYP_init_Am]	NA
18	Transcription	Irreversible	1.3E-03/s	NA	$k_{trans,18}$[CYP_init]	NA
19	Transcription	Irreversible	8E-04/s	NA	$k_{trans,19}$[CYP_init_Am]	NA
20	mRNA degradation	Irreversible	0.021/s	NA	kd_{20}[mRNA_t]	NA
21	mRNA export	Irreversible	0.002/s	NA	$k_{exp,21}$[mRNA_t]	NA
22	non CYP XRE initiation	Irreversible	1E-04/s	NA	$k_{init,22}$[XRE-AA-CoF-RNAPol]	NA
23	non CYP XRE termination	Irreversible	0.019/s	NA	$k_{term,23}$[XRE_init]	NA
24	ARNT escape from non CYP XRE	Irreversible	0.005/s	NA	kf_{24}[XRE_init]	NA
25	non CYP XRE termination	Irreversible	0.01/s	NA	$k_{term,25}$[XRE_init_Am]	NA
26	AhR synthesis	Irreversible	1.42E-03/(molecule×s)	NA	$k_{syn,26}$	NA
27	ARNT synthesis	Irreversible	1.3E-03/(molecule×s)	NA	$k_{syn,27}$	NA
28	Coregulator binding to CYP1	Reversible	4.9E-03/s	5E-03/s	kf_{28}[CYP_init][CoReg]	kb_{28}[CYP_init-CoReg]
29	Transcription	Irreversible	1.6E-03/s	NA	$k_{trans,29}$[CYP_init-CoReg]	NA
30	Coregulator binding to CYP1	Reversible	4.9E-03/s	5E-03/s	kf_{30}[CYP_init_Am][CoReg]	kb_{30}[CYP_init_Am-CoReg]
31	Transcription	Irreversible	1.1E-03/s	NA	$k_{trans,31}$[CYP_init_Am-CoReg]	NA
32	Coregulator competition	Reversible	0.05/(molecule×s)	0.0049/s	kf_{32}[CoReg][Comp]	kb_{32}[CoReg-Comp]

4.4 Modeling AhR regulated cell cycle progression in the integumentary system

One potential mechanism for air pollution induced skin disorders is the activation of AhR, through which the cell cycle progression is affected. Cell cycle is the series of events during which a growing cell replicates its DNA and all other components and divides into two daughter cells. Misregulation of the cell cycle leads to abnormal cell proliferation resulting in serious human diseases, such as cancer. In eukaryotic cells, the cell cycle is commonly split into four phases: G1 $\rightarrow$ S $\rightarrow$ G2 $\rightarrow$ M. During G1 phase, the cell grows in size, copies organelles and prepares for DNA synthesis. In S phase, the cell synthesizes a complete copy of its DNA. Then the cell enters G2 phase during which the cell grows more and prepares for mitosis. After G2 phase, the cell enters M phase, during which the cell separates its DNA into two sets and divides its cytoplasm, forming two daughter cells. Cells in G1 phase can also enter a resting phase (G0) where the cells have left cell cycle and stopped dividing.

It is well established that AhR plays a role in the regulation of the cell cycle [167]. AhR-defective variant of the mouse hepatoma Hepa 1c1c7 cell line exhibited a prolonged doubling time compared with its wild-type counterpart [168]. Elizondo *et al.* [169] reported that mouse embryonic fibroblasts (MEFs) from AhR-null mice grew more slowly than wild-type MEFs. These studies suggest that AhR could facilitate cell cycle progression. Some other studies reported seemingly contradictory results. When treated with TCDD (a typical AhR agonist), the growth of MCF-7 human breast cancer cells was inhibited. In addition, TCDD inhibited DNA synthesis in confluent mouse epithelial cells, in partially hepatectomized rat liver and in rat primary hepatocytes. TCDD also induced G1 phase arrest in SK-N-SH human neuronal [170, 171]. Collectively, it is plausible to conclude that AhR facilitate cell cycle progression in the absence of exogenous ligands; but when activated by an ex-

ogenous ligand, AhR induces cell cycle arrest and inhibits cell proliferation. Several mechanisms have been proposed by Murray *et al.* [167] based on experimental studies using cell culture models to explain the effects of AhR on the cell cycle (Figure 4.8). In Figure 4.8 (a), AhR acts as the direct transcriptional activator of genes encoding mitogenic growth factors, including vascular endothelial growth factor A (VEGFA), platelet-derived growth factor (PDGF), epiregulin, amphiregulin and fibroblast growth factor 9 (FGF9). These growth factors stimulate the entry into M phase of cell cycle and therefore promote cell proliferation. In Figure 4.8 (b), activated AhR enhances the expression of p27 which limits the phosphorylation of RB and restricts the E2F-dependent expression of genes required for S phase, therefore resulting in cell cycle arrest at G1 phase. In Figure 4.8 (c), AhR interacts with RB to attenuate the phosphorylation of RB and the release of E2F, leading to G1 arrest and inhibition of cell proliferation. In Figure 4.8 (d), activated AhR stimulates the ubiquitylation of β-catenin, leading to enhanced degradation of β-catenin which restricts the expression of factors required for cell cycle-dependent gene expression and proliferation. In Figure 4.8 (e), AhR without a bound ligand can form a complex with cyclin D and cyclin-dependent kinases 4 (CDK4) to suppress the phosphorylation of RB, leading to G1 arrest by limiting E2F regulated S phase progression. As noted, AhR has contradictory roles in cell cycle regulation; therefore, a model is developed based on the above-mentioned mechanisms as an attempt to capture both the pro- and anti-proliferative effects of AhR in the presence or absence of exogenous ligands.

Progression through the cell cycle depends on a complex interaction network involving cyclins, cyclin-dependent kinases (CDK), CDK inhibitors and other regulatory proteins. The model developed here is adapted from a model originally proposed by Swat *et al.* [172]. The core of G1 phase progression is the interactions between pRB and E2F1. pRB is a tumor suppressor that inhibits the activation of E2F proteins resulting in repression of E2F-regulated gene expression. The repression of this

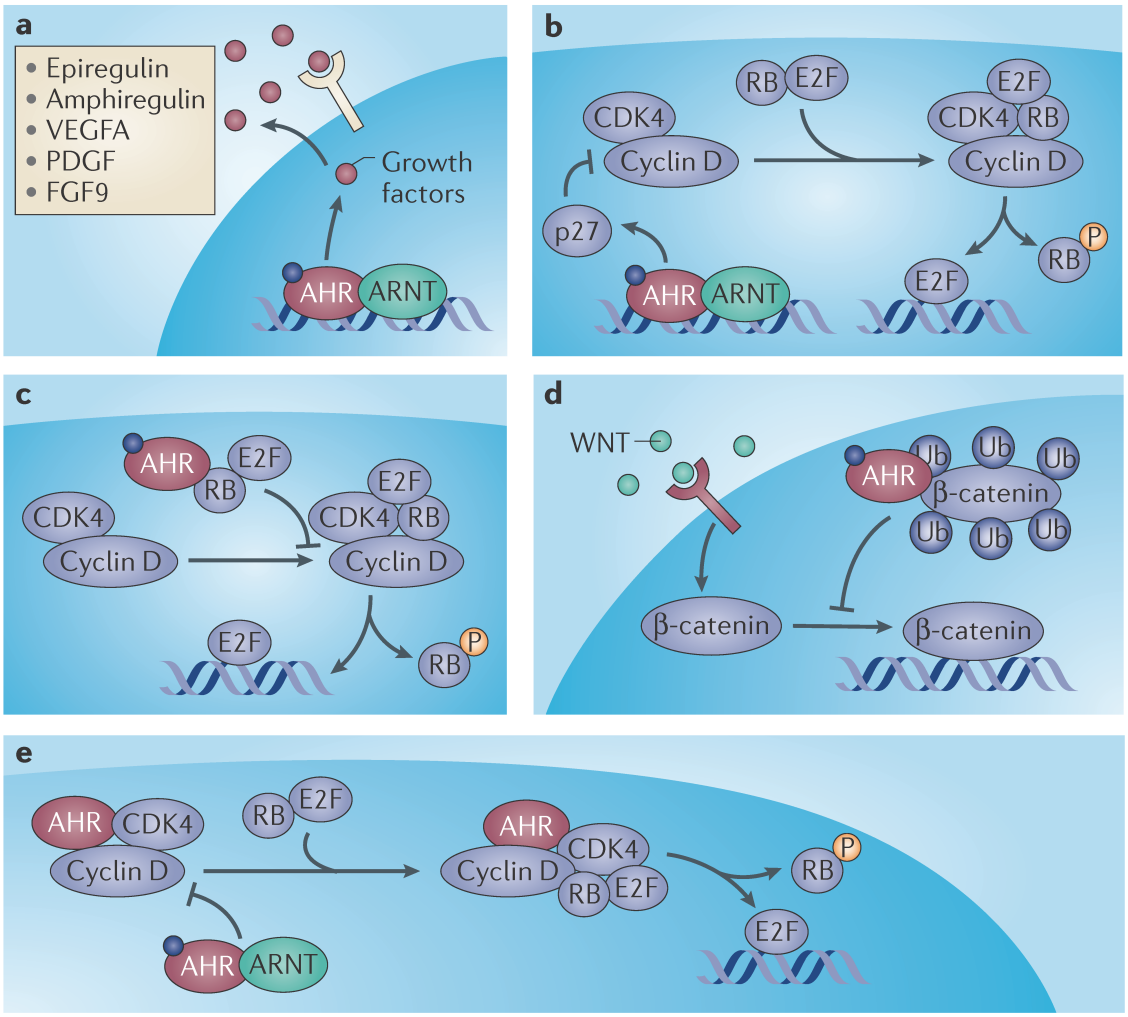

Figure 4.8: Proposed mechanisms of cell cycle modulation by AhR [167]

gene expression leads to downregulation of cell cycle required cyclins and CDKs resulting in prolonged G1 phase or even G1 phase arrest. In the absence of exogenous ligands, unbound AhR can interact with CycD/cdk4,6 to form a complex that facilitates the hyper-phosphorylation of pRB leading to enhanced activation of E2F proteins and subsequent cell cycle progression [173]. Upon binding to exogenous ligands, AhR dissociates from the AhR/CycD/cdk4, 6 complex and the bound AhR inhibits the phosphorylation process of pRB leading to G1 arrest. The cell is deemed to enter S phase when E2F1 levels cross a certain threshold value [172] and the time this occurs is recorded as the duration of G1 phase. A schematic presentation of the

model is shown in Figure 4.9. This model incorporates different mechanisms of action

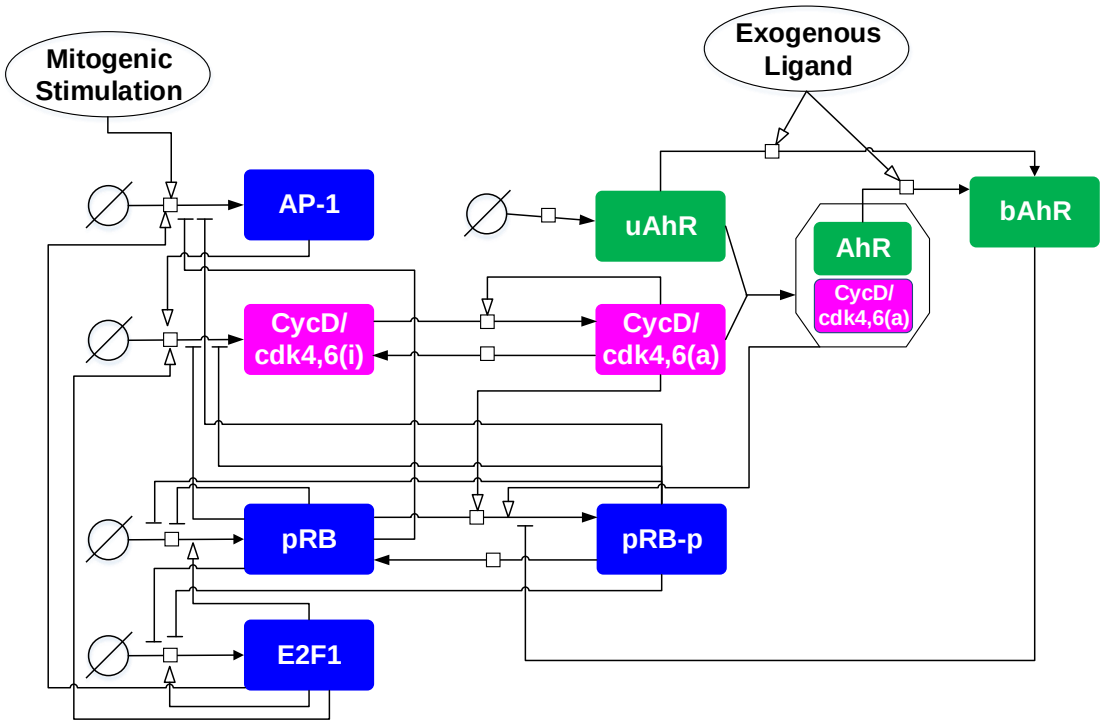

Figure 4.9: Proposed model for the dual role of AhR on cell cycle regulation (The diagram follows SBGN standards; CycD: cyclin D; cdk:cyclin-dependent kinase; pRB: retinoblastoma proteins; pRB-p: phosphorylated pRB; E2F1: transcription factor for S phase proteins; uAhR: unbound AhR; bAhR: ligand-bound AhR; (i): inactive; (a): active)

for unbound AhR and ligand-bound AhR: it aims to predict G1 phase duration in normal cells, AhR-knockout cells and exogenous AhR ligand treated cells. The model is mathematically formulated using the following ordinary differential equations:

$$\frac{d[pRB]}{dt} = k_1 \frac{[E2F1]}{K_{m1} + [E2F1]} \frac{J_{11}}{J_{11} + [pRB]} \frac{J_{61}}{J_{61} + [pRB_p]} + k_{61}[pRB_p] - k_{16}[pRB][CycD_a] \frac{[AhRCyc]}{K_{m6} + [AhRCyc]} \frac{J_{86}}{J_{86} + [bAhR]} - \phi_{pRB}[pRB] \quad (4.6)$$

$$\frac{d[E2F1]}{dt} = k_p + k_2 \frac{a^2 + [E2F1]^2}{K_{m2}^2 + [E2F1]^2} \frac{J_{12}}{J_{12} + [pRB]} \frac{J_{62}}{J_{62} + [pRB_p]} - \phi_{E2F1}[E2F1] \quad (4.7)$$

$$\frac{d[CycD_i]}{dt} = k_3[AP1] + k_{23}[E2F1]\frac{J_{13}}{J_{13}+[pRB]}\frac{J_{63}}{J_{63}+[pRB_p]} + k_{43}[CycD_a]$$
$$- k_{34}[CycD_i]\frac{[CycD_a]}{K_{m4}+[CycD_a]} - \phi_{CycD_i}[CycD_i] \quad (4.8)$$
$$\frac{d[CycD_a]}{dt} = k_{34}[CycD_i]\frac{[CycD_a]}{K_{m4}+[CycD_a]} - k_{43}[CycD_a]$$
$$- k_9[cycD_a][uAhR] - \phi_{CycD_a}[CycD_a] \quad (4.9)$$
$$\frac{d[AP1]}{dt} = F_m + k_{25}[E2F1]\frac{J_{15}}{J_{15}+[pRB]}\frac{J_{65}}{J_{65}+[pRB_p]} - \phi_{AP1}[AP1] \quad (4.10)$$
$$\frac{d[pRB_p]}{dt} = k_{16}[pRB][CycD_a]\frac{[AhRCyc]}{K_{m6}+[AhRCyc]}\frac{J_{86}}{J_{86}+[bAhR]}$$
$$- k_{61}[pRB_p] - \phi_{pRB_p}[pRB_p] \quad (4.11)$$
$$\frac{d[uAhR]}{dt} = k_7 - k_9[CycD_a][uAhR] - k_{87}[uAhR][ligand] \quad (4.12)$$
$$\frac{d[bAhR]}{dt} = k_{87}[uAhR][ligand] + k_{89}[AhRCyc][ligand] - \phi_{bAhR}[bAhR] \quad (4.13)$$
$$\frac{d[AhRCyc]}{dt} = k_9[CycD_a][uAhR] - k_{89}[AhRCyc][ligand]$$
$$- \phi_{AhRCyc}[AhRCyc] \quad (4.14)$$
$$\frac{d[ligand]}{dt} = k_{10} - k_{89}[AhRCyc][ligand] - k_{87}[uAhR][ligand] \quad (4.15)$$

The values of all parameters are summarized in Table 4.2.

In the absence of exogenous AhR agonists, model predicted effects of constitutively synthesized AhR on the keratinocyte cell cycle are shown in Figure 4.10. The alteration of cell cycle progression is characterized by the duration of G1 phase. Normal keratinocyte cells (control condition: relative constitutive AhR level = 1) have the shortest G1 phase duration. When there is less AhR synthesized, cells undergo a prolonged G1 phase. At very low AhR levels, the duration of G1 phase tends to approach "infinity" based on the trend of simulation results, indicating that the cells will be arrested in G1 phase leading to the stop of cell cycle progression and cell proliferation. The simulation results demonstrate the pro-proliferative effects of AhR and are consistent with experimental measurements from Kalmes *et al.* [174].

Table 4.2: Parameter values used to model the regulatory effects of AhR on cell cycle progression

Parameters	Values	Parameters	Values	Parameters	Values
k_1	1.0 nM/min	k_2	1.6 nM/min	k_3	0.05 /min
k_p	0.05 nM/min	k_7^*	113.4E-05 nM/min	k_9^+	0.4 /(nM·min)
k_{10}^*	43.48E-05 nM/min	k_{16}	0.4 /(nM·min)	k_{61}	0.3 /min
k_{23}	0.3 /min	k_{34}	0.04 /min	k_{43}	0.01 /min
k_{25}	0.9 /min	k_{87}^*	0.024 /(nM·min)	k_{89}^+	0.023 /(nM·min)
J_{11}	0.5 nM	J_{12}	5.0 nM	J_{13}	0.002 nM
J_{15}	0.001 nM	J_{61}	5.0 nM	J_{62}	8.0 nM
J_{63}	2.0 nM	J_{65}	6.0 nM	J_{86}^+	0.005 nM
K_{m1}	0.5 nM	K_{m2}	4.0 nM	K_{m4}	0.3 nM
K_{m6}^+	0.1 nM	a	0.04 nM	F_m^+	1.0 nM/min
ϕ_{pRB}	0.005 /min	ϕ_{E2F1}	0.1 /min	ϕ_{CycD_i}	0.023 /min
ϕ_{CycD_a}	0.03 /min	ϕ_{AP1}	0.01 /min	ϕ_{pRB_p}	0.06 /min
ϕ_{bAhR}	0.025 /min	ϕ_{AhRCyc}	0.01 /min		

*: values are estimated from Simon *et al* [158]; +: optimized values; rest of the parameters are from Swat et al [172]

In their study, cell cycle progression was investigated in both regular HaCaT cells and HaCaT cells expressing a siRNA targeted against the AhR. The siAhR HaCaT cells demonstrated a 80% reduction of AhR levels and a significantly longer G1 phase compared to regular HaCaT cells (Figure 4.10). When cells are treated with exogenous AhR ligands, AhR activation can inhibit cell cycle progression. The simulation results in Figure 4.11 show that G1 phase duration increases with the relative level of exogenous AhR ligands while with high levels of exogenous ligand, cells will undergo G1 arrest and the cell cycle will stop. The mechanistic model developed here successfully incorporates the contradictory effects of AhR on cell cycle progression into one unified model by distinguishing constitutively synthesized and ligand activated AhR in keratinocyte cells. It not only provides insights into the complex role of AhR in cell cycle regulation, but also can serve as a tool to support studies of potential AhR-targeted therapeutic strategies for diseases involving abnormal cell proliferation, such as cancer, fibrosis, atherosclerosis, diabetes, Alzheimer's disease, etc. [175].

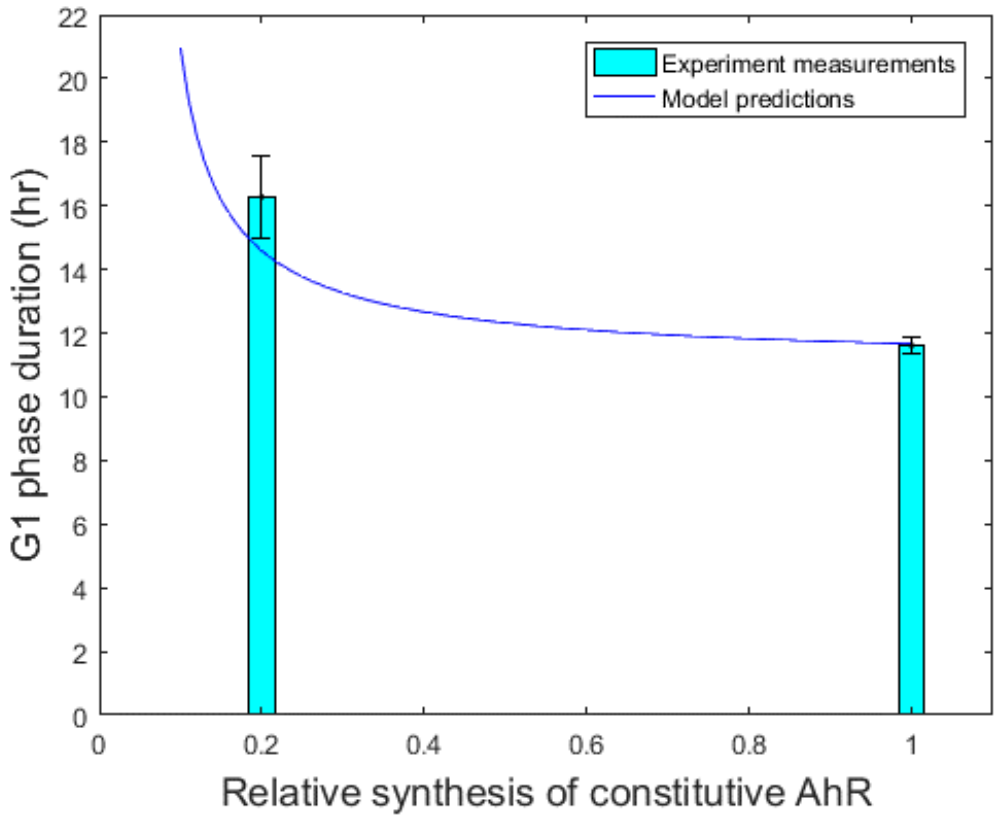

Figure 4.10: Model prediction of the effects of constitutive AhR on G1 phase duration in HaCaT cells.
(Experiment data were extracted from Kalmes *et al.* [174]; bars: mean of experiment measurements; +/-: SEM)

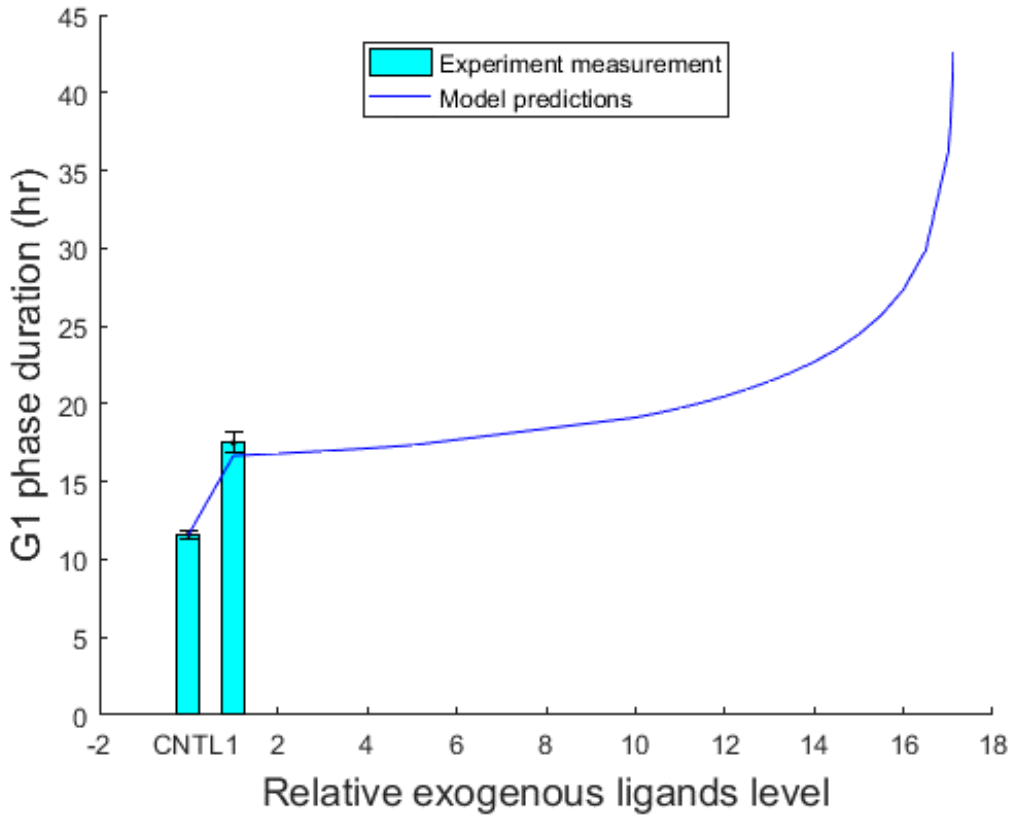

Figure 4.11: Model prediction of the effects of exogenous activated AhR on G1 phase duration in HaCaT cells
(Experiment data were extracted from Kalmes *et al.* [174]; bars: mean of experiment measurements; +/-: SEM; CNTL: control)

Chapter 5

Agent-Based Modeling of the Dynamics of Alveolar Macrophage Polarization under Pro- and Anti- Inflammatory Cytokine Signals

5.1 Introduction

Macrophages are mononuclear phagocytes formed through differentiation of circulating monocytes which are originated from bone marrow. With their versatile functions, macrophages play critical roles in the innate immune system. Functioning as scavengers, they recognize, engulf and destroy worn-out cells, debris, viruses, bacteria, apoptotic cells and some tumor cells through the process of phagocytosis [176]. Macrophages secrete various pro- and anti- inflammatory cytokines that play a vital role in regulating immune response in health and disease. The diverse biological functions of macrophages are achieved through their remarkable plasticity that allows them to efficiently respond to environmental cues and signals, polarizing toward distinct phenotypes [177]. The polarization process and diverse macrophage subsets are critical for maintaining tissue homeostasis and fighting disease. Inappropriate

polarization or imbalance of different phenotypes underlies the pathogenesis of many diseases, such as cancer, atherosclerosis, obesity and insulin resistance, bacterial and viral infections, periodontal disease, etc. [178–180]. Thus, understanding the mechanisms of macrophage polarization is important for developing therapeutic approaches through modulating the phenotypical and functional features of macrophages.

Adopting a simplified approach, macrophages can be broadly classified into two major groups: classically activated macrophages (M1) and alternatively activated macrophages (M2) which can be further divided into three subgroups: M2a, M2b and M2c. M1 macrophages are activated by type 1 cytokines, e.g., interferon-γ (IFN-γ) and tumor necrosis factor α (TNF-α), or pathogen-associated molecular patterns, such as lipopolysaccharide (LPS) which involves Toll like receptor (TLR) pathways. These cells secrete high levels of pro-inflammatory cytokines such as IL-1, TNF-α, IL-12, IL-23 and promote Th1 immune responses [181]. In addition, M1 macrophages release reactive oxygen species (ROS) and reactive nitrogen species (RNS) resulting in anti-proliferative and cytotoxic activities. M1 activation is essential for macrophage-mediated tissue injuries. In contrast to M1 macrophages which exhibit pro-inflammatory properties, M2 macrophages balance the activity of M1 macrophages by producing anti-inflammatory cytokines and initiating wound repair. Various stimuli activate M2 subpopulations. Specifically, exposures to IL-4 and IL-13 activate M2a; M2b can be activated by a combination of immune complexes and LPS or IL-1β; M2c is induced by IL-10, TGF-β and glucocorticoids [182]. It should be noted that macrophage polarization is a dynamic and reversible process. For example, given a change of microenvironment, pro-inflammatory M1 macrophages can transform into M2 macrophages to participate in the resolution of inflammation and tissue repair [183].The molecular mechanisms underlying macrophage polarization require complicated networks of intracellular signaling pathways and transcriptional factors. Upon exposures to IFN-γ, TNF-α, LPS and ROS (M1 stimuli), activations of

NFκB-Nrf2 and STAT1 pathways promote macrophage polarization toward the M1 phenotype; on the other hand, IL-4, IL-10, IL-6 and immune complex (M2 stimuli) skew macrophages toward the M2 phenotype via STAT3 and STAT6 pathways [184] (see Figure 5.1).

Several groups have attempted to build models for macrophage polarization processes. Rzosinska *et al.* developed a Petri net theory based model and conceptually incorporated current knowledge on macrophage polarization [185]. Their model was constructed based on the hypothesis that monocytes in tissues can differentiate to all phenotypic classes without considering the possibility of changing phenotype of already polarized macrophages. Macrophage phenotypes M1 and M2 were considered, as well as the subpopulations of M2 including M2a, M2b and M2c. Although comprehensive analysis of the model was conducted and biological significance was determined for each component, the model did not resolve underlying molecular mechanism and signaling cascades. Wendelsdorf *et al.* used ordinary differential equations (ODEs) to simulate M1 and M2 polarization as part of a model for immune modulatory mechanisms in inflammatory bowel diseases [186]. The macrophage phenotype was linked with pro- and anti-inflammatory cytokine levels in the system, but molecular mechanisms that regulate M1/M2 phenotypic changes were not considered in their model. The same group also developed a more sophisticated ODE-based model containing 38 reactions and 138 parameters, which took into account the dynamic behaviors of the intracellular signaling pathways that regulate macrophage polarization.

The above models are deterministic and assume homogeneity within biological compartments. Given that stochasticity and heterogeneity are key properties of all biological dynamical systems, agent-based modeling (ABM) provides more flexible alternative approaches to model molecular and cellular scale biological phenomena. ABM is a rule-based, discrete-event and discrete-time computational model-

ing method, where interactions between agents can be nonlinear, stochastic, spatial, and described by asynchronous movements through multiple compartments. Various ABMs have been developed in the literature to simulate immunological problems and thus provided substantial insights on interactions and dynamics of immune response networks at the cellular level. Brown *et al.* utilized a relatively simple ABM to investigate lung inflammation and fibrosis following exposure to particulate matter [187]. Their model predicted elevated pro- and anti-inflammatory cytokines, persistent tissue damage and fibrosis that were consistent with *in vivo* measurements. Nguyen *et al.* employed an ABM of human endotoxemia to examine the interplay between circadian controls, cellular variability and stochastic dynamics of inflammatory cytokines [188]. Cilfone *et al.* developed an ABM that spanned molecular, cellular and tissue levels to study the controlling role of balance between TNF-α and IL-10 in a granuloma environment during mycobacterium tuberculosis (Mtb) infection [189]. Later, they expanded their model to study M1 and M2 macrophage polarization during Mtb infection, taking into consideration NFκB and STAT signaling pathways [190].

In this study, we present a multiscale ABM that spans molecular, cellular and tissue levels to investigate macrophage polarization under the M1/M2 paradigm. Due to the nature of ABM, the model takes into account the stochastic, heterogeneous and discrete features of a biological system. Macrophage phenotypic changes at tissue level are mechanistically simulated by modeling selected biological events occurring at molecular and cellular levels following exposures to M1 and M2 stimuli. Novel heuristics are introduced regarding parameter tuning with process trending analysis techniques and time-scale estimation by mapping *in silico* system behaviors to *in vitro* responses. Considering the inevitable level of abstraction when representing biological events using the ABM approach, the model has been evaluated through its ability to reproduce patterns of *in vitro* measurements for mice bone marrow derived macrophage polarization. The new model provides an *in silico* system that

reflects the major characteristics of macrophage transition between M1 and M2 under external stimuli. The model allows us to study how macrophages respond to their micro-environment changes and explore effects of molecular and cellular activities on macrophage behaviors. Therefore, the model not only provides insights into the molecular basis of the M1-M2 paradigm but also has the potential to support studies involving different treatment strategies of macrophage mediated diseases.

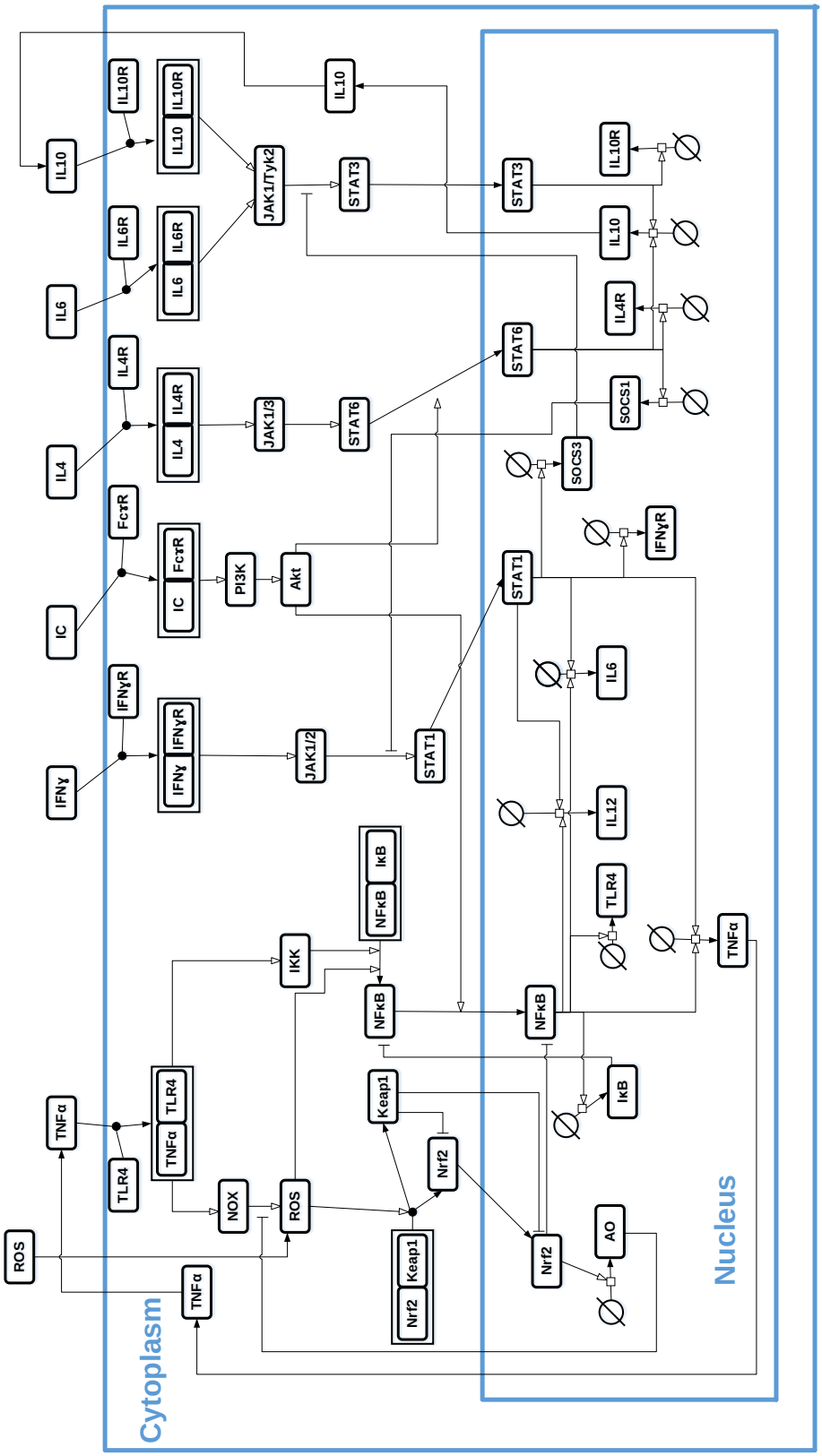

Figure 5.1: Molecular mechanisms regulating M1/M2 polarization

5.2 Methods

5.2.1 Model Construction

Assumptions and biological evidence

Two main macrophage phenotypes are considered in this study, namely: classically activated macrophages (M1) and alternatively activated macrophages (M2). Depending upon the microenvironment of a macrophage cell, multiple interacting signaling pathways are activated leading to a specific pro- or anti- inflammatory status within a cell which then determines the activation form of a macrophage.

The assumptions made for constructing the model can be summarized as follows:

1. the main behaviors of macrophages are characterized by asynchronous and stochastic activities without considering intra-cellular spatial localization and recruitment of monocytes into the system.

2. the dynamics of the pro-inflammatory response and the counter-regulatory response in macrophages can be characterized by patterns of corresponding pro-inflammatory cytokines and anti-inflammatory cytokines.

3. different types of pro-inflammatory, anti-inflammatory cytokines and anti-oxidant proteins are represented by corresponding average delegators as P, A and AO, respectively, whose main behaviors are associated with asynchronous and stochastic activities.

4. the signaling cascade triggered by the recruitment of P/A to the cytoplasm are represented by random movements of key molecules involved in corresponding signaling pathways where only relevant productions of new units are recorded when the endpoints are in the nucleus.

The expression dynamics of pro- and anti- inflammatory cytokines are assumed to

be mainly regulated by the activation of relevant transcription factors. Nuclear factor-kappa B (NFκB), nuclear factor (erythroid-derived 2)-like 2 (Nrf2) signal transducer and activator of transcription 3 (STAT3) and STAT6 were selected as the representative signaling controllers underpinning the manifestation of transcriptional responses due to their essential role in the immune system [59, 191]. NFκB serves as a critical mediator of inflammatory responses and is involved in the pathogenesis of inflammatory diseases [107]. When activated in macrophages, NFκB induces transcription of pro-inflammatory cytokines, chemokines and other inflammatory mediators [192]. The activity of NFκB is primarily modulated by the activity of its kinase (IKK) and its inhibitor (IκB) through the Toll-like receptor (TLR) signaling pathway. Nrf2 is a key transcription factor mediating responses to oxidative stress and toxic insults. Activated Nrf2 controls expression of an array of antioxidant response element-dependent genes to promote oxidant resistance [60]. The activity of Nrf2 is mainly mediated by interactions with the Kelch-like ECH-associated protein 1 (Keap1). STAT3 and STAT6 are essential for regulating anti-inflammatory responses and the activities of STAT3 and STAT6 are mainly mediated by the activity of Janus kinase 1 (JAK1), JAK3 and tyrosine kinase 2 (TYK2) following binding of anti-inflammatory cytokines to corresponding receptors [191, 193, 194]. In addition, crosstalk between NF$\varkappa$B pathways and Nrf2 pathways [59] are also considered in the model.

A schematic representation of the proposed model, including all components and associated interactions, is shown in Figure 5.2 (a). A snapshot of the implemented model is also presented in Figure 5.2 (b). Simulated agents and their corresponding characteristics are shown in Table 5.1. Details of model components, rules and parameters are discussed next.

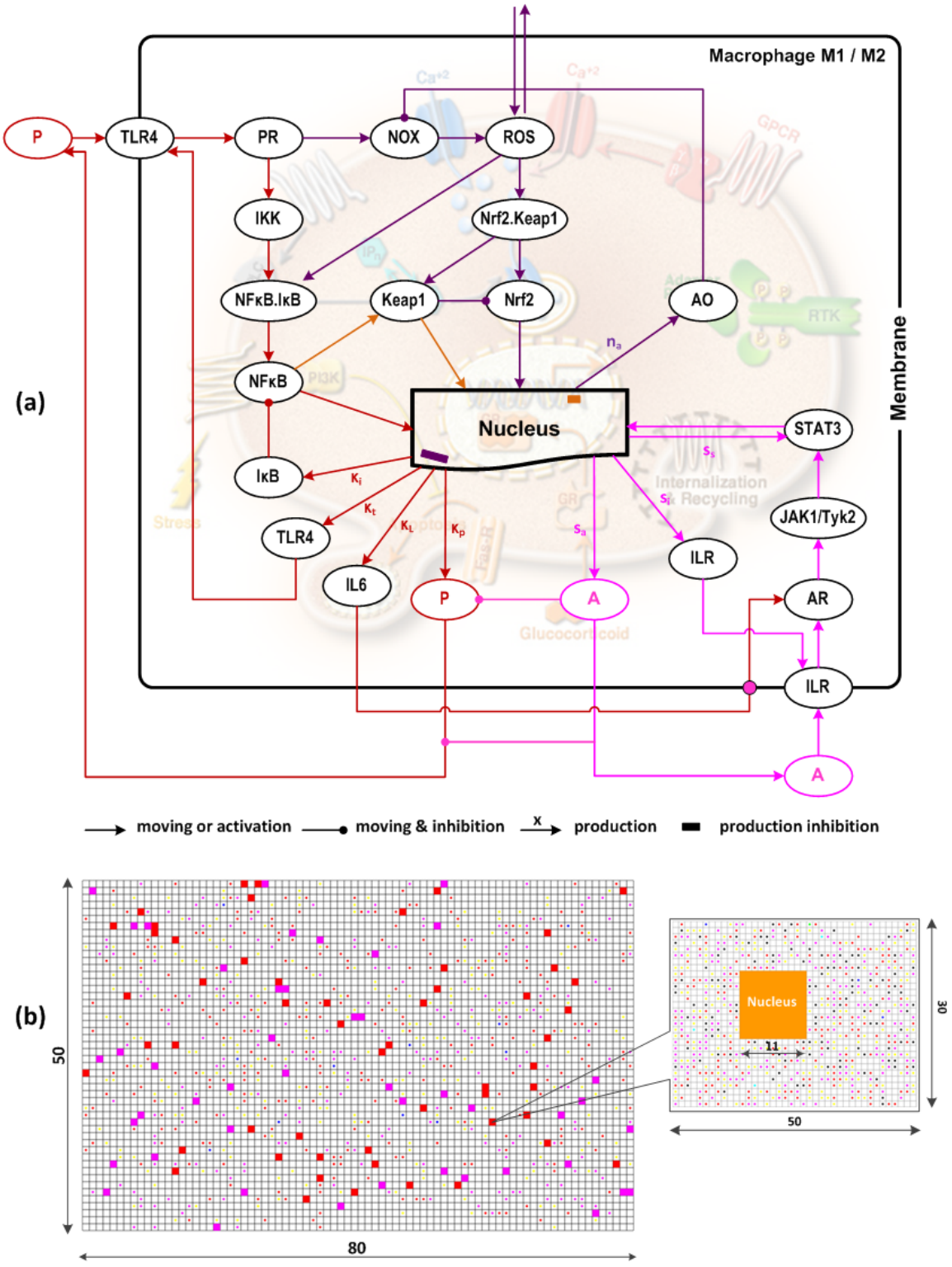

Figure 5.2: *In silico* macrophage polarization model: ABM implementation

Table 5.1: List of agents included in the macrophage polarization model

No.	Agents	Description	Half-life^{+}	Initial population size*
1	P	Pro-inflammatory molecules$^{\$}$	1.5	18 (3f)
2	A	Anti-inflammatory molecules$^{\$}$	1.5	18 (3f)
3	TLR4	Toll-like receptor 4	2.0	24 (4f)
4	PR	Active form of pro-inflammatory molecules$^{\$}$	2.0	n/a
5	IKK	I kappa-B kinase complex – actived by PR	2.5	30 (5f)
6	NFκB.IκB	NFκB complex – inactive form	2.5	30 (5f)
7	NFκB	NFκB – active form	2.0	n/a
8	IκB	I kappa-B – NFκB inhibitors	0.5	6 (f)
9	IL6	Interleukine 6	2.0	24 (4f)
10	NOX	NADPH oxidase	0.5	6 (f)
11	ROS	Reactive oxygen species	0.5	n/a
12	Nrf2.Keap1	Nrf2 complex– inactive form	2.0	24 (4f)
13	Nrf2	Nrf2 – active form	0.5	n/a
14	Keap1	Kelch-like ECH-associated protein 1-Nrf2 inhibitors	2.5	30 (5f)
15	AO	Antioxidants	2.0	24 (4f)
16	ILR	Interleukine receptor (e.g. IL10R)	2.0	24 (4f)
17	AR	Active form of anti-inflammatory molecules$^{\$}$	2.0	n/a
18	JAK1.Tyk2	JAK proteins to trigger STAT functions	2.5	30 (5f)
19	STAT3	STAT3– inactive form	1.0	12 (2f)
20	M1/M2	Macrophage M1/M2 phenotype	720	n/a

*: the initial corresponding number of molecules in a simulated cell; $^{\$}$:hypothesized molecules represent for pro-/anti- inflammatory effects during signaling cascades; $^{+}$:the half-life is approximately to the closest factor limited to [0.5, 2.5] for modeling purpose.

Agent rules and behaviors

Agents are simulated objects (cells and molecules) that follow specific instructions ("rules") on how they behave and interact with other agents within or between compartments. The rule system is listed in Table 5.2 and described briefly here. When M1 stimuli (e.g. TNF-α, LPS) are recognized by their receptor, TLR-4, a signal transduction cascade triggers downstream intracellular signaling modules to ultimately activate the transcription of inflammatory genes. Such transcriptional processes are mainly regulated by interacting NFκB and Nrf2 pathways [195]. Following the activation of NFκB through the phosphorylation of the inhibitor protein IκB by IKK, NFκB is translocated into the nucleus to activate the transcriptional processes re-

sulting in the production of pro-inflammatory cytokines (e.g. TNF-α, IκB and IL-6) [115–117, 196, 197]. After being released outside the cell, pro-inflammatory cytokines may bind to their corresponding receptors on the membrane of macrophages and either further activate the NFκB signaling pathway or lead to production of additional TLR-4 molecules [198, 199]. After recognizing M1 stimuli, the TLR-4 signaling pathway can also activate NADPH oxidase (NOX) to generate reactive oxygen species (ROS) which move in and out of cells without the involvement of receptors [200, 201]. These ROS further activate NFκB forming a positive feedback loop. ROS in cell also triggers the dissociation of Nrf2 from Nrf2-Keap1 complex [202]. Free Nrf2 translocates to the nucleus and activate antioxidant response element (ARE)-mediated gene transcription of anti-oxidant enzymes leading to elevation of cytoplasm anti-oxidant proteins which then inhibit the activity of NOX, and therefore attenuate oxidative stress in the cell [120, 121, 203]. Furthermore, mutually inhibiting effects between NFκB and Nrf2 signaling pathways are considered in the model. NFκB promotes the translocation of free cytoplasm Keap1 into the nucleus, where Keap1 dissociates Nrf2 from the ARE and therefore represses Nrf2 mediated anti-oxidant gene transcriptions, resulting in functional inactivation of Nrf2 [62]. On the other hand, overexpression of Nrf2 suppresses the DNA binding activity of NFκB [204]. In addition, when anti-inflammatory cytokines (e.g. IL-10) are recognized by their corresponding receptors, members of the Janus kinase (JAK) family are activated to phosphorylate STAT3. The phosphorylated STAT3 then enters the nucleus to activate the expression of anti-inflammatory genes and STAT3 [110, 205–209]. IL-4 and IL-13 follow a similar pattern as IL-10, except that they activate STAT6 instead of STAT3. Thus, we use STAT3-JAK in the model to represent all anti-inflammatory cytokine induced STAT-JAK signaling pathways activation during macrophage polarization. Like anti-inflammatory cytokines, IL-6 also activates JAK-STAT3 pathways upon binding to its receptor [191, 210, 211]. Therefore, it is assumed that IL-6 shares the same process

with anti-inflammatory cytokines for modeling simplicity. The activation status of a cell is determined by the "macrophage polarization ratio" (R_{MP}), which is defined as the dynamic ratio of P over A in the cytoplasm of corresponding cell [190]:

$$R_{MP} = \frac{\Sigma P}{\Sigma A} \tag{5.1}$$

$$Phenotype = \begin{cases} M_1 & \text{if } R_{Mp} > 1.25 \\ M_2 & \text{if } R_{Mp} < 0.75 \\ unchanged & \text{if } 0.75 \leq R_{Mp} \leq 1.25 \end{cases} \tag{5.2}$$

In our simulation, there are three types of compartments spanning multiple scales: the tissue, the cell cytoplasm and the nucleus. The tissue compartment contains all simulated cells; each cell contains a cytoplasm compartment and a nucleus compartment. All agents move in a random fashion following the "random walk" (discussed later) model on a 2-dimensional grid. The tissue and each cell have their own simulating grid while the nucleus directly occupies a region in its corresponding cell simulating grid. Although no special spatial arrangements are set for agents, there are a number of restrictions regarding which compartment a molecule can be in. Specifically, P, A, IL-6 and ROS can move between the tissue and the cytoplasm; NFκB, Keap1, Nrf2 and STAT3 can be in both the cytoplasm and the nucleus; after being produced, TLR4 and ILR will be transferred to the cell membrane and remain there until they are removed from the simulation; other molecules are only present in the cytoplasm.

Translocation of molecules is based on an import- and export procedure. In the tissue compartment, if a molecule has the same position with a cell, the system will check to determine whether it is imported or not. Except for P and A, other molecule types are imported to the cells with the approximate probability of P-binding

TLR4 to simulate the probability of the binding to receptors. This probability is approximately equal to the initial number of TLR4 molecules in a cell divided by the number of positions on the boundary of the cell simulating grid, which is about 20%. For P molecules, a random position on the boundary of the cell simulating grid is assigned; if it overlaps with the position of some TLR4 molecules, it will be imported (similar for A). Once imported to a cell, it combines with receptors and forms an 'active' complex PR (or AR). In the cytoplasm compartment, active molecules are translocated to the nucleus compartment when they reach the nucleus region of the corresponding simulating grid. On the other hand, when a molecule reaches the boundary of a compartment, it is exported to the outer compartment if it is not restricted.

Each agent moves in a random direction for a random number of times with a random delay time for each movement. However, two interactive molecules X_1, X_2 with current positions $\{P_x^{X_1}, P_y^{X_1}\}$, $\{P_x^{X_2}, P_y^{X_2}\}$ respectively will move towards a position where an interaction may occur if their distance is less than a threshold:

$$d(X_1, X_2) = max\{|P_x^{X_1} - P_x^{X_2}|, |P_y^{X_1} - P_y^{X_2}|\} \leq \tau, \tau = 1 \tag{5.3}$$

If two molecules have the same position on the simulating grid of the corresponding compartment, they will interact (activation, inhibition or degradation) following the rules shown in Table 5.2, e.g. A and P with the same status in any compartment, PR and IKK, activated IKK and NFκB.IκB, AR and JAK1/Tyk2 in the cytoplasm, and NFκB and IκB in cytoplasm. The rule is also applied to the movement of molecules when adjacent to cells in the tissue compartment to increase the probability of entering a cell. There are no explicit processes governing cell and molecule "movements"; the movement rules are set so as to reflect probabilities of biological plausible agent interactions following the conceptual formulation of the Agent Based Model.

Table 5.2: List of rules governing the behaviors of agents in the Macrophage polarization model

No.	Rule definition
1	Macrophage phenotype is determined by the ratio R_{mp}
2	P, A, ROS, and IL-6 can be imported to cells from the tissue if they hit a cell while moving in the tissue simulating grid or exported to the tissue if they lie on the cell membrane while moving in the cell simulating grid
3	PR can activate IKK and NOX; activated IKK turns NFκB.IκB to active NFκB while an activated NOX produces a ROS every simulated tick during the rest of its lifetime
4	An individual NFκB in the nucleus has a probability of $\kappa_p/\kappa_t/\kappa_i/\kappa_I$ to produce a new unit of P/TLR4/IκB/IL-6 respectively
5	IκB inhibits NFκB activity by forming NFκB.IκB complex
6	ROS can turn Nrf2.Keap1 complex into active Nrf2 and Keap1 or activate NFκB.IκB to NFκB
7	Keap1 inhibits Nrf2 activity by forming Nrf2.Keap1 complex
8	An individual Nrf2 in the nucleus has a probability of n_a to produce a new unit of AO
9	AO inhibits NOX activity; both are degraded when they hit each other in the corresponding simulating grid
10	NFκB triggers Keap1 to active form so that it can be translocated to the nucleus to inhibit Nrf2 activity
11	NFκB activity in the nucleus is inhibited if the number of NFκB is less than the number of Nrf2 in the nucleus
12	AR can activate JAK1.Tyk2; activated JAK1.Tyk2 triggers STAT3 to the active form
13	IL-6 shares the same pathway with A after it is translocated to the cell cytoplasm
14	An individual STAT3 in the nucleus has a probability of $s_a/s_s/s_i$ to produce a new unit of A/STAT3/ILR respectively
15	TLR4/ILR stop moving when hitting the cell membrane, waiting for recruiting P/A from the tissue
16	A inhibits P activity; both are degraded when they hit each other in the corresponding simulating grid
17	An individual NFκB in the nucleus of M1 has a probability to produce a new unit of P three times more than that if it is in the nucleus of M2
18	An individual STAT3 in the nucleus of M2 has a probability to produce a new unit of A three times more than that if it is in the nucleus of M1
19	NFκB, Nrf2, active STAT3, and active Keap1 can be translocated to the nucleus while others can not
20	Agents are degraded after t hr if there is no action except movements where t/2 is defined by the approximate half-life of the agents

Model parameters

Model parameters are classified into two categories: default- and production- parameters. Default parameters are those related to system setting and physicochemical properties of cells and molecules, such as compartment extensions, simulation scales,

molecule life-times or initial populations. For simplicity, all compartments are simulated with unitless rectangular grids in this study. The tissue compartment is represented by an 80 × 50 rectangular unitless grid and the cell by a 40 × 30 grid. The cell nucleus is approximately 10% of the total cell volume and therefore it occupies a region of about 11 × 11 in the cell simulating grid (Figure 5.2b).

Since the relationship between the system response time and the system production rate is unclear, we define two scales (an approximate number of simulated steps for an hour) in this simulation: (1) the life-scale (L) that characterizes the lifetime of molecules and the system production rate; (2) the response-scale (N_{tph}) that characterizes for system responses. The response-scale is initially equal to the life-scale but adjusted later to match *in silico* system responses. In order to identify the life-scale, the system is set to have no activity except the default system production and protein degradation; thus the number of units of each molecule type in a cell should be balanced over time. Given that the default production rate is R%, a cell will produce R × L new units for a molecule type after one hour, and thus there must be R × L units of this molecule type degraded to keep the cell at homeostasis (R% = 50% in this study). As a result, if a molecule has a certain lifetime, its average lifetime will be approximately equal to its number of units divided by R × L. In other words, the initial number of units of a molecule type is set equal to its average lifetime multiplied by R × L.

In this simulation, the average lifetime of a molecule is the double of its approximate half-life as listed in Table 5.1. The half-life is approximately equal to the closest factor limited to [0.5, 2.5] for modeling purpose. So for those molecules whose half-lives longer than 2.5 hours, we set their half-lives to be 2.5 hours; and for those molecules whose half-lives are shorter than 0.5 hours, we set their half-lives to be 0.5 hours. Specifically, the IκB half-life is about 0.5 hours and the NFκB.IκB half-life is five-fold higher than that of IκB [212, 213]; the half-lives of Nrf2, NOX and ROS are

shorter than or about 30 min and therefore are set to be 0.5 hours [214–216]; the half-life of STAT3 is about 1 hour [217]; inflammatory cytokines have an average half-life of about 1 hour [218]; the half-life of Keap1 is longer than 2.5 hours and is set to be 2.5 hours [219]; JAK1 and Tyk2 have half-lives of 2-3 hours and we set them to be 2.5 hours [220]; IKK is a large protein and is assumed to have a half-life equal to that of the NFκB.IκB complex; the rest are assumed to have an average half-life about 2 hours. Since intracellular proteins occupy 15-35% of cell volume [221], we assume that the number of molecules in a homeostatic cell would be about 25% of the cell volume, which is approximately 300 molecules. The initial number of units for each type of molecule is proportional to its corresponding half-life. Let f be the initial number of units of IκB, the total initial number of units (molecules) in a cell, under the assumption of a homeostatic system, will be around $50f$, resulting in $f = \frac{300}{50} = 6$ units. The estimated initial population size of each molecules type in a cell is shown in Table 5.1. The life-scale L, which is the number of simulated steps per hour or the number of simulated steps over the lifetime of an IκB, is therefore equal to f/R or 12 ticks per hour. Additionally, the initial number of units for P (or A/ROS/IL-6) in the tissue compartment is initialized with 10% of total P (or A/ROS/IL-6 respectively) units in all cells in the system.

Production parameters are the probabilities of producing new molecules when a particular molecule type is involved in the transcriptional process, characterized by its presence in the nucleus compartment. In order to estimate these parameters, we hypothesized that there must be a balance between protein synthesis and protein degradation in a homeostatic system [222]. Thus, under conditions of no external stimulation, production parameters need to be adjusted so that the number of units of each molecule type in the system does not change significantly over time (Table 5.3). Techniques from process trending analysis were used to obtain a set of adjusted parameters whose values remain constant for subsequently added mechanisms such as

treatment with pro- or anti- inflammatory cytokines [223, 224]. The configuration of the homeostatic system, including all agents and their properties, is saved for further *in silico* experiments.

Model implementation

The *in silico* macrophage polarization model was implemented in the Java language, using the Repast Simphony toolkit for Agent-Based Modeling and the Eclipse development environment.

"Random walk" model

Agents (cells and molecules) move on a 2-dimensional grid in a random fashion depending on two main factors: (i) the time agents wait before each movement and (ii) the number of times agents move in a particular direction. For a specific agent U, at time t, let $\gamma(t)$ be the time (number of ticks) U has to wait before moving and $\lambda(t)$ be the number of times U will move in direction D, we have

$$\gamma(t+1) = \begin{cases} \gamma(t) - 1 & \text{if } \gamma(t) > 0 \\ rand\{0,1\} + status(U) & \text{if } \gamma(t) = 0 \end{cases} \tag{5.4}$$

$$\lambda(t+1) = \begin{cases} \lambda(t) & \text{if } \gamma(t) > 0 \text{ and } \lambda(t) > 0 \\ \lambda(t) - 1 & \text{if } \gamma(t) = 0 \text{ and } \lambda(t) > 0 \\ rand\{2,3,4\} \times (N_{comp} + 1) & \text{if } \gamma(t) = 0 \end{cases} \tag{5.5}$$

$$\text{Where } status(U) = \begin{cases} rand\{1,2\} & \text{(initial value)} \\ 0 & \text{if } U \text{ is in the active form} \end{cases}$$

$N_{comp} = \{0, 1, 2\}$ if U in {nucleus, cell, tissue} respectively

Each compartment or each cell has its own 2-dimensional simulating grid. When γ(t) is zero, U will move to the next grid-space in the Moore neighborhood of the corresponding simulating grid which consists of 8 spaces immediately adjacent to and surrounding the current position based on the current direction D. D is one of the 8 directions $\{N, NE, E, SE, S, SW, W, NW\}$ (N: north, E: east, S: south, and W: west). Let P_x(t), P_y(t) be the current position of U in a 2-dimensional simulating grid, its next position is defined as follows:

$$P_x(t+1) = P_x(t) + H_x(\gamma(t), D(t)) \tag{5.6}$$

$$P_y(t+1) = P_y(t) + H_y(\gamma(t), D(t)) \tag{5.7}$$

where

$$D(t+1) = \begin{cases} D(t) & \text{if } \lambda(t) > 0 \\ rand\{N, NE, E, SE, S, SW, W, NW\} & \text{if } \lambda(t) = 0 \end{cases} \tag{5.8}$$

$$H_x(\gamma(t), D(t)) = \begin{cases} 0 & \text{if } \gamma(t) > 0 \text{ or} D(t) \in \{N, S\} \\ +1 & \text{if } \gamma(t) = 0 \text{ and} D(t) \in \{NE, E, SE\} \\ -1 & \text{if } \gamma(t) = 0 \text{ and} D(t) \in \{NW, W, SW\} \end{cases} \tag{5.9}$$

$$H_y(\gamma(t), D(t)) = \begin{cases} 0 & \text{if } \gamma(t) > 0 \text{ or} D(t) \in \{E, W\} \\ +1 & \text{if } \gamma(t) = 0 \text{ and} D(t) \in \{NW, N, NE\} \\ -1 & \text{if } \gamma(t) = 0 \text{ and} D(t) \in \{SW, W, SE\} \end{cases} \tag{5.10}$$

Parameter tuning

Based on the trend of the dynamics of each molecule type X, we adjust the probability of the associated production parameter p_X(Table 5.3) so that the total number of X in the system does not change significantly over time. For each simulated day, we sample the level of X each hour and determine whether there is a significant change based on the sample vector using ordinary least square regression and significant mean difference [223].

Let x_j be the number of molecules X in the system at hour j, $j = 1 \ldots J$, $J = 24$. The regression model used in this approach is $x_j = \alpha + \beta J + \epsilon_j$ where α is the intercept, β is the slope, and ϵ_j are random errors which are assumed to be independent and identically distributed. The estimates of the slope and intercept are given by

$$\hat{\beta} = \frac{\sum_j (j - \bar{j})(x_j - \bar{x})}{\sum_j (j - \bar{j})^2}; \;\; \hat{\alpha} = \bar{x} \text{-} \hat{\beta}\bar{j}; \;\; \bar{x} = \frac{1}{J} \sum_j x_j$$

The standard error of the slop will be $SE(\hat{\beta}) = \sqrt{\frac{\sum_j (x_j - \hat{\alpha} - \hat{\beta} j)^2}{(J-2) \sum_j (j - \bar{j})^2}}$

A 95% confidence interval for the slope β is $\hat{\beta} \pm t_{0.975, J-2} SE(\hat{\beta})$. If zero is not contained in the interval, we conclude that the trend of change is significant.

Let m_1,m_2 be the means of the first and last half of the sample vector, $m_1 = \sum_{j=1}^{J/2} x_j$; $m_2 = \sum_{j=J/2+1}^{J} x_j$. If the percentage change between the first and last half of the sample vector $(m_2 - m_1)/m_1$ is more than 10%, we conclude that the change is significant and adjust the corresponding production parameter. If the trend of the dynamics is increasing, the parameter value p_X will be decreased. Otherwise, if the trend of the dynamics is decreasing, we increase p_X. In order to estimate the changing amount of p_X, we assume that the percentage change of the parameter would be approximately to the percentage change of the molecule level between the first and last half of the

sample vector but set under the opposite effect. Thus, the estimate for the adjusted parameter value will be

$$\frac{p_X^{'} - p_X}{p_X} = -\frac{m_2 - m_1}{m_1} \;\Rightarrow\; p_X^{'} = p_X(1 - \frac{m_2 - m_1}{m_1})$$

In the case when there are two associated production parameters, the amount each parameter is changed will be half of that in the normal case. The process is repeated until there is no change of all production parameters in three consecutive simulated days.

Table 5.3: Values of production parameters used in the macrophage polarization model

No.	Parameters	Initial probability	Adjusted probability
1	$\kappa p(NF\kappa B \rightarrow P)^*$	0.8000	0.3224
2	$\kappa i(NF\kappa B \rightarrow I\kappa B)$	0.8000	0.4111
3	$\kappa t(NF\kappa B \rightarrow TLR4)$	0.8000	0.4916
4	$\kappa I(NF\kappa B \rightarrow IL6)$	0.8000	0.3430
5	na(Nrf2→AO)	0.8000	0.1155
6	sa(STAT3→A)	0.2000	0.1001
7	ss(STAT3→STAT3)	0.2000	0.1107
8	si (STAT3→ILR)	0.2000	1.0000

*x(Y→Z): x is the probability that a single unit Y can produce an individual unit Z when Y is in the cell nucleus.

5.2.2 *In vitro* measurements

The data used in this study were extracted from literature reporting *in vitro* experiments performed with primary mouse bone marrow derived macrophages [225]. Marrow from femurs of 6-12 week old female C57BL/6 mice was harvested followed by lysing red blood cells with ACK buffer. Cells were then cultured on bacteriological polystyrene plates for seven days in DMEM supplemented with 10% FBS, 2% penicillin/streptomycin, 2 mM L-glutamine and 10% conditioned media from CMG 12-14 cells expressing recombinant mouse M-CSF. Macrophages were stimulated with

LPS, IFN-γ, IL-4, or IL-13 at given doses for the indicated time, and then flow cytometry or cytokine analysis was performed. For flow cytometry, cells were first fixed in 4% formaldehyde and stored at 4 °C. After staining with anti-CD86 (clone GL-1, APC conjugate) and anti-CD206 (clone C068C2, Alexa 488 conjugate) antibodies or isotype controls, cells were analyzed on a BD LSR flow cytometer with post-processing in FlowJo (Tree Star). Cell populations were gated on forward and side scatter to select intact single cells. Events were acquired until 10000 events were collected in a preliminary analysis gate or the sample was exhausted. For cytokine analysis, macrophages were seeded at 3e5 cells/ml, allowed to adhere overnight, and then treated with indicated concentrations of IL-4, IL-13, TNF-α, and IFN-γ. The cell culture supernatants were collected at 24, 48, 72 and 96 hours after stimulation and analyzed with a Luminex 31-plex mouse cytokine array.

5.3 Results and Discussion

5.3.1 Qualitative assessment of model behaviors with experiment measurements

In vitro data were extracted from literature reporting experiments with primary mouse bone marrow derived macrophages [225]. Original experimental data were the measurements of M1 marker (CD86) and M2 marker (CD206) expressions under different treatment conditions normalized by the values of corresponding time points under condition of either M1 stimuli only or M2 stimuli only treatment. We re-normalized the experimental data by taking the ratio of measurements under different treatment conditions with respect to the control condition (no treatment with either M1 or M2 stimuli). *In silico* experiments are simulated by 'injecting' a number of new cytokine molecules into the system. Cytokine molecules are randomly allocated to the plasma compartment and M1/M2 phenotypes of cells are tracked.

In silico simulation results are compared with *in vitro* experiment measurements for macrophage polarization in Figure 5.3. Under M1 stimuli only conditions, *in silico* results show the same trend with *in vitro* data for the M1 phenotype, where the amount of M1 macrophages in the system increases rapidly, peaking around 24 hours after treatment and eventually resuming to the control values. *In vitro* data reveal a pattern of M2 macrophages which first decreases and then comes back to the control values. *In silico* results show a similar M2 pattern except that the maximum decrease happens at 24 h instead of 48 h. In conditions involving only M2 stimuli treatments, both *in silico* and *in vitro* data demonstrate that numbers of M2 macrophages first increase and then plateau, remaining at higher levels than the control even 96 hours after treatment. *In vitro* results show relatively low levels of M1 macrophages with a gradually decreasing trend, while *in silico* data display an overall decreasing M1 pattern with lowest levels around 24 h. For co-stimulations with M1 and M2 stimuli, *in silico* and *in vitro* data both show that numbers of M1 macrophages increase, peak about 24 h and come back to control levels 96 hours after treatment. *In vitro* M2 patterns exhibit a continuous increasing trend, while *in silico* M2 patterns demonstrate an overall increasing trend with an initial decrease from 0 to 24 h.

It should be noted that the total number of cells in a cell culture is dynamic. However, for modeling simplicity, the *in silico* formulation here uses a fixed total number of cells. Therefore, the increase of one phenotype during *in silico* simulation will lead to inevitable decrease of the other phenotype. When the predominant phenotype pattern is captured, this limitation of the model leads to slight differences between *in silico* and *in vitro* patterns for the other phenotype (e.g. M2 pattern under M1 stimuli only condition). Nevertheless, our results suggest that the *in silico* model qualitatively captures the major characteristics of the dynamic phenotypical changes during M1/M2 polarization. With M1 stimuli only, M1 macrophages predominate over M2 macrophages and resume to basal levels eventually. Under M2 stimuli only

conditions, most of the macrophages are activated as M2 phenotype and the levels of M2 macrophages stay higher than the control levels after a relatively long period of time. For co-stimulations with M1 and M2 stimuli, macrophages polarize toward both M1 and M2 phenotypes. M1 macrophages return to the control levels, whereas numbers of M2 macrophages increase continuously for a long period of time, suggesting the natural progression of macrophages from pro-inflammatory to anti-inflammatory phenotype in response to wounds or infections with pathogens [225, 226].

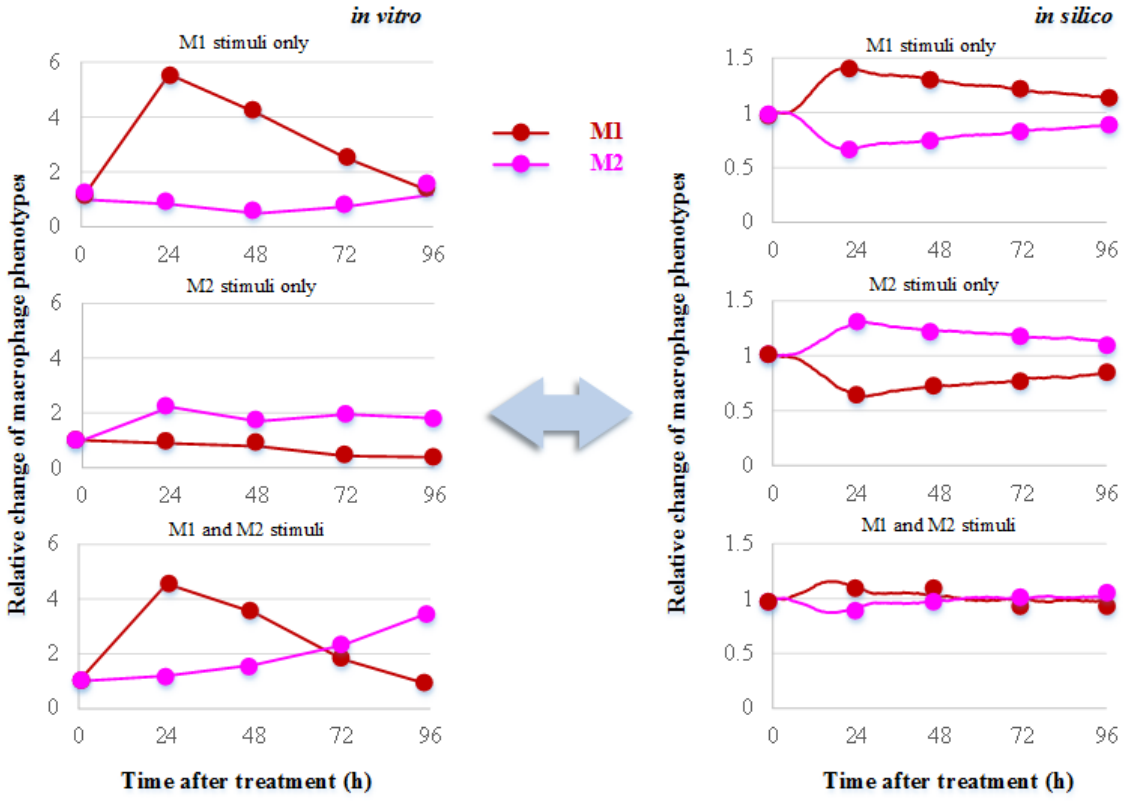

Figure 5.3: Correspondence between *in vitro* and *in silico* results of macrophage polarization

5.3.2 Patterns and implications of cellular variability

Since stochasticity is an inherent property of our Agent Based simulation, stochastic transcriptional activities have large impacts on cellular variability. Simulated cells behave differently from one to another and no individual cell behaves like the average

one. Figure 5.4 shows the pro-inflammatory cytokine levels for several individual cells and the average pattern for all the cells in the system under treatment with only M1 stimuli. Each individual cell possesses a unique dynamic pattern of pro-inflammatory molecules which is different from other cells in a stochastic way. However, the average level of pro-inflammatory molecules increases upon exposure to M1 stimuli and then abates gradually, exhibiting a pattern which is consistent with corresponding system responses characterized by the dynamic change of M1 macrophages (Figure 5.3).

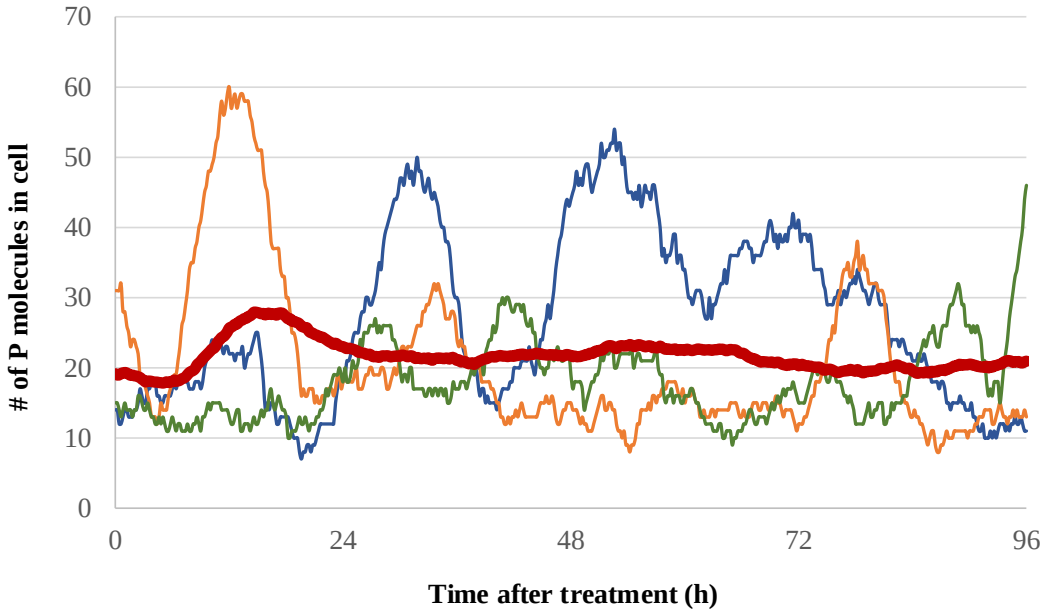

Figure 5.4: Stochastic dynamics of pro-inflammatory cytokines in cell population

5.3.3 Dynamic phenotype change of macrophages

Macrophage polarization is a dynamic and reversible process. Given an altered micro-environment, an already polarized macrophage could change its polarization status. In our model, the polarization status of a cell is determined by the P/A ratio which reflects the change of local environment for the simulated cell. Figure 5.5 shows the phenotypic change of one simulated macrophage cell under treatment with only M1

stimuli. The cell is first polarized to M1 phenotype and then re-polarizes to a M2 macrophage as the P/A ratio decreases over time. These re-polarization phenomena captured in our simulation indicate that one macrophage cell can exert both pro-inflammatory and anti-inflammatory functions during the natural inflammation resolving process by dynamically changing its polarization status.

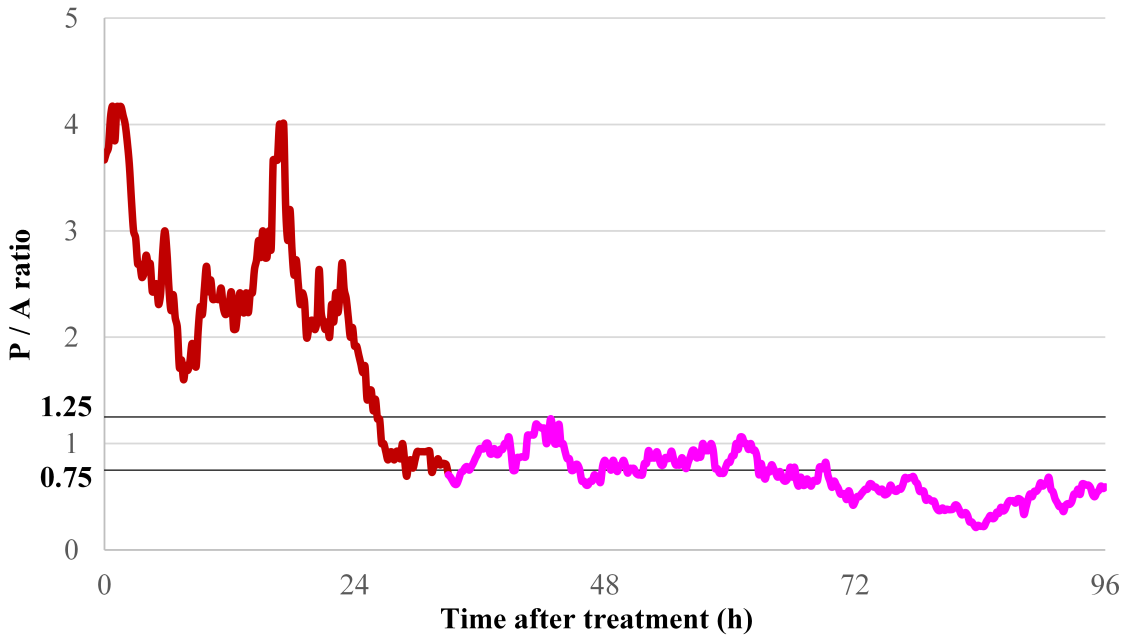

Figure 5.5: Phenotypical change of one simulated macrophage cell

5.3.4 Sensitivity analysis

Overall system behavior is characterized by the M1/M2 ratio, defined as the ratio between number of cells with M1 phenotype and number of cells with M2 phenotype in the system. Sensitivity analysis was performed to explore how perturbations in production parameter values affect the M1/M2 ratio. Each production parameter was sequentially perturbed from a control condition where no external stimulations were added to the system. The resulting changes in M1/M2 ratio were recorded. In this approach, 75% change was selected to perturb production parameters and the change of M1/M2 ratio at t = 24 h was selected to show a clear impact of production

parameter perturbation on the overall system behavior. Results are presented in Figure 5.6. Two parameters that have significant effect on the M1/M2 ratio are kp and sa, where kp is responsible for the NFκB induced production of pro-inflammatory cytokines and sa is responsible for the STAT3 induced production of anti-inflammatory cytokines. Since the phenotype of a macrophage is determined by the P/A ratio in our model, the M1/M2 ratio is mainly dependent on the dynamics of pro- and anti-inflammatory cytokines in the system. Therefore, parameters (kp and sa) relevant to the production of these cytokines should have large impacts. The positive correlation between kp and M1/M2 and the negative correlation between sa and M1/M2 further demonstrate that pro-inflammatory environment tends to skew macrophages toward the M1 phenotype, whereas macrophages tend to polarize to the M2 phenotype in an anti-inflammatory environment. In addition, the M1/M2 ratio is also significantly affected by production parameter ss which is responsible for the production of STAT3, suggesting the important role of the STAT3 pathway in anti-inflammatory responses and M2 activation upon exposure to M2 stimuli [110, 227].

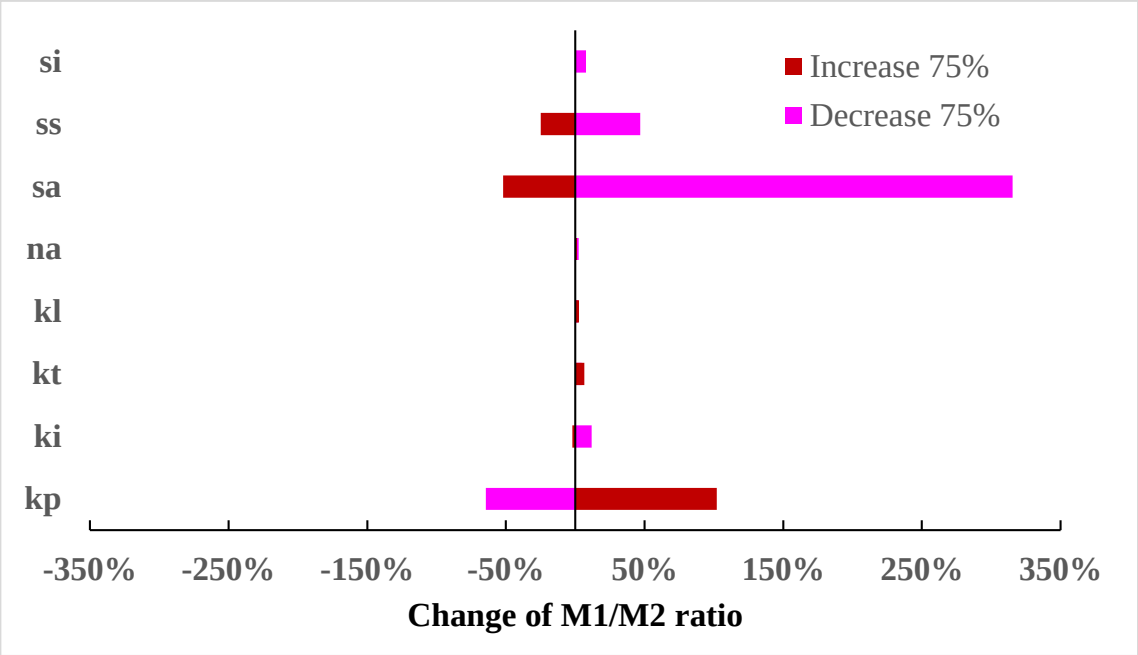

Figure 5.6: Sensitivity analysis

5.4 Summary

In this study we presented a new multiscale agent-based model that spans molecular, cellular and tissue levels to provide a computational simulation framework aimed at reproducing and elucidating the dynamics of macrophages phenotypes under various complex activation signals, while considering system stochasticity and heterogeneity. Transcription factors NFκB, Nrf2, and STAT3 are selected as representative controllers that regulate the expression dynamics of pro- and anti-inflammatory cytokines during macrophage polarization process. A macrophage polarization ratio, defined as the ratio between the concentrations of pro- and anti-inflammatory cytokines in the local microenvironment of macrophage cells, is employed to link cellular signaling events and cytokine expressions with macrophage phenotype changes. The model successfully captures the qualitative trends of macrophage phenotype changes in an *in vitro* system of mouse bone marrow-derived macrophages exposed to various doses of LPS/IFN-γ and IL-4/IL-13. In addition, the agent-based modeling approach used in this study allows the model to capture the cell-to-cell variability of macrophages under a collective phenotype pattern induced by certain external stimuli. The model also demonstrates that macrophages can shift between phenotypes to achieve different biological functions. Important regulatory processes, including the NFκB induced production of pro-inflammatory cytokines, STAT3 induced production of anti-inflammatory cytokines and the production of STAT3, are identified to have higher impacts on macrophage polarization, a result that can provide insights into studies of potential therapeutic interventions targeting macrophage phenotypes in different diseases.

Chapter 6

Conclusion and recommendations

This chapter summarizes the main findings and limitations of the work presented in this dissertation, as well as recommendations for future research. In this work, multiscale computational models that integrate multilevel mechanisms and *in vitro* / *in vivo* experimental information were developed to study biological effects of air pollutants, especially ozone and PM, in three interconnected physiological systems: the respiratory system, the cardiovascular system and the integumentary system. An essential biological phenomenon, macrophage polarization, which plays critical roles in mediating inflammatory responses, such as those elicited by exposures to air pollutants, was also studied using an Agent Based modeling approach.

6.1 Main findings and limitations

6.1.1 Respiratory effects of ozone inhalation

Effects of ozone on the respiratory system were modeled using a multiscale approach that considers two main biological mechanisms: ozone-induced pulmonary surfactant perturbation and ozone-initiated pulmonary inflammation. Information on the two biological processes was then coupled with an alveolar recruitment/decruitment module to link ozone inhalation with reduced lung function. The performance of the

model was evaluated using *in vivo* measurements from experiments involving mice. The immune response module of the model allows us to track the progression and restoration of pulmonary inflammation after ozone exposure and to explore the regulatory effect of surfactant protein D (SP-D) on inflammatory responses. Chronic pulmonary inflammation was observed in the absence of SP-D. The altered lung function at later times following ozone exposure was mainly attributed to prolonged inflammation rather than surfactant component profile changes.

However, the model described here has certain limitations:

- The lung function alterations simulated by the current model do not include the potential effects of cellular injuries induced by ozone. In fact, ozone and ozone induced ROS can damage the epithelial cells lining the respiratory tract to cause increased airway epithelial permeability and structural impairment of the alveolar epithelium [228, 229]; those effects are associated with degradation in lung function [230].

- Another limitation of the current model is that it has been evaluated only with mice data, although the design of the model actually allows its extension to other mammalian species, as it incorporates corresponding physiological structures and parameters corresponding to rats and mice [84].

6.1.2 Heart rate variability changes caused by PM exposure

A computational model for cardiovascular effects of air pollution was developed and implemented for human PM exposure, using heart rate variability (HRV) as the health endpoint. The model considers excessive oxidative stress and pro- / anti-inflammatory signaling at the cellular level, neuroendocrine-immune system interactions, and systemic inflammation propagation to the heart, where HRV is altered. The model was parameterized using human HRV data. The predictive capability of the model

was tested and evaluated by applying the model to different PM exposure scenarios. This model considers a complex network of interactions among the immune, neuroendocrine and autonomic systems for HRV regulation, and biological processes that have high impact on HRV were identified, including the production of pro- and anti-inflammatory cytokines, NFκB activation, and the interactions between epinephrine and its adrenergic receptors. This model provides a simulation framework for studying the cardiovascular effects of pollutants that are caused by excessive oxidative stress and systemic inflammation.

Limitations of the current model include:

- In this model, systemic inflammation is induced only by the pulmonary release of pro-inflammatory cytokines into the circulation system. However, inhaled fine and ultrafine particles, typically present in air with high ozone levels, can also directly enter the circulation system [231] to trigger systemic inflammation or get access to the central nervous system through the olfactory bulb [232]. Mechanisms governing the PM-initiated effects beyond the pulmonary system [84] should be added to the model.

- The model parameterization is accomplished by fitting simulation results to experimental data; therefore, model performance is largely dependent on the available experimental data sets. The current model uses only one data set for parameterization, which limits the applicability of the model to different PM exposure scenarios. A wider range of field and laboratory measurements of HRV are needed to both improve and evaluate model performance.

- The current model uses only one time-domain index (SDNN) to characterize HRV; however, this index does not fully reflect the physiological significance of HRV [233]. A module capable of generating both time-domain and frequency-domain indices of HRV should be developed to address this limitation.

6.1.3 Modeling Skin biology after air pollution exposure

Three models were developed to respectively address mechanisms of action involved in air pollution related skin disorders: (a) Skin lipids reactions with ozone were modeled to simulate the formation of secondary organic aerosol in an indoor environment; (b) A model for AhR activation and subsequent gene transcription was developed using a stochastic algorithm. The model was implemented for two different air pollution components and was evaluated using *in vitro* experimental measurements; (c) A skin cell cycle regulation model focusing on G1 phase progression was established. The contradictory effects of AhR on cell cycle progression were successfully captured by the model.

Models developed for the skin biology have their limitations as well:

- The ozone-skin lipids reaction model was developed using data from a chamber experiment; it therefore needs to be extended to a real-life indoor environment, incorporating detailed mechanistic modeling of the reaction kinetics involving ozone and skin lipids, as well as of associated physicochemical processes.

- The two AhR skin biology modules developed here need to be integrated with models of epidermal homeostasis (e.g. EPISIM [234]) in order to link air pollution with symptoms of skin disorders.

6.1.4 Agent Based Modeling (ABM) of macrophage polarization

Macrophage polarization is essential for inflammatory responses involved in the mechanisms of health effects induced by a wide range of air pollutants. A new multiscale compartmental model employed an agent-based modeling (ABM) approach to simulate: the intracellular signaling cascade mediated by relevant transcription factors, cell movements, molecule-cell interactions, cell-cell interactions, and phenotype changes

of macrophages. A quantitative metric, the macrophage polarization ratio, was defined to link macrophage phenotype with the local microenvironment around cells. The agent-based model successfully reproduced qualitative patterns of macrophage polarization in an *in vitro* cell culture model. Cellular variability was observed in the simulation results, suggesting the potential of using ABM to capture the stochasticity and heterogeneity of biological processes. The dynamic and reversible nature of macrophage polarization was reflected in the fact that individual macrophage cells in the model demonstrated different phenotypes over the course of model simulation.

The current model has its own limitations:

- The M1-M2 paradigm in this model is a simplified idealization of actual macrophage phenotype changes. In biological organisms, after circulating monocytes are recruited to tissues, an unpolarized type of macrophages (M0) is often involved before macrophages are polarized to pro- and anti-inflammatory phenotypes [235]. The M1-M2 idealization is adequate for replicating *in vitro* behavior , as was the goal of this model, but a M0-M1-M2 model will be more appropriate for simulating *in vivo* conditions.

- The model uses a fixed total number of cells (n=100) during simulations, while the cell number is much larger and can change dynamically in both *in vitro* and *in vivo* systems. The computational limitation on the number of agents the model can handle efficiently is expected to cause discrepancies between simulation results and experimental measurements.

6.2 Future research recommendations

6.2.1 Extend the ozone respiratory model to other pollutants and species

The current model was implemented for ozone induced lung function changes in mice. However, a comprehensive computational model that could be used as an *in silico* tool to study respiratory effects of air pollutants should be applicable to various pollutants in different species. The multiscale and modularized design of the present model enables such extensions. Future research steps can extend the model to other species by including more species-specific physiological information and control measurements (*in vitro* / *in vivo*) to account for the intrinsic sensitivities of different species. The immune response module can be adjusted to accommodate the cellular mechanisms of action for other pollutants (e.g. through the addition of TLR receptors for PM recognition; the addition of AhR activation for polycyclic aromatic hydrocarbons, etc.). The ultimate goal should be to increase the level of model realism and to improve the performance of the model so that it can serve as a virtual human respiratory system for risk assessments of air pollutants.

6.2.2 Improve the performance of the cardiovascular model

One limitation of the current model is that the simulation results only represent the time domain HRV index —SDNN. Other HRV indices with different physiological meanings are not calculated. This is due to the lack of a detailed model that describes the autonomic control of heartbeats. Next steps should include development of a more sophisticated module for autonomic heart rate control. The improved model should be able to generate discrete heartbeats, so that HRV indices (both time-domain and frequency-domain) can be calculated as simulation results to fully characterize HRV alterations induced by PM exposures.

6.2.3 Integration of skin biology models

The three computational models developed for the skin system are rather preliminary and isolated from each other. Future research work should include: (a) Besides the formation of SOA, addition of reaction kinetics for lipid ozonation to the skin surface reaction model; (b) identification of AhR ligands from the ozone-lipid reaction products and simulation of their effects on AhR activation and gene transcriptions in keratinocytes; (c) incorporation of AhR-mediated cellular signaling pathways that regulate oxidative stress and pro- / anti-inflammatory responses; (d) incorporation of the three models in a comprehensive multiscale model for skin health effects associated with ozone exposure, that should consider: skin surface reactions, cellular signaling events and keratinocyte cell cycle regulation.

6.2.4 Improvements of the macrophage polarization model

In the current model, the number of macrophage cells is set to be a fixed number (100). This limits the model's ability to reproduce the real-life polarization processes. To further improve model performance, two initial steps should be taken: (a) increase the number of cells in the system as allowed by computational resource that can be obtained; (b) allow the total number of cells in the system to be dynamic so that the model can mimic the natural proliferation and apoptosis of macrophages. In order to extend the model from *in vitro* to *in vivo* systems, the unpolarized macrophages(M0) should be incorporated into the current M1-M2 model.

6.2.5 Incorporation of new modules into an integrative simulation framework

The multiscale models developed for the three physiological systems as well as the macrophage polarization model should be incorporated into the MENTOR (Modeling

ENvironment for TOtal Risk) [28] whole body human toxicokinetics and toxicodynamics modeling framework to facilitate studies of risks associated with air pollution exposures.

References

[1] World Health Organization. Ambient air pollution: A global assessment of exposure and burden of disease. 2016.

[2] American Lung Association. State of the Air 2020. Report, American Lung Association, 2020.

[3] Ioannis Manisalidis, Elisavet Stavropoulou, Agathangelos Stavropoulos, and Eugenia Bezirtzoglou. Environmental and health impacts of air pollution: A review. *Frontiers in public health*, 8, 2020.

[4] US EPA. The Benefits and Costs of the Clean Air Act from 1990 to 2020. 2011.

[5] US EPA. Integrated Science Assessment of Ozone and Related Photochemical Oxidants. EPA/600/R-10/076F., 2013.

[6] Meng Ji, Daniel S Cohan, and Michelle L Bell. Meta-analysis of the association between short-term exposure to ambient ozone and respiratory hospital admissions. *Environmental Research Letters*, 6(2):024006, 2011.

[7] US EPA. Integrated science assessment for particulate matter, 2009.

[8] Robert D. Brook, Barry Franklin, Wayne Cascio, Yuling Hong, George Howard, Michael Lipsett, Russell Luepker, Murray Mittleman, Jonathan Samet, Sidney C. Smith Jr, et al. Air pollution and cardiovascular disease: a statement for healthcare professionals from the Expert Panel on Population and Prevention Science of the American Heart Association. *Circulation*, 109(21):2655–2671, 2004.

[9] Francesca Dominici, Roger D. Peng, Michelle L. Bell, Luu Pham, Aidan McDermott, Scott L. Zeger, and Jonathan M. Samet. Fine particulate air pollution and hospital admission for cardiovascular and respiratory diseases. *Jama*, 295(10):1127–1134, 2006.

[10] C. Arden Pope III, Richard T. Burnett, George D. Thurston, Michael J. Thun, Eugenia E. Calle, Daniel Krewski, and John J. Godleski. Cardiovascular mortality and long-term exposure to particulate air pollution: epidemiological evidence of general pathophysiological pathways of disease. *Circulation*, 109(1):71–77, 2004.

[11] Barbara Buckley and Aimen Farraj. Conceptual model for assessing criteria air pollutants in a multipollutant context: a modified adverse outcome pathway approach. *Toxicology*, 335:85–94, 2015.

[12] Julie E. Goodman, Robyn L. Prueitt, Sonja N. Sax, Daniella M. Pizzurro, Heather N. Lynch, Ke Zu, and Ferdinand J. Venditti. Ozone exposure and systemic biomarkers: Evaluation of evidence for adverse cardiovascular health impacts. *Critical reviews in toxicology*, 45(5):412–452, 2015.

[13] Gin C. Chuang, Zhen Yang, David G. Westbrook, Melissa Pompilius, Carol A. Ballinger, C. Roger White, David M. Krzywanski, Edward M. Postlethwait, and Scott W. Ballinger. Pulmonary ozone exposure induces vascular dysfunction, mitochondrial damage, and atherogenesis. *American Journal of Physiology-Lung Cellular and Molecular Physiology*, 297(2):L209–L216, 2009.

[14] Prem Kumarathasan, Erica Blais, Anushuyadevi Saravanamuthu, Agnieszka Bielecki, Ballari Mukherjee, Stephen Bjarnason, Josée Guénette, Patrick Goegan, and Renaud Vincent. Nitrative stress, oxidative stress and plasma endothelin levels after inhalation of particulate matter and ozone. *Particle and fibre toxicology*, 12(1):1–18, 2015.

[15] Aimen K. Farraj, Fatiha Malik, Najwa Haykal-Coates, Leon Walsh, Darrell Winsett, Dock Terrell, Leslie C. Thompson, Wayne E. Cascio, and Mehdi S. Hazari. Morning NO2 exposure sensitizes hypertensive rats to the cardiovascular effects of same day O3 exposure in the afternoon. *Inhalation Toxicology*, 28(4):170–179, 2016.

[16] Robert D. Brook, Jeffrey R. Brook, Bruce Urch, Renaud Vincent, Sanjay Rajagopalan, and Frances Silverman. Inhalation of fine particulate air pollution and ozone causes acute arterial vasoconstriction in healthy adults. *Circulation*, 105(13):1534–1536, 2002.

[17] Asghar A. Fakhri, Ljubomir M. Ilic, Gregory A. Wellenius, Bruce Urch, Frances Silverman, Diane R. Gold, and Murray A. Mittleman. Autonomic effects of controlled fine particulate exposure in young healthy adults: effect modification by ozone. *Environmental health perspectives*, 117(8):1287–1292, 2009.

[18] Raziye Akcilar, Sezer Akcer, Hasan Simsek, Aydin Akcilar, Zeynep Bayat, and Osman Genc. Effects Ozone Therapy on Blood Pressure in DOCA-salt Hypertension Model. 2015.

[19] Barbara Hoffmann, Heike Luttmann-Gibson, Allison Cohen, Antonella Zanobetti, Celine de Souza, Christopher Foley, Helen H. Suh, Brent A. Coull, Joel Schwartz, Murray Mittleman, et al. Opposing effects of particle pollution, ozone, and ambient temperature on arterial blood pressure. *Environmental health perspectives*, 120(2):241–246, 2012.

[20] S. E. Mancebo and S. Q. Wang. Recognizing the impact of ambient air pollution on skin health. *Journal of the European Academy of Dermatology and Venereology*, 29(12):2326–2332, 2015.

[21] Sanghwan Song, Kiyoung Lee, Young-Mi Lee, Jung-Hyun Lee, Sang Il Lee, Seung-Do Yu, and Domyung Paek. Acute health effects of urban fine and ultrafine particles on children with atopic dermatitis. *Environmental research*, 111(3):394–399, 2011.

[22] Andrea Vierkötter, Tamara Schikowski, Ulrich Ranft, Dorothea Sugiri, Mary Matsui, Ursula Krämer, and Jean Krutmann. Airborne particle exposure and extrinsic skin aging. *Journal of investigative dermatology*, 130(12):2719–2726, 2010.

[23] Riccardo Puntoni, Marcello Ceppi, Valerio Gennaro, Donatella Ugolini, Matteo Puntoni, Gaspare La Manna, Claudia Casella, and Domenico Franco Merlo.

Occupational exposure to carbon black and risk of cancer. *Cancer Causes & Control*, 15(5):511–516, 2004.

[24] Jinrong Zeng and Jianyun Lu. Mechanisms of action involved in ozone-therapy in skin diseases. *International immunopharmacology*, 56:235–241, 2018.

[25] F. Xu, S. Yan, M. Wu, F. L. L., and X. Xu. Ambient ozone pollution as a risk factor for skin disorders. *British journal of dermatology (1951)*, 165(1):224–225, 2011.

[26] A. Hüls, T. Schikowski, U. Krämer, D. Sugiri, S. Stolz, A. Vierkoetter, and J. Krutmann. Ozone exposure and extrinsic skin aging: Results from the SALIA cohort. In *JOURNAL OF INVESTIGATIVE DERMATOLOGY*, volume 135, pages S49–S49. NATURE PUBLISHING GROUP 75 VARICK ST, 9TH FLR, NEW YORK, NY 10013-1917 USA, 2015.

[27] Gerald T. Ankley, Richard S. Bennett, Russell J. Erickson, Dale J. Hoff, Michael W. Hornung, Rodney D. Johnson, David R. Mount, John W. Nichols, Christine L. Russom, Patricia K. Schmieder, et al. Adverse outcome pathways: a conceptual framework to support ecotoxicology research and risk assessment. *Environmental Toxicology and Chemistry: An International Journal*, 29(3):730–741, 2010.

[28] Panos G. Georgopoulos, Sastry Isukapalli, Ioannis P. Androulakis, Marianthi G. Ierapetritou, and William J. Welsh. Multiscale Integration of Toxicokinetic and Toxicodynamic Processes: From Cell and Tissue to Organ and "Whole Body" Models. *General, Applied and Systems Toxicology*, 2009.

[29] US EPA. Integrated Science Assessment (ISA) for Ozone and Related Photochemical Oxidants (Final Report). Report, U.S. Environmental Protection Agency, 2020.

[30] Junfeng Zhang, Yongjie Wei, and Zhangfu Fang. Ozone Pollution: A Major Health Hazard Worldwide. *Frontiers in Immunology*, 10:2518, 2019.

[31] V. R. Sunil, K. N. Vayas, J. A. Cervelli, E. V. Ebramova, A. J. Gow, M. Goedken, R. Malaviya, J. D. Laskin, and D. L. Laskin. Protective Role of Surfactant Protein-D Against Lung Injury and Oxidative Stress Induced by Nitrogen Mustard. *Toxicological Sciences*, 166(1):108–122, 2018.

[32] E. Parra and J. Perez-Gil. Composition, structure and mechanical properties define performance of pulmonary surfactant membranes and films. *Chemistry and Physics of Lipids*, 185:153–175, 2015.

[33] D. Mukherjee, D. Botelho, A. J. Gow, J. F. Zhang, and P. G. Georgopoulos. Computational Multiscale Toxicodynamic Modeling of Silver and Carbon Nanoparticle Effects on Mouse Lung Function. *Plos One*, 8(12), 2013.

[34] W. Z. Martini, D. L. Chinkes, R. E. Barrow, E. D. Murphey, and R. R. Wolfe. Lung surfactant kinetics in conscious pigs. *American Journal of Physiology-Endocrinology and Metabolism*, 277(1):E187–E195, 1999.

[35] A. V. Andreeva, M. A. Kutuzov, and T. A. Voyno-Yasenetskaya. Regulation of surfactant secretion in alveolar type II cells. *American Journal of Physiology-Lung Cellular and Molecular Physiology*, 293(2):L259–L271, 2007.

[36] R. W. Walters, R. R. Jenq, and S. B. Hall. Distinct steps in the adsorption of

pulmonary surfactant to an air-liquid interface. *Biophysical Journal*, 78(1):257–266, 2000.

[37] J. R. Wright. Clearance and Recycling of Pulmonary Surfactant. *American Journal of Physiology*, 259(2):L1–L12, 1990.

[38] A. Pettenazzo, A. Jobe, J. Humme, S. Seidner, and M. Ikegami. Clearance of Surfactant Phosphatidylcholine Via the Upper Airways in Rabbits. *Journal of Applied Physiology*, 65(5):2151–2155, 1988.

[39] S. A. Rooney, S. L. Young, and C. R. Mendelson. Molecular and Cellular Processing of Lung Surfactant. *Faseb Journal*, 8(12):957–967, 1994.

[40] N. Palaniyar, R. A. Ridsdale, S. A. Hearn, F. Possmayer, and G. Harauz. Formation of membrane lattice structures and their specific interactions with surfactant protein A. *American Journal of Physiology-Lung Cellular and Molecular Physiology*, 276(4):L642–L649, 1999.

[41] Y. Suzuki, Y. Fujita, and K. Kogishi. Reconstitution of Tubular Myelin from Synthetic Lipids and Proteins Associated with Pig Pulmonary Surfactant. *American Review of Respiratory Disease*, 140(1):75–81, 1989.

[42] R. Qanbar, S. Cheng, F. Possmayer, and S. Schurch. Role of the palmitoylation of surfactant-associated protein C in surfactant film formation and stability. *American Journal of Physiology-Lung Cellular and Molecular Physiology*, 271(4):L572–L580, 1996.

[43] S. Hawgood, M. Derrick, and F. Poulain. Structure and properties of surfactant protein B. *Biochimica Et Biophysica Acta-Molecular Basis of Disease*, 1408(2-3):150–160, 1998.

[44] K. C. Thompson, S. H. Jones, A. R. Rennie, M. D. King, A. D. Ward, B. R. Hughes, C. O. M. Lucas, R. A. Campbell, and A. V. Hughes. Degradation and Rearrangement of a Lung Surfactant Lipid at the Air-Water Interface during Exposure to the Pollutant Gas Ozone. *Langmuir*, 29(14):4594–4602, 2013.

[45] J. M. Hemming, B. R. Hughes, A. R. Rennie, S. Tomas, R. A. Campbell, A. V. Hughes, T. Arnold, S. W. Botchway, and K. C. Thompson. Environmental Pollutant Ozone Causes Damage to Lung Surfactant Protein B (SP-B). *Biochemistry*, 54(33):5185–5197, 2015.

[46] R. S. Oosting, M. M. J. Vangreevenbroek, J. Verhoef, L. M. G. Vangolde, and H. P. Haagsman. Structural and Functional-Changes of Surfactant Protein-a Induced by Ozone. *American Journal of Physiology*, 261(2):L77–L83, 1991.

[47] H. I. Kim, H. Kim, Y. S. Shin, L. W. Beegle, W. A. Goddard, J. R. Heath, I. Kanik, and J. L. Beauchamp. Time Resolved Studies of Interfacial Reactions of Ozone with Pulmonary Phospholipid Surfactants Using Field Induced Droplet Ionization Mass Spectrometry. *Journal of Physical Chemistry B*, 114(29):9496–9503, 2010.

[48] H. I. Kim, H. J. Kim, Y. S. Shin, L. W. Beegle, S. S. Jang, E. L. Neidholdt, W. A. Goddard, J. R. Heath, I. Kanik, and J. L. Beauchamp. Interfacial Reactions of Ozone with Surfactant Protein B in a Model Lung Surfactant System. *Journal of the American Chemical Society*, 132(7):2254–2263, 2010.

[49] R. M. Uppu, R. Cueto, G. L. Squadrito, and W. A. Pryor. What Does Ozone

React with at the Air Lung Interface - Model Studies Using Human Red-Blood-Cell Membranes. *Archives of Biochemistry and Biophysics*, 319(1):257–266, 1995.

[50] P. A. Bromberg. Mechanisms of the acute effects of inhaled ozone in humans. *Biochimica Et Biophysica Acta-General Subjects*, 1860(12):2771–2781, 2016.

[51] A. M. Groves, A. J. Gow, C. B. Massa, J. D. Laskin, and D. L. Laskin. Prolonged Injury and Altered Lung Function after Ozone Inhalation in Mice with Chronic Lung Inflammation. *American Journal of Respiratory Cell and Molecular Biology*, 47(6):776–783, 2012.

[52] G. C. Donaldson, T. A. R. Seemungal, I. S. Patel, A. Bhowmik, T. M. A. Wilkinson, J. R. Hurst, P. K. MacCallum, and J. A. Wedzicha. Airway and systemic inflammation and decline in lung function in patients with COPD. *Chest*, 128(4):1995–2004, 2005.

[53] M. Lodovici and E. Bigagli. Oxidative stress and air pollution exposure. *Journal of Toxicology*, 2011:487074, 2011.

[54] T. Liu, L. Zhang, D. Joo, and S. C. Sun. NF-kappaB signaling in inflammation. *Signal Transduct Target Ther*, 2, 2017.

[55] M. J. Morgan and Z. G. Liu. Crosstalk of reactive oxygen species and NF-kappaB signaling. *Cell Research*, 21(1):103–15, 2011.

[56] M. Yamazoe, C. Nishitani, M. Takahashi, T. Katoh, S. Ariki, T. Shimizu, H. Mitsuzawa, K. Sawada, D. R. Voelker, H. Takahashi, and Y. Kuroki. Pulmonary Surfactant Protein D Inhibits Lipopolysaccharide (LPS)-induced Inflammatory Cell Responses by Altering LPS Binding to Its Receptors. *Journal of Biological Chemistry*, 283(51):35878–35888, 2008.

[57] S. Kierstein, F. R. Poulain, Y. Cao, M. Grous, R. Mathias, G. Kierstein, M. F. Beers, M. Salmon, R. A. Panettieri, and A. Haczku. Susceptibility to ozone-induced airway inflammation is associated with decreased levels of surfactant protein D. *Respiratory Research*, 7, 2006.

[58] P. S. Kingma and J. A. Whitsett. In defense of the lung: surfactant protein A and surfactant protein D. *Current Opinion in Pharmacology*, 6(3):277–283, 2006.

[59] J. D. Wardyn, A. H. Ponsford, and C. M. Sanderson. Dissecting molecular cross-talk between Nrf2 and NF-kappa B response pathways. *Biochemical Society Transactions*, 43:621–626, 2015.

[60] Q. Ma. Role of Nrf2 in Oxidative Stress and Toxicity. *Annual Review of Pharmacology and Toxicology*, 53:401–426, 2013.

[61] R. K. Thimmulappa, H. Lee, T. Rangasamy, S. P. Reddy, M. Yamamoto, T. W. Kensler, and S. Biswal. Nrf2 is a critical regulator of the innate immune response and survival during experimental sepsis. *Journal of Clinical Investigation*, 116(4):984–995, 2006.

[62] M. A. Yu, H. Li, Q. M. Liu, F. Liu, L. J. Tang, C. Y. Li, Y. Z. Yuan, Y. Q. Zhan, W. X. Xu, W. Li, H. Chen, C. H. Ge, J. A. Wang, and X. M. Yang. Nuclear factor p65 interacts with Keap1 to repress the Nrf2-ARE pathway. *Cellular Signalling*, 23(5):883–892, 2011.

[63] A. B. Otis, C. B. McKerrow, R. A. Bartlett, J. Mead, M. B. McIlroy, N. J. Selver-Stone, and Jr. Radford, E. P. Mechanical factors in distribution of pulmonary ventilation. *Journal of Applied Physiology*, 8(4):427–43, 1956.

[64] J. Hildebrandt. Pressure-volume data of cat lung interpreted by a plastoelastic, linear viscoelastic model. *Journal of Applied Physiology*, 28(3):365–72, 1970.

[65] C. Thamrin, T. Z. Janosi, R. A. Collins, P. D. Sly, and Z. Hantos. Sensitivity analysis of respiratory parameter estimates in the constant-phase model. *Annals of Biomedical Engineering*, 32(6):815–22, 2004.

[66] Z. Hantos, B. Daroczy, B. Suki, S. Nagy, and J. J. Fredberg. Input impedance and peripheral inhomogeneity of dog lungs. *Journal of Applied Physiology*, 72(1):168–78, 1992.

[67] Z. Hantos, B. Suki, T. Csendes, and B. Daroczy. Constant-Phase Modeling of Pulmonary Tissue Impedance. *Bulletin Europeen De Physiopathologie Respiratoire-Clinical Respiratory Physiology*, 23:S325–S325, 1987.

[68] J. H. T. Bates. *Lung Mechanics An Inverse Modeling Approach*. Cambridge University Press, 2009.

[69] C. G. Irvin and J. H. Bates. Measuring the lung function in the mouse: the challenge of size. *Respiratory Research*, 4:4, 2003.

[70] M. S. Ludwig, I. Dreshaj, J. Solway, A. Munoz, and Jr. Ingram, R. H. Partitioning of pulmonary resistance during constriction in the dog: effects of volume history. *Journal of Applied Physiology*, 62(2):807–15, 1987.

[71] B. Suki, F. Petak, A. Adamicza, Z. Hantos, and K. R. Lutchen. Partitioning of airway and lung tissue properties: comparison of in situ and open-chest conditions. *Journal of Applied Physiology*, 79(3):861–9, 1995.

[72] W. C. Cheng, D. S. DeLong, G. N. Franz, E. L. Petsonk, and D. G. Frazer. Contribution of opening and closing of lung units to lung hysteresis. *Respiration Physiology*, 102(2-3):205–215, 1995.

[73] L. Brancazio, G. N. Franz, E. L. Petsonk, and D. G. Frazer. Lung area–volume models in relation to the recruitment–derecruitment of individual lung units. *Annals of Biomedical Engineering*, 29(3):252–62, 2001.

[74] D. P. Gaver, R. W. Samsel, and J. Solway. Effects of Surface-Tension and Viscosity on Airway Reopening. *Journal of Applied Physiology*, 69(1):74–85, 1990.

[75] C. B. Massa, G. B. Allen, and J. H. T. Bates. Modeling the dynamics of recruitment and derecruitment in mice with acute lung injury. *Journal of Applied Physiology*, 105(6):1813–1821, 2008.

[76] J. H. T. Bates and C. G. Irvin. Time dependence of recruitment and derecruitment in the lung: a theoretical model. *Journal of Applied Physiology*, 93(2):705–713, 2002.

[77] D. Halpern and J. B. Grotberg. Surfactant Effects on Fluid-Elastic Instabilities of Liquid-Lined Flexible Tubes - a Model of Airway-Closure. *Journal of Biomechanical Engineering-Transactions of the Asme*, 115(3):271–277, 1993.

[78] R. S. Harris. Pressure-volume curves of the respiratory system. *Respiratory care*, 50(1):78–99, 2005.

[79] J. G. Venegas, R. S. Harris, and B. A. Simon. A comprehensive equation for the pulmonary pressure-volume curve. *Journal of Applied Physiology*, 84(1):389–395, 1998.

[80] J. P. Archie. A mathematical model for pulmonary mechanics: The alveolar surface contribution. *International Journal of Engineering Science*, 11(6):659–671, 1973.

[81] S. G. Taneva and K. M. W. Keough. Dynamic Surface-Properties of Pulmonary Surfactant Proteins Sp-B and Sp-C and Their Mixtures with Dipalmitoylphosphatidylcholine. *Biochemistry*, 33(49):14660–14670, 1994.

[82] Z. D. Wang, S. B. Hall, and R. H. Notter. Dynamic Surface-Activity of Films of Lung Surfactant Phospholipids, Hydrophobic Proteins, and Neutral Lipids. *Journal of Lipid Research*, 36(6):1283–1293, 1995.

[83] L. Qiao, A. M. Ge, M. Osawa, and S. Ye. Structure and stability studies of mixed monolayers of saturated and unsaturated phospholipids under low-level ozone. *Physical Chemistry Chemical Physics*, 15(41):17775–17785, 2013.

[84] Dwaipayan Mukherjee. *Computational modeling of nanoparticle distribution and toxicity in biological systems*. Thesis, 2015.

[85] C. M. Starling, C. M. Prado, E. A. Leick-Maldonado, T. Lancas, F. G. Reis, L. R. C. B. Aristoteles, M. Dolhnikoff, M. A. Martins, and I. F. L. C. Tiberio. Inducible nitric oxide synthase inhibition attenuates lung tissue responsiveness and remodeling in a model of chronic pulmonary inflammation in guinea pigs. *Respiratory Physiology & Neurobiology*, 165(2-3):185–194, 2009.

[86] D. G. Xisto, L. L. Farias, H. C. Ferreira, M. R. Picanco, D. Amitrano, L. R. L. E. Silva, E. M. Negri, T. Mauad, D. Carnielli, L. F. F. Silva, V. L. Capelozzi, D. S. Faffe, W. A. Zin, and P. R. M. Rocco. Lung parenchyma remodeling in a murine model of chronic allergic inflammation. *American Journal of Respiratory and Critical Care Medicine*, 171(8):829–837, 2005.

[87] D. L. Dixon, H. R. De Smet, and A. D. Bersten. Lung mechanics are both dose and tidal volume dependant in LPS-induced lung injury. *Respiratory Physiology & Neurobiology*, 167(3):333–340, 2009.

[88] G. Nieman, D. Brown, J. Sarkar, B. Kubiak, C. Ziraldo, J. Dutta-Moscato, C. Vieau, D. Barclay, L. Gatto, K. Maier, G. Constantine, T. R. Billiar, R. Zamora, Q. Mi, S. Chang, and Y. Vodovotz. A two-compartment mathematical model of endotoxin-induced inflammatory and physiologic alterations in swine. *Critical Care Medicine*, 40(4):1052–1063, 2012.

[89] A. M. Groves, A. J. Gow, C. B. Massa, L. Hall, J. D. Laskin, and D. L. Laskin. Age-related increases in ozone-induced injury and altered pulmonary mechanics in mice with progressive lung inflammation. *American Journal of Physiology-Lung Cellular and Molecular Physiology*, 305(8):L555–L568, 2013.

[90] E. Putman, A. J. F. Boere, L. Vanbree, L. M. G. Vangolde, and H. P. Haagsman. Pulmonary Surfactant Subtype Metabolism Is Altered after Short-Term Ozone Exposure. *Toxicology and Applied Pharmacology*, 134(1):132–138, 1995.

[91] E. Putman, W. Liese, W. F. Voorhout, L. VanBree, L. M. G. VanGolde, and H. P. Haagsman. Short-term ozone exposure affects the surface activity of

pulmonary surfactant. *Toxicology and Applied Pharmacology*, 142(2):288–296, 1997.

[92] Health Effects Institute. State of Global Air 2019. Report, Health Effects Institute, 2019.

[93] M. Lippmann, K. Ito, A. Nadas, and R. T. Burnett. Association of particulate matter components with daily mortality and morbidity in urban populations. *Research Report, Health Effects Institute*, (95):5–72, discussion 73–82, 2000.

[94] M. Franklin, A. Zeka, and J. Schwartz. Association between PM2.5 and all-cause and specific-cause mortality in 27 US communities. *Journal of Exposure Science and Environmental Epidemiology*, 17(3):279–287, 2007.

[95] Y. G. Wei, Y. Wang, Q. Di, C. Choirat, Y. Wang, P. Koutrakis, A. Zanobetti, F. Dominici, and J. D. Schwartz. Short term exposure to fine particulate matter and hospital admission risks and costs in the Medicare population: time stratified, case crossover study. *Bmj-British Medical Journal*, 367, 2019.

[96] N. Martinelli, O. Olivieri, and D. Girelli. Air particulate matter and cardiovascular disease: a narrative review. *European Journal of Internal Medicine*, 24(4):295–302, 2013.

[97] A. J. Seely and N. V. Christou. Multiple organ dysfunction syndrome: exploring the paradigm of complex nonlinear systems. *Critical Care Medicine*, 28(7):2193–200, 2000.

[98] N. Chattipakorn, T. Incharoen, N. Kanlop, and S. Chattipakorn. Heart rate variability in myocardial infarction and heart failure. *International Journal of Cardiology*, 120(3):289–96, 2007.

[99] S. Hillebrand, K. B. Gast, R. de Mutsert, C. A. Swenne, J. W. Jukema, S. Middeldorp, F. R. Rosendaal, and O. M. Dekkers. Heart rate variability and first cardiovascular event in populations without known cardiovascular disease: meta-analysis and dose-response meta-regression. *Europace*, 15(5):742–749, 2013.

[100] A. Zanobetti, D. R. Gold, P. H. Stone, H. H. Suh, J. Schwartz, B. A. Coull, and F. E. Speizer. Reduction in Heart Rate Variability with Traffic and Air Pollution in Patients with Coronary Artery Disease. *Environmental Health Perspectives*, 118(3):324–330, 2010.

[101] F. He, M. L. Shaffer, X. A. Li, S. Rodriguez-Colon, D. L. Wolbrette, R. Williams, W. E. Cascio, and D. P. Liao. Individual-level PM2.5 exposure and the time course of impaired heart rate variability: the APACR Study. *Journal of Exposure Science and Environmental Epidemiology*, 21(1):65–73, 2011.

[102] M. S. Lee, K. D. Eum, E. G. Rodrigues, S. R. Magari, S. C. Fang, G. A. Modest, and D. C. Christiani. Effects of Personal Exposure to Ambient Fine Particulate Matter on Acute Change in Nocturnal Heart Rate Variability in Subjects Without Overt Heart Disease. *American Journal of Cardiology*, 117(1):151–156, 2016.

[103] K. Shrey, A. Suchit, D. Deepika, K. Shruti, and R. Vibha. Air pollutants: The key stages in the pathway towards the development of cardiovascular disorders. *Environmental Toxicology and Pharmacology*, 31(1):1–9, 2011.

[104] D. P. Williams, J. Koenig, L. Carnevali, A. Sgoifo, M. N. Jarczok, E. M. Sternberg, and J. F. Thayer. Heart rate variability and inflammation: A meta-analysis of human studies. *Brain Behavior and Immunity*, 80:219–226, 2019.

[105] J. I. Webster, L. Tonelli, and E. M. Sternberg. Neuroendocrine regulation of immunity. *Annual Review of Immunology*, 20:125–163, 2002.

[106] K. J. Tracey. The inflammatory reflex. *Nature*, 420(6917):853–859, 2002.

[107] M. S. Hayden and S. Ghosh. NF-kappaB, the first quarter-century: remarkable progress and outstanding questions. *Genes & Development*, 26(3):203–34, 2012.

[108] A. Hoffmann, A. Levchenko, M. L. Scott, and D. Baltimore. The I kappa B-NF-kappa B signaling module: Temporal control and selective gene activation. *Science*, 298(5596):1241–1245, 2002.

[109] D. Lee, Y. F. Ding, A. Jayaraman, and J. S. Kwon. Mathematical Modeling and Parameter Estimation of Intracellular Signaling Pathway: Application to LPS-induced NF kappa B Activation and TNF alpha Production in Macrophages. *Processes*, 6(3), 2018.

[110] D. Yang, S. G. Elner, Z. M. Bian, G. O. Till, H. R. Petty, and V. A. Elner. Pro-inflammatory cytokines increase reactive oxygen species through mitochondria and NADPH oxidase in cultured RPE cells. *Experimental Eye Research*, 85(4):462–472, 2007.

[111] H. Blaser, C. Dostert, T. W. Mak, and D. Brenner. TNF and ROS Crosstalk in Inflammation. *Trends in Cell Biology*, 26(4):249–261, 2016.

[112] J. Shoenfelt, R. J. Mitkus, R. Zeisler, R. O. Spatz, J. Powell, M. J. Fenton, K. A. Squibb, and A. E. Medvedev. Involvement of TLR2 and TLR4 in inflammatory immune responses induced by fine and coarse ambient air particulate matter. *Journal of Leukocyte Biology*, 86(2):303–312, 2009.

[113] R. D. Brook and S. Rajagopalan. Particulate Matter Air Pollution and Atherosclerosis. *Current Atherosclerosis Reports*, 12(5):291–300, 2010.

[114] P. R. Reynolds, K. M. Wasley, and C. H. Allison. Diesel Particulate Matter Induces Receptor for Advanced Glycation End-Products (RAGE) Expression in Pulmonary Epithelial Cells, and RAGE Signaling Influences NF-kappa B-Mediated Inflammation. *Environmental Health Perspectives*, 119(3):332–336, 2011.

[115] P. P. Tak and G. S. Firestein. NF-kappaB: a key role in inflammatory diseases. *Journal of Clinical Investigation*, 107(1):7–11, 2001.

[116] J. D. Kearns, S. Basak, S. L. Werner, C. S. Huang, and A. Hoffmann. IkappaBepsilon provides negative feedback to control NF-kappaB oscillations, signaling dynamics, and inflammatory gene expression. *Journal of Cell Biology*, 173(5):659–64, 2006.

[117] P. Tripathi and A. Aggarwal. NF-kB transcription factor: a key player in the generation of immune response. *Current Science*, 90(4):519–531, 2006.

[118] A. Protti and M. Singer. Bench-to-bedside review: Potential strategies to protect or reverse mitochondrial dysfunction in sepsis-induced organ failure. *Critical Care*, 10(5), 2006.

[119] P. T. Foteinou, S. E. Calvano, S. F. Lowry, and I. P. Androulakis. Modeling

endotoxin-induced systemic inflammation using an indirect response approach. *Mathematical Biosciences*, 217(1):27–42, 2009.

[120] G. Schreibelt, J. van Horssen, S. van Rossum, C. D. Dijkstra, B. Drukarch, and H. E. de Vries. Therapeutic potential and biological role of endogenous antioxidant enzymes in multiple sclerosis pathology. *Brain Research Reviews*, 56(2):322–30, 2007.

[121] S. M. Ahmed, L. Luo, A. Namani, X. J. Wang, and X. Tang. Nrf2 signaling pathway: Pivotal roles in inflammation. *Biochim Biophys Acta Mol Basis Dis*, 1863(2):585–597, 2017.

[122] W. Krzyzanski and W. J. Jusko. Integrated functions for four basic models of indirect pharmacodynamic response. *Journal of Pharmaceutical Sciences*, 87(1):67–72, 1998.

[123] S. J. Snow, A. R. Henriquez, D. L. Costa, and U. P. Kodavanti. Neuroendocrine Regulation of Air Pollution Health Effects: Emerging Insights. *Toxicological Sciences*, 164(1):9–20, 2018.

[124] J. Thomas, J. Guenette, and E. M. Thomson. Stress axis variability is associated with differential ozone-induced lung inflammatory signaling and injury biomarker response. *Environmental Research*, 167:751–758, 2018.

[125] P. T. Foteinou, S. E. Calvano, S. F. Lowry, and I. P. Androulakis. Multiscale model for the assessment of autonomic dysfunction in human endotoxemia. *Physiological Genomics*, 42(1):5–19, 2010.

[126] J. Y. Jin, R. R. Almon, D. C. Dubois, and W. J. Jusko. Modeling of corticosteroid pharmacogenomics in rat liver using gene microarrays. *Journal of Pharmacology and Experimental Therapeutics*, 307(1):93–109, 2003.

[127] D. A. Padgett and R. Glaser. How stress influences the immune response. *Trends in Immunology*, 24(8):444–448, 2003.

[128] I. J. Elenkov, R. L. Wilder, G. P. Chrousos, and E. S. Vizi. The sympathetic nerve - An integrative interface between two supersystems: The brain and the immune system. *Pharmacological Reviews*, 52(4):595–638, 2000.

[129] I. J. Elenkov. Effects of Catecholamines on the Immune Response. *Hypothalamus-Pituitary-Adrenal Axis*, 7:189–206, 2008.

[130] F. Lombardi, G. Sandrone, S. Pernpruner, R. Sala, M. Garimoldi, S. Cerutti, G. Baselli, M. Pagani, and A. Malliani. Heart-Rate-Variability as an Index of Sympathovagal Interaction after Acute Myocardial-Infarction. *American Journal of Cardiology*, 60(16):1239–1245, 1987.

[131] H. Tsuji, M. G. Larson, F. J. Venditti, E. S. Manders, J. C. Evans, C. L. Feldman, and D. Levy. Impact of reduced heart rate variability on risk for cardiac events - The Framingham Heart Study. *Circulation*, 94(11):2850–2855, 1996.

[132] D. R. Gold, A. Litonjua, J. Schwartz, E. Lovett, A. Larson, B. Nearing, G. Allen, M. Verrier, R. Cherry, and R. Verrier. Ambient pollution and heart rate variability. *Circulation*, 101(11):1267–1273, 2000.

[133] A. Wheeler, A. Zanobetti, D. R. Gold, J. Schwartz, P. Stone, and H. H. Suh. The relationship between ambient air pollution and heart rate variability dif-

fers for individuals with heart and pulmonary disease. *Environmental Health Perspectives*, 114(4):560–566, 2006.

[134] M. Franchini and P. M. Mannucci. Short-term effects of air pollution on cardiovascular diseases: outcomes and mechanisms. *Journal of Thrombosis and Haemostasis*, 5(11):2169–2174, 2007.

[135] P. T. Foteinou, S. E. Calvano, S. F. Lowry, and I. P. Androulakis. A Physiological Model for Autonomic Heart Rate Regulation in Human Endotoxemia. *Shock*, 35(3):229–239, 2011.

[136] A. Zaza and F. Lombardi. Autonomic indexes based on the analysis of heart rate variability: a view from the sinus node. *Cardiovascular Research*, 50(3):434–442, 2001.

[137] D. E. Mager, E. Wyska, and W. J. Jusko. Diversity of mechanism-based pharmacodynamic models. *Drug Metabolism and Disposition*, 31(5):510–8, 2003.

[138] U.S. EPA. Integrated Science Assessment (ISA) For Particulate Matter (Final Report, Dec 2009). Report, U.S. Environmental Protection Agency, Washington, DC, 2009.

[139] P. J. Barnes and M. Karin. Nuclear factor-kappaB: a pivotal transcription factor in chronic inflammatory diseases. *New England Journal of Medicine*, 336(15):1066–71, 1997.

[140] T. van der Poll, S. M. Coyle, K. Barbosa, C. C. Braxton, and S. F. Lowry. Epinephrine inhibits tumor necrosis factor-alpha and potentiates interleukin 10 production during human endotoxemia. *Journal of Clinical Investigation*, 97(3):713–9, 1996.

[141] S. R. Magari, R. Hauser, J. Schwartz, P. L. Williams, T. J. Smith, and D. C. Christiani. Association of heart rate variability with occupational and environmental exposure to particulate air pollution. *Circulation*, 104(9):986–991, 2001.

[142] Stefan Sammito and Irina Böckelmann. Factors influencing heart rate variability. *International Cardiovascular Forum Journal*, 6, 2016.

[143] R. B. Devlin, A. J. Ghio, H. Kehrl, G. Sanders, and W. Cascio. Elderly humans exposed to concentrated air pollution particles have decreased heart rate variability. *European Respiratory Journal*, 21:76s–80s, 2003.

[144] J. Unosson, A. Blomberg, T. Sandstrom, A. Muala, C. Boman, R. Nystrom, R. Westerholm, N. L. Mills, D. E. Newby, J. P. Langrish, and J. A. Bosson. Exposure to wood smoke increases arterial stiffness and decreases heart rate variability in humans. *Particle and Fibre Toxicology*, 10, 2013.

[145] A. Sajadieh, O. W. Nielsen, V. Rasmussen, H. O. Hein, S. Abedini, and J. F. Hansen. Increased heart rate and reduced heart-rate variability are associated with subclinical inflammation in middle-aged and elderly subjects with no apparent heart disease. *European Heart Journal*, 25(5):363–370, 2004.

[146] A. Haensel, P. J. Mills, R. A. Nelesen, M. G. Ziegler, and J. E. Dimsdale. The relationship between heart rate variability and inflammatory markers in cardiovascular diseases. *Psychoneuroendocrinology*, 33(10):1305–1312, 2008.

[147] M. Kox, L. T. van Eijk, J. Zwaag, J. van den Wildenberg, F. C. G. J. Sweep,

J. G. van der Hoeven, and P. Pickkers. Voluntary activation of the sympathetic nervous system and attenuation of the innate immune response in humans. *Proceedings of the National Academy of Sciences of the United States of America*, 111(20):7379–7384, 2014.

[148] Y. Z. Yoon, J. Kim, B. C. Lee, Y. U. Kim, S. K. Lee, and K. S. Soh. Changes in ultraweak photon emission and heart rate variability of epinephrine-injected rats. *General Physiology and Biophysics*, 24(2):147–159, 2005.

[149] M. Stewart, J. R. Webster, K. J. Stafford, A. L. Schaefer, and G. A. Verkerk. Technical note: Effects of an epinephrine infusion on eye temperature and heart rate variability in bull calves. *Journal of Dairy Science*, 93(11):5252–5257, 2010.

[150] M.-A. Lefebvre, D.-M. Pham, B. Boussouira, D. Bernard, C. Camus, and Q.-L. Nguyen. Evaluation of the impact of urban pollution on the quality of skin: a multicentre study in Mexico. *International journal of cosmetic science*, 37(3):329–338, 2015.

[151] Abraham L. Kierszenbaum and Laura Tres. *Histology and Cell Biology: an introduction to pathology E-Book*. Elsevier Health Sciences, 2015.

[152] Apostolos Pappas. Epidermal surface lipids. *Dermato-endocrinology*, 1(2):72–76, 2009.

[153] David R. Fooshee, Paige K. Aiona, Alexander Laskin, Julia Laskin, Sergey A. Nizkorodov, and Pierre F. Baldi. Atmospheric oxidation of squalene: molecular study using COBRA modeling and high-resolution mass spectrometry. *Environmental science & technology*, 49(22):13304–13313, 2015.

[154] L. Petrick and Y. Dubowski. Heterogeneous oxidation of squalene film by ozone under various indoor conditions. *Indoor Air*, 19(5):381–391, 2009.

[155] Shouming Zhou, Matthew W. Forbes, Yasmine Katrib, and Jonathan P. D. Abbatt. Rapid oxidation of skin oil by ozone. *Environmental Science & Technology Letters*, 3(4):170–174, 2016.

[156] Chunyi Wang and Michael S. Waring. Secondary organic aerosol formation initiated from reactions between ozone and surface-sorbed squalene. *Atmospheric Environment*, 84:222–229, 2014.

[157] Alvin C. K. Lai and William W. Nazaroff. Modeling indoor particle deposition from turbulent flow onto smooth surfaces. *Journal of aerosol science*, 31(4):463–476, 2000.

[158] Ted W. Simon, Robert A. Budinsky, and J. Craig Rowlands. A model for aryl hydrocarbon receptor-activated gene expression shows potency and efficacy changes and predicts squelching due to competition for transcription coactivators. *Plos one*, 10(6):e0127952, 2015.

[159] Farrukh Afaq, Mohammad Abu Zaid, Edward Pelle, Naghma Khan, Deeba N. Syed, Mary S. Matsui, Daniel Maes, and Hasan Mukhtar. Aryl hydrocarbon receptor is an ozone sensor in human skin. *Journal of investigative dermatology*, 129(10):2396–2403, 2009.

[160] Lucie Stejskalova, Zdenek Dvorak, and Petr Pavek. Endogenous and exogenous ligands of aryl hydrocarbon receptor: current state of art. *Current drug metabolism*, 12(2):198–212, 2011.

[161] Ram K. Sindhu, Ronald E. Rasmussen, and Yutaka Kikkawa. Induction of cytochrome P4501A1 by ozone-oxidized tryptophan in Hepa lclc7 cells. In *Tryptophan, Serotonin, and Melatonin*, pages 409–418. Springer, 1999.

[162] Ram K. Sindhu, Frances E. Wagner, and Yutaka Kikkawa. Induction of cytochrome p450 1A1 and 1B1 by photooxidized tryptophan in transformed human keratinocytes. In *Developments in Tryptophan and Serotonin Metabolism*, pages 297–306. Springer, 2003.

[163] Eli V. Hestermann and Myles Brown. Agonist and chemopreventative ligands induce differential transcriptional cofactor recruitment by aryl hydrocarbon receptor. *Molecular and Cellular Biology*, 23(21):7920–7925, 2003.

[164] Arjun Raj and Alexander Van Oudenaarden. Nature, nurture, or chance: stochastic gene expression and its consequences. *Cell*, 135(2):216–226, 2008.

[165] Sudhir Nair, Vikram D. Kekatpure, Benjamin L. Judson, Arleen B. Rifkind, Richard D. Granstein, Jay O. Boyle, Kotha Subbaramaiah, Joseph B. Guttenplan, and Andrew J. Dannenberg. UVR exposure sensitizes keratinocytes to DNA adduct formation. *Cancer Prevention Research*, 2(10):895–902, 2009.

[166] Gaku Tsuji, Masakazu Takahara, Hiroshi Uchi, Satoshi Takeuchi, Chikage Mitoma, Yoichi Moroi, and Masutaka Furue. An environmental contaminant, benzo (a) pyrene, induces oxidative stress-mediated interleukin-8 production in human keratinocytes via the aryl hydrocarbon receptor signaling pathway. *Journal of dermatological science*, 62(1):42–49, 2011.

[167] Iain A. Murray, Andrew D. Patterson, and Gary H. Perdew. Aryl hydrocarbon receptor ligands in cancer: friend and foe. *Nature Reviews Cancer*, 14(12):801–814, 2014.

[168] Qiang Ma and J. P. Whitlock. The aromatic hydrocarbon receptor modulates the Hepa 1c1c7 cell cycle and differentiated state independently of dioxin. *Molecular and cellular biology*, 16(5):2144–2150, 1996.

[169] Guillermo Elizondo, Pedro Fernandez-Salguero, M. Saeed Sheikh, Geum-Yi Kim, Albert J. Fornace, Kyung S. Lee, and Frank J. Gonzalez. Altered cell cycle control at the G2/M phases in aryl hydrocarbon receptor-null embryo fibroblast. *Molecular pharmacology*, 57(5):1056–1063, 2000.

[170] Alvaro Puga, Ying Xia, and Cornelis Elferink. Role of the aryl hydrocarbon receptor in cell cycle regulation. *Chemico-biological interactions*, 141(1-2):117–130, 2002.

[171] Jennifer L. Marlowe and Alvaro Puga. Aryl hydrocarbon receptor, cell cycle regulation, toxicity, and tumorigenesis. *Journal of cellular biochemistry*, 96(6):1174–1184, 2005.

[172] Maciej Swat, Alexander Kel, and Hanspeter Herzel. Bifurcation analysis of the regulatory modules of the mammalian G1/S transition. *Bioinformatics*, 20(10):1506–1511, 2004.

[173] Melissa A. Barhoover, Julie M. Hall, William F. Greenlee, and Russell S. Thomas. Aryl hydrocarbon receptor regulates cell cycle progression in human breast cancer cells via a functional interaction with cyclin-dependent kinase 4. *Molecular pharmacology*, 77(2):195–201, 2010.

[174] Michaela Kalmes, Andrea Neumeyer, Paola Rio, Helmut Hanenberg, Ellen Fritsche, and Brunhilde Blömeke. Impact of the arylhydrocarbon receptor on eugenol-and isoeugenol-induced cell cycle arrest in human immortalized keratinocytes (HaCaT). *Biological chemistry*, 387(9):1201–1207, 2006.

[175] Ehab H. Sarsour, Maneesh G. Kumar, Leena Chaudhuri, Amanda L. Kalen, and Prabhat C. Goswami. Redox control of the cell cycle in health and disease. *Antioxidants & redox signaling*, 11(12):2985–3011, 2009.

[176] D. L. Laskin. Macrophages and Inflammatory Mediators in Chemical Toxicity: A Battle of Forces. *Chemical Research in Toxicology*, 22(8):1376–1385, 2009.

[177] D. M. Mosser and J. P. Edwards. Exploring the full spectrum of macrophage activation. *Nature Reviews Immunology*, 8(12):958–969, 2008.

[178] Y. C. Liu, X. B. Zou, Y. F. Chai, and Y. M. Yao. Macrophage polarization in inflammatory diseases. *International journal of biological sciences*, 10(5):520–9, 2014.

[179] B. N. Brown, B. D. Ratner, S. B. Goodman, S. Amar, and S. F. Badylak. Macrophage polarization: an opportunity for improved outcomes in biomaterials and regenerative medicine. *Biomaterials*, 33(15):3792–802, 2012.

[180] A. C. Labonte, A. C. Tosello-Trampont, and Y. S. Hahn. The role of macrophage polarization in infectious and inflammatory diseases. *Molecules and Cells*, 37(4):275–85, 2014.

[181] D. L. Laskin, V. R. Sunil, C. R. Gardner, and J. D. Laskin. Macrophages and tissue injury: agents of defense or destruction? *Annual Review of Pharmacology and Toxicology*, 51:267–88, 2011.

[182] G. Arango Duque and A. Descoteaux. Macrophage cytokines: involvement in immunity and infectious diseases. *Frontiers in Immunology*, 5:491, 2014.

[183] M. J. Davis, T. M. Tsang, Y. Qiu, J. K. Dayrit, J. B. Freij, G. B. Huffnagle, and M. A. Olszewski. Macrophage M1/M2 polarization dynamically adapts to changes in cytokine microenvironments in Cryptococcus neoformans infection. *MBio*, 4(3):e00264–13, 2013.

[184] A. Sica and A. Mantovani. Macrophage plasticity and polarization: in vivo veritas. *Journal of Clinical Investigation*, 122(3):787–95, 2012.

[185] K. Rzosinska, D. Formanowicz, and P. Formanowicz. The study of the influence of micro-environmental signals on macrophage differentiation using a quantitative Petri net based model. *Archives of Control Sciences*, 27(2):331–349, 2017.

[186] K. Wendelsdorf, J. Bassaganya-Riera, R. Hontecillas, and S. Eubank. Model of colonic inflammation: Immune modulatory mechanisms in inflammatory bowel disease. *Journal of Theoretical Biology*, 264(4):1225–1239, 2010.

[187] B. N. Brown, I. M. Price, F. R. Toapanta, D. R. DeAlmeida, C. A. Wiley, T. M. Ross, T. D. Oury, and Y. Vodovotz. An agent-based model of inflammation and fibrosis following particulate exposure in the lung. *Mathematical Biosciences*, 231(2):186–96, 2011.

[188] T. T. Nguyen, S. E. Calvano, S. F. Lowry, and I. P. Androulakis. An agent-based model of cellular dynamics and circadian variability in human endotoxemia. *PLoS One*, 8(1):e55550, 2013.

[189] N. A. Cilfone, C. R. Perry, D. E. Kirschner, and J. J. Linderman. Multi-scale modeling predicts a balance of tumor necrosis factor-alpha and interleukin-10 controls the granuloma environment during Mycobacterium tuberculosis infection. *PLoS One*, 8(7):e68680, 2013.

[190] S. Marino, N. A. Cilfone, J. T. Mattila, J. J. Linderman, J. L. Flynn, and D. E. Kirschner. Macrophage Polarization Drives Granuloma Outcome during Mycobacterium tuberculosis Infection. *Infection and Immunity*, 83(1):324–338, 2015.

[191] P. J. Murray. STAT3-mediated anti-inflammatory signalling. *Biochemical Society Transactions*, 34(Pt 6):1028–31, 2006.

[192] L. B. Ivashkiv. Inflammatory signaling in macrophages: transitions from acute to tolerant and alternative activation states. *European Journal of Immunology*, 41(9):2477–81, 2011.

[193] A. V. Villarino, Y. Kanno, J. R. Ferdinand, and J. J. O'Shea. Mechanisms of Jak/STAT signaling in immunity and disease. *Journal of Immunology*, 194(1):21–7, 2015.

[194] F. Wermeling, R. M. Anthony, F. Brombacher, and J. V. Ravetch. Acute inflammation primes myeloid effector cells for anti-inflammatory STAT6 signaling. *Proceedings of the National Academy of Sciences of the United States of America*, 110(33):13487–91, 2013.

[195] W. Li, T. O. Khor, C. Xu, G. Shen, W. S. Jeong, S. Yu, and A. N. Kong. Activation of Nrf2-antioxidant signaling attenuates NFkappaB-inflammatory response and elicits apoptosis. *Biochemical Pharmacology*, 76(11):1485–9, 2008.

[196] A. R. Brasier. The nuclear factor-kappaB-interleukin-6 signalling pathway mediating vascular inflammation. *Cardiovascular Research*, 86(2):211–8, 2010.

[197] T. A. Libermann and D. Baltimore. Activation of Interleukin-6 Gene-Expression through the Nf-Kappa-B Transcription Factor. *Molecular and Cellular Biology*, 10(5):2327–2334, 1990.

[198] T. Calandra and T. Roger. Macrophage migration inhibitory factor: a regulator of innate immunity. *Nature Reviews Immunology*, 3(10):791–800, 2003.

[199] T. Roger, J. David, M. P. Glauser, and T. Calandra. MIF regulates innate immune responses through modulation of Toll-like receptor 4. *Nature*, 414(6866):920–924, 2001.

[200] J. L. Meitzler, S. Antony, Y. Z. Wu, A. Juhasz, H. Liu, G. J. Jiang, J. M. Lu, K. Roy, and J. H. Doroshow. NADPH Oxidases: A Perspective on Reactive Oxygen Species Production in Tumor Biology. *Antioxidants & Redox Signaling*, 20(17):2873–2889, 2014.

[201] A. Panday, M. K. Sahoo, D. Osorio, and S. Batra. NADPH oxidases: an overview from structure to innate immunity-associated pathologies. *Cellular and Molecular Immunology*, 12(1):5–23, 2015.

[202] J. Qu, W. X. Chen, R. Hu, and H. Feng. The Injury and Therapy of Reactive Oxygen Species in Intracerebral Hemorrhage Looking at Mitochondria. *Oxidative Medicine and Cellular Longevity*, 2016.

[203] T. Maraldi. Natural Compounds as Modulators of NADPH Oxidases. *Oxidative*

Medicine and Cellular Longevity, 2013.

[204] M. Y. Song, E. K. Kim, W. S. Moon, J. W. Park, H. J. Kim, H. S. So, R. Park, K. B. Kwon, and B. H. Park. Sulforaphane protects against cytokine- and streptozotocin-induced beta-cell damage by suppressing the NF-kappa B pathway. *Toxicology and Applied Pharmacology*, 235(1):57–67, 2009.

[205] W. T. Watford and J. J. O'Shea. Human Tyk2 kinase deficiency: Another primary immunodeficiency syndrome. *Immunity*, 25(5):695–697, 2006.

[206] T. Kisseleva, S. Bhattacharya, J. Braunstein, and C. W. Schindler. Signaling through the JAK/STAT pathway, recent advances and future challenges. *Gene*, 285(1-2):1–24, 2002.

[207] D. X. Zhou, L. Chen, K. Yang, H. Jiang, W. K. Xu, and J. J. Luan. SOCS molecules: the growing players in macrophage polarization and function. *Oncotarget*, 8(36):60710–60722, 2017.

[208] J. S. Rawlings, K. M. Rosler, and D. A. Harrison. The JAK/STAT signaling pathway. *Journal of Cell Science*, 117(8):1281–1283, 2004.

[209] A. P. Hutchins, D. Diez, and D. Miranda-Saavedra. The IL-10/STAT3-mediated anti-inflammatory response: recent developments and future challenges. *Brief Funct Genomics*, 12(6):489–98, 2013.

[210] J. Scheller, A. Chalaris, D. Schmidt-Arras, and S. Rose-John. The pro- and anti-inflammatory properties of the cytokine interleukin-6. *Biochimica Et Biophysica Acta-Molecular Cell Research*, 1813(5):878–888, 2011.

[211] K. C. El Kasmi, J. Holst, M. Coffre, L. Mielke, A. de Pauw, N. Lhocine, A. M. Smith, R. Rutschman, D. Kaushal, Y. Shen, T. Suda, R. P. Donnelly, Jr. Myers, M. G., W. Alexander, D. A. Vignali, S. S. Watowich, M. Ernst, D. J. Hilton, and P. J. Murray. General nature of the STAT3-activated anti-inflammatory response. *Journal of Immunology*, 177(11):7880–8, 2006.

[212] E. L. O'Dea, D. Barken, R. Q. Peralta, K. T. Tran, S. L. Werner, J. D. Kearns, A. Levchenko, and A. Hoffmann. A homeostatic model of IkappaB metabolism to control constitutive NF-kappaB activity. *Molecular Systems Biology*, 3:111, 2007.

[213] M. P. Pando and I. M. Verma. Signal-dependent and -independent degradation of free and NF-kappa B-bound IkappaBalpha. *Journal of Biological Chemistry*, 275(28):21278–86, 2000.

[214] H. K. Bryan, A. Olayanju, C. E. Goldring, and B. K. Park. The Nrf2 cell defence pathway: Keap1-dependent and -independent mechanisms of regulation. *Biochemical Pharmacology*, 85(6):705–17, 2013.

[215] M. Tamura, M. Takeshita, J. T. Curnutte, D. J. Uhlinger, and J. D. Lambeth. Stabilization of Human Neutrophil Nadph Oxidase Activated in a Cell-Free System by Cytosolic Proteins and by 1-Ethyl-3-(3-Dimethylaminopropyl) Carbodiimide. *Journal of Biological Chemistry*, 267(11):7529–7538, 1992.

[216] B. C. Dickinson and C. J. Chang. Chemistry and biology of reactive oxygen species in signaling or stress responses. *Nature Chemical Biology*, 7(8):504–11, 2011.

[217] S. P. Campos, Y. Wang, and H. Baumann. Insulin modulates STAT3 pro-

tein activation and gene transcription in hepatic cells. *Journal of Biological Chemistry*, 271(40):24418–24, 1996.

[218] A. Waage, P. Brandtzaeg, A. Halstensen, P. Kierulf, and T. Espevik. The Complex Pattern of Cytokines in Serum from Patients with Meningococcal Septic Shock - Association between Interleukin-6, Interleukin-1, and Fatal Outcome. *Journal of Experimental Medicine*, 169(1):333–338, 1989.

[219] K. Taguchi, N. Fujikawa, M. Komatsu, T. Ishii, M. Unno, T. Akaike, H. Motohashi, and M. Yamamoto. Keap1 degradation by autophagy for the maintenance of redox homeostasis. *Proceedings of the National Academy of Sciences of the United States of America*, 109(34):13561–13566, 2012.

[220] E. Siewert, W. Muller-Esterl, R. Starr, P. C. Heinrich, and F. Schaper. Different protein turnover of interleukin-6-type cytokine signalling components. *European Journal of Biochemistry*, 265(1):251–257, 1999.

[221] G. C. Brown. Total Cell Protein-Concentration as an Evolutionary Constraint on the Metabolic Control Distribution in Cells. *Journal of Theoretical Biology*, 153(2):195–203, 1991.

[222] S. Rothman. How is the balance between protein synthesis and degradation achieved? *Theoretical Biology and Medical Modelling*, 7, 2010.

[223] A. Hess, H. Iyer, and W. Malm. Linear trend analysis: a comparison of methods. *Atmospheric Environment*, 35(30):5211–5222, 2001.

[224] R. S. H. Mah, A. C. Tamhane, S. H. Tung, and A. N. Patel. Process Trending with Piecewise-Linear Smoothing. *Computers & Chemical Engineering*, 19(2):129–137, 1995.

[225] T. D. Smith, M. J. Tse, E. L. Read, and W. F. Liu. Regulation of macrophage polarization and plasticity by complex activation signals. *Integrative Biology*, 8(9):946–955, 2016.

[226] T. Lucas, A. Waisman, R. Ranjan, J. Roes, T. Krieg, W. Muller, A. Roers, and S. A. Eming. Differential roles of macrophages in diverse phases of skin repair. *Journal of Immunology*, 184(7):3964–77, 2010.

[227] X. L. Fu, W. Duan, C. Y. Su, F. Y. Mao, Y. P. Lv, Y. S. Teng, P. W. Yu, Y. Zhuang, and Y. L. Zhao. Interleukin 6 induces M2 macrophage differentiation by STAT3 activation that correlates with gastric cancer progression. *Cancer Immunology Immunotherapy*, 66(12):1597–1608, 2017.

[228] Robert B Devlin, James A Raub, and Lawrence J Folinsbee. Health effects of ozone. *Science and Medicine*, 4:8–17, 1997.

[229] Bernhard RYFFEL, Milena Sokolowska, Valerie FJ Quesniaux, Cezmi A Akdis, Kian Fan Chung, and Dieudonnée Togbe. Acute respiratory barrier disruption by ozone exposure in mice. *Frontiers in immunology*, 10:2169, 2019.

[230] Katharine L Hamlington, Bradford J Smith, Celia M Dunn, Chantel M Charlebois, Gregory S Roy, and Jason HT Bates. Linking lung function to structural damage of alveolar epithelium in ventilator-induced lung injury. *Respiratory physiology & neurobiology*, 255:22–29, 2018.

[231] Timothy D Nelin, Allan M Joseph, Matthew W Gorr, and Loren E Wold. Direct and indirect effects of particulate matter on the cardiovascular system.

Toxicology letters, 208(3):293–299, 2012.

[232] Günther Oberdörster, Zachary Sharp, Viorel Atudorei, Alison Elder, Robert Gelein, Wolfgang Kreyling, and Christopher Cox. Translocation of inhaled ultrafine particles to the brain. *Inhalation toxicology*, 16(6-7):437–445, 2004.

[233] Marek Malik, J Thomas Bigger, A John Camm, Robert E Kleiger, Alberto Malliani, Arthur J Moss, and Peter J Schwartz. Heart rate variability: Standards of measurement, physiological interpretation, and clinical use. *European heart journal*, 17(3):354–381, 1996.

[234] Thomas Sütterlin, Erika Tsingos, Jalil Bensaci, Georgios N Stamatas, and Niels Grabe. A 3D self-organizing multicellular epidermis model of barrier formation and hydration with realistic cell morphology based on EPISIM. *Scientific reports*, 7:43472, 2017.

[235] Alexander N Orekhov, Varvara A Orekhova, Nikita G Nikiforov, Veronika A Myasoedova, Andrey V Grechko, Elena B Romanenko, Dongwei Zhang, and Dimitry A Chistiakov. Monocyte differentiation and macrophage polarization. *Vessel Plus*, 3(10), 2019.

[236] Ewald R. Weibel, André Frédérick Cournand, and Dickinson W. Richards. *Morphometry of the human lung*, volume 1. Springer, 1963.

[237] Jean Krutmann, Wei Liu, Li Li, Xiaochuan Pan, Martha Crawford, Gabrielle Sore, and Sophie Seite. Pollution and skin: from epidemiological and mechanistic studies to clinical implications. *Journal of dermatological science*, 76(3):163–168, 2014.

[238] Jens J. Thiele, Maret G. Traber, Thomas G. Polefka, Carroll E. Cross, and Lester Packer. Ozone-exposure depletes vitamin E and induces lipid peroxidation in murine stratum corneum. *Journal of investigative dermatology*, 108(5):753–757, 1997.

[239] Q. C. He, A. Tavakkol, K. Wietecha, R. Begum-Gafur, S. A. Ansari, and T. Polefka. Effects of environmentally realistic levels of ozone on stratum corneum function. *International journal of cosmetic science*, 28(5):349–357, 2006.

[240] Giuseppe Valacchi, V. Fortino, and V. Bocci. The dual action of ozone on the skin. *British Journal of Dermatology*, 153(6):1096–1100, 2005.

[241] Clive R. Harding. The stratum corneum: structure and function in health and disease. *Dermatologic therapy*, 17:6–15, 2004.

[242] Giuseppe Valacchi, Elisa Pagnin, Ana M. Corbacho, Estibaliz Olano, Paul A. Davis, Lester Packer, and Carroll E. Cross. In vivo ozone exposure induces antioxidant/stress-related responses in murine lung and skin. *Free Radical Biology and Medicine*, 36(5):673–681, 2004.

[243] Giuseppe Valacchi, Albert Van der Vliet, Bettina C. Schock, Tatsuya Okamoto, Ute Obermuller-Jevic, Carroll E. Cross, and Lester Packer. Ozone exposure activates oxidative stress responses in murine skin. *Toxicology*, 179(1-2):163–170, 2002.

[244] Giuseppe Valacchi, Elisa Pagnin, Tatsuya Okamoto, Ana M. Corbacho, Estibaliz Olano, Paul A. Davis, Albert Van Der Vliet, Lester Packer, and Car-

roll E. Cross. Induction of stress proteins and MMP-9 by 0.8 ppm of ozone in murine skin. *Biochemical and biophysical research communications*, 305(3):741–746, 2003.

[245] Robert Barouki, Xavier Coumoul, and Pedro M. Fernandez-Salguero. The aryl hydrocarbon receptor, more than a xenobiotic-interacting protein. *FEBS letters*, 581(19):3608–3615, 2007.

[246] S. Pillai, C. Oresajo, and J. Hayward. Ultraviolet radiation and skin aging: roles of reactive oxygen species, inflammation and protease activation, and strategies for prevention of inflammation-induced matrix degradation–a review. *International journal of cosmetic science*, 27(1):17–34, 2005.

[247] Ian S. Mudway, David Housley, Ronald Eccles, Roy J. Richards, Avijit K. Datta, Teresa D. Tetley, and Frank J. Kelly. Differential depletion of human respiratory tract antioxidants in response to ozone challenge. *Free radical research*, 25(6):499–513, 1996.

[248] Jesús Pérez-Gil. Structure of pulmonary surfactant membranes and films: the role of proteins and lipid–protein interactions. *Biochimica et Biophysica acta (BBA)-Biomembranes*, 1778(7-8):1676–1695, 2008.

[249] Anthony N. Passannante, Milan J. Hazucha, Philip A. Bromberg, Elston Seal, Larry Folinsbee, and Gary Koch. Nociceptive mechanisms modulate ozone-induced human lung function decrements. *Journal of Applied Physiology*, 85(5):1863–1870, 1998.

[250] Steven R. Kleeberger, Sekhar Reddy, Liu-Yi Zhang, and Anne E. Jedlicka. Genetic susceptibility to ozone-induced lung hyperpermeability: role of toll-like receptor 4. *American journal of respiratory cell and molecular biology*, 22(5):620–627, 2000.

[251] R. B. Devlin, K. P. McKinnon, T. Noah, S. Becker, and H. S. Koren. Ozone-induced release of cytokines and fibronectin by alveolar macrophages and airway epithelial cells. *American Journal of Physiology-Lung Cellular and Molecular Physiology*, 266(6):L612–L619, 1994.

[252] Robert B. Devlin, Kelly E. Duncan, Melanie Jardim, Michael T. Schmitt, Ana G. Rappold, and David Diaz-Sanchez. Controlled exposure of healthy young volunteers to ozone causes cardiovascular effects. *Circulation*, 126(1):104–111, 2012.

[253] Edward S. Schelegle, M. L. Carl, H. M. Coleridge, J. C. Coleridge, and J. F. Green. Contribution of vagal afferents to respiratory reflexes evoked by acute inhalation of ozone in dogs. *Journal of Applied Physiology*, 74(5):2338–2344, 1993.

[254] Jeremy D. Scheff. *Heart rate variability and rhythmic influences in human endotoxemia*. PhD thesis, Rutgers University-Graduate School-New Brunswick, 2013.

[255] Carlo R. Bartoli, Gregory A. Wellenius, Edgar A. Diaz, Joy Lawrence, Brent A. Coull, Ichiro Akiyama, Lani M. Lee, Kazunori Okabe, Richard L. Verrier, and John J. Godleski. Mechanisms of inhaled fine particulate air pollution–induced arterial blood pressure changes. *Environmental health perspectives*, 117(3):361–

366, 2009.

[256] Jingkun Jiang, Günter Oberdörster, Alison Elder, Robert Gelein, Pamela Mercer, and Pratim Biswas. Does nanoparticle activity depend upon size and crystal phase? *Nanotoxicology*, 2(1):33–42, 2008.

[257] Florence Tao, Beatriz Gonzalez-Flecha, and Lester Kobzik. Reactive oxygen species in pulmonary inflammation by ambient particulates. *Free Radical Biology and Medicine*, 35(4):327–340, 2003.

[258] Susanne Becker, Matthew J. Fenton, and Joleen M. Soukup. Involvement of microbial components and toll-like receptors 2 and 4 in cytokine responses to air pollution particles. *American journal of respiratory cell and molecular biology*, 27(5):611–618, 2002.

[259] Rodney L. Rouse, Gleeson Murphy, Marc J. Boudreaux, Daniel B. Paulsen, and Arthur L. Penn. Soot nanoparticles promote biotransformation, oxidative stress, and inflammation in murine lungs. *American journal of respiratory cell and molecular biology*, 39(2):198–207, 2008.

[260] Hasan Bayram, Kazuhiro Ito, Razao Issa, Misako Ito, Maria Sukkar, and Kian Fan Chung. Regulation of human lung epithelial cell numbers by diesel exhaust particles. *European Respiratory Journal*, 27(4):705–713, 2006.

[261] Ilona Jaspers, Jonathan M. Ciencewicki, Wenli Zhang, Luisa E. Brighton, Johnny L. Carson, Melinda A. Beck, and Michael C. Madden. Diesel exhaust enhances influenza virus infections in respiratory epithelial cells. *Toxicological Sciences*, 85(2):990–1002, 2005.

[262] Erin E. Mann, Leslie C. Thompson, Jonathan H. Shannahan, and Christopher J. Wingard. Changes in cardiopulmonary function induced by nanoparticles. *Wiley interdisciplinary reviews: Nanomedicine and nanobiotechnology*, 4(6):691–702, 2012.

[263] Janine Pöss, Dominik Lorenz, Christian Werner, Valerie Pavlikova, Christoph Gensch, Thimoteus Speer, Francesca Alessandrini, Vincent Berezowski, Mélanie Kuntz, Martin Mempel, et al. Diesel exhaust particles impair endothelial progenitor cells, compromise endothelial integrity, reduce neoangiogenesis, and increase atherogenesis in mice. *Cardiovascular toxicology*, 13(3):290–300, 2013.

Appendix A

Basics of human respiratory physiology

A.1 Basic structure of the human respiratory tract

The human lung is divided into three major regions as shown in Figure A.1: the extrathoracic (ET) region or upper respiratory tract (URT, from the nose/mouth to the end of the larynx); the tracheobronchial (TB) tree (from trachea to the terminal bronchioles); and the alveolar or pulmonary region (from the respiratory bronchioles to the terminal alveolar sacs). The TB region together with the alveolar region comprise the lower respiratory tract (LRT).

A thin layer of fluid covers the air-facing surface of the lung. It consists of the airway surface lining, which is a mucus gel-aqueous sol complex, and the alveolar surface lining, which includes subphase fluid and pulmonary surfactant. The thickness of the lining fluid layer decreases distally.

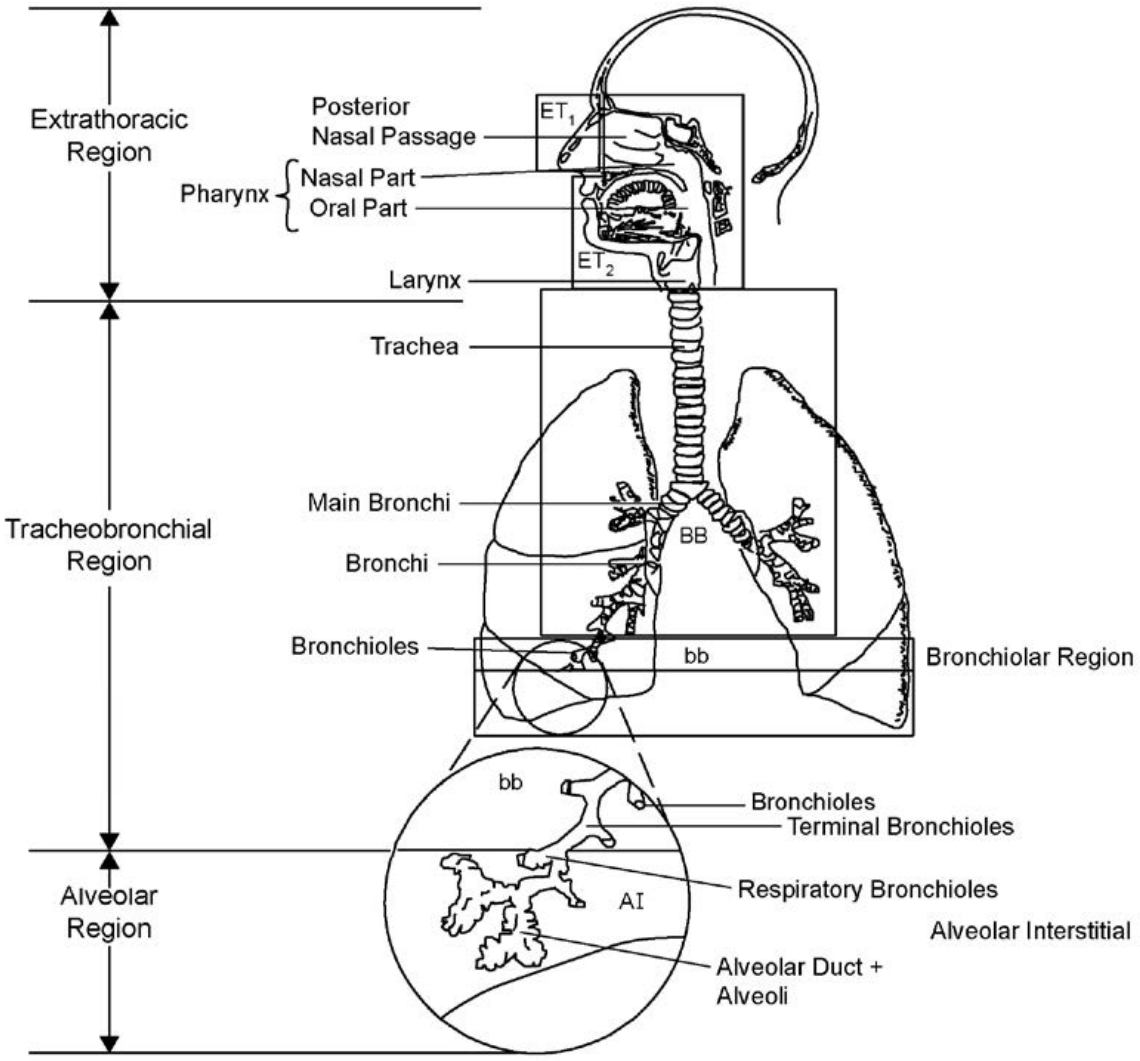

Figure A.1: Respiratory regions in humans [5]

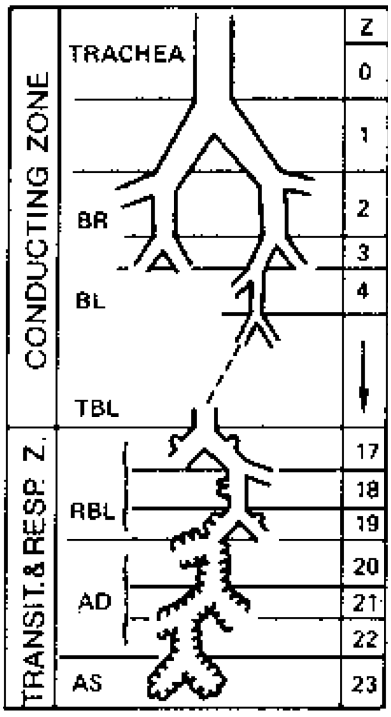

Figure A.2: Idealization of the human airways according to Weibel's model. Z = airway generation; BR = bronchus; BL = bronchiole; TBL = terminal bronchiole; RBL = respiratory bronchiole; AD = alveolar duct; AS = alveolar sac. Note that the RBL, AD, and AS make up the transitional and respiratory zone.[236]

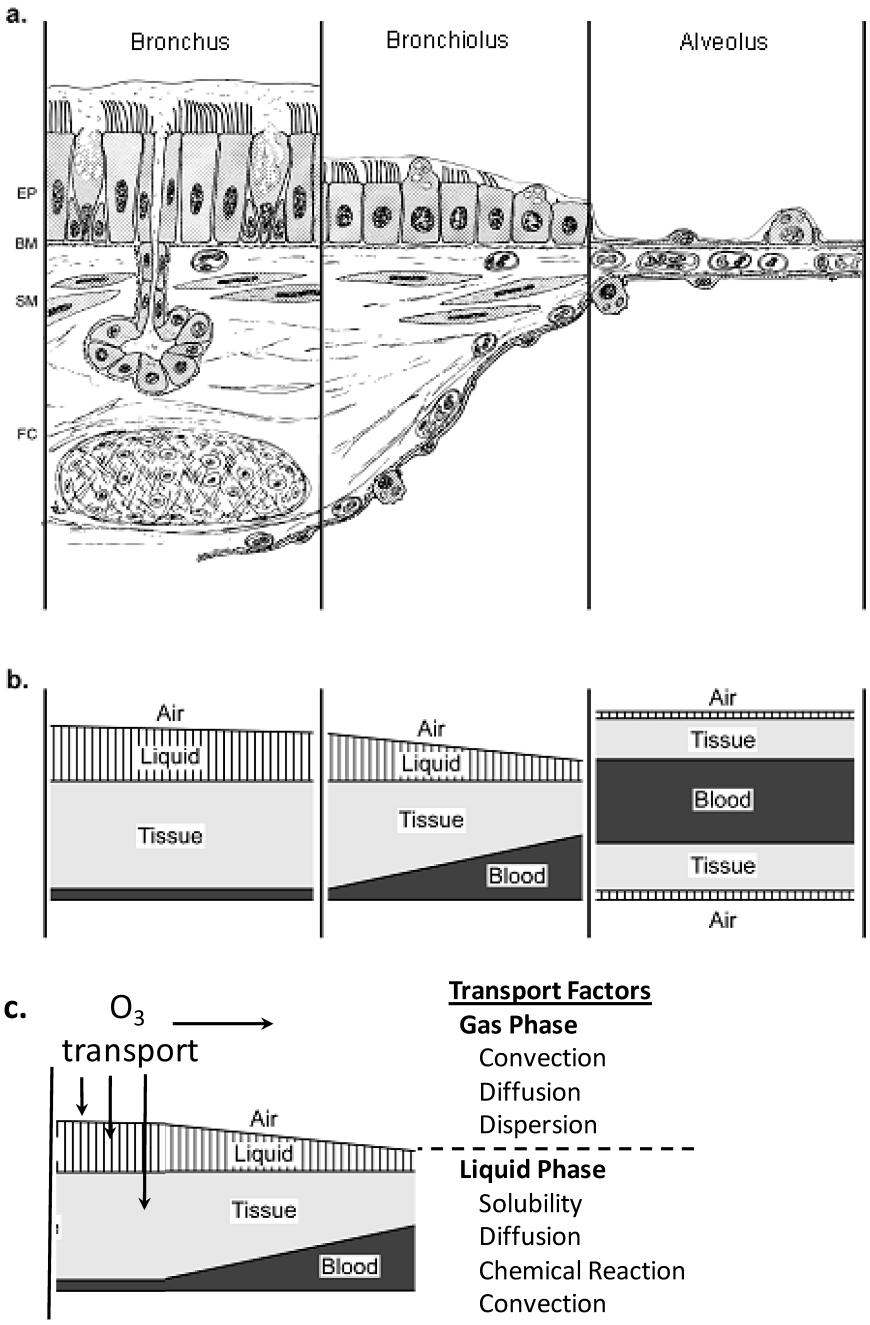

Figure A.3: Illustration of the LRT structure with progression from the larger airways to the alveolus. (a) Illustrates basic airway anatomy. Structures are epithelial cells, EP; basement membrane, BM; smooth muscle cells, SM; and fibrocartilaginous coat, FC. (b) Illustrates the relative amounts of liquid, tissue, and blood with distal progression. In the bronchi there is a thick surface lining over a relatively thick layer of tissues. With distal progress, the lining diminishes allowing increased access of compounds crossing the air-liquid interface to the tissues and the blood. (c) Presents the factors acting in the gas and liquid phases of ozone transport. [5]

Appendix B

Adverse Outcome Pathways (AOP) for ozone and PM

This section contains the details of AOP for ozone and PM in each physiological system included in this thesis

B.1 AOP for ozone

B.1.1 Ozone and skin health outcomes

- Molecular initiating events

  In vivo animal and human studies have demonstrated that ozone does not exert direct effects on viable skin cells but reacts with molecules in the stratum corneum characterized by antioxidants depletion and lipid peroxidation [237]. Thiele *et al.* exposed hairless mice to various concentrations of ozone (from 0 ppm to 10 ppm) for 2 h [238]. They also exposed some mice to either 0 ppm or 1 ppm of ozone for six consecutive days. After exposure to increasing ozone doses, the depletion of antioxidants and formation of lipid peroxidation products both increased in a dose-depend manner. Repeated low-level ozone exposure resulted in cumulative oxidative effects in the stratum corneum. He *et al.* conducted *in*

vivo ozone exposure on female Caucasian volunteers aged 18-55 years [239]. 2 h of ozone exposure at 0.8 ppm caused a 70% decrease in vitamin E (antioxidant) levels and a 230% increase in lipid hydroperoxide levels. Thus, ozone reactions with surface lipids and subsequent formation of reactive oxygen species (ROS) comprise the molecular initiating events.

- Cellular/Extracellular level responses

  Ozone not only exerts direct effects at the stratum corneum, but also has indirect effects in the deeper functional layers of the skin [240] and causes various responses at cellular level.

  - Ozone reactions at the stratum corneum alter components in the extracellular lipid matrix which serves as the continuous phase of the skin barrier [241].
  - Afaq *et al.* exposed cultured normal human epidermal keratinocytes (NHEKs) to 0.3 ppm of ozone for 20 min [159]. In their study, the activation of aryl hydrocarbon receptor (AhR) was observed. Furthermore, cytochrome P450 family 1 (CYP1) isoforms were induced through the activation of AhR.
  - Valacchi *et al.* exposed hairless mice to 0.8 ppm ozone 6 h/day for six consecutive days and observed the activation of NFκB pathway [242].
  - Valacchi *et al.* exposed SKH-1 hairless mice to 8 ppm ozone for 2 h [243]. In addition to antioxidant depletion in stratum corneum, they observed significant upregulation of heat shock protein 27 (HSP 27), HSP 70 and HSP 32. In a similar study conducted by the same group, they observed increased levels of proliferating cell nuclear antigen (PCNA) and keratin 10 (K10) in hairless mice after exposure to 0.8 ppm of ozone [242].

  - Valacchi *et al.* also demonstrated that after exposing SKH-1 hairless mice to 0.8 ppm ozone for 6 h, expressions of matrix metalloproteinase-9 (MMP-9) was significantly upregulated [244].

- Tissue level responses

  Cellular responses may lead to corresponding tissue level responses.

  - Skin barrier function is highly associated with the integrity of epidermal lipids in the lipid matrix of the stratum corneum. Therefore, damaged skin barrier function directly results from lipid depletion in stratum corneum due to ozone exposure.
  - AhR is known to mediate most of the toxic and carcinogenic effects of various contaminants [245]. Therefore, the activation of AhR at cellular level due to ozone exposure will alter the metabolism of xenobiotics and endogenous compounds in human skin.
  - The NFκB pathway plays a critical role in the expression of numerous pro-inflammatory responses, thus the activation of NFκB after ozone exposure will result in skin inflammation at tissue level.
  - HSPs and PCNA are involved in cell proliferation [240]. K10 is produced in well differentiated, suprabasal keratinocytes and is involved in keratinocyte differentiation [151]. Therefore, ozone induced changes of HSPs, PCNA and K10 may lead to abnormal skin cell proliferation and differentiation.
  - MMPs are a group of endopeptidases capable of degrading skin extracellular matrix components [246]. Thus, the upregulation of MMP-9 after ozone exposure could result in enhanced degradation of collagen leading to a loss of skin's ability to resist stretching.

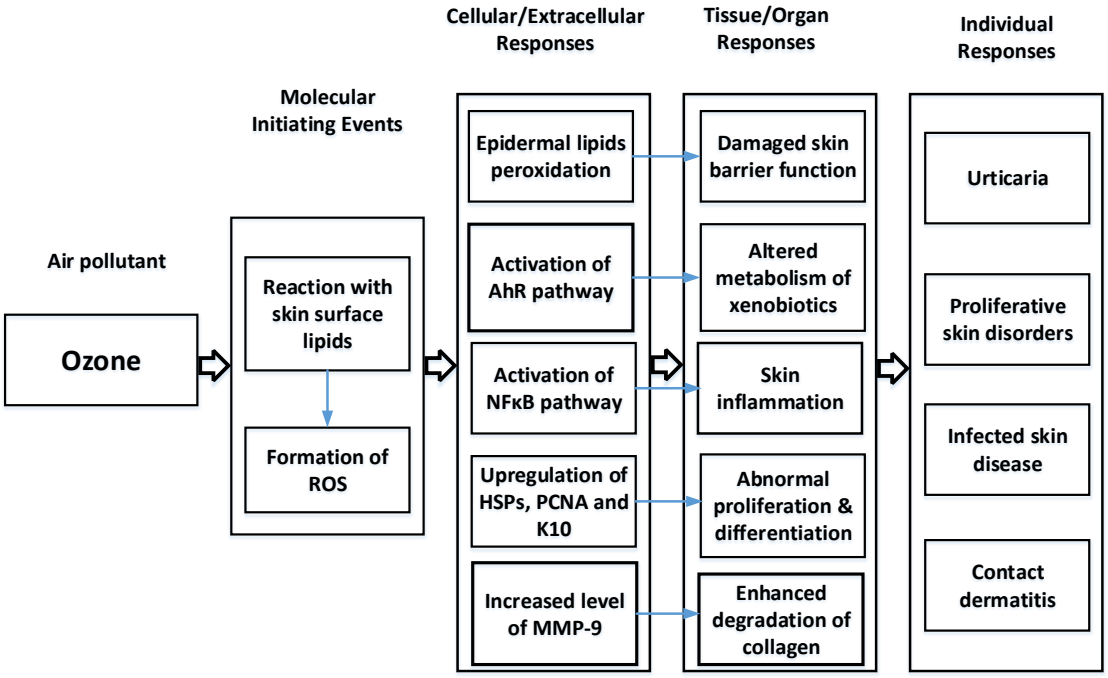

Figure B.1: Adverse Outcome Pathways for ozone and skin outcomes (ROS: reactive oxygen species; HSP: heat shock protein; PCNA: proliferating cell nuclear antigen; K10: keratin 10; AhR: aryl hydrocarbon receptor; MMP-9: matrix metalloproteinase-9)

B.1.2 Ozone and respiratory health outcomes

- Molecular initiating events

  Inhalation of ozone leads to reactions with components of lung lining fluid including depletion of antioxidants [247] and formation of many ROS such as ozonized lipids, lipid peroxidation products, etc. [248]. These molecular interactions comprise the molecular initiating events in the AOP.

- Cellular/Extracellular level responses

  At the cellular response level, the ozone induced ROS can trigger activation of neural reflexes by stimulating bronchial C-fibers [249]. These ROS may also promote injury or apoptosis of airway epithelial cells leading to increased airway epithelial permeability [250]. In addition, ROS can activate macrophages and

other immune cells to release multiple inflammatory mediators [51, 251]. The ROS-induced redox reactions may generate hyaluronan fragments or other products that stimulate TLR signaling in airway epithelial cells and inflammatory cells [11]. Furthermore, products of redox reactions can change the pulmonary surfactant profile by reacting with surfactant phospholipids and surfactant proteins [47].

- Tissue/Organ level responses

  Cellular level responses may lead to tissue/organ level responses. The activation of neural reflexes and the release of inflammatory mediators may cause airway smooth muscle sensitization. The upregulation of inflammatory mediators can cause acute airway inflammation. The activation of TLR signaling pathways will enhance immune responses to allergens and endotoxin. Recurrent epithelial injury and subsequent increased epithelial permeability will promote persistent airway inflammation and remodeling. Alterations in the pulmonary surfactant profile may cause abnormal changes of alveolar surface tension leading to impaired lung function.

B.1.3 Ozone and cardiovascular health outcomes

- Molecular initiating events

  Upon inhalation, ozone reacts with lung lining fluids components to form ROS leading to oxidative stress and initiation of pulmonary inflammation. Those oxidative and pro-inflammatory mediators then enter the circulation system. All these molecular interactions comprise molecular initiating events.

- Cellular/Extracellular level responses

  At the cellular level, bioavailability of vascular NO is reduced [13] and blood levels of pro-inflammatory cytokines are increased [252]. Pulmonary afferents are

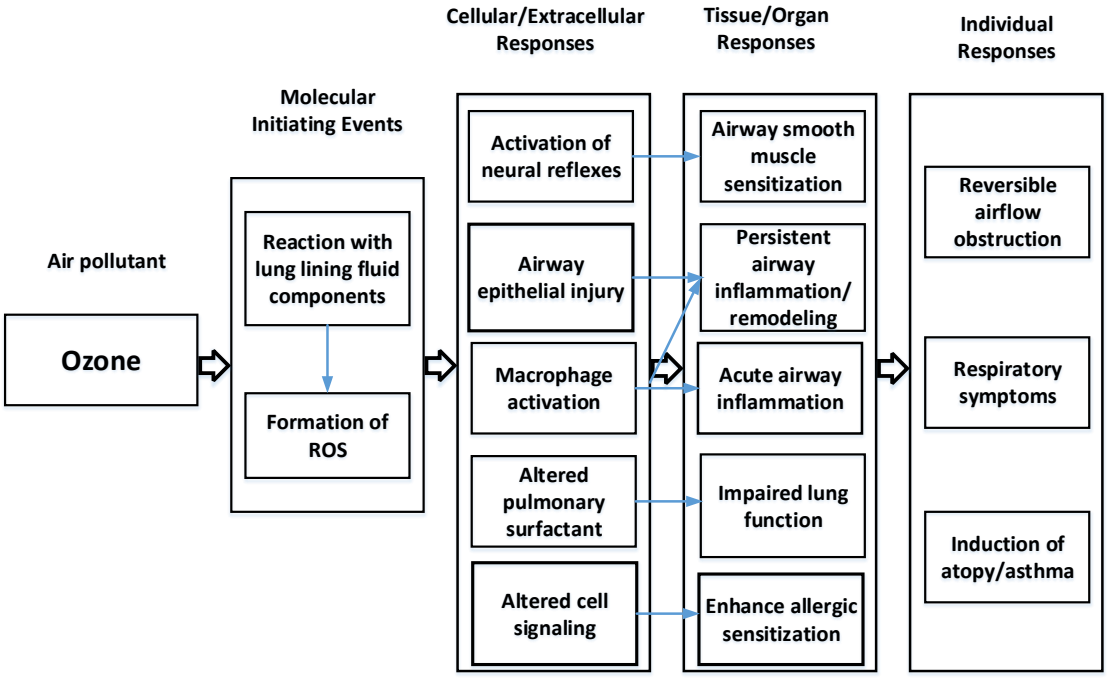

Figure B.2: Adverse Outcome Pathways for ozone and respiratory outcomes

activated after ozone inhalation [253]. The increased levels of pro-inflammatory cytokines may stimulate the secretion of stress hormones [254].

- Tissue/Organ level responses

  Cellular level responses may lead to tissue/organ level responses. Loss of vascular NO bioavailability may lead to abnormal vascular tone, endothelium dysfunction and platelet aggregation. Activation of pulmonary afferents and stress hormone secretions induced by increased pro-inflammatory cytokines can cause autonomic imbalance. Norepinephrine released from sympathetic nerves and circulating norepinephrine released from the adrenal medulla binds to $\alpha 1$ adrenergic receptors and induces vasoconstriction [255].

- Individual responses

  Finally, clinical consequences, such as altered blood pressure, myocardial ischemia, altered HRV and myocardial infarction, may result from those tissue/or-

gan level responses.

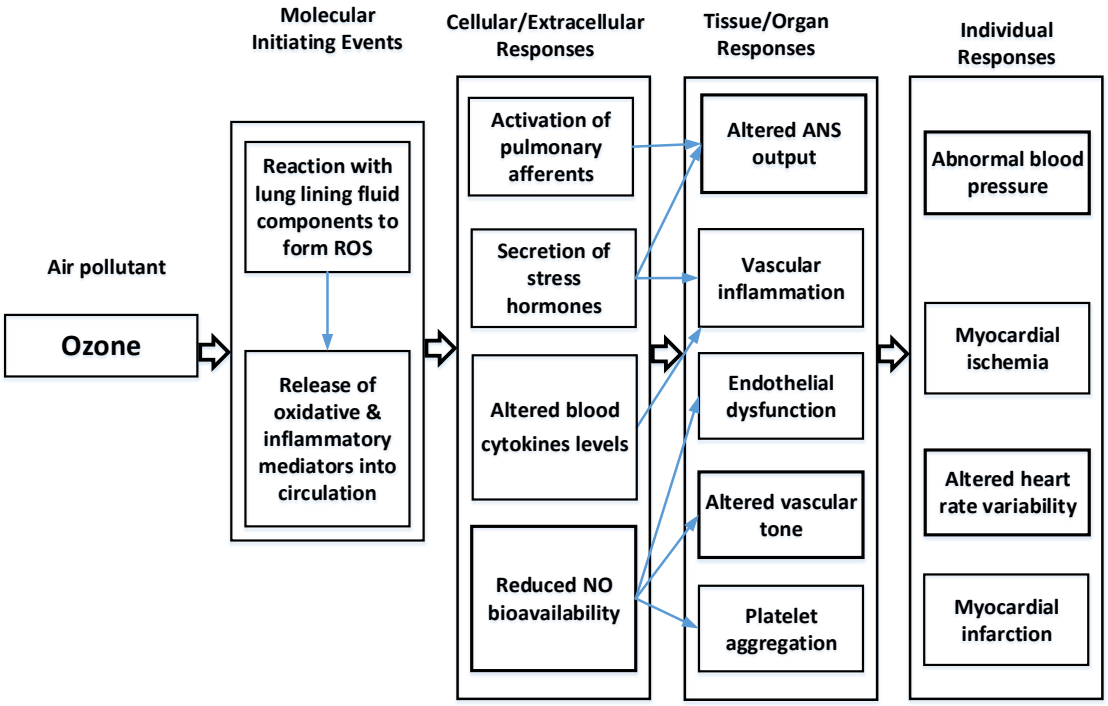

Figure B.3: Adverse Outcome Pathways for ozone and cardiovascular outcomes

B.2 AOP for particulate matter

B.2.1 PM and respiratory health outcomes

- Molecular initiating events

  Inhaled PM may be a direct source of ROS due to the redox active surface components, such as metals and organic species, and the surface characteristics of crystal structures; PM may also act as an indirect source of ROS by stimulating cells to produce ROS [256, 257]. In addition, exogenous or endogenous surface components carried by PM may directly interact with respiratory cells initiating a series of events without involving ROS [258, 259]. All these interactions comprise the molecular initiating events in the AOP.

- Cellular/Extracellular level responses

  At the cellular level, cell signaling pathways, such as the NFκB and AhR pathways, are activated in immune cells either by the PM-induced ROS or PM surface components [259, 260]. Pro- and anti-inflammatory mediators are released by different immune cells and may recruit more immune cells leading to pulmonary inflammation. Airway epithelial cells can be damaged by inflammation as well as by the direct contact with PM, resulting in increased epithelial permeability. Fine PM can also alter the pulmonary surfactant profile.

- Tissue/Organ level responses

  Cellular level responses lead to tissue/organ level responses. The activation of cell signaling pathways and the release of inflammatory mediators contribute to the pulmonary inflammation induced by PM. Interactions between PM and immune cells mediate the cytotoxicity of macrophages, which may affect pathogen clearance and cause impaired lung defense mechanisms [261]. Increased epithelial permeability caused by epithelial injury leads to impaired respiratory barrier function. The PM induced secretion of IL-4, IL-5, IL-13 and the alternative macrophage activation are associated with allergic disorders [138]. Alteration of the pulmonary surfactant profile can cause changes of alveolar surface tension and impaired lung function.

B.2.2 PM and cardiovascular health outcomes

- Molecular initiating events

  Inhalation of PM causes excessive oxidative stress and subsequent inflammation in pulmonary system. Those mediators of oxidative stress and inflammation (e.g. cytokines and activated immune cells) can then enter the circulation system. In addition, inhaled fine and ultrafine particles can also migrate from

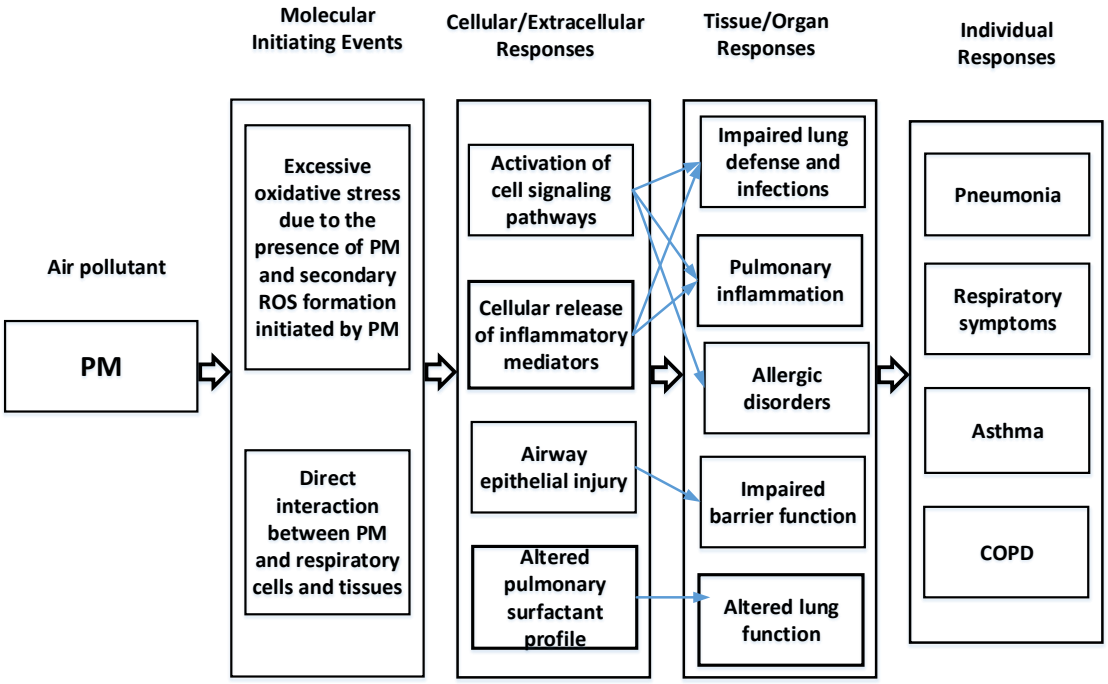

Figure B.4: Adverse Outcome Pathways for PM and respiratory outcomes

the respiratory system into the circulation system or get access to the central nervous system (CNS) through the olfactory bulb [232]. These molecular interactions and translocations of PM comprise molecular initiating events.

- Cellular/Extracellular level responses

  At the cellular level, vascular nitric oxide (NO) bioavailability is reduced via multiple pathways, including decreased eNOS protein levels, decreased eNOS substrate levels, decreased eNOS activation and destruction of NO by superoxide anion [11]. Pulmonary afferents can be activated by secondary ROS or PM itself [262]. PM in the circulation and those deposited in the olfactory bulb may enter CNS and directly exert their effects. These inflammation mediators, released from the pulmonary system, may activate immune cells to secrete more inflammatory cytokines and stimulate the secretion of stress hormones [254]. Furthermore, PM in blood vessels can directly affect endothelial integrity [263].

- Tissue/Organ level responses

  Cellular level responses may lead to tissue/organ level responses. Reduced NO bioavailability and impaired endothelial integrity lead to altered vascular tone and endothelium dysfunction causing abnormal vasoconstriction and platelet aggregation. Activation of pulmonary afferents, direct interaction with CNS and the secretion of stress hormones can cause autonomic dysfunction leading to imbalance of sympathetic and parasympathetic activities. Changes in peripheral vascular resistance—mediated by neurohormonal activation or local metabolic factors such as nitric oxide (NO)—are important for acute blood pressure regulation. In the peripheral circulation, norepinephrine released from sympathetic nerves and circulating nor-epinephrine released from the adrenal medulla binds to $\alpha 1$ adrenergic receptors and induces vasoconstriction [255].

- Individual responses

  Eventually, tissue/organ responses result in physiological consequences that can be measured clinically, including increased blood pressure, myocardial ischemia, altered heart rate variability (HRV), and myocardial infarction, etc.

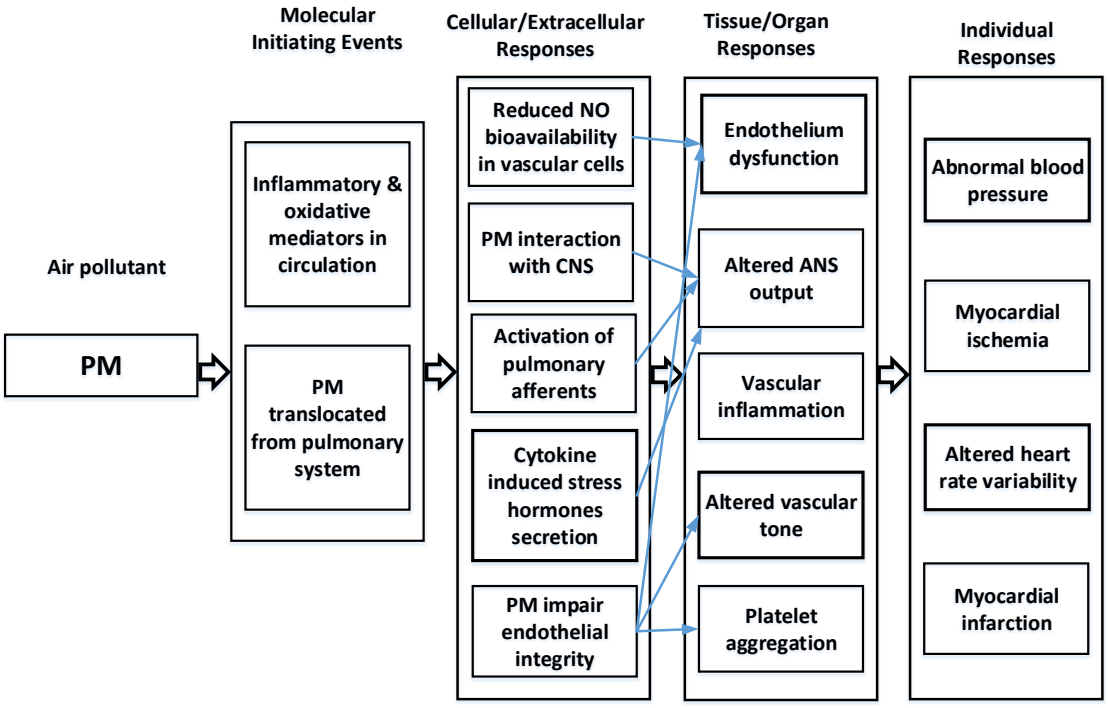

Figure B.5: Adverse Outcome Pathways for PM and cardiovascular outcomes

Appendix C

Matlab codes for ozone / lung function model

This section contains guidelines for executing the ozone / lung function models implemented in Matlab. The model first simulates the toxicodynamics of ozone in the alveolar region and then uses a lung mechanics module to the link toxicodynamics biomarkers to measurable pulmonary biomarkers that characterize lung functions. (The model was implemented in Matlab R2018b).

C.1 Matlab codes structure

Matlab code files are classified into two modules: the toxicodynamics module and the lung mechanics module. The toxicodynamics module simulates the dynamics of the lining fluids and cells in the alveolar region as well as their interactions with ozone. Since ozone is known for invoking excessive oxidative stress and inflammation, the immune responses were added to the toxicodynamics module. The relations among different Matlab code files are illustrated in Figure C.1. 'O3_mice_run.m' is the master script that runs the entire model. The toxicodynamics module consists of four Matlab function files: 'O3_TD_withInfla_case_study.m', 'O3_TD_withInfla_driver.m', 'O3_mice_deriv_withInfla.m' and 'O3_mice_config.m'. The lung mechanics module

is made of the following Matlab function files: 'alv_config_O3.m', 'alv_mech_O3.m', 'PV_O3.m' which calls 'openclose.m', 'time2freq.m', 'O3_Cons_fit.m' and 'CPM.m'.

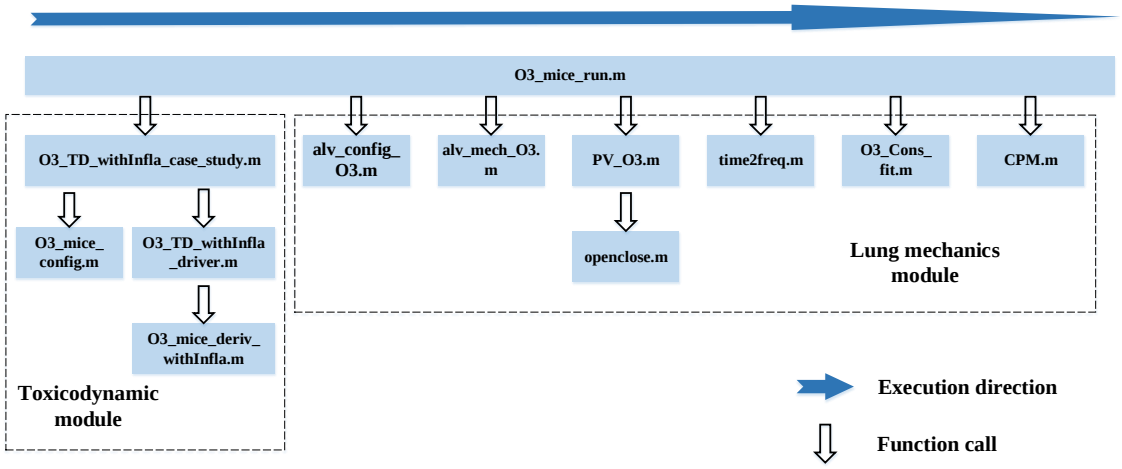

Figure C.1: The structure of Matlab code files for the lung function model upon ozone exposure

C.2 Matlab codes summaries

O3_mice_run.m

'O3_mice_run.m' is the master script that runs all necessary files for the entire model. It outputs simulated toxicodynamics, pulmonary and inflammatory biomarkers.

O3_TD_withInfla_case_study.m

'O3_TD_withInfla_case_study.m' is the function that runs the toxicodynamics module. It defines ozone inhalation scenarios for mice and calls 'O3_TD_withInfla_driver.m'. Inputs for this function are necessary parameter values obtained from 'O3_mice_config.m'. Outputs for this function are toxicodynamics biomarkers that will be used by the lung mechanics module.

O3_TD_withInfla_driver.m

'O3_TD_withInfla_driver.m' is a function within the toxicodynamics module. It tells Matlab how to solve the differential equations for our model (e.g. solver type, time span, etc.), checks mass balance of the model and calls 'O3_mice_deriv_withInfla.m'. Inputs for this function are information of ozone inhalation scenarios, necessary model parameter values and initial amounts of compounds considered in the toxicodynamics module. The major outputs of this function are time profiles of compounds in the model.

O3_mice_deriv_withInfla.m

'O3_mice_deriv_withInfla.m' is a function within the toxicodynamics module. This function contains all the ordinary differential equations (ode) for the toxicodynamics module. Particularly, equations that describe the immune responses initiated by ozone exposure are included in this file. Inputs of this function are time span for the selected ode solver, initial amounts of all compounds and necessary model parameters. The output of this function is a set of ordinary differential equations in a format that meets the requirement of Matlab ode solvers.

O3_mice_config.m

'O3_mice_config.m' stores all parameters required by the toxicodynamics module for ozone exposure to mice.

alv_config_O3.m

'alv_config_O3.m' is a function that defines the parameters used in the lung mechanics module. It has three input arguments: choice of species, positive end expiratory pressure (PEEP) and pressure amplitude. The output of this function is a set of

parameter values which will be used to simulate alveolar recruitment and decruitment.

alv_mech_O3.m

'alv_mech_O3.m' estimates alveolar mechanical parameters. The inputs for this function are physiological parameters obtained from 'O3_mice_config.m', alveolar parameters from 'alv_config_O3.m' and outputs from the toxicodynamics module. The main outputs of this function are the parameters that controls opening pressure and opening rate of alveoli in the lung mechanics module.

PV_O3.m

'PV_O3.m' is a function within the lung mechanics module. The inputs of this function are alveolar parameters from 'alv_config_O3.m' and alveolar mechanical parameters from 'alv_mech.m'. It loads two mat files (Primewave timeseries and Primewave frequencies) which replicate the mechanical oscillator used for the artificial breathing in mice. PV_O3.m also calls 'openclose.m' which models the sequential opening and closing of individual alveolar unit. Based on all these, PV_O3.m then calculates time series of pressure, volume, open-close status and fractional recruitment of alveoli (i.e. fraction of alveolar units that are open).

openclose.m

'openclose.m' is a function that decides the open/close status of alveoli. It is called by 'PV_O3.m' and its output is a set of binary numbers (0 or 1) corresponding to the closed or open status of alveoli.

time2freq.m.m

'time2freq.m' is a tool to convert time domain data to frequency domain data using Fast-Fourier transform algorithm. In this lung mechanics module, time series results from 'PV_O3.m' are converted to frequency domain via 'time2freq.m'.

O3_Cons_fit.m

'O3_Cons_fit.m' is a function within the lung mechanics module. It fits the frequency domain results to Constant Phase Model. Inputs of this function are frequency domain lung impedance and corresponding frequencies. Outputs of this function are airway resistance, tissue resistance, tissue elastance and tissue inertance.

CPM.m

'CPM.m' is a function that calculates the real and imaginary parts of pulmonary impedance using Constant Phase Model

C.3 Detailed Matlab code

O3_mice_run.m

```
clear
rng(1);

%% ************   User-defined parameters   ************************
%% ************** Species selection *******************************
species = 1; % Mouse = 1, SD rat = 2, BN rat = 3, Human = 4
%% **************  Breathing properties   ...
    *****************************
```

```
8  PEEP = 9; % Postive End-Expiratory Pressure (cmH2O)
9  Pamp = 30; % Breathing pressure amplitude (cmH2O)
10
11 %% running simulation of toxicodynamic model to get results
12  c = O3_mice_config; % we only model mouse(Gow's data is mice data)
13
14  %% Assign inflammation parameters
15
16  TTT = load('Initial_X_Hill_66_PAadded.mat');
17  x = TTT.X;
18 % NFkB related
19
20 c.R_NFkB = x(1);
21 c.x_NFkB_Nrf2 = x(2);
22 c.deg_NFkB = x(3);
23
24 % Nrf2 related
25 c.R_Nrf2 = x(4);
26 c.x_Nrf2_NFkB = x(5);
27 c.deg_Nrf2 = x(6);
28
29 % AO related
30 c.R_AO = x(7);
31 c.deg_AO = x(8);
32
33 % P A related
34 c.R_P = x(9);
35 c.x_P_NFkB = x(10);
36 c.n_P_NFkB = x(11);
37 c.x_P_A = x(12);
38 c.x_P_SPD = x(13);
39 c.deg_P = x(14);
40
```

```
41 % A related
42 c.R_A = x(15);
43 c.x_A_AO = x(16);
44 c.n_A_AO = x(17);
45 c.deg_A = x(18);
46
47 % ROS related
48 c.R_ROS = x(19);
49 c.x_ROS_AO = x(20);
50 c.deg_ROS = x(21);
51
52 % P effect on A
53 c.x_A_P = x(22);
54 c.n_A_P = x(23);
55 %%
56 CID = c.ChemID;
57 ID = c.IDNum;
58 res = O3_TD_withInfla_case_study(c); % Results of the ToxD model
59
60 %% ****************** Get BAF endpoints when lung function is ...
       measured ***************
61
62 t =  (240+72)* 60; % min, Timepoint of biomarker 72 hours after ...
       3h O3 exposure
63 t_crl = 240*60; % Timepoint of control is 0,corresponding to the ...
       first item in the result matrix
64
65 %% Total PL
66 % Ratio of total PL at endpoint over control (at 72 hrs)
67
68 PL_end = res.amounts(t, ID.AF + (CID.PL-1).*c.N_Comp) +...
69              res.amounts(t, ID.Int + (CID.PL-1).*c.N_Comp) + ...
70                 res.amounts(t, ID.LB + (CID.PL-1).*c.N_Comp);
```

```
71
72 PL_con = res.amounts(t_crl, ID.AF + (CID.PL-1).*c.N_Comp) +...
73              res.amounts(t_crl, ID.Int + (CID.PL-1).*c.N_Comp) + ...
74                 res.amounts(t_crl, ID.LB + (CID.PL-1).*c.N_Comp);
75 PL = PL_end/PL_con;
76
77
78
79 %% Total SA
80 % Ratio of total SA at endpoint over control (at 72 hrs)
81 SA_end = res.amounts(t, ID.AF + (CID.SA-1).*c.N_Comp) +...
82              res.amounts(t, ID.Int + (CID.SA-1).*c.N_Comp) + ...
83                 res.amounts(t, ID.LB + (CID.SA-1).*c.N_Comp);
84
85 SA_con = res.amounts(t_crl, ID.AF + (CID.SA-1).*c.N_Comp) +...
86              res.amounts(t_crl, ID.Int + (CID.SA-1).*c.N_Comp) + ...
87                 res.amounts(t_crl, ID.LB + (CID.SA-1).*c.N_Comp);
88
89 SA = SA_end/SA_con;
90
91 %
92
93 %% ******************  Alveolar Model  ...
       *********************************
94 c_alv = alv_config_O3(species,PEEP,Pamp); % Get param values for ...
       alveolar model
95
96 [mu_Po, ...
       beta_So,gamma_PL_ratio,gamma_SA_ratio,gamma_ratio,eta_ratio] = ...
       alv_mech_O3(c, c_alv, PL, SA,PL_con,SA_con); % Getting ...
       mechanical params
97
98 res_alv = PV_O3(c_alv, mu_Po, beta_So);    % Alveolar model results
```

```
99
100 res.sv.Nfr = res_alv.Nfr;       % Fractional recruitment of alveoli
101 res.sv.Pf = res_alv.Pf;       % Pressure (cmH2O) values in breathing
102 res.sv.tf = res_alv.tf;       % Time points of breathing
103 res.sv.Vt = res_alv.Vt;       % Vol. values (mL) in breathing
104
105 %% ************** Fourier Transform *****************
106 % This section converts predicted temporal pressure-volume data
107 % to CPM parameters G & H
108 freq = res_alv.freq;           % Primewave frequencies
109 prime_time = res_alv.prime_t;  % Primewave time points
110 N_prime = length(prime_time);  % No. of prime timepoints
111 Pw = time2freq(res.sv.Pf(end-N_prime+1:end),freq,0);  % Freq. ...
       domain pressure
112 Vw = time2freq(res.sv.Vt(end-N_prime+1:end),freq,0);  % Freq. ...
       domain volume
113 Zw = Pw ./ (1i .* (2*pi.*freq) .* Vw);      % Freq. domain impedance
114 params = O3_Cons_fit(Zw, freq);              % Estimating CPM ...
       parameters
115 res.sv.G = params(3); res.sv.H = params(4);
116 % [ZR,ZI] = CPM(params, freq);
117
118 %% incorporate P effect into H
119
120 P = res.amounts(:, ID.Cell + (CID.P-1).*c.N_Comp);
121 P_end = P(t); % P value at the time point of interested, end is ...
       72h after exposure
122 load ('h_all.mat');
123 Damage = (P_end-1)^h(2)./(h(1)+(P_end-1)^h(2));
124 H = res.sv.H*(1+Damage);
125 PARA = params;
126 PARA(4) = H;
127 [ZR,ZI] = CPM(PARA, freq);
```

O3_TD_withInfla_case_study.m

```
1  function res = O3_TD_withInfla_case_study(config)
2
3  global T_Infla
4
5  T_Infla = 240*60;
6
7
8  c = config;
9  CID = c.ChemID;
10 ID = c.IDNum;
11
12 %%%%%%%%%%%%%%%%% User-defined initial amounts  %%%%%%%%%%%%%%%%
13 amount_initial = c.amount_init;
14
15 % events.timestages = [0 240 243 267 291 1000].* 60;  % Time (in ...
       mins), add 10 days for the model to reach steady state before ...
       O3 exposure
16
17 events.timestages = [0 240 243 246 252 264 288 312].* 60;  % 3 ...
       hour O3 exposure
18
19 %  events.timestages = [0 2 6 12 24 48 72].* 60;  % for Kierstein ...
       2006, 2 hour O3 exposure
20
21 events.timeincrements = ones(1,length(events.timestages)-1); % ...
       output increments
22
```

```
%% ********** Inhalation scenarios ************************
events.rate_inhale.O3 = c.L.Resp_rate .* ...
    ones(1,length(events.timeincrements)); % L/min
events.air_concs.O3 = zeros(1,length(events.timeincrements));

Dose = 0.036 ; % umol/L (0.8 ppm),O3 conc used in Groves paper


 events.air_concs.O3 = [0 Dose 0 0 0 0 0]; % micro.g/L

res = O3_TD_withInfla_driver(c, events, amount_initial); % ...
    consider ozone reacts with AF

end
```

O3_TD_withInfla_driver.m

```
function simout = O3_TD_withInfla_driver(config, events, ...
    amount_initial)

global E


c = config;
ID = c.IDNum;
CID = c.ChemID;

if nargin ≥ 3
    amount = amount_initial;
    amount(ID.Intake,:) = sum(amount(1:end-1,:),1);
else
```

```
14      amount = zeros(c.N_Comp, c.N_Chem);
15  end
16
17  nstages = length(events.timestages)-1;
18
19
20  saved_amounts = [];
21  saved_times = [];
22  saved_mass_balances = [];
23  saved_sv = [];
24  saved_percents = [];
25
26  % odeset('RelTol', 1e-8, 'AbsTol', 1e-12, 'MaxOrder', 5, 'BDF', ...
        'on');
27  odeset('RelTol', 1e-6, 'AbsTol', 1e-8, 'MaxOrder', 5, 'BDF', 'on');
28  for istage=1:nstages % run simulation segments ...
        0-3,3-27,27-51,51-75 h
29    stage_beg = events.timestages(istage);
30    stage_end = events.timestages(istage+1);
31    tspan = stage_beg:events.timeincrements(istage):stage_end;
32    E = local_get_event(events, istage); % get exposure scenaios
33    amount(ID.Intake,CID.O3)=amount(ID.Intake,CID.O3)+c.K.pulmonary.* ...
          E.C.Inh * E.Q.Inh;
34
35     [cur_time_new, amount_new] = ...
           ode15s(@O3_mice_deriv_withInfla,tspan,amount,[],c);
36
37    saved_amounts = [saved_amounts(1:end-1,:); amount_new];
38    saved_times = [saved_times(1:end-1); cur_time_new];
39    amount = amount_new(end,:)';  % Set the state for the next stage
40    amount = reshape(amount, c.N_Comp, c.N_Chem);
41  end
42
```

```
43 simout.amounts = saved_amounts; % amounts in compartments
44 simout.times = saved_times; % times at which model outputs are saved
45 simout.TD_config = c;
46 simout.event_config = events;
47
48 function thisevent = local_get_event(events, istage)
49 thisevent.Q.t = istage;
50 thisevent.Q.Inh = events.rate_inhale.O3(istage);
51 thisevent.C.Inh = events.air_concs.O3(istage);
52 end
53
54 end
```

O3_mice_deriv_withInfla.m

```
1 function [d_amount, optSV] = O3_mice_deriv_withInfla(t, amount, c)
2 % Derivative function defined in a manner the ODE solver in ...
     Matlab expects.
3 % Inputs:
4 %   t -- current time of the simulation (time variable in the ODE ...
     system)
5 %   amount -- amount of chemical in each tissue (state variables)
6 % Outputs: d_amount -- derivatives
7 %   optSV -- optional state variables such as intermediate conC_s
8
9 global E
10
11
12 global T_Infla
13
14 if t > T_Infla
```

```
15      boolean = 1;
16  else
17      boolean = 0;
18  end
19
20
21
22
23  ID = c.IDNum;    % Compartment IDs by name
24  CID = c.ChemID; % Chemical IDs
25
26  amount = reshape(amount, c.N_Comp, c.N_Chem); %
27
28  c.V = repmat(c.V, 1, c.N_Chem);         % repmat: copy Volume ...
        vector into a 1 by 4 matrix
29  conc = amount ./ c.V;                   % Concentrations in all ...
        compartments
30
31  d_amount = zeros(c.N_Comp,c.N_Chem); % set up a matrix for d_amount
32
33  %% ************ Inhalation dosimetry *********************
34  % Inhalation dosimetry of ozone
35  inhale_dose = c.K.pulmonary.* E.C.Inh * E.Q.Inh; % Actual ...
        inhalation dose into pulmonary alveolar region
36
37  %% ************ Surfactant dynamics***********************
38  %% Surfactant regulation
39  PL_Re = c.K.Re(CID.PL) .* (1 + c.K.PL.Re_C .* amount(ID.AF,CID.C) ...
        ./ c.V(ID.AF)); % effect of C on PL recycle,eqn 4.8 in DP thesis
40
41  LB_effect = c.K.LB_C .* amount(ID.AF,CID.C) ./ c.V(ID.AF); % ...
        Effect of C on LB
42  K_LB = c.K.LB .* (1 - min(1,LB_effect)); % eqn 4.8 in DP thesis
```

```
43
44 PL_Ad = c.K.Ads(CID.PL) .* (1 + c.K.Ads_SA .* amount(ID.AF, ...
       CID.SA) ./ c.V(ID.AF)...
45                     + c.K.Ads_C .* amount(ID.AF, CID.C) ./ ...
                           c.V(ID.AF)); % effect of SA and C on PL ...
                           adsorption,eqn 4.6 in DP thesis
46
47 % Rate of generation (R_Gen,i in eqn 4.1 DP thesis) of surfactant
48 % components (R_Gen = steady state amount - amount, see page 90 ...
       DP thesis)
49 PL_Gen = 1 * (c.L.AT2pool(CID.PL) * c.L.Mass - amount(ID.AT2, ...
       CID.PL));
50 SA_Gen = 1 * (c.L.AT2pool(CID.SA) * c.L.Mass - amount(ID.AT2, ...
       CID.SA));
51 C_Gen = 1 * (c.L.AT2pool(CID.C) * c.L.Mass - amount(ID.AT2, CID.C));
52
53 % Rate of secretion of surfactant components into lamellar body(LB)
54 PL_Sec = c.K.Sec(CID.PL) .* amount(ID.AT2, CID.PL);
55 SA_Sec = c.K.Sec(CID.SA) * amount(ID.AT2, CID.SA);
56 C_Sec = c.K.Sec(CID.C) * amount(ID.AT2, CID.C);
57 C_DSec = c.K.DSec .* amount(ID.AT2, CID.C); % secretion of ...
       collectin (SP-A&D) into alveolar fluids(AF) independent of LB
58
59 %% Rate of exocytosis of surfactant components (from LB to AF)
60 PL_Exo = K_LB .* amount(ID.LB,CID.PL);
61 SA_Exo = K_LB .* amount(ID.LB,CID.SA);
62 C_Exo = K_LB .* amount(ID.LB,CID.C);
63
64 %% Rate of recycle of surfactant components from AF
65 PL_Rec = PL_Re .* amount(ID.AF,CID.PL);
66 SA_Rec = c.K.Re(CID.SA) .* amount(ID.AF,CID.SA);
67 C_Rec = c.K.Re(CID.C) .* amount(ID.AF,CID.C);
68
```

```
69 %% Degradation of surfactant in AF
70 Deg_Loss_PL = c.K.Loss.Deg(CID.PL) .* max(0,amount(ID.AF,CID.PL));
71 Deg_Loss_SA = c.K.Loss.Deg(CID.SA) .* max(0,amount(ID.AF,CID.SA));
72 Deg_Loss_C = c.K.Loss.Deg(CID.C) .* max(0,amount(ID.AF,CID.C));
73
74 %% Loss to airway from Int
75 AW_Loss_PL = c.K.Loss.AW .* max(0,amount(ID.Int,CID.PL));
76 AW_Loss_SA = c.K.Loss.AW .* max(0,amount(ID.Int,CID.SA));
77 AW_Loss_C = c.K.Loss.AW .* max(0,amount(ID.Int,CID.C));
78
79 %% Mass balance of surfactant in Alveolar type 2(AT2) cells ...
       (Generation - Secretion + Recycle)
80
81 d_amount(ID.AT2,CID.PL) = PL_Rec - PL_Sec + PL_Gen;
82 d_amount(ID.AT2,CID.SA) = SA_Rec - SA_Sec + SA_Gen;
83 d_amount(ID.AT2,CID.C) = C_Rec - C_Sec - C_DSec + C_Gen;
84
85 %% Mass balance of surfactant in LB (Secretion - exocytosis)
86 d_amount(ID.LB,CID.PL)= PL_Sec - PL_Exo;
87 d_amount(ID.LB,CID.SA)= SA_Sec - SA_Exo;
88 d_amount(ID.LB,CID.C)= C_Sec - C_Exo;
89
90 %% Mass balance of surfactant in Alveolar fluids(AF)
91 d_amount(ID.AF,CID.PL) = PL_Exo - PL_Rec - Deg_Loss_PL - ...
       AW_Loss_PL-c.K.O3_PL.*(conc(ID.AF,CID.PL)).*amount(ID.AF,CID.O3);
92 d_amount(ID.AF,CID.SA) = SA_Exo - SA_Rec - Deg_Loss_SA - ...
       AW_Loss_SA-c.K.O3_SA.*(conc(ID.AF,CID.SA)).*amount(ID.AF,CID.O3);
93 d_amount(ID.AF,CID.C) = C_Exo - C_Rec - Deg_Loss_C - AW_Loss_C + ...
       C_DSec-c.K.O3_C.*(conc(ID.AF,CID.C)).*amount(ID.AF,CID.O3);
94 d_amount(ID.AF,CID.O3) = ...
       inhale_dose-c.K.O3_PL.*(conc(ID.AF,CID.PL)).*amount(ID.AF,CID.O3)...
95      -c.K.O3_SA.*(conc(ID.AF,CID.SA)).*amount(ID.AF,CID.O3)...
96      -c.K.O3_C.*(conc(ID.AF,CID.C)).*amount(ID.AF,CID.O3);
```

```
97
98
99  d_amount(ID.Intake,CID.O3) = inhale_dose;
100 %% Mass balance of surfactant in the Loss compartment  (Reaction ...
        with ozone + Airway Loss + Degradation in AF - Generation in AT2)
101 d_amount(ID.Loss,CID.PL)= ...
        c.K.O3_PL.*conc(ID.AF,CID.PL).*amount(ID.AF,CID.O3)+AW_Loss_PL ...
        + Deg_Loss_PL - PL_Gen;
102 d_amount(ID.Loss,CID.SA)= ...
        c.K.O3_SA.*conc(ID.AF,CID.SA).*amount(ID.AF,CID.O3)+AW_Loss_SA ...
        + Deg_Loss_SA - SA_Gen;
103 d_amount(ID.Loss,CID.C)= ...
        c.K.O3_C.*conc(ID.AF,CID.C).*amount(ID.AF,CID.O3)+AW_Loss_C + ...
        Deg_Loss_C - C_Gen;
104
105
106 %% Equations for the inflammatory module of the Hill version ...
        equations
107
108 % regulatory terms
109
110   Reg_NFkB_Nrf2 = ...
          c.x_NFkB_Nrf2./(c.x_NFkB_Nrf2+amount(ID.Cell,CID.Nrf2));
111   Reg_Nrf2_NFkB = ...
          c.x_Nrf2_NFkB./(c.x_Nrf2_NFkB+amount(ID.Cell,CID.NFkB));
112   Reg_P_NFkB = (amount(ID.Cell,CID.NFkB).^c.n_P_NFkB)./(c.x_P_NFkB...
113       +(amount(ID.Cell,CID.NFkB).^c.n_P_NFkB));
114   Reg_P_A = c.x_P_A./(c.x_P_A+amount(ID.Cell,CID.A));
115
116   Reg_P_SPD = (c.x_P_SPD ...
          ./(c.x_P_SPD+amount(ID.AF,CID.C)./0.0011))*1;
117
118   Reg_A_AO = (amount(ID.Cell,CID.AO).^c.n_A_AO)./(c.x_A_AO ...
```

```
119         +(amount(ID.Cell,CID.AO).^c.n_A_AO));
120     Reg_ROS_AO = c.x_ROS_AO./(c.x_ROS_AO+amount(ID.Cell,CID.AO));
121
122     Reg_A_P = ...
            (amount(ID.Cell,CID.P).^c.n_A_P)./(c.x_A_P+(amount(ID.Cell,CID.P).^c.n_A_P))
            % Add P effect on A
123
124     % NFkB related
125     d_amount(ID.Cell,CID.NFkB) = boolean*(...
126         c.R_NFkB.*amount(ID.Cell,CID.ROS).*(1+Reg_NFkB_Nrf2)-c.deg_NFkB ...
                .*amount(ID.Cell,CID.NFkB)...
127         ); % NFkB
128
129
130   %%%%%%%% % P,A,E related
131
132
133     d_amount(ID.Cell,CID.P)= boolean*(...
134         c.R_P.*(1.*Reg_P_NFkB.*Reg_P_A.*Reg_P_SPD)-...
135         c.deg_P.*amount(ID.Cell,CID.P)...
136         ); % P response
137
138
139
140 %     d_amount(ID.Cell,CID.P)= boolean*(...
141 %         ...
        c.R_P.*(1.*Reg_P_NFkB.*Reg_P_A)-c.deg_P.*amount(ID.Cell,CID.P)...
142 %         ); % P response, Remove SPD regulatory term
143
144     d_amount(ID.Cell,CID.A) = boolean*(...
145         c.R_A .*(1+Reg_A_AO)-c.deg_A.*amount(ID.Cell,CID.A)...
146         ); % A response,
147
```

```
148    d_amount(ID.Cell,CID.A) = boolean*(...
149        c.R_A .*(1+Reg_A_AO*Reg_A_P)-c.deg_A.*amount(ID.Cell,CID.A)...
150        ); % A response, Added P effect on A
151
152
153
154    % Nrf2 related
155    d_amount(ID.Cell,CID.Nrf2) =boolean*(...
156        c.R_Nrf2.*amount(ID.Cell,CID.ROS).*(1+Reg_Nrf2_NFkB)-c.deg_Nrf2 ...
               .*amount(ID.Cell,CID.Nrf2)...
157        ); % Nrf2
158
159    d_amount(ID.Cell,CID.AO) = boolean*(...
160        c.R_AO.*amount(ID.Cell,CID.Nrf2)-c.deg_AO.*amount(ID.Cell,CID.AO)...
161        ); % AO
162
163
164    d_amount(ID.Cell,CID.ROS) = boolean*(...
165        c.R_ROS.*amount(ID.AF,CID.O3).*(1+Reg_ROS_AO)-...
166        c.deg_ROS.*amount(ID.Cell,CID.ROS)+amount(ID.Cell,CID.P).*...
167        (amount(ID.Cell,CID.ROS).^2)./(1+(amount(ID.Cell,CID.ROS).^2)));%ROS
168
169
170
171
172  %% Reshape d_amount to a vector
173  d_amount = reshape(d_amount, size(d_amount,1) * size(d_amount,2), 1);
174  optSV.conc_s.tissue = 0; % All tissues
175
176  end
```

O3_mice_config.m

```
function c = O3_mice_config()
% provide default configuration values for the model of ozone induced
% changes in pulmonary surfactant

%% Compartments considered in ozone_surfactant model
c.IDNum.Int = 1;    c.CompName{1} = 'Int';   % Alveolar Interface
c.IDNum.AF  = 2;    c.CompName{2} = 'AF';    % Alveolar Fluid
c.IDNum.LB  = 3;    c.CompName{3} = 'LB';    % Lamellar Bodies
c.IDNum.AT2 = 4;    c.CompName{4} = 'AT2';   % Type II cells
c.IDNum.Mph = 5;    c.CompName{5} = 'Mph';   % Macrophage
c.IDNum.Loss  = 6;  c.CompName{6} = 'Loss';   % Net Loss of ...
    surfactant
c.IDNum.Intake= 7;  c.CompName{7} = 'Intake'; % Amount of intake ...
    in alveoli

%% Chemicals species considered in ozone_surfactant model
c.ChemID.O3 = 1;   c.ChemName{1} = 'O3';   % Ozone
c.ChemID.PL = 2;   c.ChemName{2} = 'PL';   % Phospholipids
c.ChemID.SA = 3;   c.ChemName{3} = 'SA';   % Surface-Active ...
    proteins(SP-B, SP-C)
c.ChemID.C  = 4;   c.ChemName{4} = 'C';    % Collectins (SP-A, SP-D)

%% Add a 'Cell' compartment and chemicals for the inflammation module
c.IDNum.Cell= 8;  c.CompName{8} = 'Cell'; % A general 'Cell' ...
    compartment in which inflammatory responses happen.
% chemicals involved in the inflammation module
% c.ChemID.IKK = 5;   c.ChemName{5} = 'IKK';   % IKK
c.ChemID.NFkB  = 5;   c.ChemName{6} = 'NFkB';    % NFkB
% c.ChemID.mIkBa  = 7;   c.ChemName{7} = 'mIkBa';    % mRNA of IkBa
% c.ChemID.IkBa  = 8;   c.ChemName{8} = 'IkBa';    % IkBa
```

```
27 c.ChemID.P  = 6;   c.ChemName{9} = 'P';    % pro-inflammatory ...
      response
28 c.ChemID.A  = 7;   c.ChemName{10} = 'A';    % anti-inflammatory ...
      response
29 % c.ChemID.En  = 11;   c.ChemName{11} = 'En';    % energetic response
30 c.ChemID.Nrf2  = 8;   c.ChemName{12} = 'Nrf2';    % Nrf2
31 c.ChemID.AO  = 9;   c.ChemName{13} = 'AO';    % Anti-oxidative ...
      species
32 % c.ChemID.mAO  = 14;   c.ChemName{14} = 'mAO';    % mRNA of ...
      anti-oxidative species
33 c.ChemID.ROS  = 10;   c.ChemName{15} = 'ROS';    % ROS
34
35
36 %%
37 ID = c.IDNum;     % A temporary variable for compartment IDs
38 CID = c.ChemID; % A temporary variable for chemical IDs
39
40 c.N_Comp = length(c.CompName); % No. of tissue compartments
41 c.N_Chem = length(c.ChemName);   % No. of different chemicals
42
43 %% ************ Biological parameters *********************
44 c.Density = 1.0;        % Body and tissue density
45 c.BW = 0.140;      % Reference BW for mice (in kg)[Wu et al., 2008]
46 c.BW_exp = 0.02482;  % BW of subject mice (C57J/BL6) (kg) [bw of ...
      male C57BL/6J WT is about the same]
47 %% *********** ozone dosimetry in pulmonary  ******************
48 c.K.pulmonary = 0.215; % 43% of O3 absorption in the Lower ...
      Respiration Tract(O3 ISA), 32%-66% of O3 in the alveolar ...
      region(Overton etal. 1987), thus 50% is used here. Therfore, ...
      43% * 50% = 21.5%;
49
50 %% *********** Cell parameters of lung  ******************
```

```
51 c.L.Mass = 0.43 .* c.BW_exp ./ c.BW;    % Mass of mouse lung(in ...
       g) [Based on 140g mouse in Wu et al., 2008]
52 c.L.Vol = 0.17/25 .* (c.BW_exp*1000);  % Total mouse lung vol ...
       (ml)(SimCYP)
53 c.L.Resp_rate = 1.5 * c.BW_exp; % Respiratory flow rate (L/min/kg ...
       BW) from Groves paper, 150 breath/min with tidal volume of 10 ...
       ml/kg-bw
54 c.L.N_AT2 = 9.13e7 .* c.L.Mass; % No. of Type II cells per g lung ...
       (Gurel et al.,2001)
55 c.L.N_AT1 = c.L.N_AT2 ./ 2; % No. of Type I cells per g lung ...
       (assumend half of AT2)
56 c.L.N_Mph = 1.66e5;   % No. of macrophages per mouse (Kubota et ...
       al.,1999)
57 c.L.N_ICell = 60e5;   % No. of Icells per lung (assumed half of ...
       macrophages)
58 c.L.N_LB = 150;      % No. of LB per Type II cell
59 c.L.AT2pool(CID.PL) = 10;    % PL pool size in Type II ...
       cells(mu-mol per g lung)
60 c.L.AT2pool(CID.SA) = 0.175;    % SA pool size in Type II ...
       cells(mu-mol per g lung)
61 c.L.AT2pool(CID.C) = 1.7848;    % C pool size in Type II ...
       cells(mu-mol per g lung)
62 c.L.PL_dens = 1.04;   % PL density (in g/ml)
63 c.L.BD_ratio = 0.0035/0.0146;  % Basal SP-B/SP-D ratio
64 %%%%%%%%%%%%%%%%%%%%%%%%%%%%%%%%%%%%%%%%%%%%%%%%%%%%%%%%%%%%%%%%
65 c.P.alv_area = 0.0082/0.3; % Avg. alveolar area(m2) per ml vol of ...
       lung (Knust et al.,2009)
66 c.P.alv_area = c.P.alv_area .* c.L.Vol; % (m2)
67 c.P.alv_thick = 0.2;   % Avg. thickness of alv. interface(mu-m)
68
69 %% Volume of various compartments (in ml for 0.43g lung)
70 c.V = ones(length(c.CompName),1);
71 c.V(ID.LB) = 2.2;
```

```
72  c.V(ID.AF) = 1.4;  % in ml (Moessinger et al., 1990)
73  c.V(ID.Int) = c.P.alv_area * c.P.alv_thick;
74  c.V(ID.AT2) = 1.51e-2;
75  c.V(ID.Mph) = 8.35e-5;
76  c.V = c.V .* c.L.Mass ./ 0.43;    % Scaling to actual subject lungs
77
78  %% ********** Initial and SS amounts  ******************
79  c.amount_init = zeros(c.N_Comp, c.N_Chem); % Initial amounts in ...
        body (mu-mol)
80  c.amount_init(ID.AT2,CID.PL) = c.L.AT2pool(CID.PL);
81  c.amount_init(ID.AT2,CID.SA) = c.L.AT2pool(CID.SA);
82  c.amount_init(ID.AT2,CID.C) = c.L.AT2pool(CID.C);
83  c.amount_init(ID.AF,CID.PL) = 0.0818; % See Page 89 Table 4.1
84  c.amount_init(ID.AF,CID.SA) = 0.0035; % See Page 89 Table 4.1
85  c.amount_init(ID.AF,CID.C) = 0.0146;  % See Page 89 Table 4.1
86  c.amount_init(ID.LB,CID.PL) = 1.14; % See Page 89 Table 4.1
87  c.amount_init(ID.LB,CID.SA) = 1.995e-2; % See Page 89 Table 4.1
88  c.amount_init(ID.LB,CID.C) = 6.84e-6;  % See Page 89 Table 4.1
89  c.amount_init(ID.Int,CID.PL) = 0;
90  c.amount_init(ID.Int,CID.SA) = 0;
91  c.amount_init(ID.Int,CID.C) = 0;
92
93  %
94  c.amount_init = c.amount_init .* c.L.Mass; % Scaling to lung weight
95
96  %% Add initial amounts for chemicals in the Cell compartment of ...
        the inflammation module
97  % c.amount_init(ID.Cell,CID.IKK) = 0;
98  c.amount_init(ID.Cell,CID.NFkB) = 0;
99  % c.amount_init(ID.Cell,CID.mIkBa) = 1;
100 % c.amount_init(ID.Cell,CID.IkBa) = 0;
101 c.amount_init(ID.Cell,CID.P) = 1;
102 c.amount_init(ID.Cell,CID.A) = 1;
```

```
103 % c.amount_init(ID.Cell,CID.En) = 1;
104 c.amount_init(ID.Cell,CID.Nrf2) = 0;
105 c.amount_init(ID.Cell,CID.AO) = 0;
106 % c.amount_init(ID.Cell,CID.mAO) = 1;
107 c.amount_init(ID.Cell,CID.ROS) = 0;
108
109 %% Equlibrium amount at interface
110 c.amount_eq(CID.PL) = 1.46; % See Page 89 Table 4.1
111 c.amount_eq(CID.SA) = 0.0301; % See Page 89 Table 4.1
112 c.amount_eq(CID.C) = 0.0151; % See Page 89 Table 4.1
113 c.amount_eq = c.amount_eq .* c.L.Mass; % Scaling to lung weight
114 %% *********  Surfactant Rate Constants  ***************************
115 % Rate constant for secretion into LB (per min)
116 c.K.Sec(CID.PL:CID.C) = 3.833e-5;
117 % Rate of LB release into BALF (per min)
118 c.K.LB = 0.002;
119 % Rate constant for recycling into cell (per min)
120 c.K.Re(CID.PL:CID.SA) = 1.798e-5;
121 c.K.Re(CID.C) = 9.63e-4;
122 % Constitutive secretion
123 c.K.DSec = 1.222e-4;
124 % Adsorption rate constant into Int (per min)
125 % c.K.Ads(CID.PL) = 3.795e-5;
126
127  c.K.Ads(CID.PL) = 1000;
128 c.K.Ads(CID.SA:CID.C) = 0.0402;
129 % Desorption rate constant from Int (per min)
130 c.K.Des(CID.PL:CID.C) = 0.0646;
131
132 %% ************ Surfactant Loss fractions  **********************
133 c.K.Loss.Deg(CID.PL) = 0.0466e-5; % Fractional loss due to ...
       degradation(PL)0.0466e-5
```

```
134 c.K.Loss.Deg(CID.SA) = 0.0611e-1; % Fractional loss due to ...
       degradation(SA)0.0611e-1
135 c.K.Loss.Deg(CID.C) = 0.0014; % Fractional loss due to ...
       degradation(C)0.0014
136 c.K.Loss.AW = 2.083e-5;   % Fractional loss to the airway
137
138 %% *********** Regulatory parameters ************************
139 c.K.Ads_SA = 7.312e4;  % Activation parameter of SA on PL ...
       adsorption(per umol/ml)
140 c.K.Ads_C = 2.185e5;   % Activation parameter of C on PL ...
       adsorption(per umol/ml)
141 c.K.LB_C = 1.7342e1;   % Inhibition parameter of C on LB ...
       exocytosis(per umol/ml)
142 c.K.PL.Re_C = 3.078e4; % Activation parameter of C on PL ...
       recycle(per umol/ml)
143
144 %% Rate constant for ozone reaction with surfactant components
145 c.K.O3_PL = 16262; % ml/(umol*min) from Kim et al. 2010, 4.5e-16 ...
       ml/(molecules*s)
146
147 c.K.O3_PL = 16.262*50;
148
149 c.K.O3_SA = c.K.O3_PL/0.37; % from Uppu et al 1995, table 3, ...
       relative reactivity c.K.O3_PL/0.37
150 c.K.O3_C = c.K.O3_PL/0.37;
151
152 %% Inflammation module related parameters
153
154 % NFkB related
155 c.k4 = 2.24;
156 c.k_NFkB1 = 16.294;
157 c.k_NFkB2 = 1.1861;
158 c.K_in_mIkBa = 0.46337;
```

```
159 c.k_IkBa1 = 13.273;
160 c.K_out_mIkBa = 0.46337;
161 c.k_I1 = 1.4;
162 c.k_I2 = 0.87;
163 c.k3 = 5;
164
165 % P,A,E related
166 c.K_in_P = 0.033116;
167 c.k_P_NFkB = 29.741;
168 c.k_P_E = 9.0505;
169 c.K_out_P = 0.332832358;
170 c.K_in_A = 0.46089;
171 c.k_A_E = 0.534;
172 c.k_A_SPD = 0.401;
173 c.K_out_A = 0.80952;
174 c.K_in_E =  0.08;
175 c.k_E_P = 2.216;
176 c.K_out_E = 0.25728;
177
178 % Nrf2 related
179 c.k_synNrf2 = 7.46924565238776;
180 c.k_degNrf2 = 0.0115428188310558;
181 c.k_synAO = 8.86676515958695;
182 c.k_degAO = 12.9865089720687;
183 c.k_mAO = 2.42456162185853;
184 c.k_syn_mAO = 14.6653411502872;
185
186 % ROS related
187 c.k_in_ROS = 1.32468364935054;
188 c.k_deg_ROS = 18.4718695869607;
189
190 %% Inflammation related for Hill version equations
191 % NFkB related
```

```
192 c.R_NFkB = 16.294;
193 c.x_NFkB_Nrf2 = 1;
194 c.deg_NFkB = 1.1861;
195
196 % Nrf2 related
197 c.R_Nrf2 = 7.46924565238776;
198 c.x_Nrf2_NFkB = 1;
199 c.deg_Nrf2 = 0.0115428188310558;
200 c.R_AO = 8.86676515958695;
201 c.deg_AO = 12.9865089720687;
202
203 % P A related
204 c.R_P = 0.033116;
205 c.x_P_NFkB = 1;
206 c.n_P_NFkB =1;
207 c.x_P_A = 1;
208 c.x_P_SPD = 1;
209 c.deg_P = 0.332832358;
210 c.R_A =0.46089;
211 c.x_A_AO = 1;
212 c.n_A_AO = 1;
213 c.deg_A = 0.80952;
214
215 % ROS related
216 c.R_ROS = 1.32468364935054;
217 c.x_ROS_AO = 1;
218 c.deg_ROS = 18.4718695869607;
219
220 % P effect on A
221 c.x_A_P = 1;
222 c.n_A_P = 1;
223
224 end
```

alv_config_O3.m

```
function c = alv_config_O3(i,PEEP,Pamp)
% This function defines the parameters for the alveolar R/D model
% Argument i represents species, i = 1(Mouse), 2(BN rat), 3 (SD rat), 4(Human)
% Argument PEEP, Pamp are in cmH2O
%% ***** Body weight (kg) and Pulmonary parameters **********
switch i
    case 1
        BW = 0.025;
        c.TLC = 1.175;
        c.FRC = 0.341;
        c.K_SK = 0.169; %(McGovern et al., 2013)
%         c.BR = 480; % Breathing rate (breaths per min) (Vaickus et al., 2010)

        c.BR = 150; % Breathing rate (breaths per min) (Grove et al., 2013)
        c.Qav = 67;  % Air flow rate (mL/min) (Vaickus et al., 2010)
    case 2
        BW = 0.15;
        c.TLC = 9.72;
        c.FRC = 3.91;
        c.K_SK = 0.2;
        c.BR = 105; % Breathing rate (breaths per min) (Strohl et al., 1997)
        c.Qav = 30 * (BW*1000/100); % Air flow rate (mL/min per 100g) (Strohl et al., 1997)
```

```
23      case 3
24          BW = 0.4;
25          c.TLC = 14.9;
26          c.FRC = 6.18;
27          c.K_SK = 0.2;      %(Ask et al., 2008)
28          c.BR = 92; % Breathing rate (breaths per min) (Strohl et ...
                al., 1997)
29          c.Qav = 30 * (BW*1000/100); % Air flow rate (mL/min per ...
                100g) (Strohl et al., 1997)
30      case 4
31          BW = 70;
32          c.TLC = 6800;
33          c.FRC = 2200;
34          c.K_SK = 0.2;
35          c.BR = 15; % Breathing rate (breaths per min)
36          c.Qav = 402000; % Air flow rate (mL/min) (Heathcote et ...
                al., 2011)
37  end
38
39  %% ***** Alveolar parameters ***************
40  c.Po_mu = 66;
41  c.Pc_mu = 66;
42  c.Po_sig = 3;
43  c.Pc_sig = 3;
44  c.So_beta = 0.465;
45  c.Sc_beta = 0.465;
46  c.N = 1250;
47  Q_mice = 67;  % Air flow rate for mice for scaling
48  c.Runit = 2500 * (c.Qav/Q_mice);   % R for alveolar unit ...
        (cmH2O/s/ml)(Massa et al.)
49  c.Eunit = 27500;   % E for alveolar unit (cmH2O/ml)(Massa et al.)
50  c.k_gamma = 0.5;
51  c.mu_fac = 1;       % Scaling factor
```

```
52 c.beta_fac = 1;      % Scaling factor
53 %% ********** Breathing parameters *************
54 c.PEEP = PEEP;          % PEEP (cmH2O)
55 c.VT = 10 * BW;       % Tidal vol. (ml)
56 c.Pamp = Pamp;         % Pressure amplitude (cmH2O)
```

alv_mech_O3.m

```
1  function [mu_Po, ...
       beta_So,gamma_PL_ratio,gamma_SA_ratio,gamma_ratio,eta_ratio] = ...
       alv_mech_O3(c, c_alv, PL, SA,PL_con,SA_con)
2  % ** This function estimates alveolar mechanical parameters
3  % mu_Po, mu_Pc, beta_So, beta_Sc
4  % Arguments are BAFs and parameters
5  % PL = Ratio of PL in alveolar fluid to baseline
6  % SA = Ratio of SA in alveolar fluid to baseline
7  % NP = total of NP & SfNP in alveolar fluid
8  % c = Physiological parameters for the species
9  % c_alv = Alveolar parameters
10 ID = c.IDNum;     % A temporary variable for compartment IDs
11 CID = c.ChemID; % A temporary variable for chemical IDs
12
13 eta_ratio = 1;
14
15 %% *************Adjust to DP's ...
       code*****************************************
16 C_PL_normal = c.amount_init(ID.AF,CID.PL) .* c.L.Mass ./ ...      %
17                 c.P.alv_area; % Normal free PL conc. in alveolar ...
                       fluid(mu-mol/m2)
18 C_SA_normal = c.amount_init(ID.AF,CID.SA) .* c.L.Mass ./ ...
```

```
                    c.P.alv_area; % Normal free SA conc. in alveolar ...
                        fluid(mu-mol/m2)   % ORIGINALLY FROM DP

%%
C_PL = C_PL_normal * PL;
C_SA = C_SA_normal * SA;



term = (C_PL ^ 1.6) / (0.01 + (C_PL ^ 1.6));
term0 = (C_PL_normal ^ 1.6) / (0.01 + (C_PL_normal ^ 1.6));

gamma_PL_ratio = (1 - term) / (1 - term0); % Fold change in gamma_PL
gamma_SA_ratio = (1 - C_SA) / (1 - C_SA_normal); % Fold change in ...
    gamma_SA
gamma_ratio = gamma_PL_ratio * gamma_SA_ratio;

mu_Po = 4.* gamma_ratio;
beta_So = 0.0313.* ((1/gamma_ratio) * (1/eta_ratio));
end
```

PV_O3.m

```
function res = PV_O3(c_alv, mu_Po, beta_So)
% ** This function estimates macroscopic pulmonary variables
% by adding volumes of alveolar units due to an input signal pressure
% It calls function openclose.m
% Output variables: [Pf,Vt,tf,xf,y,Nfr]

%% ********** Parameters *****************
N = c_alv.N;   % No. of alveolar units to be simulated
```

```
9
10 Vfrc = c_alv.FRC;   % FRC vol. (ml) Functional residual capacity
11 VT = c_alv.VT;     % Tidal vol. (ml)
12 PEEP = c_alv.PEEP;  % PEEP (cmH2O)
13 % Parameters for PV function for alveoli (Salazar-Knowles)
14 A = c_alv.TLC / N;     % ml (assuming the entire lung divided ...
       into N units)
15 B = c_alv.FRC / N;    % ml
16 K = c_alv.K_SK;       % 1/cmH2O
17 Vexp = A - B * exp(-K * PEEP); % Minimum vol. at the end of ...
       expiration (mL)
18 V0 = Vexp .* ones(N,1);       % Initial alveolar volumes (mL)
19 %% *********** Input pressure signal **************
20 Amp = c_alv.Pamp;            % Max Pressure amplitude (cmH2O)
21 T = 60/c_alv.BR;              % Period for pressure signal (secs)
22
23 %% *********** Primewave ******************
24 load Prime8_Ptr_time_series % Flexivent primewave data
25 load Primewave_freqs        % Flexivent frequencies
26
27 prime_time = t;         % Primewave time points (secs)
28 eval(['prime_pr = Ptr_PEEP', num2str(PEEP), ';']) % Primewave ...
       pressure vals (cmH2O)
29 % ***************************************
30 % Stages in pressure signal
31 stage1 = 0:0.05:30;      % Time series 1 for regular breathing (secs)
32 stage2 = stage1(end):0.05:30+3*T; % Time series 2 for deep ...
       breaths (secs)
33 stage3 = stage2(end) + prime_time'; % Time series 3 for Prime ...
       wave stage (secs)
34 t_series = [stage1(1:end-1),stage2(1:end-1),stage3];
35
36 Pamp1 = Amp * VT / Vfrc; % Pr. amplitude for stage 1
```

```
37 Pamp2 = Amp;              % Pr. amplitude for stage 2
38 P1 = (Pamp1 / 2) + (Pamp1 / 2) * sin(2*pi.*(stage1./T) + 1.5*pi) ...
       + PEEP; % for stage 1
39 P2 = (Pamp2 / 2) + (Pamp2 / 2) * sin(2*pi.*(stage2./T) + 1.5*pi) ...
       + PEEP;
40 P3 = prime_pr';
41 p_series = [P1(1:end-1), P2(1:end-1), P3];
42 %% ***********************************************
43 % sim.time = [0 30 30+3*T]; % Timepoints for pressure signal (sec)
44 % sim.time = [sim.time, sim.time(end) + prime_time];
45 % sim.delT = 0.05 .* ones(length(sim.time) - 1); % Time intervals ...
       (sec)
46 %sim.delT(end) = 0.1666;   % Bigger delT for regular inflations
47 % sim.Pamp = (Amp * VT / Vfrc) .* ones(length(sim.time) - 1); % P ...
       amplitudes (cmH2O)
48 % sim.Pamp(2) = Amp;  % Pressure for deep breaths (cmH2O)
49
50 % tp = 0:0.1:Ncyc*T;   % Time array for pressure signal (secs)
51 % P = (Amp/2) + (Amp/2) * sin(2*pi*(tp/T) + 1.5*pi);      % ...
       Pressure signal (cmH2O)
52
53 %% **** Generating random values for individual airways *****
54 Pcrit = zeros(N,2);    % Critical opening & closing pressure
55 Pcrit(:,1) = normrnd(mu_Po,c_alv.Po_sig,N,1);
56 % Pcrit(:,2) = normrnd(Pc,sig_Pc,N,1);
57 Pcrit(:,2) = Pcrit(:,1);     % Same opening & closing pressures
58 s = zeros(N,2);          % Opening & closing rates
59 s(:,1) = beta_So ./ unifrnd(0,1,N,1);
60 s(:,2) = s(:,1);        % Same opening & closing rates
61
62 %% This is Massa et al. 2008
63 % Excellent fits to the data were obtained when the normally ...
       distributed critical
```

```
% opening pressures were about 5 cmH2O above the closing ...
    pressures and
% when the hyperbolically distributed opening velocities were ...
    about an order of magnitude greater than the closing velocities.
Pcrit(:,2) = max(0,Pcrit(:,1)-5);
s(:,2) = s(:,1)./10;

Ri = repmat(c_alv.Runit, N, 1);   % Spatially homogenous units
Ei = repmat(c_alv.Eunit, N, 1);   % Spatially homogenous units
%% ************** PV computation ******************
% Input pressure
x0 = zeros(N,1);       % Initial state of alveoli (0=closed, 1 = ...
    open)
% Pf = [];        % Array of all values of pressure (cmH2O)
% tf = [];        % Array of all time points (sec)
Vt = [];        % Array of volumes (ml)
yf = [];        % Array of open-close statuses (binary)
Po = Pcrit(:,1); Pc = Pcrit(:,2); so = s(:,1); sc = s(:,2);
% ************* Quasi-static simulation ***************
xf = yf;
%nstages = length(sim.delT);   % No. of static stages
% for i = 1:nstages
%     timestart = sim.time(i);
%     timeend = sim.time(i+1);
%     timeint = sim.delT(i);
%     time = timestart:timeint:timeend;
%     Pmax = sim.Pamp(i);
%     P = (Pmax/2) + (Pmax/2) * sin(2*pi.*(time./T) + 1.5*pi) + ...
    PEEP;      % Pressure signal (cmH2O)
for j = 1:length(t_series)-1
    timeint = t_series(j+1) - t_series(j); % Length of time interval
    P = p_series; % Pr. time series
    x = x0;
```

```
93      x(x0 < 1) = so(x0 < 1) .* (P(j) - Po(x0 < 1)) .* timeint + ...
            x0(x0 < 1);
94      x(x0 > 0) = sc(x0 > 0) .* (P(j) - Pc(x0 > 0)) .* timeint + ...
            x0(x0 > 0);
95      x(x > 1) = x(x > 1) ./ x(x > 1); % Binding x to 1
96      x(x < 0) = x(x < 0) + abs(x(x < 0)); % Binding x to 0
97      y = openclose(x,x0);  % Compute open/close status (N X 1)
98      Pi = repmat(P(j), N, 1); % Same input pressure for all units
99      Q = (y ./ Ri) .* (Pi - V0 .* Ei);  % Flow rates (N X 1) (ml/s)
100     Valv = V0 + timeint .* Q;     % Update volumes based on flow ...
            rate (ml)
101     x0 = x;
102     V0 = Valv;
103     Vt = [Vt, sum(Valv)];
104     yf = [yf, y];
105     xf = [xf, x];
106 end
107
108 Pf = p_series(1:end-1);
109 tf = t_series(1:end-1);
110
111 % s = size(xf)
112 % s1 = size(Pf)
113 % y = openclose(xf);                    % Compute open/close ...
        status (N X t)
114 % V = A - B * exp(-K*Pf);               % Salazar-Knowles equation
115 % Valv = zeros(N, length(V));          % Final alveolar volumes (ml)
116
117 % for i = 1:length(tf)
118 %     yi = y(:,i);           % Open/close statuses at that time ...
        (N X 1)
119 %     Valv(yi == 0,i) = V0(yi == 0,1); % Alveoli closed; takes ...
        last alveolar vol.
```

```
120 %     Valv(yi == 1,i) = repmat(V(i), length(yi(yi == 1)), 1); % ...
      Alveoli open
121 %     V0(yi == 1) = repmat(V(i), length(yi(yi == 1)), 1);   % ...
      Update V0
122 % end
123
124 % Vt = sum(Valv, 1);   % Total volume of all alveolar units (ml)
125 Pcr = Pcrit(:,1);
126 Nfr = sum(yf) ./ N; % Fractional recruitment at each time point
127 res.Pf = Pf; res.Vt = Vt; res.tf = tf; res.xf = xf; res.y = yf;
128 res.Nfr = Nfr;
129 res.freq = freq;
130 res.prime_t = prime_time;
131 %% Plotting
132 % subplot(1,3,1)
133 % plot(res.tf, res.Pf)
134 % title('Time vs pressure')
135 % subplot(1,3,2)
136 % plot(res.tf, res.Vt)
137 % title('Time vs volume')
138 % subplot(1,3,3)
139 % plot(res.tf, res.Nfr)
140 % title('Time vs Fr.recruit')
141
142 end
```

O3_Cons_fit.m

```
1 function [R,I,G,H] = O3_Cons_fit(Zw, freq)
2 % This function fits real and imaginary parts of freq. domain ...
      lung impedance to
```

```
% the Constant Phase Model and calculates the parameters R,G,H
% Argument Zw contains freq. domain lung impedance values
% Freq contains the array of freqs. corr. to the impedance values

R0 = 0.2997; I0 = 0.58e-3; G0 = 3.6892; H0 = 149.9555;

x0 = [R0,I0,G0,H0];      % Initial estimates for data fitting


options = optimset('MaxFunEvals',20000);
lb = [0 0 0 0];

[R,I,G,H] = fmincon(@func,x0,[],[],[],[],lb,[],[],options,Zw);
% [R,I,G,H] = fminsearch(@func,x0,options,Zw);

function f = func(x,Zw)
% This function constructs the Constant Phase Model equations
% and calculates errors between model and results
% Argument x contains R, G, H
% Argument imp contains the exp values of ZR and ZI
freq = [0.5 0.75 1.25 1.75 2.75 3.25 4.25 4.75 5.75 7.25 9.25 ...
    10.25...
          11.75 14.75 16.75 18.25 19.75];
R = x(1).*ones(size(freq));
I = x(2).*ones(size(freq));
G = x(3).*ones(size(freq)); H = x(4).*ones(size(freq));
om = 2 * pi .* freq;
alpha = (2/pi).*atan(H./G);
ZR_sim = G./(om.^alpha) + R;
ZI_sim = I.*om - H./(om.^alpha);
ZR_exp = real(Zw); ZI_exp = imag(Zw);
err1 = (ZR_sim - ZR_exp).^2;
err2 = (ZI_sim - ZI_exp).^2;
```

```
35 f = sum(err1 + err2);
36 end
37
38 end
```

time2freq.m

```
1  function f_data = time2freq(time_data,freq,mag)
2  % This function converts time domain data to frequency domain
3  % using the Fast Fourier Transform algorithm
4  % Argument time_data is the time domain data
5  % freq is the array of frequencies
6  % mag is a decision variable taking 1 if magnitude of the ...
       transformed data is required and
7  % 0 if the transformed data is reqd in complex form
8
9  Nt = length(time_data);  % Length of time data
10 Nf = length(freq);       % Length of freqeuncy array
11
12 NFFT = 2^nextpow2(Nt);
13 Fs = Nt / (Nf - 1);
14 f = Fs .* linspace(0,1,NFFT/2 + 1);
15 %% ****** Finding indices of resonant frequencies ******
16 ids = zeros(1,Nf);
17 i = 1;
18 for F = freq
19     fr = repmat(F,1,length(f));
20     tmp = abs(f - fr);
21     [tmp, id] = min(tmp);
22     ids(i) = id;
23     i = i + 1;
```

```
24 end
25
26 %% *********** Finding Amplitudes at Resonant Frequencies ****
27 data_f = fft(time_data,NFFT);
28 if mag == 1
29     f_data = abs(data_f(ids));
30 else
31     f_data = data_f(ids);
32 end
33 end
```

CPM.m

```
1  function [ZR, ZI] = CPM(params, freq)
2  % Constant Phase Model
3  % params is a 1X4 array containing R, I, G, H
4
5  R = params(1).*ones(size(freq));
6  I = params(2).*ones(size(freq));
7  G = params(3).*ones(size(freq));
8  H = params(4).*ones(size(freq));
9
10 om = 2 * pi .* freq;
11 alpha = (2/pi) .* atan(H./G);
12 ZR = G./(om.^alpha) + R;
13 ZI = I.*om - H./(om.^alpha);
14 end
```